

## INFORMATION TO USERS

This manuscript has been reproduced from the microfilm master. UMI films the text directly from the original or copy submitted. Thus, some thesis and dissertation copies are in typewriter face, while others may be from any type of computer printer.

**The quality of this reproduction is dependent upon the quality of the copy submitted.** Broken or indistinct print, colored or poor quality illustrations and photographs, print bleedthrough, substandard margins, and improper alignment can adversely affect reproduction.

In the unlikely event that the author did not send UMI a complete manuscript and there are missing pages, these will be noted. Also, if unauthorized copyright material had to be removed, a note will indicate the deletion.

Oversize materials (e.g., maps, drawings, charts) are reproduced by sectioning the original, beginning at the upper left-hand corner and continuing from left to right in equal sections with small overlaps.

ProQuest Information and Learning  
300 North Zeeb Road, Ann Arbor, MI 48106-1346 USA  
800-521-0600

UMI<sup>®</sup>



University of Alberta

Photonic Crystal Engineering in Glancing Angle Deposition Thin Films

by

Hans Martin Overgaard Jensen



A thesis submitted to the Faculty of Graduate Studies and Research in  
partial fulfillment of the requirements for the degree of Doctor of Philosophy

Department of Electrical and Computer Engineering

Edmonton, Alberta  
Spring 2005



Library and  
Archives Canada

Bibliothèque et  
Archives Canada

0-494-08253-4

Published Heritage  
Branch

Direction du  
Patrimoine de l'édition

395 Wellington Street  
Ottawa ON K1A 0N4  
Canada

395, rue Wellington  
Ottawa ON K1A 0N4  
Canada

*Your file* *Votre référence*

*ISBN:*

*Our file* *Notre référence*

*ISBN:*

#### NOTICE:

The author has granted a non-exclusive license allowing Library and Archives Canada to reproduce, publish, archive, preserve, conserve, communicate to the public by telecommunication or on the Internet, loan, distribute and sell theses worldwide, for commercial or non-commercial purposes, in microform, paper, electronic and/or any other formats.

The author retains copyright ownership and moral rights in this thesis. Neither the thesis nor substantial extracts from it may be printed or otherwise reproduced without the author's permission.

#### AVIS:

L'auteur a accordé une licence non exclusive permettant à la Bibliothèque et Archives Canada de reproduire, publier, archiver, sauvegarder, conserver, transmettre au public par télécommunication ou par l'Internet, prêter, distribuer et vendre des thèses partout dans le monde, à des fins commerciales ou autres, sur support microforme, papier, électronique et/ou autres formats.

L'auteur conserve la propriété du droit d'auteur et des droits moraux qui protègent cette thèse. Ni la thèse ni des extraits substantiels de celle-ci ne doivent être imprimés ou autrement reproduits sans son autorisation.

---

In compliance with the Canadian Privacy Act some supporting forms may have been removed from this thesis.

Conformément à la loi canadienne sur la protection de la vie privée, quelques formulaires secondaires ont été enlevés de cette thèse.

While these forms may be included in the document page count, their removal does not represent any loss of content from the thesis.

Bien que ces formulaires aient inclus dans la pagination, il n'y aura aucun contenu manquant.

  
**Canada**

# Abstract

From living rooms to operating rooms, our world is becoming dependent on information technology. For half a century a transformation in computing and communications has been borne by semiconductor microelectronics, but to serve us tomorrow, new materials transcending the performance and cost of current technology must be developed. An emerging optical material is the photonic bandgap crystal, which so fundamentally manipulates the emission and propagation of light that photons may be harnessed to eclipse what electronics accomplish today. However, the crystals consist of intricate, sub-micrometre structures that are complex to fabricate, and even harder to engineer for technological applications. Indeed, fabrication challenges have inhibited photonic crystal progress. This thesis responds by enabling photonic crystal engineering through a chiral thin film fabrication technique known as glancing angle deposition. By oblique vapour deposition onto rotating substrates, the approach creates tetragonal lattices of square spirals with widths of a few hundred nanometres, predicted to yield strong photonic bandgaps at useful optical wavelengths. Within the scope of the thesis research, high resolution, high density direct write lithography is developed

to deliver large area crystal substrates with extensive design freedom. The evolution of square spiral photonic crystal thin films on such substrates is analyzed, and new deposition methods are devised to allow engineering of the photonic bandgap by reducing the dimensions and enhancing the fine structure of the square spirals. Optical characterization is performed to evaluate the presence of a complete, three dimensional photonic bandgap, confirm an engineered bandgap at  $1.65 \mu\text{m}$ , and quantify the improvement in crystal quality to a bandgap width of 10.9%. With a potential for use as photonic waveguides, the engineering of embedded, functional air and dielectric defects is also established. Furthermore, the thesis develops solutions to enhance existing applications of glancing angle deposition thin films, including the ability to control the porosity and generate nanoscale, fibrous film morphologies. Microfluidic networks are demonstrated as a new application of columnar thin films. Through the achievement of crystal engineering in square spiral thin films, the thesis seeks to contribute to the realization of photonic crystals as a key technology for a demanding future.

# Acknowledgement

This thesis for the degree of *Philosophiæ Doctor* is the final product of many years of learning and studying. I am indebted to all who inspired and supported me along the way.

Since the earliest transatlantic correspondence on the possibility of a graduate career at the University of Alberta, my supervisor Prof. Michael Brett has provided an outstanding setting for my research. With his openness to entertain new research idea, his constant efforts to build laboratory resources, and a network of contacts that few other senior professors can match, I have enjoyed great academic freedom. Yet, what has really made my graduate experience so rewarding is that Mike Brett puts his students first, and places his full confidence in them. It has been a privilege to be a part of his Group, and I am truly grateful to Mike for all that he has done for me.

Among the past and present colleagues in the GLAD Research Group at the University of Alberta, I wish to acknowledge Dr. Scott Kennedy for his initial work on GLAD photonic crystals, and thank Dr. Gregory Kiema for having been a patient and cheerful research partner on the GLAD micro-

fluidics project. I also want to thank Barb Djurfors for the TEM work, Dr. Mary Seto for help with the nanoindentation experiments, Dr. Doug Vick, Andy van Popta, and Peter Hrudey for numerous stimulating scientific and technical discussions, and the rest of the Group for proofreading the thesis. Karin Hayward has supplied invaluable logistical assistance and chocolates.

Much of my research was performed at the University of Alberta Micro-machining and Nanofabrication Facility. I would like to thank Dr. Ken Westra for readily dispensing his vast knowledge of microfabrication and for striving to build a world-class facility, and Keith Franklin for tirelessly ensuring that said facility operates. Staff members Steph, Mirwais and Aruna gave me choice assistance whenever I asked for help. If it is true that a picture says more than a thousand words, then I owe George Braybrook of the Department of Earth and Atmospheric Sciences an encyclopedia. His exceptional skills in sub micrometre imaging shine through in the hundreds of electron micrographs critical to the thesis.

As a student I have been blessed with splendid teachers. These are people dedicated to a very noble profession, and I thank them all for the gift of education. Among them, I want to pay special tribute to Ole Hansen of the Technical University of Denmark, and to Erik Strandgaard Andersen of the Langkær Gymnasium high school, for inspiring and challenging me and hence sending me down the road to this thesis.

On a more personal note I want to express my deepest gratitude to my family for their love and encouragement throughout my years as a student. My parents Birgitta and Jens always provided the best possible environment

for a child to learn, and are the foundation from which any achievements of mine derive. Beating me to the Ph.D. degree by two years, my sister Anna is the example to follow in academic excellence and the pursuit of new frontiers. And with every letter and colourful drawing received from my sister Kirsten and her family, I have been reminded of their unwavering support even across oceans.

I also wish to thank the Norbys of Edmonton for their incredible hospitality and generosity, which have encompassed not only setting me up like a local, but supplying me with an honours degree in Albertan culture.

Finally, I extend my sincerest gratitude to the agencies and foundations which have backed my research and education: The Alberta Ingenuity Fund, The Danish State Education Grant Scheme, The Alberta Informatics Circle of Research Excellence, The University of Alberta, The Peter and Emma Thomsen Foundation, The Marie and M. B. Richter Foundation, The Reinholdt W. Jorck Foundation, The Julie Damm Foundation for Education, The Vera and Carl Johan Michaelsen Foundation, The Unidanmark Foundation, The Thomas B. Thrige Foundation for Education, The Valdemar Selmer Trane and Elisarane Foundation, The Otto Mønsted Foundation, The Julie Marie Hansen Foundation, The Frants Alling Foundation, The Henry and Mary Skov Foundation, and The Alexandre Haynman and Nina Haynman Foundation.

# Contents

<b>1</b>	<b>Introduction</b>	<b>1</b>
1.1	Context . . . . .	1
1.2	Objectives . . . . .	2
1.3	Scope and Structure . . . . .	3
<b>2</b>	<b>The Promise of Photonic Bandgap Crystals</b>	<b>7</b>
2.1	The Origins . . . . .	8
2.2	The Theory of Photonic Crystals . . . . .	9
2.2.1	Electrodynamics in Periodic Media . . . . .	9
2.2.2	Photonic Bandgaps . . . . .	12
2.2.3	Electromagnetic Energy and Scaling . . . . .	14
2.3	Properties and Characteristics of Photonic Crystals . . . . .	15
2.3.1	Group Velocity . . . . .	15
2.3.2	Modified Radiative Emission . . . . .	16
2.3.3	Light Localization . . . . .	17
2.4	Photonic Crystal Architectures and Fabrication . . . . .	19
2.4.1	Basic Crystal Requirements . . . . .	20

## CONTENTS

2.4.2	Modelling . . . . .	21
2.4.3	Fabrication of Three Dimensional Photonic Crystals . . . . .	21
2.4.4	Yablonovite . . . . .	22
2.4.5	Woodpile . . . . .	24
2.4.6	Inverse Opals . . . . .	25
2.4.7	Two Dimensional Photonic Crystals . . . . .	26
2.5	Applications of Photonic Bandgap Crystals . . . . .	27
2.5.1	Waveguides . . . . .	27
2.5.2	Integrated Photonics . . . . .	30
2.5.3	Optoelectronics . . . . .	31
2.6	Looking Ahead . . . . .	33
<b>3</b>	<b>Glancing Angle Deposition Thin Films</b>	<b>35</b>
3.1	The Science of Thin Film Growth . . . . .	36
3.1.1	Nucleation and Film Growth . . . . .	36
3.1.2	Film Characteristics and Structure Zone Models . . . . .	39
3.2	The Technology of Thin Film Deposition . . . . .	41
3.2.1	Physical Vapour Deposition by Evaporation . . . . .	42
3.2.2	Physical Vapour Deposition by Sputtering . . . . .	44
3.3	The Fundamentals of Glancing Angle Deposition . . . . .	45
3.3.1	The History of Oblique Thin Film Deposition . . . . .	45
3.3.2	Definition of Glancing Angle Deposition . . . . .	47
3.3.3	The Science of Glancing Angle Deposition Thin Films . . . . .	47
3.3.4	The Technology of Glancing Angle Deposition . . . . .	55
3.4	Characteristics and Applications of GLAD Thin Films . . . . .	57

## CONTENTS

3.4.1	Characteristics and Advantages of GLAD Films . . . . .	57
3.4.2	Properties and Applications of GLAD Films . . . . .	63
<b>4</b>	<b>The Proposition of PBC Engineering in GLAD Thin Films</b>	<b>67</b>
4.1	Helical Photonic Crystal Architectures . . . . .	67
4.1.1	Circular Helical Architectures . . . . .	67
4.1.2	Polygonal Helical Architectures . . . . .	69
4.2	Square Spiral GLAD Photonic Crystals . . . . .	72
4.2.1	Matching Architecture and Fabrication . . . . .	72
4.2.2	Theoretical and Practical Merits . . . . .	72
4.2.3	The History of GLAD Square Spirals . . . . .	73
4.3	Enabling GLAD for Photonic Crystal Engineering . . . . .	75
<b>5</b>	<b>Seed Layer Design and Fabrication</b>	<b>77</b>
5.1	The Principles of Periodic GLAD Films . . . . .	77
5.2	Design of Seed Layers . . . . .	79
5.3	Fabrication of Seed Layers . . . . .	83
5.3.1	Lithographic Requirements . . . . .	83
5.3.2	Electron Beam Lithography . . . . .	84
5.3.3	Laser Direct Write Lithography . . . . .	88
5.4	SU-8 as a Negative Electron Beam Resist . . . . .	90
5.5	Seed Layers Fabricated using Electron Beam Lithography . . . . .	94
5.5.1	EBL System Optimization . . . . .	94
5.5.2	Seed Layers in PMMA . . . . .	96
5.5.3	Seed Layers in SU-8 . . . . .	100
5.6	Seed Layers Fabricated using Laser Direct Write Lithography . . . . .	103

## CONTENTS

5.6.1	Hardware Optimization . . . . .	103
5.6.2	Seed Layer Fabrication . . . . .	104
5.6.3	Seed Layers on Transparent Substrates . . . . .	107
<b>6</b>	<b>Growth and Characteristics of Periodic GLAD Films</b>	<b>109</b>
6.1	The Importance of Periodically Structured GLAD Films . . .	110
6.2	Growth Evolution of Periodic GLAD Films . . . . .	111
6.2.1	Experimental Details . . . . .	111
6.2.2	Nucleation . . . . .	111
6.2.3	Column Growth . . . . .	114
6.2.4	Suppression of Inter-Seed Growth . . . . .	117
6.2.5	Impact of Seed Layer Design . . . . .	119
6.3	Characteristics of Periodic GLAD Films . . . . .	123
6.3.1	Film Uniformity . . . . .	124
6.3.2	Column Uniformity . . . . .	126
6.3.3	Elimination of Column Chaining . . . . .	127
6.3.4	Suppression of Column Competition . . . . .	128
6.3.5	Film Structure Control . . . . .	129
<b>7</b>	<b>Bandgap Engineering: Square Spiral PBC Fabrication</b>	<b>131</b>
7.1	GLAD PBC Design Considerations . . . . .	131
7.2	Fabrication and Materials Considerations . . . . .	134
7.2.1	Substrate Seed Layers . . . . .	134
7.2.2	Materials . . . . .	135
7.2.3	Square Spiral GLAD Deposition . . . . .	137
7.3	Scaling of Square Spiral GLAD Films . . . . .	138

## CONTENTS

7.3.1	Growth Iterations . . . . .	138
7.3.2	Scaling Results . . . . .	141
7.4	Challenges of Square Spiral GLAD Growth . . . . .	144
7.4.1	Spiral Arm Broadening . . . . .	144
7.4.2	Column Cross-Section and Fanning . . . . .	147
7.4.3	Column Bifurcation and Spiral Corners . . . . .	150
7.5	Advanced GLAD Growth Algorithms . . . . .	152
7.6	The PhiSweep GLAD Algorithm . . . . .	153
7.6.1	Definition of the PhiSweep Method . . . . .	153
7.6.2	PhiSweep GLAD PBC Films . . . . .	155
7.6.3	Evaluation of PhiSweep GLAD . . . . .	158
7.7	The Off-Axis GLAD Algorithm . . . . .	161
7.7.1	Definition of the Off-Axis Method . . . . .	161
7.7.2	Off-Axis GLAD PBC Films . . . . .	163
7.7.3	Evaluation of Off-Axis GLAD . . . . .	164
<b>8</b>	<b>Bandgap Engineering: Optical Characterization</b>	<b>169</b>
8.1	Methodology . . . . .	169
8.1.1	Transmittance and Reflectance . . . . .	169
8.1.2	Instrumentation Requirements . . . . .	170
8.1.3	FTIR Spectrometry . . . . .	171
8.1.4	Spectrophotometry . . . . .	172
8.2	GLAD PBC Bandgap Verification . . . . .	174
8.2.1	Initial Spectral Response . . . . .	174
8.2.2	Confirming the Bandgap: Reflectance . . . . .	174

## CONTENTS

8.2.3	Confirming the Bandgap: Transmittance . . . . .	180
8.2.4	Optical References . . . . .	182
8.3	GLAD PBC Bandgap Characterization . . . . .	183
8.3.1	Directional Invariance of the Bandgap: Reflectance . .	184
8.3.2	Directional Invariance of the Bandgap: Transmittance	187
8.3.3	Polarization Invariance of the Bandgap . . . . .	188
8.4	Interpretation and Evaluation . . . . .	192
8.4.1	A Real and Complete Photonic Bandgap . . . . .	192
8.4.2	Bandgap Engineering . . . . .	192
8.4.3	Bandgap Enhancement and Comparison with Theory	193
<b>9</b>	<b>Defect Engineering in GLAD Films</b>	<b>201</b>
9.1	Defect Engineering in GLAD PBCs . . . . .	201
9.2	Seed Layer Induced Defect Engineering . . . . .	206
9.2.1	The Principles of Seed Layer Induced Defects . . . . .	206
9.2.2	Seed Layer Defect Design Rules . . . . .	207
9.2.3	Seed Layer Defect Fabrication . . . . .	208
9.3	Traditional GLAD Defect Engineering . . . . .	209
9.4	PhiSweep GLAD Defect Engineering . . . . .	213
9.4.1	Air Filled PhiSweep GLAD Defects . . . . .	215
9.4.2	Evaporant Filled PhiSweep GLAD Defects . . . . .	217
9.4.3	The Mechanisms of PhiSweep Defect Engineering . . .	219
9.5	Applications and Advanced Defects . . . . .	224
9.6	Toward GLAD PBC Waveguides . . . . .	225
9.6.1	Seed Layer Induced Waveguides . . . . .	225

## CONTENTS

9.6.2	Multilayer Waveguides . . . . .	228
<b>10</b>	<b>Porosity Engineering and Nanofibrous GLAD Films</b>	<b>231</b>
10.1	The Context of Porosity Engineering . . . . .	231
10.2	Aperiodic PhiSweep GLAD Films . . . . .	232
10.3	Analysis of PhiSweep and Nanofibrous GLAD Films . . . . .	237
10.3.1	SEM Analysis and Film Density . . . . .	237
10.3.2	TEM and EDX Analyses . . . . .	239
10.3.3	The Realization of Porosity Engineering . . . . .	241
10.4	The Mechanisms of PhiSweep and Nanofibrous GLAD . . . . .	242
10.5	The Impact of Porosity Engineering in GLAD Film . . . . .	248
10.6	Characteristics of Nanofibrous GLAD Films . . . . .	248
10.6.1	Surface Area Estimates . . . . .	248
10.6.2	Mechanical Properties . . . . .	249
<b>11</b>	<b>Microfluidics in GLAD Films</b>	<b>253</b>
11.1	The Principles of GLAD Microfluidics . . . . .	253
11.2	Design and Implementation of GLAD Microfluidic Networks .	257
11.3	Demonstration of Flow in a GLAD Microfluidic Network . . .	259
<b>12</b>	<b>Conclusions and Perspectives</b>	<b>265</b>
12.1	Summary of Results . . . . .	265
12.2	Thesis Perspectives . . . . .	269
	<b>Bibliography</b>	<b>273</b>

# List of Tables

7.1	Seed lattice periods and ideal square spiral dimensions . . .	134
7.2	Square spiral dimensions on 700 nm seed lattices . . . . .	139
7.3	Optimized square spiral dimensions on various seed lattices .	141
8.1	Bandgap position for high frequency GLAD PBC . . . . .	194

# List of Figures

2.1	The diamond lattice PBC and its band structure . . . . .	12
2.2	The density of states and transmission spectrum for a PBC .	17
2.3	Light localization in a point defect . . . . .	18
2.4	Light localization in a line defect . . . . .	19
2.5	The Brillouin zone of the FCC lattice . . . . .	20
2.6	The yablonovite architecture . . . . .	23
2.7	The woodpile architecture . . . . .	24
2.8	The inverse opal architecture . . . . .	25
2.9	Waveguiding in woodpile 3D PBCs . . . . .	28
2.10	Lasing in a 2D PBC . . . . .	32
3.1	The nucleation of thin films . . . . .	37
3.2	Movchan and Demchishin's structure zone model . . . . .	40
3.3	The components of a physical vapour deposition system . . .	42
3.4	The glancing angle deposition setup . . . . .	48
3.5	A slanted post GLAD film . . . . .	49
3.6	The formation of a slanted post GLAD film . . . . .	50

## LIST OF FIGURES

3.7	Tait's Rules for column inclination and volume fill factor . . .	52
3.8	A square spiral GLAD film . . . . .	53
3.9	The formation of a polygonal chiral GLAD film . . . . .	54
3.10	A typical GLAD system . . . . .	56
3.11	A chevron GLAD film . . . . .	58
3.12	Circular helical GLAD films . . . . .	59
3.13	A vertical post GLAD film . . . . .	60
3.14	The interaction between GLAD films and liquid crystals . . .	64
3.15	A perforated GLAD thin film . . . . .	66
4.1	The diamond lattice as a collection of spirals . . . . .	68
4.2	The square spiral 3D PBC architecture . . . . .	69
4.3	The band structure for a square spiral 3D PBC . . . . .	70
4.4	Reflectance spectra for a square spiral PBC structure . . . . .	74
5.1	The principle of substrate seed layers . . . . .	79
5.2	Substrate seed layer design parameters . . . . .	80
5.3	An electron beam lithography system . . . . .	87
5.4	The acousto-optic modulator and deflector . . . . .	89
5.5	A laser direct write lithography system . . . . .	90
5.6	The chemical structure of the epoxy novolak SU-8 . . . . .	92
5.7	Spin curves for SU-8 . . . . .	93
5.8	High resolution EBL line patterns in SU-8 negative resist . . .	94
5.9	Write field stitching in EBL . . . . .	95
5.10	Spin curves for PMMA . . . . .	97
5.11	An EBL test pattern in PMMA . . . . .	98

## LIST OF FIGURES

5.12	EBL seed layers in PMMA: Top views . . . . .	99
5.13	EBL seed layers in PMMA: Oblique views . . . . .	100
5.14	EBL seed layers in SU-8: Top views . . . . .	101
5.15	EBL seed layers in SU-8: Oblique views . . . . .	102
5.16	Amplification of single pixel EBL seeds . . . . .	103
5.17	LDWL seed layers: Top views . . . . .	105
5.18	LDWL seed layers: Oblique views . . . . .	106
5.19	Large area LDWL seed layers . . . . .	107
6.1	The nucleation of GLAD films on substrate seed layers . . .	112
6.2	Film nucleation on a single seed . . . . .	114
6.3	Stages of periodic GLAD film growth . . . . .	115
6.4	The conformity of GLAD films to seed layers . . . . .	116
6.5	The uniformity of periodic GLAD films . . . . .	117
6.6	The origin of inter-seed growth . . . . .	118
6.7	Inter-seed growth in a periodic square spiral GLAD film . .	119
6.8	The impact of seed aspect ratio . . . . .	120
6.9	The impact of seed layer planar fill factor . . . . .	121
6.10	Simulations of the impact of the seed layer design . . . . .	122
6.11	Periodic and aperiodic GLAD films: Top view . . . . .	124
6.12	Periodic and aperiodic GLAD films: Oblique view . . . . .	125
6.13	Periodic and aperiodic GLAD films: Side view . . . . .	126
6.14	Column chaining in aperiodic GLAD films . . . . .	127
7.1	Square spiral GLAD growth on low aspect ratio seeds . . . .	135
7.2	Iterations of GLAD growth on 700 nm period seed lattices .	140

## LIST OF FIGURES

7.3	GLAD square spiral growth on various seed lattices . . . . .	142
7.4	A single square spiral from traditional GLAD growth . . . . .	143
7.5	Spiral arm broadening in square spiral GLAD films . . . . .	145
7.6	Broadening of seeded and inter-seed columns . . . . .	146
7.7	The origins of spiral arm broadening . . . . .	147
7.8	Column fanning in square spiral GLAD films . . . . .	148
7.9	Crescent shaped column cross-sections . . . . .	149
7.10	The origins of column fanning . . . . .	150
7.11	Simulation of column fanning in periodic GLAD films . . . . .	151
7.12	Suppression of column bifurcation with ‘slow corners’ . . . . .	152
7.13	The principle of the PhiSweep GLAD growth algorithm . . . . .	154
7.14	Simulation of PhiSweep square spirals . . . . .	155
7.15	PhiSweep square spiral films with varying sweep angles . . . . .	156
7.16	Cross-section of PhiSweep square spirals . . . . .	157
7.17	A PhiSweep GLAD PBC film . . . . .	158
7.18	Suppression of inter-seed growth in PhiSweep films . . . . .	159
7.19	The principle of the Off-Axis GLAD growth algorithm . . . . .	162
7.20	Off-Axis square spiral GLAD films: Side views . . . . .	164
7.21	Off-Axis square spiral GLAD films: Oblique views . . . . .	165
7.22	Cross-section of Off-Axis square spirals . . . . .	166
7.23	A single square spiral from Off-Axis GLAD growth . . . . .	167
8.1	Reflectance of square spiral films with varying dimensions . . . . .	177
8.2	Reflectance of the constituents in GLAD PBC samples . . . . .	179
8.3	Transmittance of GLAD square spiral film . . . . .	180

*LIST OF FIGURES*

8.4 Transmittance of the constituents in GLAD PBC samples . 181

8.5 Reflectance of GLAD PBC at various light incidence angles . 184

8.6 Reflectance of GLAD PBC at various crystal orientations . . 187

8.7 Reflectance of low frequency GLAD PBC . . . . . 188

8.8 Transmittance of GLAD PBC at various incidence angles . . 189

8.9 Transmittance of low frequency GLAD PBC . . . . . 190

8.10 Reflectance of GLAD PBC at various light polarizations . . 191

8.11 Consistency in transmittance of two different GLAD PBCs . 199

9.1 The three classes of defect engineering in GLAD films . . . . 203

9.2 Heterostructure waveguides in square spiral 3D PBCs . . . . 205

9.3 The principle of seed layer induced defect engineering . . . . 206

9.4 EBL seed layers with line defects . . . . . 209

9.5 Defects in traditional GLAD films: Top views . . . . . 210

9.6 Defects in traditional GLAD films: Oblique views . . . . . 211

9.7 Incomplete defect in traditional GLAD film . . . . . 212

9.8 The principle of defect engineering in PhiSweep GLAD . . . 214

9.9 Air filled PhiSweep defects: Top views . . . . . 215

9.10 Air filled PhiSweep defects: Side views . . . . . 216

9.11 Air filled PhiSweep defects: Oblique view . . . . . 217

9.12 Dielectric filled PhiSweep defects: Top views . . . . . 218

9.13 Dielectric filled PhiSweep defects: Details . . . . . 219

9.14 Dielectric filled PhiSweep defects: Oblique view . . . . . 220

9.15 The mechanism of PhiSweep defect engineering . . . . . 221

9.16 Advanced defects in a periodic square spiral GLAD film . . . 224

## LIST OF FIGURES

9.17	Capping layer on square spiral GLAD film . . . . .	227
9.18	Multilayer defect engineering in square spiral GLAD films . . . . .	229
10.1	Aperiodic $\gamma = 45^\circ$ PhiSweep GLAD films . . . . .	235
10.2	Aperiodic $\gamma = 30^\circ$ PhiSweep GLAD films . . . . .	236
10.3	Aperiodic $\gamma = 15^\circ$ PhiSweep GLAD film . . . . .	237
10.4	SEM image of a nanofibrous GLAD film . . . . .	238
10.5	TEM diffraction pattern of a nanofibrous GLAD film . . . . .	239
10.6	TEM bright field images of a nanofibrous GLAD film . . . . .	240
10.7	EDX analysis of a silicon nanofibrous GLAD film . . . . .	241
10.8	The mechanism of PhiSweep nanofibrous film growth . . . . .	244
10.9	Initial growth evolution of aperiodic PhiSweep GLAD films . . . . .	245
10.10	Column competition in aperiodic PhiSweep GLAD films . . . . .	246
10.11	Nanoindentation of a nanofibrous GLAD film . . . . .	250
10.12	Nanoindentation of PhiSweep and traditional GLAD films . . . . .	251
11.1	A GLAD microfluidic network design . . . . .	257
11.2	The principle of microfluidics in GLAD thin films . . . . .	258
11.3	A prototype defect engineered GLAD microfluidic network . . . . .	259
11.4	A GLAD microfluidic channel . . . . .	260
11.5	Liquid flow in a GLAD microfluidic device . . . . .	262

# List of Symbols and Abbreviations

## Symbols

$\alpha$	Vapour incidence angle/substrate tilt angle.
$\beta$	Column inclination angle.
$\Delta$	Seed lattice period.
$\epsilon$	Permittivity.
$\epsilon_{eff}$	Effective medium permittivity.
$\gamma$	PhiSweep sweep angle.
$\lambda$	Wavelength.
$\lambda_b$	Bulk diffusion length.
$\lambda_{centre}$	Bandgap centre wavelength.
$\lambda_p$	Mean free path.
$\lambda_s$	Surface diffusion length.
$\mu$	Permeability.
$\omega$	Angular frequency.
$\phi$	Vapour arrival direction/substrate rotation angle.

## LIST OF SYMBOLS AND ABBREVIATIONS

$\psi$	Off-Axis vapour arrival direction angular deviation.
$\rho$	Free charge distribution.
$\rho_{bulk}$	Mean density of bulk material.
$\rho_{GLAD}$	Mean density of GLAD film.
$\rho_V$	Mean volume density/packing factor.
$\sigma$	Conductivity.
$\theta$	Vapour throw angle.
$a$	Column spacing.
$\mathbf{a}_1, \mathbf{a}_2, \mathbf{a}_3$	Primitive lattice vectors.
$A$	Area.
$\mathbf{b}_1, \mathbf{b}_2, \mathbf{b}_3$	Primitive reciprocal lattice vectors.
$\mathbf{B}$	Magnetic induction.
$c$	Velocity of light in vacuum.
$d$	Seed width.
$D$	Diffusion coefficient.
$\mathbf{D}$	Electric displacement.
$E$	Energy.
$\mathbf{E}$	Electric field.
$E_a$	Activation energy.
$E_f$	Electromagnetic energy functional.
$ff_{A,seeds}$	Seed layer planar fill factor.
$ff_V$	Film volume fill factor.
$\mathbf{G}$	Reciprocal lattice vector; Gibbs energy.
$h$	Seed height.
$\mathbf{H}$	Magnetic field.

## LIST OF SYMBOLS AND ABBREVIATIONS

$J$	Free electric current.
$k$	Wave vector.
$k_B$	Boltzmann's constant.
$l$	Vapour throw distance.
$L$	Square spiral horizontal side length.
$n$	Band index; refractive index.
$n_c$	Dielectric contrast.
$n_{eff}$	Effective refractive index.
$N(\omega)$	Density of states.
$p$	Helical pitch.
$P$	Pressure.
$P_i$	Incident optical power.
$P_r$	Reflected optical power.
$P_t$	Transmitted optical power.
$q$	PhiSweep sweep pitch.
$Q$	Quality factor.
$r$	Distance vector.
$R$	Reflectance.
$\%R$	Relative reflectance.
$R$	Lattice vector.
$s$	Seed spacing.
$s_l$	Seed layer line defect width.
$s_{l,\parallel}$	PhiSweep parallel line defect width.
$s_{l,\perp}$	PhiSweep perpendicular line defect width.
$s_p$	Seed layer point defect width.

## LIST OF SYMBOLS AND ABBREVIATIONS

$S$	Ratio of surface binding to desorption.
$S_A$	Average area stiffness.
$S_{fibre}$	Average stiffness per fibre.
$t$	Time.
$T$	Transmittance; temperature.
$\%T$	Relative transmittance.
$T_m$	Melting point.
$v_g$	Group velocity.
$v_p$	Phase velocity.
$V$	Volume.
$w$	Column width.
$z$	Film thickness.

### Abbreviations

AO	Acousto-optic.
BCC	Body centred cubic.
CAD	Computer assisted design.
CCW	Counter-clockwise.
CTM	Crystal thickness monitor.
CVD	Chemical vapour deposition.
CW	Clockwise.
EBL	Electron beam lithography.
EDX	Energy dispersive x-ray analysis.
FCC	Face centred cubic.
FTIR	Fourier transform infrared spectroscopy.
GLAD	Glancing angle deposition.

## *LIST OF SYMBOLS AND ABBREVIATIONS*

IR	Infrared.
LDWL	Laser direct write lithography.
LED	Light emitting diode.
LH	Left handed.
MEMS	Micro electro mechanical system.
NA	Numerical aperture.
NIR	Near infrared.
PBC	Photonic bandgap crystal.
PDMS	Polydimethylsiloxane.
PEB	Post exposure bake.
PMMA	Polymethylmethacrylate.
PVD	Physical vapour deposition.
RH	Right handed.
RIE	Reactive ion etch.
SEC	Size exclusion chromatography.
SEM	Scanning electron microscopy.
TE	Transverse electric.
TEM	Transmission electron microscopy.
TIR	Total internal reflection.
TM	Transverse magnetic.
UV	Ultraviolet.
VIS	Visible.

# Chapter 1

## Introduction

### 1.1 Context

Humans have long endeavoured to control and utilize light. Today, optics plays a role in virtually all areas of science and engineering, and society at large increasingly utilizes optical technology: Lasers play music and diagnose patients, the capacity of optical fibres is crucial to modern communications, and with the emergence of integrated optical circuits a potential successor of microelectronics may have been born. These technological advances have been enabled by new optical materials that exploit the interaction between light and matter.

The most sophisticated optical material yet proposed is the photonic bandgap crystal (PBC). By radically aiming to manipulate light at the smallest possible length scale and in all three dimensions, the potential of PBCs to control the emission and transmission of light is unprecedented. Indeed, the modus operandi of photonic bandgap crystals is so fundamental that they could replace and outperform existing laser cavities, low loss fibres (over short distances), and integrated optical circuits, all at once. They would be the ultimate medium for information processing, and undoubtedly deliver new and revolutionary optical applications.

However, the design and fabrication requirements of PBCs are as immense as their promise, and experimental realization remains a major challenge. Not only is it difficult to achieve the complex, sub micrometre crystal structures needed, but engineering the architectures with designed optical characteristics and functions is even harder. Some have tried a top-down fabrication approach, but despite half a century of semiconductor processing progress, uniform three dimensional structures are not easily achievable.

Others have looked to bottom-up assembly, which is a strong method for sub micrometre fabrication but forfeits the flexibility required to introduce functional defects.

An opportunity to address these challenges has been provided by a recently proposed photonic crystal architecture based on tetragonal lattices of square spirals. In addition to approaching the theoretically ideal lattice structure for photonic crystals, this new architecture is suitable for fabrication by glancing angle deposition (GLAD), a method for deposition of highly porous thin films with a chiral microstructure. By combining aspects of both top-down and bottom-up fabrication, GLAD holds a potential for providing uniform, large area crystals, as well as allowing modification of the optical properties through control over the crystal fine structure and intentional defects.

## 1.2 Objectives

The objective of this thesis is to enable engineering of square spiral photonic bandgap crystals using glancing angle deposition. Bandgap engineering – or the ability to adjust the frequency response of a PBC – must be demonstrated by mastering the physical fine structure of the GLAD thin films, and showing that a modification of the square spiral dimensions yield an expected change in the optical characteristics. Specifically, it will be attempted to make the square spiral PBCs operate at frequencies close to those currently being used for optical communications. Defect engineering – or the ability to introduce intentional dislocations in the crystal lattice – must be demonstrated by developing methods for removing or inserting crystal material at designed locations, without destroying the crystal structure and uniformity.

To achieve these objectives, a number of new capabilities pertaining to glancing angle deposition must be developed:

- Since square spiral photonic crystal thin films rely on seed layers to induce crystal periodicity, large area seed layers with complete design freedom must be enabled. These seed layers must also allow for integration of intentional defects.
- An analysis of the growth of periodic square spiral GLAD films must be performed to identify any details of the film structure that might be detrimental to the photonic crystal architecture. New GLAD methods

must be devised to alleviate such structural problems and improve the square spiral morphology.

- Comprehensive optical evidence supporting GLAD square spiral thin films as complete, three-dimensional PBCs must be obtained. In comparison with earlier reports on square spiral crystals, an enhancement of the optical response relating to improvements in the thin film fine structure must be documented.
- The ability to scale the dimensions of the square spirals must be established, and a change in the frequency response of the crystals corresponding to the scaled physical dimensions must be shown.
- The ability to introduce defects with waveguiding potential in square spiral thin films must be demonstrated, and such defects must not significantly alter the square spiral fine structure.

The thesis does not aim to produce a complete photonic crystal optical device. Achieving this will require considerably more research. But the development of bandgap and defect engineering is a critical step toward establishing the viability of GLAD for photonic bandgap crystals, and thus help provide new techniques for practical realization of the applications envisioned for photonic crystals.

### 1.3 Scope and Structure

The GLAD capabilities listed above have applications well beyond photonic crystals, and the scope of the thesis is not exclusively confined to photonic crystals. The research on seed layers, for example, is relevant not just for periodic thin films, but for any application relying on dense arrays of small lithographic features. The development of seed layer based defect engineering is a general approach to the patterning of porous thin films. And improved GLAD growth methods have lead to a new field of thin film porosity engineering now being pursued by other researchers. Indeed, although the *raison d'être* for the thesis is the advancement of photonic crystal technology, this is a thin film thesis more than an optical thesis, with innovation centred on practical crystal fabrication.

Following this introductory chapter 1, chapters 2 and 3 provide reviews of photonic bandgap crystals and glancing angle deposition, respectively. In addition to introducing the physics behind their behaviour, the review of

PBCs includes a survey of the most important architectures and applications, and a discussion of the challenges currently impeding further progress in the field. The review of GLAD analyzes the ability of this technique to generate thin films with microstructures of free-standing columns, and presents the characteristics and applications of the films.

The short chapter 4 ties together the review findings by examining the idea of using GLAD for photonic crystal fabrication. The theory of chiral crystal architectures and previously published experimental work on square spirals are presented, and the proposal for photonic crystal engineering in GLAD films is put forward.

Chapters 5 to 11 constitute the body of original thesis research.

In chapter 5 a set of design rules for periodicity inducing seed layers is derived, and electron beam and laser direct write lithography are presented as the most suitable prototype seed layer fabrication methods. Processes developed to optimize the performance of both technologies are described – including the establishment of SU-8 as a high resolution negative resist – and a variety of large area, high density seed layers are demonstrated.

Chapter 6 provides an analysis of the nucleation and evolution of periodic GLAD thin films, with emphasis on the importance of appropriately matching the seed layer with the structure and density of the desired film. Periodically structured films are compared with aperiodic, or randomly nucleated, films, and the morphological advantages of the periodic structures are identified.

In chapter 7, focus shifts to the fabrication of bandgap engineered square spiral photonic crystals and efforts to downscale the square spiral GLAD film microstructure. Film growth problems inherent in traditional deposition method are analyzed to uncover their root causes, leading to the proposal of new, enhanced deposition algorithms. Implementation of these generates superior square spiral structures closely resembling the theoretically ideal architecture.

Optical characterization of the optimized and bandgap engineered square spiral thin films is performed in chapter 8. After verification that key features in their optical spectra do derive from the periodic square spiral structure, and hence provide evidence of a photonic bandgap, a series of measurements is presented to evaluate the stability of the bandgap response with respect to crystal direction and light polarization. The data is compared with theoretical expectations and with previously reported results to conclude that bandgap engineering has been achieved, and that enhancement of the film fine structure has yielded a stronger bandgap response.

Chapter 9 treats defect engineering in GLAD films. Seed layer induced

film defects are developed as a new way of patterning porous thin films – either with air filled or evaporant filled defects – and methods for turning such defects into photonic crystal waveguides are discussed. Multilayer defects, consisting of stacked thin films with different microstructures, are also demonstrated.

An adjunct research area spun off from the efforts to provide new deposition methods for better square spirals is presented in chapter 10, namely the capability to engineer the porosity of GLAD films. This technique offers a high level of control over the thin film fine structure, and is used to make thin films with a uniform and highly porous microstructure of tightly interwoven nanoscale fibres. Together with the new defect engineering tools, manipulation of the film porosity enables GLAD as a new approach to the fabrication of microfluidic networks, which is demonstrated in chapter 11.

Conclusions and perspectives on the thesis research are provided in chapter 12.

No Text

## Chapter 2

# The Promise of Photonic Bandgap Crystals

The principal applications of any sufficiently new and innovative technology always have been – and will continue to be – applications *created* by that technology. H. Kroemer [1].

The year 2000 was an important one for electrical engineers, as Alferov, Kroemer and Kilby were awarded the Nobel Prize in Physics for their development of semiconductor heterostructures and the integrated circuit. This was deserved recognition of the vast impact that micro- and optoelectronics have had on society in the past few decades. I had the honour of attending talks by two of the Laureates in Sweden, and the above quote by Kroemer (included in his enjoyable Nobel Lecture as well [1]) was both memorable and descriptive of the torrent of technological progress that these Laureates initiated. The quote and the occasion also epitomize the promise of the photonic bandgap crystal, a new type of artificial material as fundamental to optics as the semiconductor is to electronics. Photonic bandgap crystals have the potential to improve Alferov and Kroemer's semiconductor lasers, re-achieve Kilby's integrated circuits with photons, and merge the two great technologies of optical communications and microcomputing. Yet, even with such promise the most exciting applications of photonic bandgap crystals are probably still to come.

This review chapter seeks to describe the fundamental theory and characteristics of photonic bandgap crystals, introduce the most common crystal architectures, and discuss the key applications proposed so far.

## 2.1 The Origins

One of the pillars of science is the concept of electromagnetic radiation, which represents the transport of energy in oscillating electric and magnetic fields. Maxwell's Equations couple the electric displacement  $\mathbf{D}$  and field  $\mathbf{E}$  to the magnetic induction  $\mathbf{B}$  and field  $\mathbf{H}$  [2, 3]:

$$\nabla \cdot \mathbf{D} = \rho, \quad (2.1)$$

$$\nabla \cdot \mathbf{B} = 0, \quad (2.2)$$

$$\nabla \times \mathbf{E} = -\frac{\partial \mathbf{B}}{\partial t}, \quad (2.3)$$

$$\nabla \times \mathbf{H} = \mathbf{J} + \frac{\partial \mathbf{D}}{\partial t}, \quad (2.4)$$

where  $\rho$  is the free charge distribution and  $\mathbf{J}$  is the free electric current. The behaviour of electromagnetic fields further depends on the media in which they propagate, and additional relations are required to include these effects, such as in the case of linear materials [3]:

$$\mathbf{D} = \epsilon \mathbf{E}, \quad (2.5)$$

$$\mathbf{B} = \mu \mathbf{H}, \quad (2.6)$$

$$\mathbf{J} = \sigma \mathbf{E}. \quad (2.7)$$

Here  $\epsilon$  is the permittivity,  $\mu$  is the permeability, and  $\sigma$  is the conductivity. These relations have allowed engineers and scientists to deduce innumerable technological breakthroughs in the past century.

Compared with other types of electromagnetic radiation and electronic systems, the optical section of the electromagnetic spectrum has many advantages as a signal carrier: The bandwidth is large, energy losses and distortion are small in many materials, high intensities are achievable, and optical signals can co-exist without interaction. From simple refractive lenses to optical fibres to semiconductor optoelectronics, interaction between light and matter is central to applications exploiting these benefits. In optical fibres, for example, reflection off the interface between high and low permittivity materials confines light to the former material.

Since monochromatic light can be considered a periodic wave with a frequency  $\omega$  and a wavelength  $\lambda$ , it interacts particularly strongly with materials whose permittivity  $\epsilon$  varies with a spatial periodicity similar to  $\lambda$ . This concept has been used for years in multilayer dielectric thin films, consisting of a succession of periodically spaced planar interfaces between high

and low index materials. Multiple scattering off the interfaces leads to constructive wave interference in the forward or backward direction, provided that the optical thickness of each layer is a multiple of one quarter of the wavelength of the light. Careful design of the thickness and permittivity of the thin film layers then allows for the engineering of either a pass band or a stop band centred on the design wavelength [4, 5]. This approach is regularly used to fabricate anti-reflection coatings and high-reflection dielectric mirrors or filters.

Equally useful are optical microcavities, which rely on combinations of dielectric mirrors and high  $\epsilon$  confinement to create resonators. These resonators can localize light in small volumes, control the emission spectrum from distributed feedback semiconductor lasers, and even impact the radiative processes of excited atoms [6]. However, multilayer dielectric materials only work perfectly along the direction perpendicular to the interfaces, and confinement by a contrast in permittivity alone is lossy.

Aspiring to lift these limitations and provide both radiation emission control and light localization in all three dimensions, Yablonovitch [7] and John [8] in 1987 conceived a new optical medium: Photonic bandgap crystals.

## 2.2 The Theory of Photonic Crystals

### 2.2.1 Electrodynamics in Periodic Media

Before the promise of photonic crystals can be appreciated, the nature and consequences of interaction between periodic structures and electromagnetic fields must be established. Since the ultimate objective is to manipulate light, only dielectric materials with low losses at optical frequencies are relevant. The imaginary part of the permittivity or dielectric function  $\epsilon$  can then be ignored, the permeability  $\mu$  set to that of vacuum ( $\mu_0$ ), and free charge  $\rho$  and currents  $\mathbf{J}$  can be assumed absent. If the dielectric material is further assumed to be linear (at least for weak fields), isotropic (reducing  $\epsilon$  from a tensor to a scalar), and frequency independent (at least for a narrow  $\omega$  range of interest), Maxwell's Equations 2.1-2.4 and the material relations 2.5-2.7 can be recast as:

$$\nabla \cdot [\epsilon(\mathbf{r})\mathbf{E}(\mathbf{r}, t)] = 0, \quad (2.8)$$

$$\nabla \cdot \mathbf{H}(\mathbf{r}, t) = 0, \quad (2.9)$$

$$\nabla \times \mathbf{E}(\mathbf{r}, t) = -\mu_0 \frac{\partial \mathbf{H}(\mathbf{r}, t)}{\partial t}, \quad (2.10)$$

$$\nabla \times \mathbf{H}(\mathbf{r}, t) = \epsilon_0 \epsilon(\mathbf{r}) \frac{\partial \mathbf{E}(\mathbf{r}, t)}{\partial t}, \quad (2.11)$$

with the time and space dependence made explicit.

Rearrangement of 2.10 and 2.11 now yields [8]:

$$\nabla \times \left( \frac{1}{\epsilon(\mathbf{r})} \nabla \times \mathbf{H}(\mathbf{r}, t) \right) = -\frac{1}{c^2} \frac{\partial^2 \mathbf{H}(\mathbf{r}, t)}{\partial t^2}, \quad (2.12)$$

where  $c$  is  $1/\sqrt{\epsilon_0\mu_0}$ , or the velocity of light in vacuum. From basic wave theory this is recognized as a wave equation [9] (a similar equation can be arranged for  $\mathbf{E}(\mathbf{r}, t)$ ), for which one solution is the harmonic, electromagnetic wave with angular frequency  $\omega$ :

$$\mathbf{H}(\mathbf{r}, t) = \mathbf{H}(\mathbf{r})e^{-i\omega t}. \quad (2.13)$$

Harmonic modes are a judicious choice for a wave solution, since any other solution can be formed by Fourier superposition of harmonic modes [10]. When the harmonic wave is inserted into the wave equation 2.12:

$$\nabla \times \left( \frac{1}{\epsilon(\mathbf{r})} \nabla \times \mathbf{H}(\mathbf{r}) \right) = \frac{\omega^2}{c^2} \mathbf{H}(\mathbf{r}), \quad (2.14)$$

the time dependence is eliminated and an eigenvalue problem emerges. For a material with a given dielectric function  $\epsilon(\mathbf{r})$ , equation 2.14 determines which harmonic modes or eigenfunctions  $\mathbf{H}(\mathbf{r})$  can propagate in the material, as well as the frequencies  $\omega$  or eigenvalues of those modes. A corresponding electric field mode  $\mathbf{E}(\mathbf{r})$  with the same frequency  $\omega$  accompanies each solution (given by 2.11), thus specifying a complete electromagnetic wave.

So far, none of the above derivations have been specific to materials with a periodic structure. Consider now a material whose dielectric function  $\epsilon$  repeats itself periodically in all three dimensions:

$$\epsilon(\mathbf{r}) = \epsilon(\mathbf{r} + \mathbf{R}), \quad (2.15)$$

where  $\mathbf{R}$  is any lattice vector defined as a linear combination of the primitive

lattice vectors  $[\mathbf{a}_1, \mathbf{a}_2, \mathbf{a}_3]$  spanning the unit cell of the periodic dielectric lattice. The modes that can exist in such a periodic environment are given by Bloch's Theorem [11]:

$$\mathbf{H}(\mathbf{r}) = e^{i\mathbf{k}\cdot\mathbf{r}}\mathbf{u}_{\mathbf{k}}(\mathbf{r}), \quad (2.16)$$

stating that the modes are plane waves modulated by some function  $\mathbf{u}_{\mathbf{k}}(\mathbf{r})$  with the same periodicity in  $\mathbf{r}$  as the dielectric:

$$\mathbf{u}_{\mathbf{k}}(\mathbf{r}) = \mathbf{u}_{\mathbf{k}}(\mathbf{r} + \mathbf{R}). \quad (2.17)$$

The allowed modes, or 'Bloch states', are characterized by wave vectors  $\mathbf{k}$  specifying their phase during translation. The wave vectors also represent points in the reciprocal lattice (existing in a spatial frequency space complementary to the physical space), defined by the primitive reciprocal lattice vectors  $[\mathbf{b}_1, \mathbf{b}_2, \mathbf{b}_3]$ , where  $\mathbf{a}_i\mathbf{b}_j = 2\pi\delta_{ij}$ . The reciprocal lattice, or  $\mathbf{k}$ -space, is periodic with lattice vectors  $\mathbf{G}$  providing invariant translations. The smallest non-redundant volume of the lattice defines the (first) Brillouin zone, which succinctly includes the wave vectors for all the possible Bloch modes or eigenfunction  $\mathbf{H}_{\mathbf{k}}(\mathbf{r})$  (with eigenvalues  $\omega(\mathbf{k})$ ) that can exist in the physical lattice  $\epsilon(\mathbf{r})$ . Often the dielectric lattice exhibits rotation, reflection, or inversion symmetry in addition to translation symmetry, and the Brillouin zone can then be further reduced to an 'irreducible' version that still includes all possible modes [11].

To determine the periodic function  $\mathbf{u}_{\mathbf{k}}(\mathbf{r})$ , the Bloch states from Bloch's Theorem (equation 2.16) are inserted into the original eigenvalue problem (equation 2.14) for the harmonic modes  $\mathbf{H}(\mathbf{r})$ :

$$\nabla \times \left( \frac{1}{\epsilon(\mathbf{r})} \nabla \times \mathbf{H}(\mathbf{r}, t) \right) = \frac{\omega^2(\mathbf{k})}{c^2} \mathbf{H}(\mathbf{r}) \Rightarrow \quad (2.18)$$

$$(\mathbf{i}\mathbf{k} + \nabla) \times \left( \frac{1}{\epsilon(\mathbf{r})} (\mathbf{i}\mathbf{k} + \nabla) \times \mathbf{u}_{\mathbf{k}}(\mathbf{r}) \right) = \frac{\omega^2(\mathbf{k})}{c^2} \mathbf{u}_{\mathbf{k}}(\mathbf{r}). \quad (2.19)$$

A new eigenvalue problem has now popped up, which is tractable to solve using iterative numerical computation. For each wave vector  $\mathbf{k}$  an infinite set of discrete modes  $\mathbf{H}_{\mathbf{k}}(\mathbf{r})$  exists. Each mode is identified by a band index  $n$  and has a frequency  $\omega_n(\mathbf{k})$ , and when the frequencies of all possible modes are charted as a function of  $\mathbf{k}$ , the result is the dispersion relation or photonic band structure for the dielectric medium. A representative band structure is shown in figure 2.1.

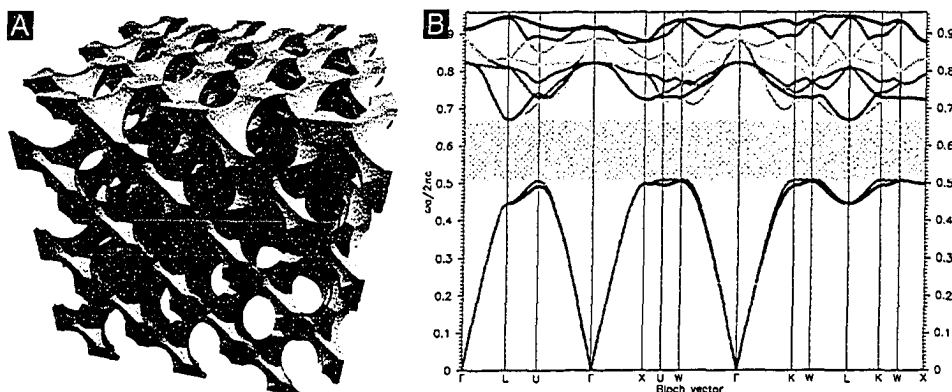


Figure 2.1: a) Photonic bandgap crystal with a diamond lattice of air spheres in a dielectric background. From [12]. b) Theoretical band structure (dispersion relation)  $\omega_n(\mathbf{k})$  for the crystal. A full bandgap with no allowed propagation modes exists in the relative frequency range 0.51 to 0.67, yielding a relative gap size of 27%. From [13].

### 2.2.2 Photonic Bandgaps

For most periodic dielectric structures, at least one mode  $\mathbf{H}_{\mathbf{k}}(\mathbf{r})$  exists for every frequency  $\omega_n(\mathbf{k})$ , meaning that electromagnetic waves of all frequencies can propagate through the material (the electric field  $\mathbf{E}_{\mathbf{k}}(\mathbf{r})$  is straightforward to derive once the magnetic field  $\mathbf{H}$  has been found). In photonic bandgap crystals (PBCs), however, the geometry of the dielectric yields a band structure in which a range of frequencies is *not* represented by any modes, i.e., for the frequency range in question no Bloch states satisfy the eigenvalue problem specified by  $\epsilon(\mathbf{r})$ . Consequently, as in figure 2.1 a gap in the band structure arises, and no electromagnetic waves with frequencies inside this gap can propagate in the crystal [7, 8]. Strictly speaking, a ‘photonic crystal’ is any periodic dielectric medium which interacts with electromagnetic radiation, while only ‘photonic *bandgap* crystals’ (PBCs) prohibit wave propagation for some frequencies in some directions. The former term is often used for both cases, however.

Physically, photonic bandgaps can be interpreted as arising from coherent, multiple Bragg scattering of light waves off the periodic interfaces between regions of high and low permittivity inside the crystal, and from Mie resonances due to scattering off the individual dielectric structural features themselves. The Bragg scattered light interferes, and for some frequencies the interference is destructive in all directions, while coinciding with the Mie

resonances. This is possible when both the spacing of the Bragg scattering interfaces (the overall lattice) and the size of the Mie scattering structures (at the lattice points) is on the order of the radiation wavelength [8, 14].

An equivalent point of view is that the heterogeneity of the dielectric function  $\epsilon(\mathbf{r})$  forces the displacement field  $\mathbf{D}(\mathbf{r})$  to concentrate either in the high or the low permittivity regions, rather than flow uniformly as in homogeneous media. Where adjacent bands  $\omega_n(\mathbf{k})$  in a uniform medium would normally meet in a degenerate point, the forced field concentration in regions of higher and lower permittivity slightly lower and raise the frequencies, respectively, so that the bands split and bend away from each other to leave a frequency gap, as is evident in figure 2.1. The low frequency band below the gap is sometimes called the ‘dielectric band’, and the above-gap band the ‘air band’ [15].

The bandgaps tend to arise at high symmetry points in the Brillouin zone where the modes spatially match the lattice constant. Thus, the bandgap wavelengths are often roughly twice the periodic length scale of the crystal [8]. This is what happens in multilayer thin film stacks, which indeed are one dimensional photonic crystals. Two dimensional photonic crystals prohibit the propagation of light in planes, whereas ‘complete’ 3D photonic crystals inhibit the propagation of light in all directions and of all polarizations.

If a wave with a frequency inside the bandgap impinges on the surface of a photonic bandgap crystal, it does excite a mode in the crystal. However, the mode has a complex wave vector and the imaginary part causes the mode amplitude to decay exponentially inside the crystal. The electromagnetic energy of this evanescent mode is reflected out of the crystal, as from a perfect mirror (unless it can couple to a defect inside the crystal), and the incident light has effectively been shut out of the crystal [15].

The way in which electromagnetic waves propagate in periodic dielectric media and can be described by eigenfunctions and Bloch states is quite similar to the quantum mechanical theory for electron transport in semiconductors. In the latter case the periodic environment is the electronic potential in atomic crystals, the operator in the eigenvalue problem is the Schrödinger equation, and the desired solution is a scalar electronic wave function  $\Psi$ . Correspondingly, semiconductors have gaps in the allowed spectrum of electronic modes. These electronic bandgaps are the foundation of pn junctions, and anyone appreciating their impact should have little trouble recognizing the desirability of achieving analogous bandgap materials for photonics.

### 2.2.3 Electromagnetic Energy and Scaling

Some properties of modes in photonic crystals are worth noting. The differential operator on the mode  $\mathbf{H}_{\mathbf{k}}(\mathbf{r})$  in the eigenvalue equation 2.14 is a Hermitian (as is the Hamiltonian operator in quantum mechanics), i.e., a linear operator that is invariant to which field it operates on in an inner product of two fields. This can be shown to imply that all resulting eigenvalues or allowed frequencies  $\omega_n(\mathbf{k})$  are real [15]. Furthermore, two different allowed modes are orthogonal (meaning that their inner product is zero), and while remaining orthogonal to modes with a lower order  $n$ , a given mode will always tend to minimize the electromagnetic energy functional by concentrating its electric displacement  $\mathbf{D}$  in regions of high permittivity  $\epsilon$ . The latter fact governs the field patterns around defects, and is evident from the electromagnetic variational theorem:

$$E_f(\mathbf{H}) = \left( \frac{1}{2(\mathbf{H}, \mathbf{H})} \right) \int \frac{1}{\epsilon(\mathbf{r})} \left| \frac{\omega}{c} \mathbf{D} \right|^2 d\mathbf{r}, \quad (2.20)$$

where  $E_f$  is the electromagnetic energy functional and  $(\mathbf{H}, \mathbf{H})$  is the inner product of the magnetic field.

It was mentioned above that whenever a relation for the magnetic field  $\mathbf{H}_{\mathbf{k}}(\mathbf{r})$  is derived, a similar – though not identical – version can be derived for the electric field  $\mathbf{E}_{\mathbf{k}}(\mathbf{r})$ . However, in the  $\mathbf{E}_{\mathbf{k}}(\mathbf{r})$  version of the central eigenvalue problem 2.14 the operator is not Hermitian, and this drastically complicates both the analytical understanding and numerical computation [15]. It is therefore preferable to work with  $\mathbf{H}_{\mathbf{k}}(\mathbf{r})$  throughout, and simply find  $\mathbf{E}_{\mathbf{k}}(\mathbf{r})$  at the end using Maxwell's Equations.

Another key property of the electromagnetic relations for photonic crystals is the lack of restrictions on the physical dimensions. As long as the assumptions regarding the dielectric medium used to obtain the simplified Maxwell's Equations in 2.8-2.11 hold true, the modes scale with both the periodicity and magnitude of the dielectric function. Specifically, the frequency location of the bandgap scales inversely with the periodicity of  $\epsilon$  and with the inverse root of the magnitude of  $\epsilon$ , without altering the qualitative nature of the modes [16]. This is both a blessing and a curse: Numerical computations are independent of physical scale and macroscopic models can be used to test new structures, but to obtain bandgaps at optical frequencies there is no avoiding difficult fabrication of sub micrometre structures.

## 2.3 Properties and Characteristics of Photonic Crystals

### 2.3.1 Group Velocity

The phase velocity  $v_p$ , given as the ratio of the angular frequency to the magnitude of the wave vector, becomes non-constant near bandgap edges, and may even tend toward infinity at points in a photonic crystal dispersion relation where the wave vector approaches zero while the frequency remains finite [17]. Meanwhile, the group velocity  $v_g$  – which represents the velocity with which electromagnetic energy propagates and is equivalent to the slope of the dispersion relation – is purely imaginary inside bandgaps [18]. Unlike in uniform, non-dispersive media where  $v_g$  is a constant:

$$v_g = \frac{c}{\sqrt{\epsilon}}, \quad (2.21)$$

the group velocity in photonic crystals varies with the band index  $n$  and the wave vector  $\mathbf{k}$ . It was just previously argued that the bands bend at the edges of photonic bandgaps (also seen in figure 2.1), and this reduction in slope implies a reduction in the group velocity relative to the situation of steep, constant slopes in uniform media. Furthermore, even away from the gaps many higher order bands in photonic crystals are unusually flat, resulting in a low group velocity over a fairly large bandwidth. This latter effect is called the ‘group velocity anomaly’ [16].

Since the dispersion relation  $\omega_n(\mathbf{k})$  of a photonic crystal cannot directly be determined experimentally, it is hard to evaluate  $v_g$ . However, under the approximation that for each band in each direction the photonic crystal is an ‘invariant’ medium with some average index of refraction, each such band and direction has an effective refractive index  $n_{eff}$ . Then, from

$$v_g \cong \frac{d\omega}{d\mathbf{k}} = \frac{c}{n_{eff}} \quad (2.22)$$

it might be expected that a low group velocity is equivalent to a large effective refractive index  $n_{eff}$ . This is indeed the case, as argued by Sakoda [16]. The significance of this is that  $n_{eff}$  can be found experimentally, namely via the transmission spectrum  $T(\omega)$ . The transmission spectra for photonic crystals reflect the complexity of the band structure, one crystal direction at a time, with bandgaps showing up as frequency ranges with zero or low transmission, and frequency ranges containing only a single allowed mode

containing high transmission interference patterns. This is illustrated in figure 2.2b. For each single-mode band the effective refractive index  $n_{eff}$  can be derived from the spacing  $\Delta\omega$  of the interference fringes in the transmission spectrum [16]:

$$n_{eff} = \frac{1}{2L} \frac{2\pi c}{\Delta\omega}, \quad (2.23)$$

where  $L$  is the physical thickness of the photonic crystal. This allows for experimental identification of frequency regions with a low group velocity.

At low frequencies the band structure  $\omega_n(\mathbf{k})$  of photonic crystals tends to be linear, as if the crystal was a uniform, non-dispersive medium. This is evident in figure 2.1, and derives from the fact that at long wavelengths the electromagnetic modes hardly notice the rapid variation of the dielectric function  $\epsilon(\mathbf{r})$ . For each crystal direction the crystal then looks like a uniform medium with a constant permittivity, and the effective refractive index  $n_{eff}$  can be measured and compared with numerical values from effective medium theory [15].

In wrapping up the discussion of  $v_g$ , it is worthwhile mentioning that Snell's law of refraction is invalid for frequencies within photonic bandgaps. The direction of propagation of the refracted wave no longer depends just on the refracted wave vector  $\mathbf{k}_{refrac}$ , but on the derivative  $\partial\omega/\partial\mathbf{k}$  of the dispersion relation at the location  $\omega_n(\mathbf{k}_{refrac})$  in the band structure. Since  $\omega_n(\mathbf{k})$  is highly complex, the monotonical dependence of the angle of refraction on the angle of incidence that Snell's law requires is ruined [16].

### 2.3.2 Modified Radiative Emission

In one of the two founding papers on photonic crystals, Yablonovitch discussed the ability to suppress spontaneous emission in semiconductors where the edge of the conduction band overlaps a photonic bandgap [7].

The *density of states*  $N(\omega)$  of a photonic crystal specifies the total number of allowed, propagating modes as a function of frequency [19]:

$$N(\omega) = \sum_n \int_{\text{BZ}} \delta(\omega - \omega_n(\mathbf{k})) d^3k, \quad (2.24)$$

where the integration of the dispersion relation  $\omega_n(\mathbf{k})$  on a Dirac delta function proceeds over the entire Brillouin zone and for all bands  $n$ . A representative density of states is plotted in figure 2.2a. By specifying the availability of propagating modes, the density of states determines the radiative properties of atoms, molecules or any other emitters embedded in the photonic

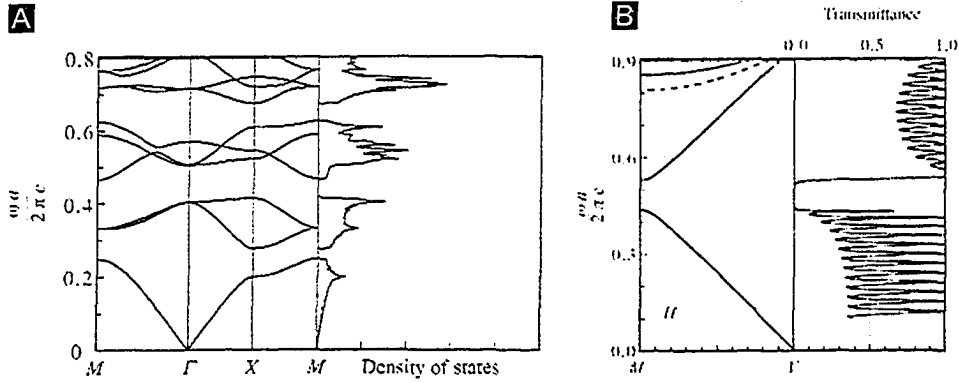


Figure 2.2: a) Band structure  $\omega(\mathbf{k})$  and density of states  $N(\omega)$  for a two dimensional square lattice photonic bandgap crystal. Bandgaps correspond to a vanishing density of states. b) Band structure and theoretical transmission  $T(\omega)$  for a hexagonal lattice 2D photonic crystal. The crystal becomes opaque at bandgap frequencies, and interference patterns appear in the transmission spectrum between bandgaps. Adapted from [16].

crystal. Inside a bandgap  $N(\omega_{\text{gap}}) = 0$ , and in accordance with Fermi's golden rule for radiative electron transitions [20, 21]:

$$W(\omega) = \frac{2\pi}{\hbar} |V|^2 N(\omega), \quad (2.25)$$

the corresponding rate  $W$  of photon emission is zero ( $|V|$  is the Rabi matrix for coupling between excited and relaxed electron states). Photon emission is therefore forbidden inside bandgaps [7].

The increased radiation/medium interaction caused by the low group velocity also makes some PBCs exhibit non-linear optical properties, such as sum-frequency generation [16].

### 2.3.3 Light Localization

In the second founding paper on photonic crystals, John discussed the potential for light localization in crystal defects [8], inspired by the similar effect of Anderson localization of electrons [22].

Defects represent the intentional removal, addition or modification of dielectric material, either at a point, along a line, or along a plane. Such a perturbation destroys the global symmetry of a crystal, although in practise the crystal can still be considered perfect far away from the defect. Inside a

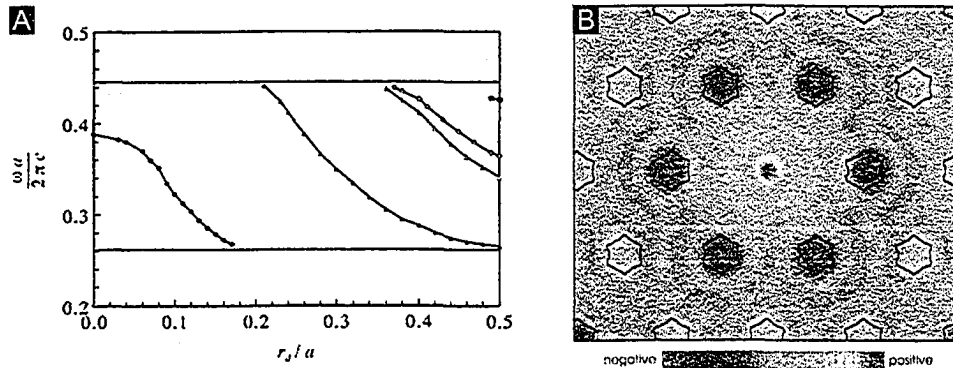


Figure 2.3: a) Localized mode frequencies for a point defect in a hexagonal lattice 2D photonic bandgap crystal, plotted as a function of the defect size. For radii greater than 0.36 (relative to the lattice period), not one but three defect modes appear. Adapted from [16]. b) Displacement field strength of a localized mode in a point defect in a yablonovite 3D photonic bandgap crystal. The mode is localized to the defect. From [15].

bandgap, defects may be able to support evanescent modes which decay exponentially in the remaining crystal, as illustrated by the field distributions in figures 2.3b and 2.4b. These modes are localized to the defect – as if the defect had perfectly reflecting walls – and make the density of states  $N(\omega)$  non-zero for discrete frequencies (point defects) or ranges of frequencies (line defects) in the gap. In accordance with Fermi's Rule (equation 2.25), the extra defect modes also promote photon emission from a source close to or inside the defect [15].

The finite dimensions of any defect quantize the defect modes to allow single or multiple modes, as shown for a point defect in figure 2.3a. Minimum threshold dimensions are required for any localized modes to show up, and as a rule of thumb the defect dimensions should be roughly equal to the bandgap wavelength. Furthermore, the defect dimensions and permittivity determine where in the gap the defect mode(s) are located. Modes closer to the gap centre are more closely bound by way of a higher amplitude decay rate in the surrounding crystal, and higher  $\epsilon$  defects have lower frequencies. Defects arising from the addition of dielectric material appear at the top of the bandgap, while the opposite is true for defects consisting of air [24, 25].

Point defects in PBCs constitute ultra small resonant cavities. Since the evanescent decay outside the defects is rapid (on the order of a few wavelengths), with negligible leakage to the outside world for appropriately

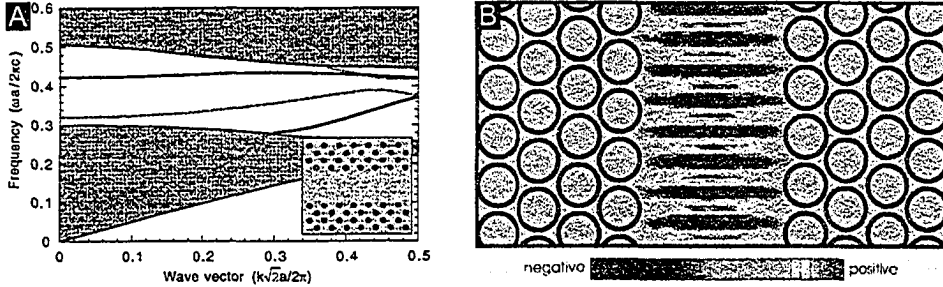


Figure 2.4: a) Unidirectional band structure for a hexagonal lattice 2D PBC with a line defect. The four row wide defect has introduced four defect bands for multi mode propagation at frequencies inside the bandgap. Adapted from [23]. b) Field intensity of light propagating down a line defect in a hexagonal lattice 2D PBC. From [15].

sized crystals, the modal volume is on the order of a cubic wavelength [25–28]:

$$V_{mode} = \left( \frac{\lambda}{2n} \right)^3. \quad (2.26)$$

This in turn leads to high quality factors  $Q$  (i.e., narrow spectral width):

$$Q = \frac{\lambda_{centre}}{\Delta\lambda}. \quad (2.27)$$

Linear and planar defects distinguish themselves by permitting the localized modes to be guided along the defects, not by total internal reflection (TIR) as in fibre optics and traditional integrated optics, but by excluding propagation in all other directions than those dictated by the defects. In analogy to fibre optics, the linear and planar defects support bands  $\omega_{defect}(\mathbf{k})$  of allowed modes, which for a given frequency can provide single or multi mode propagation, as shown in figure 2.4a [15].

## 2.4 Photonic Crystal Architectures and Fabrication

Up to this point photonic crystals have been discussed more or less analytically, without reference to the actual lattice geometry or band structure. Theory does provide indications as to which crystal architectures might provide bandgaps, but the actual dimensions and dielectric characteristics can

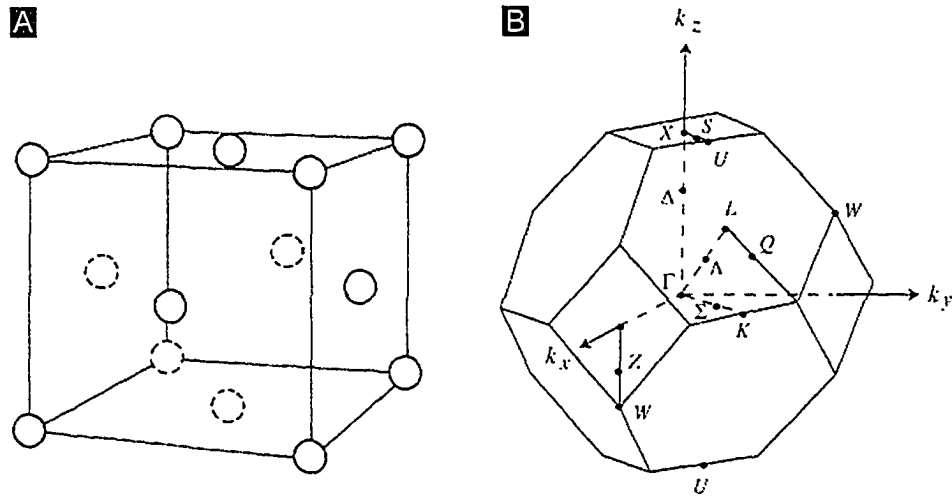


Figure 2.5: a) The face-centred cubic (FCC) lattice and b) its first Brillouin zone. The Brillouin zone is a truncated octahedron whose shape approaches a sphere, making FCC lattices highly suitable for photonic bandgap crystals. High symmetry locations are indicated. From [29] and [16].

only be established by numerically resolving the band structure. Even then, successfully identified architectures may be highly challenging to fabricate.

#### 2.4.1 Basic Crystal Requirements

Only certain lattice geometries produce bandgaps. Those dielectric networks comprising lattices whose Brillouin zone approach a sphere generally favour larger and more complete bandgaps, since a pseudo-isotropic  $k$ -space helps ensure that the bandgaps overlap in all directions [21]. FCC lattices with a truncated octahedron shaped Brillouin zone provide the best approximation to a sphere, as shown in figure 2.5 [7]. In particular, diamond like lattices – i.e., FCC lattices with a two-body basis aligned along the  $\langle 111 \rangle$ -direction – are superior for creating photonic bandgaps, as shown in figure 2.1 [30,31]. The largest bandgap computed for a PBC of dielectric structures in an air background is 28% (namely for a PBC of cylinders connecting diamond lattice points), but only approximations of this have been fabricated in practice [32]. In 2D the best equivalent is the hexagonal lattice [33].

Additionally, the dielectric contrast

$$\frac{\epsilon_{\text{high}}}{\epsilon_{\text{low}}} \quad (2.28)$$

between high and low permittivity regions of the medium must be large enough – typically  $> 2$  [8] – to effect sufficient scattering off the interfaces of these regions. The crystal material must have low losses, both in terms of absorption and diffuse scattering from irregularities, and the length scale of the structural features must be similar to the optical wavelength of interest.

### 2.4.2 Modelling

Once a good candidate for a photonic crystal has been envisioned, numerical modelling is needed to analyze its band structure and determine the presence of any bandgaps. This is typically done by parameterising the physical dimensions and dielectric contrast, and mapping out the band structure to identify the optimum architecture.

One method to calculate the band structure of a uniform photonic crystal is the ‘plane-wave expansion’ method, in which both the dielectric function  $\epsilon(\mathbf{r})$  and the eigenmodes  $\mathbf{H}_{kn}(\mathbf{r})$  are Fourier expanded into orthogonal plane waves in the reciprocal lattice. When these expansions are substituted into the original eigenvalue problem in equation 2.14, the result is a Hermitian (and thus linear) equation system that can be solved numerically, e.g., by iteratively minimizing the previously mentioned variational energy [30, 34–37]. A similar approach for photonic crystals based on spheres or cylinders is the spherical wave expansion method [16].

When the photonic crystal contains intentional defects, the full symmetry required for the plane-wave expansion method is lost. However, this hurdle can be negotiated by defining a super cell, i.e., a large new ‘unit cell’ that incorporates both a piece of the defect and the surrounding crystal, and then use this as the repetitive geometry [16].

Another numerical approach is the finite difference time domain method (FDTD), in which Maxwell’s Equations are approximated to finite differences in a real space grid (not  $\mathbf{k}$ -space as in plane-wave expansion) and iteratively calculated at discrete time points. At the edges of the real space grid, absorbing or periodic boundary conditions are imposed. The FDTD method is particularly useful for modelling of defects and embedded radiation sources, and for PBCs with lossy or frequency dependent dielectric functions  $\epsilon(\mathbf{r}, \omega)$  [38, 39].

### 2.4.3 Fabrication of Three Dimensional Photonic Crystals

With no shortage of models and theoretical predictions, the challenge for photonic bandgap crystals has always been practical fabrication. While

nature readily supplies diamond and FCC atomic lattices, such intricate, three-dimensional structures are complicated to replicate at length scales similar to optical wavelengths.

In top-down PBC fabrication, sub micrometre lithographic patterning and etching by directed energized beams are used to micromachine multi-layer structures of inter-connected dielectric. This approach affords great design flexibility, but is tedious and costly especially for large area crystals. Furthermore, it is difficult to achieve long-range uniformity as well as short-range surface smoothness and dimensional control. Bottom-up PBC fabrication relies on self-assembly or three-dimensional lithography to produce large area crystals, but traditionally at the expense of defect engineering flexibility.

The traditional choice of materials has been elemental and III-V compound semiconductors, including silicon and gallium arsenide, which deliver high refractive indices (for a large dielectric contrast) and low absorption at optical frequencies. Although metals and oxides have also been used for PBC fabrication, semiconductor photonic crystals have the further advantage of inherent electronic bandgaps for ready exploitation of the radiation modifying properties of PBCs. However, perhaps the biggest advantage of semiconductors is the range of sub micrometre machining techniques available. It is a stroke of luck that good dielectric candidates for PBCs are the very same semiconductors that the electronics industry has spent decades and billions of dollars learning how to process!

Tracing out representative elements of the history of photonic crystals, and indicating why new techniques for 3D PBC fabrication are still needed, the next few sections will discuss the most important and widely studied architectures.

#### 2.4.4 Yablonovite

The first complete, 3D photonic bandgap crystal was developed by Yablonovitch *et al.*, and subsequently termed 'yablonovite' [40]. Inspired by diamond lattice predictions by Ho *et al.* [30], yablonovite is fabricated by drilling holes into a dielectric facet along three directions, each  $35^\circ$  from the facet normal as shown in figure 2.6b. When the dielectric is considered a close packed assembly of FCC Wigner-Seitz cells (real space irreducible cells for the lattice), this drilling corresponds to leaving a cylindrical void in the centre of each cell, in a manner that is self-aligned and thus ensures periodicity throughout the crystal. In turn, these FCC arranged voids resemble a diamond like lattice.

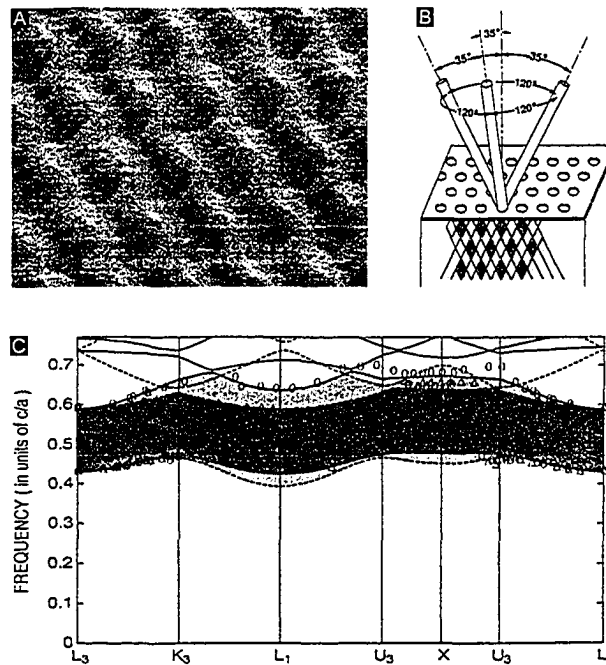


Figure 2.6: a) SEM micrograph of yablonovite fabricated in gallium arsenide. Each hole is approximately 330 nm in diameter. From [41]. b) The three drilling directions required to achieve a diamond like lattice of voids. From [40]. c) Part of the band structure for yablonovite, including computed (lines) and measured (markers) data. Yablonovite has a complete 3D bandgap. From [40].

As shown in figure 2.6c, both experimental and computational results reveal a relative bandgap width as large as 19% for air holes in a dielectric with a refractive index of 3.6, and with a dielectric volume fill factor of 22% [40]. In experiments conducted in the microwave range, impinging waves with frequencies inside the bandgap were effectively reflected by attenuation on the order of 10 dB per unit cell. Cheng *et al.* were the first to achieve 3D PBCs at near infrared wavelengths (including the crucial ‘second’ and ‘third windows’ used in optical fibre telecommunications), by fabricating 1.5  $\mu\text{m}$  thick yablonovite crystals in gallium arsenide using reactive ion etching through electron beam lithography defined masks (see figure 2.6a). In-gap attenuation up to 90% was reported, but structural irregularities in the sub micrometre structures were found to negatively impact the optical response [41–43].

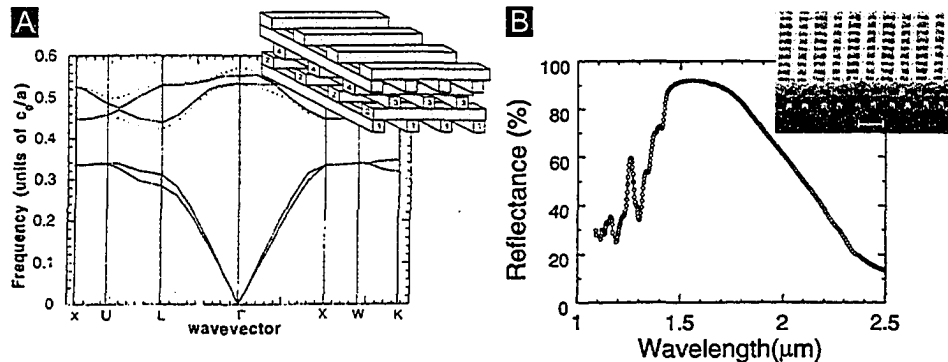


Figure 2.7: a) Band diagram and schematic of the woodpile 3D PBC architecture, consisting of stacked dielectric rods. From [44] and [45]. b) Experimental reflectance spectrum for the silicon woodpile structure shown in the inset. The reflectance peak indicates the presence of a bandgap around 1.6  $\mu\text{m}$ . From [46].

#### 2.4.5 Woodpile

The ‘woodpile’ PBC architecture was first conceived by Ho *et al.*, and consists of stacked layers of dielectric rods [44]. For every layer the rods are rotated  $90^\circ$  and translated one half lattice period sideways, so that the structure repeats itself for every four layers (one unit cell), as shown in the inset in figure 2.7a. This architecture emulates a diamond lattice in the sense that the rods roughly coincide with the  $\langle 110 \rangle$ -directed bonds between diamond lattice sites, and it has been modelled to exhibit a complete 3D bandgap as large as 18% for dielectric contrasts larger than 1.9 (see figure 2.7a). For inverted structures (air rods in a dielectric background) the maximum relative bandgap is 28% [44].

A motivator for the woodpile design was its compatibility with planar microfabrication, and the experimental development of woodpile PBCs followed the now classical approach of gradually shrinking feature sizes: First Özbay *et al.* demonstrated a full bandgap in silicon at microwave frequencies (340  $\mu\text{m}$  wide rods) [47], then Lin *et al.* reached mid infrared bandgaps (1.2  $\mu\text{m}$  wide rods) [45], and finally Lin and Fleming achieved a bandgap at a wavelength of 1.6  $\mu\text{m}$  (180 nm wide rods) [46]. The latter used advanced lithography and repeated etching, chemical mechanical polishing (CMP) planarization, and polysilicon deposition. This structure is shown in the inset in figure 2.7b, and in spite of the complicated processing good wafer wide uniformity was obtained. Even for a crystal thickness of only five layers,

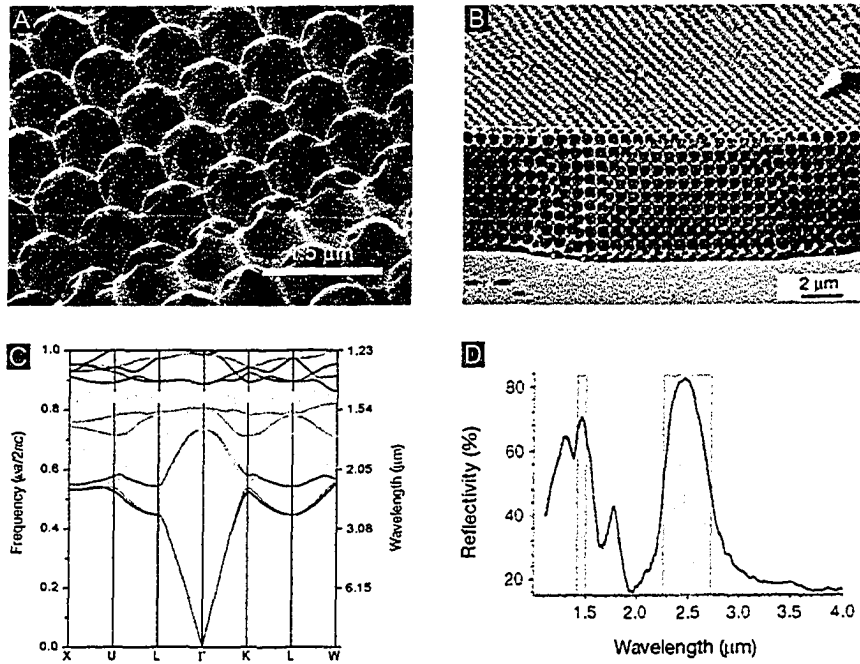


Figure 2.8: a,b) Detail and bulk SEM images of silicon inverse opal 3D PBCs. From [48] and [49]. c) Theoretical band structure for an optimized inverse opal structure with a complete bandgap. d) Experimental reflectance data for an inverse opal with a bandgap located at  $1.5 \mu\text{m}$ . The peak in reflectance at  $2.5 \mu\text{m}$  is from a pseudo-gap. From [50] and [48].

a  $450 \text{ nm}$  wide and  $10 \text{ dB}$  deep complete bandgap was recorded, in fine accordance with theory (see figure 2.7b).

#### 2.4.6 Inverse Opals

As early as 1990, Martorell and Lawandy considered colloidal suspensions of sub micrometre spheres for photonic bandgap effects [51], but no complete bandgaps were found in structures of close-packed spheres (whose resultant FCC lattice resembles that of natural opals). However, later modelling by Sözüer *et al.* and by Busch and John showed that a complete bandgap could be obtained by inverting the self-assembled spheres to obtain ‘inverse opals’ of air spheres in a dielectric background [36,52]. Specifically, Busch and John required that the original opal FCC lattice of spheres be sintered to make the spheres overlap, and then incompletely infiltrated with a high permittivity material ( $n > 2.8$ ) before removal of the original colloid template, creating

a highly interconnected dielectric network. Relative bandgaps of 5 to 15% were predicted (see figure 2.8c), i.e., somewhat less than diamond lattice based PBCs [52].

Blanco *et al.* created inverse opals by first self-assembling mono disperse silicon dioxide (silica) spheres of 600 to 1000 nm diameter, then sintering the silica at 1200 K, backfilling the structure with silicon using disilane chemical vapour deposition (CVD), annealing the silicon, and finally removing the silica by etching. The final structure is shown in figure 2.8a, and had a complete, relative bandgap of 5.1% centered at 1.5  $\mu\text{m}$ , as well as a pseudo-gap at 2.5  $\mu\text{m}$  (see figure 2.8d) [48]. Similar results were obtained in inverse opal germanium PBCs by Míguez *et al.* [53]. Being a bottom-up architecture, inverse opals can produce large, thick PBCs with good local uniformity, as shown in figure 2.8b. However, stacking faults arising during colloid sedimentation typically create numerous crystal defects and reduce the domain size to 100  $\mu\text{m}$ . This problem has only been partly alleviated by improved sedimentation [49], and is compounded by the band structure being inherently sensitive to structural roughness and lattice dislocations.

#### 2.4.7 Two Dimensional Photonic Crystals

Given the experimental complexity of the above and other proposed [12, 54] 3D PBC architectures, two dimensional PBCs have attracted attention as a compromise platform for examining photonic bandgap effects.

2D PBCs consist of a square or hexagonal lattice with a basis of one or more air cylinders in a dielectric background – or dielectric cylinders in an air background – extruded to infinite extension in the third dimension normal to the lattice plane. In numerical analyses, the simple architecture with the strongest bandgap has been identified as air cylinders in dielectric, with a relative gap size of 19% for a dielectric contrast of 3.5 [33, 55–57]. A unique feature of 2D PBCs is that the mirror symmetry about any lattice plane allows modes to be classified as either transverse electric (TE) or transverse magnetic (TM) polarized, depending on which of the two fields are in the lattice plane [15]. Each polarization has its own dispersion relation, and the gaps of both polarizations must overlap for a ‘full’ 2D bandgap.

In practise infinite 2D PBCs are, of course, impossible, and the actual crystals are planar PBC slabs. Fabrication is most often performed top-down by drilling holes in a semiconductor, such as reported by Krauss *et al.* for ion beam etched holes in aluminium gallium arsenide with lattice periods less than 200 nm [58]. Another approach is bottom-up fabrication in macroporous silicon off < 100 > silicon wafers, with etched pore seeds defining the

lattice [19]. This approach readily produces large crystals with mid infrared bandgaps. However, an intrinsic problem of all 2D PBC slabs is the lack of confinement in the third dimension, which introduces a continuum of states in the band structure [59], and causes leakage out of the crystal of light scattered out of the lattice plane. Suspending the PBC slabs in lower index materials provides guided modes (by total internal reflection) with reduced out-of-plane losses, but the bandgaps then exist only for guided modes – not all modes as in true photonic bandgaps [60]. Thus, while 2D PBCs are easier to fabricate than 3D architectures, they are not quite as useful: Propagating and localized modes are non-leaky and confined only for some wave vectors  $\mathbf{k}$ , waveguides work only for narrow frequency ranges, and resonant cavity modes decay more rapidly [61, 62].

## 2.5 Applications of Photonic Bandgap Crystals

Numerous applications have been proposed to exploit the unique optical properties of photonic bandgap crystals. The most important of these are waveguiding, integrated photonics, and optoelectronics, which will be discussed in some detail below for the benefit of subsequent thesis chapters on photonic crystal engineering. Other recent applications include optical sensing of fluids, relying on their absorption in the crystal resulting in a change in effective refractive index [63], and ‘light bulbs’ based on metal PBCs that alter the ordinary blackbody radiation spectrum to emit more light at specified wavelengths [64].

### 2.5.1 Waveguides

Waveguides transport electromagnetic energy along well-defined conduits, and the potential for waveguiding in PBCs was realized from the beginning as a key application. The ability to guide waves derives directly from the previously discussed localization of bandgap modes in linear lattice defects [8]. While localized bandgap modes cannot propagate into the bulk of the crystal, they are free to propagate up and down the defects. Furthermore, where two linear defects meet in a bend, a localized mode in one defect may couple by scattering to a new, similar mode in the other defect, and thus effectively make the wave propagate around the bend. This is illustrated in figure 2.9a.

By not relying on confinement in a high index material, as in traditional TIR waveguides, PBC waveguides can be engineered as air defects

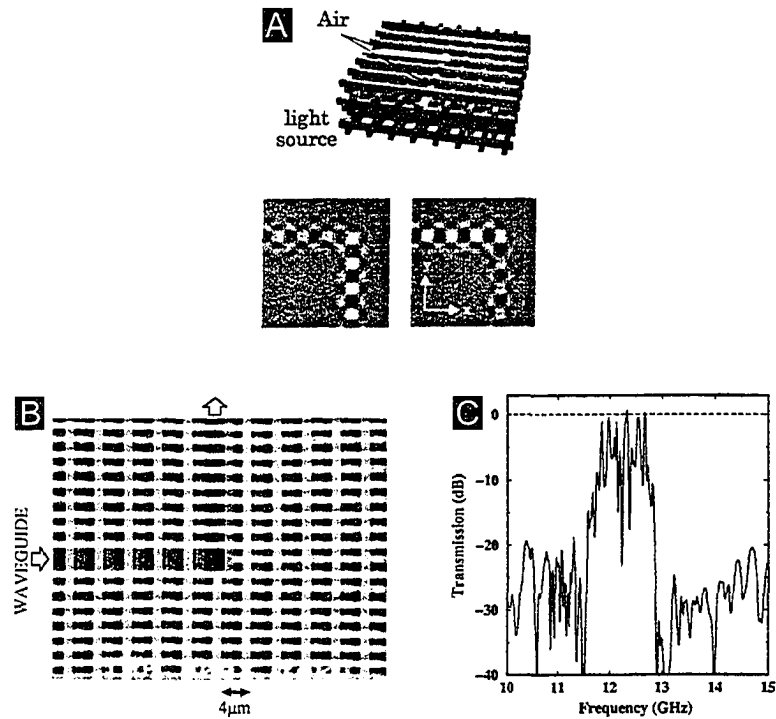


Figure 2.9: a) Displacement field distribution for a waveguide bend modelled in a woodpile 3D PBC. From [65]. b) Experimental realization of such a bend. No experimental verification exists of the waveguiding properties. From [66]. c) Transmission data for a similar but much larger woodpile bend, operating at microwave frequencies with almost full transmission. From [67].

and hence reduce the effects of chromatic dispersion and intrinsic and extrinsic absorption. In ideal PBC waveguides the only losses then arise from back-reflection off the end walls of waveguide bends, although in practise losses from scattering off structural imperfections must be considered as well. PBCs therefore emerge as a superior new solution for waveguiding at optical frequencies, compared with dielectric waveguides and optical fibres which suffer from absorption losses, material dispersion, and scattering out of the guides by internal or surface perturbations. In particular, mode hopping allows for very tight PBC waveguide bends with radii of curvature on the order of the wavelength, whereas TIR systems are notorious for bending losses that increase exponentially with decreasing radius of curvature, due to fields radiating out of the waveguides [68–70]. Such bending losses have long been an obstacle to miniaturization of optical waveguides. The methodol-

ogy of PBC waveguides is not unlike that of hollow metallic waveguides at microwave frequencies.

As mentioned earlier, the defect dimensions are crucial to determining the availability and frequency of waveguiding modes, including cut-off frequencies and whether PBC waveguides are single mode or multi mode. A rule of thumb is that for the lowest order defect mode, one half of the wavelength should approximately fit into the width of the guide. For many architectures this translates into a single mode defect width of one lattice period [15]. In fact, the number of defect modes is generally and roughly equal to the defect size in lattice periods, as already seen for the waveguide band structure in figure 2.4a [23, 71]. If adjoining linear defects are to serve as a waveguide bend, they must have similar dispersion relations with overlapping frequencies. Non-contact proximity of two defects may be used to couple fields from one defect to another, as in traditional integrated and fibre optics.

Since the introduction of engineered defects adds yet another level to the complexity of fabricating 3D PBC architectures, the majority of PBC waveguiding studies have focused on 2D waveguides, in spite of their inherent light leakage. 2D PBC waveguides were introduced early by Meade *et al.* [69], and modelling of waveguiding through bends was performed by Mekis *et al.* and by Chutinan and Noda, who found up to 98% transmission even for bends with zero curvature [23, 61, 72]. In traditional TIR waveguide bends equivalent transmission efficiencies require the use of corner mirrors or corner resonators, or larger radii of curvature [73]. In PBC bends with a curvature of just a few crystal lattice periods perfect transmission have been noted for some frequencies, but the transmission efficiency oscillates as a consequence of the PBC bends functioning by discrete coupling between two defect modes, rather than by smooth reflection [23, 72]. Numerous researchers have provided experimental confirmation in different 2D PBC architectures [62, 71, 74, 75].

For 3D PBC waveguiding, Chutinan and Noda provided the first modelling results in 1999 with higher than 95% transmission in sharp bends in woodpile architectures, and oscillatory coupling behaviour similar to that seen for 2D PBCs [65]. They subsequently fabricated the same woodpile waveguide structures (shown in figure 2.9b) [66], but only in 2001 did Temelkuran *et al.* confirm the predicted 3D PBC waveguiding properties [67, 76]. Yet, these results – represented in figure 2.9c – covered the microwave regime for a woodpile of millimetre sized alumina rods. 3D PBC waveguiding at optical frequencies thus remains elusive.

On a side note, one of the more successful applications of photonic crystals to date is waveguiding in ‘photonic crystal fibres’, which are optical fibres whose cross section is a 2D photonic crystal with a central defect. A full 2D bandgap in the cross sectional plane provides confinement of the light (as opposed to TIR off the cladding in conventional fibres), and using an air defect in the centre permits high power, loss loss optical transmission [77]. Extruded photonic crystal fibres are the best real-world approximation to ‘infinite’ 2D photonic crystals.

### 2.5.2 Integrated Photonics

While bending light around corners is original, efficient waveguides become especially useful when connected to achieve optical functionality.

Passive devices for PBC waveguides include Y-shaped splitters and combiners, tapers, and couplers between adjacent waveguides. In slightly more advanced devices, PBC waveguides with different modal characteristics – engineered via the defect dimensions or local dielectric constant – can be arranged to allow frequency selective filtering of light [78]. This is used, e.g., in add-drop multiplexers for wavelength division multiplexing communications systems [68, 79].

Active devices such as switches, modulators, and adjustable filters require dynamic tuning of the waveguide frequency. For PBC waveguides this can be achieved by using electro-optic materials, or by infiltration with liquid crystals whose electronically controllable orientation can change the index of refraction. The inherent porosity of PBCs makes the latter approach relatively easy to implement. Switching with liquid crystals has been modelled [80] and demonstrated [81] for inverse opals, with response times currently on the order of milliseconds.

Complete photonic integrated circuits can be constructed from the above components, with applications in optical telecommunications and other systems relying on processing of optical signals. For many years such optical circuitry has been made from conventional TIR based waveguides and optical fibres, mixed with electronic components where no optical devices are available. However, PBC based integrated optics has the potential to provide significant advantages and new opportunities, and not just from the previously discussed benefits of air core PBC waveguides over high index TIR waveguides.

First of all, the absence of curvature losses and the strong damping of evanescent modes over just a few lattice periods allow for high integration of optical devices. Secondly, 3D PBCs permit multilayer optical circuitry

with vertical linkage, all built on one monolithic substrate. And third, the radiative properties of PBCs (discussed in the next section) could be used for on-chip integration of efficient light sources. PBCs could thus contribute to the development of all-optical integrated circuitry, where the elimination of signal conversion between optics and electronics could allow full exploitation of the high speed and bandwidth of optical signal processing. Coupling such PBC circuits to external components, however, would require appropriate techniques for mode matching to the PBC waveguides.

At the extreme end of PBC photonics applications, schemes for all-optical PBC transistors have been proposed. The transistor action would derive from one laser beam causing population inversion in an active gain region on a PBC chip, with a second beam modulating the gain, so that a third beam passing through the gain region could be amplified, modulated, and switched on and off [82]. Eventually, such transistors might be used for photonic computing, with greater processing speed, greater data handling capacity, and less cross-talk and signal loss than in existing electronic computers.

### 2.5.3 Optoelectronics

Among the optoelectronic applications of PBCs are highly efficient light emitting diodes (LEDs). By placing a LED inside a photonic crystal with a bandgap coinciding with the LED emission range, engineered defect modes can be used both to force the spontaneously emitted light into specific modes, and to then extract the light along a desired direction [21]. Specifically, the high quality factor  $Q$  and low volume  $V$  of a PBC point defect resonant cavity can enhance spontaneous emission into a single mode, and thereby increase overall output and reduce the normally broad emission spectrum. Point defect resonant cavities have been fabricated in 1D [27], 2D [83] and 3D [84, 85] PBCs, and Noda *et al.* recently demonstrated cavity modes in a point defect in a woodpile 3D PBC with suppression of spontaneous emission outside the defect [86]. No energy is lost by omnidirectional random emission (a major energy sink in ordinary LEDs), and the PBC LED exhibits laser like traits such as single mode, pseudo-coherent emission, even while maintaining operation below the lasing threshold [21, 87, 88].

PBCs with an embedded active gain region constitute a highly efficient medium for lasing with zero or low threshold currents. This was first described by Yablonovitch as a key motivation for the development of photonic crystals [7]. The presence of spectrally broad spontaneous emission in ordinary lasers reduces the internal quantum efficiency to 0.6-0.7, which means

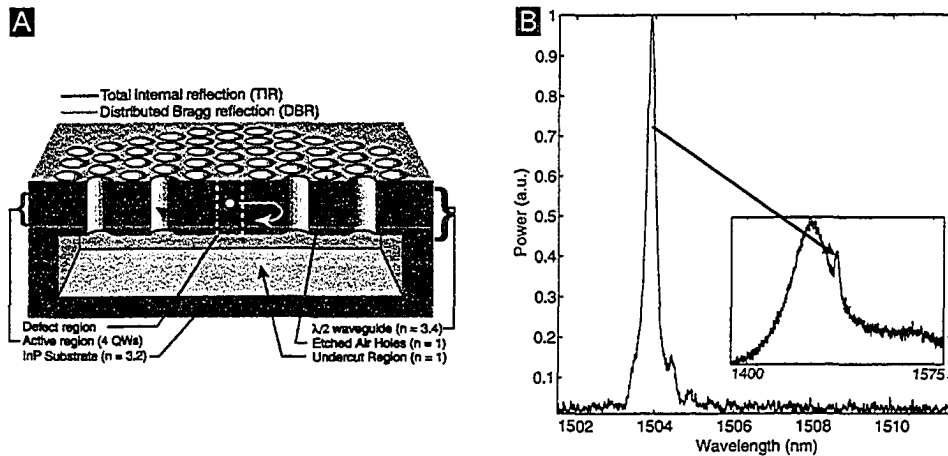


Figure 2.10: a) Schematic of the first PBC based laser by Painter *et al.*, built from light emitting quantum wells embedded in a 2D planar photonic bandgap crystal. The central point defect in the PBC constitutes an ultra small laser cavity. b) Corresponding laser emission spectrum with a narrow peak close to  $1.5 \mu\text{m}$ . The inset shows the spectrum below threshold. From [83].

that a minimum threshold current must be applied before lasing from stimulated emission becomes dominant [70]. Inside a complete PBC bandgap, however, spontaneous emission is inhibited, except that a point defect can be engineered to simultaneously increase radiation right at the stimulated emission frequency *and* act as a single-mode laser resonance cavity. Consequently:

- All radiation is forced to occur at the lasing frequency, bringing the internal quantum efficiency close to unity and lowering the threshold current.
- The laser output is strictly single mode – as given by the laser resonant cavity – since the remaining PBC bandgap eliminates the emission at neighbouring resonance frequencies seen in ordinary lasers.
- The high quality factor and minute volume of the PBC resonant cavity lower the energy consumption.

Aside from reduced energy losses, lower thresholds also improve the reliability of laser modulation [7, 21, 27].

Another PBC effect with potential use for lasing is the previously mentioned low group velocity at band anomalies and near bandgap edges. When  $v_g$  goes down the interaction time between the electromagnetic radiation and the medium goes up, and hence also the interaction time between the radiation and any embedded atoms with an inversion population. Light passing through an active gain medium under such conditions experience a strong enhancement of the amplitude amplification factor, which lowers the lasing threshold [16, 18].

A number of other benefits characterize PBC lasers. Lasers (and LEDs) embedded in photonic crystals can be monolithically integrated with other optical PBC components in the same crystal, for a complete all-optical circuit. Indeed, to tap light from within a bandgap cavity a nearby defect waveguide is required [89], and by the virtues of PBC waveguiding this coupling can be designed lossless, unlike the situation for ordinary solid-state lasers. The fact that dopable elemental and III-V semiconductors simultaneously possess the optical and electronic properties for light emission and light localization further advance the case for embedding LEDs and lasers inside PBCs. On their own, the minute physical dimensions of PBC lasers make them fit into applications with extreme space constraints.

The first PBC laser was demonstrated by Painter *et al.*, emitting pulsed, single-mode laser light at a wavelength of  $1.5 \mu\text{m}$  from within a  $0.03 \mu\text{m}^3$  small cavity in an indium gallium arsenic phosphide 2D PBC slab [83]. This laser is illustrated in figure 2.10.

## 2.6 Looking Ahead

Fully developed, photonic bandgap crystals promise to do for optics what semiconductors have done for electronics, delivering great improvements over existing photonic and optoelectronic technologies, and providing new possibilities for scientists and engineers across research disciplines. The potential socio-economic impact should not be underestimated. However, as illustrated by this chapter, many challenges remain even after two decades of progress in photonic crystal research.

The current status is that practical 3D PBC architectures do not yet deliver the localization and radiative properties required to pursue viable optical applications. Architectures relying on top-down fabrication, such as yablonovite and the woodpile, are complicated to fabricate and leave little room for control over the fine structural roughness and lattice disorders. This degrades the optical properties and impedes reliable engineering of

bandgap and waveguiding characteristics. Bottom-up architectures, such as inverse opals, have better local uniformity, but the ability to modify the crystal structure is limited. This makes it particularly difficult to introduce functional defects and tune the bandgap. In the absence of better fabrication methods, almost all experimental research on PBC applications has been performed in two dimensions, despite the fact that 2D crystals compromise the advances promised by 3D crystals.

Optical 3D PBC research would benefit from an architecture that not only delivers large bandgaps robust to disorder, but lends itself to fabrication by a technology proven to produce three dimensional, sub micrometre porous dielectric structures over large areas. The success of such a fabrication method would depend on demonstration of the ability to manage the fine structure, engineer the location of the bandgap, and pattern defects.

This thesis aims to investigate such an architecture, with the enabling fabrication method being one that combines the simplicity and uniformity of bottom-up self-assembly with the flexibility of top-down engineering: Porous, columnar thin films.

## Chapter 3

# Glancing Angle Deposition Thin Films

Thin films are of tremendous technological and scientific importance. Defined in the broadest sense as layers of solid matter deposited onto supporting substrates, thin films are relatively easy to fabricate yet extremely versatile. As continuous layers, thin films are applied to everything from shiny door knobs to space telescopes, while as patterned layers, lithographically processed thin films are fundamental to the fabrication of micro- and optoelectronics. In a third and recent thin film approach, functionality is realized not through uniformity or post deposition patterning, but by bottom-up tailoring of inhomogeneous film microstructures during the fabrication process itself. One such method is glancing angle deposition, which enables highly porous films with complex sub micrometre columnar morphologies to be realized in a single deposition step.

This review chapter will provide the scientific and technical background to thin films in general and oblique vapour deposition in particular, before focusing on the principles, characteristics, opportunities, and limitations of glancing angle deposition thin films. In due course it will become evident that these thin films address the requirements for the fabrication and engineering of three-dimensional photonic bandgap crystals.

## 3.1 The Science of Thin Film Growth

### 3.1.1 Nucleation and Film Growth

The nucleation and growth of all thin films follow the same fundamental mechanisms, which determine the eventual structure and properties of the films, and are crucial to understanding glancing angle deposition and any other thin film deposition method. Although practical thin film deposition is an art that depends on the deposition technique and the materials being used, the science of thin film growth is primarily a thermodynamic problem, with some impact from geometry as well. The nature of thin film nucleation and film growth thus depends largely on the energy available in the substrate/thin film system.

In vapour phase thin film deposition (liquid phase deposition will not be considered here), an incessant and random impingement of vapour phase clusters of atoms provides a continuous supply of material at the substrate. Some of the evaporant adsorbs to the substrate and subsequently condenses to the solid phase, and this solidification releases energy on the order of a few electron volts per atom. Meanwhile, arriving adatoms possess up to 10 eV of kinetic energy to be converted to thermal energy upon impact. Intentional substrate heating is another source of thermal energy, as is unintentional heating by thermal radiation originating from hot vapour sources. Thus, for most thin film systems the key drivers of film growth are the substrate temperature and the vapour impingement rate [90,91].

The formation of a thin film proceeds in a series of indistinct steps, as shown in figure 3.1. When evaporant atoms hit and adsorb to the substrate, some desorb after a shorter or longer sojourn, whilst others remain on the surface as adatoms. To prevent immediate reevaporation of adsorbed atoms, the vapour above the substrate must be supersaturated. Furthermore, the condition for net creation of adatoms is [29]:

$$S = \frac{\lambda^2}{L^2} \exp\left(\frac{\Delta G_d - \Delta G_s}{kT}\right) > 1. \quad (3.1)$$

A surface that is rough (the distance  $L$  between surface binding sites being small) and cold (the temperature  $T$  being small) clearly makes the ratio  $S$  of surface binding to desorption large and favourable for film growth. ( $\lambda$  is the jump distance between neighbouring surface sites, and  $\Delta G_d$  and  $\Delta G_s$  are the Gibbs energies for atom desorption and atom movement between surface sites, respectively.) The first adatoms to arrive migrate short distances to join together in small nuclei, fuelled by the available thermal energy,

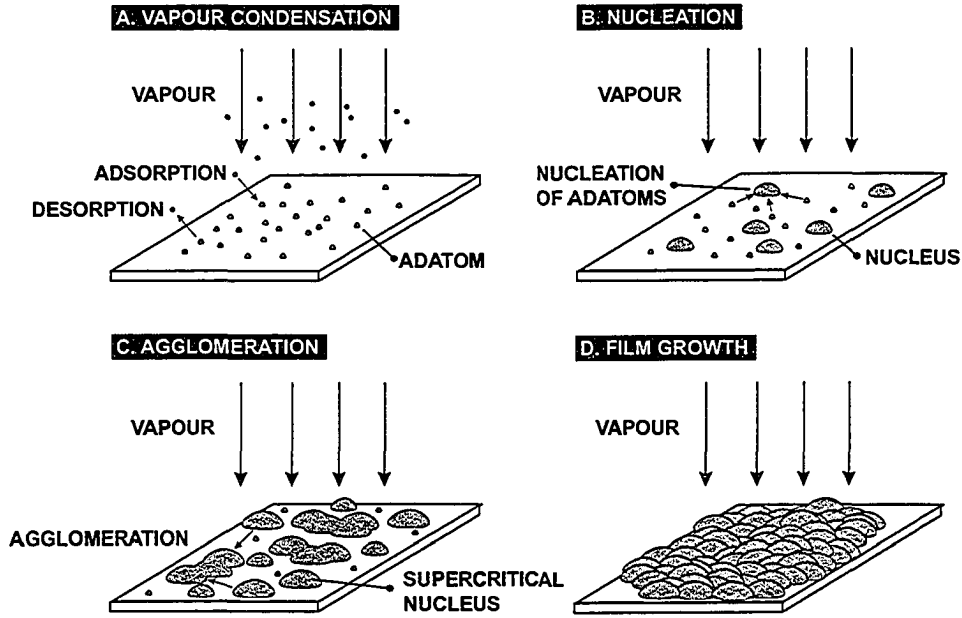


Figure 3.1: Schematic drawing of the formation of a thin film. Following adsorption of adatoms from the vapour phase (a), nuclei begin to assemble (b), grow, and agglomerate (c) to create a continuous film (d).

and driven by the fact that nucleation minimizes their surface energy by reducing the combined surface area, and hence the number of energetically unfavourable dangling bonds. The nuclei subsequently receive more incoming evaporant, and under the quest to minimize the overall surface energy they begin gobbling up nearby adatoms and smaller nuclei. For example, when two hemispherical nuclei of radius  $r$  join together, the surface energy  $E_{tot}$  of the new, combined nucleus of radius  $r_{tot}$  is related to the previous surface energy  $2E$  of the individual nuclei as follows [29, 92]:

$$\frac{E_{tot}}{2E} = \frac{2\pi r_{tot}^2 \gamma}{2(2\pi r^2 \gamma)} = \frac{2\pi(2^{1/3}r)^2 \gamma}{2(2\pi r^2) \gamma} = \frac{2^{2/3}}{2} < 1, \quad (3.2)$$

where  $\gamma$  is the surface tension (surface energy per area) between the nuclei material and the surrounding vapour. Likewise, the surface energy of the nucleus/substrate interface is reduced as well. In turn, the nuclei become super-critical (too large for desorption), and begin agglomerating with other nuclei clusters through ripening or coalescence to form islands and eventually a continuous thin film of the evaporant material [92].

Subsequent accumulation of film proceeds under the continued influence of three growth mechanisms:

- Geometrical shadowing.
- Surface diffusion.
- Bulk diffusion.

The interplay between these mechanisms has a large impact on the characteristics of any thin film, with the kinetics of the two diffusion mechanisms being responsible for the dependence of film growth on thermal energy. As alluded to above, surface diffusion in particular has an impact not only on film growth, but also on the initial nucleation phase.

Geometrical shadowing derives from the fact that each nucleus or protrusion in a growing film acts as an interceptor of evaporant, and casts an atomic shadow behind it into which no additional impinging vapour can reach. The shadows are defined by the geometry of the random protrusions and the distribution of the impinging evaporant. For geometrical shadowing to have an impact, diffusion must be so slow that adatoms cannot move in and fill the voids in the shadows.

Surface diffusion is capable of transporting evaporant material along the substrate and film surfaces as well as along grain boundaries. This growth mechanism assists in the agglomeration of nuclei, but also helps filling in voids left in the growing film, since mass transport tends to move material from regions of small radii curvatures to regions of large radii curvatures, thus decreasing the net surface area and smoothing out the film structure [29]. Surface diffusion has a strong Arrhenius-type dependence on temperature, as given by the diffusion laws and represented by the diffusion coefficient  $D$  [29]:

$$D = D_0 \exp\left(-\frac{E_a}{k_B T}\right). \quad (3.3)$$

Here  $D_0$  is a material specific constant,  $E_a$  is the activation energy,  $k_B$  is Boltzmann's constant, and  $T$  is the temperature. The mobility of adatoms is often described by a characteristic surface diffusion length  $\lambda_s$ :

$$\lambda_s = \sqrt{Dt}, \quad (3.4)$$

where  $t$  is the time available for diffusion (before desorption or nucleation with other adatoms).

The final growth mechanism is bulk diffusion, which involves the transport of material in the depth of the growing film. Whereas surface diffusion

can occur relatively freely on a two-dimensional surface, bulk diffusion is hampered by the limited availability of vacant sites in the bulk of both amorphous and crystalline films. Bulk diffusion therefore requires much more energy to be activated than the previous two growth mechanisms, and the characteristic bulk diffusion length  $\lambda_b$  is much lower for a given temperature than the surface diffusion length  $\lambda_s$ . However, bulk diffusion can cause sufficient rearrangement of atoms to yield a poly or single crystalline film structure, as in annealing [93].

In any thin film deposition process, all three growth mechanisms will impact the final film structure. However, from the above it is evident that geometrical shadowing is important only at low temperatures, when insufficient thermal energy is present to cause noticeable diffusion. At higher temperatures, diffusion becomes the dominant mechanism, with surface diffusion dominating over bulk diffusion. Every film/substrate material combination behaves differently, since the interface and bulk energy characteristics are different, but in general high substrate temperatures and low deposition rates tend to yield crystalline films, whereas low substrate temperatures and high deposition rates tend to yield amorphous or nanocrystalline films [90, 91, 93].

### 3.1.2 Film Characteristics and Structure Zone Models

The nucleation and growth of a thin film has tremendous impact on the film morphology and microstructure, i.e., the overall physical appearance and the fine structure of the constituent grains or columns. These in turn affect the properties of the thin film, which – be they mechanical, optical, electrical, or thermal – typically vary significantly from the bulk properties of the film material. The film morphology indirectly affects the density of the thin film, since the presence of voids or pores reduces the film mean density below that of bulk. Meanwhile, the film microstructure depends on the crystallographic structure of the film, be it amorphous, polycrystalline or monocrystalline. In very general terms, the increased disorder in as-deposited thin films give them poorer characteristics than their corresponding bulk materials, such as lower density, lower conductivity, and greater optical scattering. However, this is outweighed by the ability to carefully engineer the thin film microstructure and related properties, in a way not possible for bulk materials.

Structure zone models are a means to describe the structural characteristics of thin films. The first structure zone model was presented by Movchan and Demchishin in 1969 [94], based on experimental data from evaporations

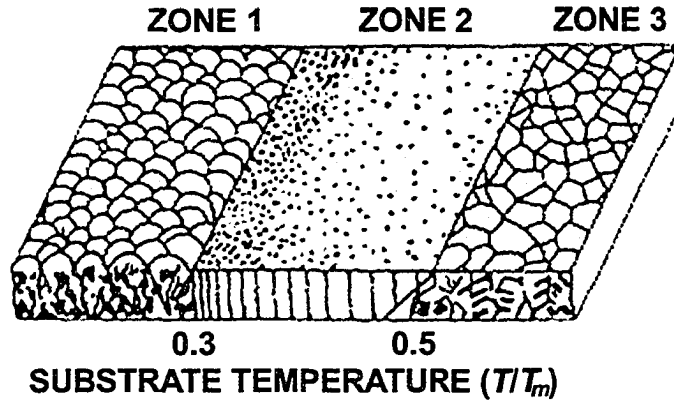


Figure 3.2: Movchan and Demchishin's structure zone model for thin films. Depending on the substrate temperature  $T$  relative to the film material melting point  $T_m$ , the film structure can be columnar and voided (zone 1), granular and faceted (zone 2), or dense and polycrystalline (zone 3). Adapted from [94].

of several different metals and oxides onto heated substrates. They found three distinct types of film growth, as illustrated in figure 3.2: In zone 1, performed on substrates with temperatures less than  $0.3T_m$  ( $T_m$  being the melting point of the film material), the films consisted of tapered grains separated by voids. In zone 2, for substrate temperatures between  $0.3T_m$  and  $0.45 - 0.50T_m$ , the film structure was columnar with fewer voids and tighter grain boundaries. In zone 3, with substrate temperatures higher than  $0.5T_m$ , the film structure became polycrystalline, consisting of grains with co-parallel crystal orientations. Other researchers have subsequently elaborated on Movchan and Demchishin's results, notably Sanders with a five zone model [95], Thornton with a four zone model for sputtered thin films [96], and Hentzell *et al.* on evaporated metal films [97]. However, the fundamental three structure zones remain valid and sufficient for an integrated understanding of the structure and characteristics of glancing angle deposition thin films.

In zone 1, the low substrate temperature means that geometrical shadowing is the dominant growth mechanism. The limited adatom mobility not only prevents the voids in the film from being erased, but furthermore causes the film structure to be columnar, since each dome-like grain is sup-

plied with evaporant primarily from the impinging vapour above the film, rather than by lateral surface or bulk transport of adatoms [93]. In other words, the voided, columnar structure is formed by extruding the initial shadow-dominated islands nucleated on the substrate into the third dimension. To whatever extent surface diffusion does exist, it may contribute to determining the width of the columnar structures. Thin films in zone 1 are amorphous, with a low mean density relative to the bulk density of the film material, and – conversely – a high surface area maintained constant throughout the thickness of the film [92]. Glancing angle deposition thin films belong in this structure zone.

In zone 2, surface diffusion is the dominant growth mechanism. The mobility is large enough to smoothen out any geometrical voids, resulting in a granular, columnar film structure of faceted, close-packed fibres or grains growing from the substrate to the top of the film. The width of the columns depends on the diffusion length, and is larger than in zone 1. For zone 2 films the density is close to bulk [98].

In zone 3, film growth takes place sufficiently close to the melting point of the film material that bulk diffusion becomes the dominant growth mechanism. Recrystallization takes place within each grain, originating from the substrate and propagating up through the film to create equiaxed grains with few defects. The film structure is dense and polycrystalline, or in some cases even monocrystalline, allowing epitaxial films to be grown. The properties of these films approach the bulk properties of the evaporant material [92].

The behaviour of each structure zone thus corresponds to the dominant growth mechanisms discussed in the previous section, and each structure zone represents a distinct class of thin films. Depending on the desired thin film properties, a deposition technique must be chosen which delivers films belonging to the right structure zone, from amorphous, sacrificial oxides to optoelectronics quality epitaxial layers of single crystalline gallium arsenide.

## 3.2 The Technology of Thin Film Deposition

The preceding section provided a general and mostly theoretical discussion of the growth and structure of thin films deposited from the vapour phase. In practise, the properties of a thin film depend heavily on the method used for its deposition, and for each method particular importance must be paid to the deposition rate, the substrate temperature, the pressure of the ambient vapour, and the geometry of the vapour flow incident on the substrate [98]. A myriad of thin film deposition technologies exist, and almost all elemental

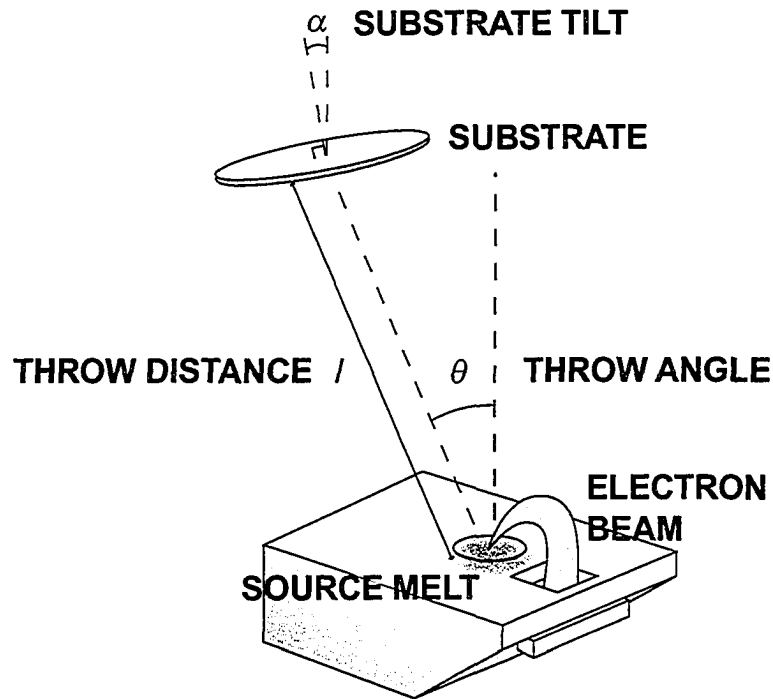


Figure 3.3: Schematic drawing of physical vapour deposition by electron beam evaporation, performed in a high vacuum chamber. High energy electrons cause the source material to melt and emit vapour, which travels ballistically to impinge and condense on the substrate. The throw distance, angle, and substrate tilt determine the vapour distribution.

and compound inorganic materials (as well as some organic materials) can be deposited as thin films. However, in the context of glancing angle deposition the following treatment will narrow the focus to physical vapour deposition techniques.

### 3.2.1 Physical Vapour Deposition by Evaporation

In physical vapour deposition (PVD) the evaporant is emitted from a source as a vapour and transported under vacuum to impinge and physically condense on the substrate. The emission of vapour occurs either by evaporation or (as described in the next section) by sputtering. For evaporation, the source material is heated beyond its melting point until it begins releasing substantial amounts of vapour. The preferred way of heating the

source material is to place it in a cooled crucible and bombard it with a focused beam of high-energy electrons, as shown in the illustration of an e-beam evaporation system in figure 3.3. Melting and evaporation of the source material then occurs at the point of impact of the electron beam in the centre of the crucible, while the surrounding cooled source material in the crucible provides thermal and contamination isolation of the melt. The electron emitter is a heated filament, which is mounted underneath the crucible to protect it from the source vapour, and whose emitted electrons are first accelerated by an anode into a unidirectional beam by an electric field, before being steered into the crucible by variable magnetic fields. An alternative to e-beam evaporation is thermal evaporation, in which the source material is wound as a wire around a coil of refractory metal or placed in refractory foil boat, and then resistively heated by sending a large electrical current through the refractory carrier [92, 99].

Once ejected from the source, the evaporant vapour travels to the substrate by ballistic transport. In order to maintain straight-line trajectories, the mean free path  $\lambda_p$  of the evaporant (whether atoms or molecules) must be larger than the source to substrate throw distance  $l$  (see figure 3.3) [92]:

$$\lambda_p = \frac{k_B T}{P \pi \sqrt{2} d_0^2} > l. \quad (3.5)$$

$P$  is the pressure inside the deposition chamber, and  $d_0$  is the molecular diameter. For chamber dimensions  $l$  on the order of 0.5 m, the pressure must be:

$$P < \frac{k_B T}{l \pi \sqrt{2} d_0^2} = 20 \text{ mPa}. \quad (3.6)$$

A high vacuum system is therefore necessary for PVD by evaporation. A second but equally important reason for maintaining high vacuum is minimization of film contamination. Even at a pressure of 20 mPa, the time for formation of a monolayer of ambient gas molecules is on the order of 10 ms, leading to partial film oxidation and/or incorporation of impurities in the deposited films [93]. Finally, high vacuum increases the evaporation rate from the source.

When collinear impingement of evaporant vapour on the substrate is desired – as in glancing angle deposition – a large mean free path is not sufficient, since the evaporant is emitted hemispherically from the source with the mass distribution following a cosine law. For a substrate element  $dA$ , the differential mass  $dM$  deposited per unit time is [100]:

$$\frac{dM(\alpha, \theta)}{dA} = \frac{M_e}{\pi l^2} \cos \alpha \cos \theta, \quad (3.7)$$

where  $l$  is the source-substrate throw-distance,  $M_e$  is the evaporation rate from an area element of the source,  $\alpha$  is the substrate tilt relative to the source normal, and  $\theta$  is the angular location of the substrate relative to the source normal (see figure 3.3). The closest approximation to a uniform, collinear vapour impingement on the substrate is achieved when the throw-distance  $l$  is large, the substrate is centred over the source ( $\theta = 0$ ), and the substrate is tilted obliquely ( $\alpha$  close to  $90^\circ$ ), minimizing the substrate solid angle as viewed from the source.

One side effect of PVD by evaporation is unintentional substrate heating caused by thermal radiation from the molten source. This can be countered by passive substrate cooling or active substrate temperature control. Furthermore, the process chambers of PVD systems often require cooling to prevent adsorbed contaminants from outgassing once the systems heats up. Chamber cooling also has the additional benefit of increasing the sticking coefficient of impinging molecules, thus capturing contaminants and preventing source vapour from reflecting off the chamber walls and hitting the substrate from random directions. [92]

The main advantages of PVD by evaporation are its versatility, the purity of the produced films, and the ability to obtain a uniform, nearly collinear impingement of vapour onto the substrate. All of these attributes are essential for glancing angle deposition.

### 3.2.2 Physical Vapour Deposition by Sputtering

A second PVD method of relevance to glancing angle deposition is PVD by sputtering. In this techniques, a vapour is created by bombarding a solid state target of the source material with high energy ions. The ions are supplied by a plasma of a heavy, inert gas (typically argon), and accelerated toward the target by a cathode biased up to a few kilovolts. When the ions hit the target, a cascade of momentum transfer leads to the ejection of neutral source atoms with energies up to a few tens of electron volts. The vapour of source atoms then travels through the plasma to the substrate [93].

The presence of a plasma necessitates a higher pressure than in PVD by evaporation, typically on the order of 1 Pa [93]. The high pressure in turn scatters the source vapour flux and precludes straight-line ballistic transport of the source material to the substrate. Compared with PVD by evaporation, sputtering thus leads to a much broader angular incidence of vapour onto the substrate, which is the main drawback of sputtering for glancing

angle deposition. This is compounded by the facts that sputter targets are larger than evaporation sources, and that sputtered atoms are much more energetic than evaporated atoms (leading to more adatom diffusion and less geometrical shadowing) [98].

Nevertheless, under the right conditions sputtering can be and has been used for glancing angle deposition. The primary advantages are reduced radiant substrate heating from the target (which works in favour of glancing angle deposition), the ability to use sputtering in varied geometries, and the applicability of sputtering to industrial scale production.

A third PVD method for glancing angle deposition is pulsed laser deposition, which was demonstrated by Vick *et al.* for carbon [101]. This technique provides small source areas and hence collinear vapour streams at the substrate, and allows for the deposition of materials incompatible with traditional PVD systems (such as certain compounds or materials with very high melting points).

### 3.3 The Fundamentals of Glancing Angle Deposition

Before delving into the details and characteristics of glancing angle deposition, it is instructive to consider the history of oblique thin film deposition, from which GLAD is derived.

#### 3.3.1 The History of Oblique Thin Film Deposition

It has long been known that the angle of incidence of the evaporant during thin film deposition has a profound impact on the film structure. Traditional thin film applications, such as optics and microelectronics, require dense, uniform coatings, and these are best achieved when the evaporant impinges on the substrate at normal or near-normal angles, accounting for the vast majority of historic thin film research. In contrast, thin film deposition at oblique angles – commonly considered to comprise incidence angles higher than  $75^\circ$  relative to the substrate normal – is a recent research area for porous, heterogeneous film structures.

The first report on oblique thin film deposition was provided by Holland in 1953 [102]. He evaporated aluminium onto glass at various incidence angles, and noted that films deposited at  $80^\circ$  and  $85^\circ$  transmitted light selectively with respect to the incidence direction of the evaporant. Maximum transmission was observed for light incident at  $40^\circ$  to  $50^\circ$  relative to the

substrate normal, and parallel to the evaporant incidence direction. Holland (correctly) assumed that this behaviour was due to a “tendency for the grains to grow in the direction of the vapour beam” [102], but rather than pursuing the new-found properties he simply concluded that oblique incidence should be avoided for the production of aluminium mirrors.

In 1959, Smith [103] and Knorr and Hoffmann [104], followed by Cohen in 1961 [105], studied iron and nickel films deposited at oblique incidence angles. They found strong magnetic anisotropy for angles greater than  $70^\circ$ , with the magnetic easy axis aligned parallel to the vapour incidence direction. Using scanning electron microscopy, the anisotropy was explained by “self-shadowing” inside the growing film, leading to elongation of crystallites in the incidence direction of the vapour [105].

After these early discoveries little happened until the 1980s, when advances in computer modelling sparked interest in simulating the growth of thin films. The simulations revealed that deposition at oblique incidence angles lead to a very porous film microstructure of inclined, columnar grains [106]. Among the key investigators were Dirks and Leamy, who proposed a numerical relation between the angle of evaporant incidence and the inclination angle of the resulting film structures [107]. Meakin and Krug studied the increase in film surface roughness with vapour incidence angle, and described the evolution of columnar, anisotropic microstructures [108,109].

Practical oblique thin film deposition re-emerged in the 1990s with a focus on optical applications. Bloemer *et al.* evaporated anisotropic columnar silver films [110], and Le Bellac *et al.* did AFM studies of oblique chromium films [111]. Taga and Motohiro fabricated birefringent optical retardation plates by oblique deposition of metal oxide films [112], while Hodgkinson *et al.* elaborated further on the birefringence and anisotropic optical scattering of porous, columnar thin films [113,114]. Non-optical applications were sought by Dohnálek *et al.*, who investigated the catalytic and sensor properties of high surface area films [115].

With the renewed interest in oblique thin film deposition, researchers began investigating the impact of varying not just the vapour incidence angle relative to the substrate normal, but also the vapour arrival direction in the plane of the substrate. As early as 1959, Young and Kowal deposited thin films onto modestly oblique, rotating substrates, and noted that the films exhibited optical activity, i.e., rotated the polarization direction of linearly polarized light [116]. Taga and Motohiro had the vapour arriving from alternating, opposite directions to fabricate a zig-zag or chevron film structure [117], and McPhun, Wu and Hodgkinson used both oscillating and rotating substrates to create rugate optical filters [118,119].

### 3.3.2 Definition of Glancing Angle Deposition

On this historic background, Robbie and Brett developed Glancing Angle Deposition (GLAD) in 1995 as a new platform for experimental research into the potential benefits of highly porous columnar thin films [120, 121]. GLAD is a method for oblique angle physical vapour deposition, in which the exact angle of vapour incidence can be adjusted during film deposition, and the substrate furthermore be rotated about a second axis normal to the substrate. This allows for pseudo-three-dimensional motion of the substrate, while maintaining a near-constant throw distance from the vapour source to the substrate. Beyond the simultaneous and independent motion of the substrate about two axes, a second critical innovation in GLAD is that substrate motion is dynamically controlled by a pre-programmed computer that precisely adjusts both position and axis rotation speed, with system feedback correcting for fluctuations in the deposition rate. Unlike systems with pre-set or manually adjusted substrate orientations, GLAD thereby permits the development and reproduction of algorithms representing highly complex substrate motion schemes [122–124].

Figure 3.4 illustrates the GLAD experimental setup, consisting of a dual-axis substrate holder mounted inside a PVD chamber. The substrate tilt axis defines the vapour incidence angle  $\alpha$ , relative to the substrate normal. It can be kept constant or varied during a deposition, but is usually kept higher than  $80^\circ$  to accentuate the effects of oblique thin film deposition. The substrate rotation axis defines the vapour arrival direction  $\phi$ , which can be constant, adjusted in a step-wise fashion, or cycled continuously during a deposition. The plane containing the substrate normal and the vapour arrival direction constitute the deposition plane.

By exploiting the ability to dynamically adjust the vapour incidence directions, GLAD is able to create complex and previously unattainable porous film microstructures of sub micrometre columns in many different shapes [125–127].

### 3.3.3 The Science of Glancing Angle Deposition Thin Films

#### Impact of Substrate Tilt

In order to describe the science behind GLAD thin films, it is beneficial to initially look at the effect of each of the two rotation axes separately. Figure 3.5 portrays the effect of the substrate tilt axis by showing a GLAD thin film deposited at a fixed vapour incidence angle  $\alpha$  of  $85^\circ$  and with no substrate rotation. The film microstructure is seen to be extremely porous, consisting

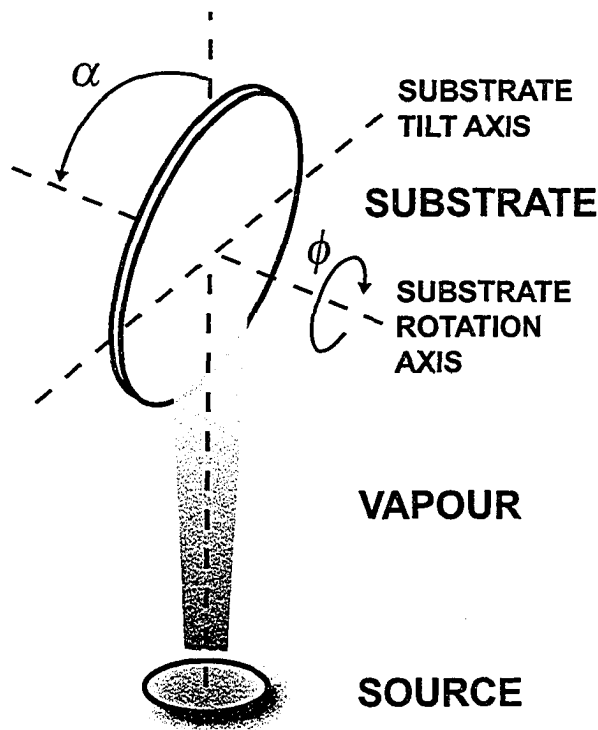


Figure 3.4: The Glancing Angle Deposition (GLAD) setup. In a PVD system, vapour impinges onto a substrate which can rotate about two axes. The substrate tilt axis sets the vapour incidence angle  $\alpha$  (usually  $> 80^\circ$ ), and the substrate rotation axis regulates the vapour arrival direction  $\phi$ .

of independent columns or posts tilted to an angle  $\beta$  of approximately  $56^\circ$ . This film structure of voided, domed columns is reminiscent of zone 1 in the structure zone models discussed in section 3.1.2, in which geometrical shadowing dominates over surface and bulk diffusion for low temperature depositions. Indeed, GLAD is a low temperature deposition process, since it relies on a large throw distance from the PVD source to the substrate (for minimization of the angular spread of the impinging vapour), and since dedicated substrate heating is rarely used. Furthermore, intrinsic geometrical shadowing in the growing GLAD film is bound to be heavily amplified by the grazing vapour incidence angles.

Figure 3.6 schematically illustrates the thin film growth mechanics induced by the highly oblique vapour incidence angle and responsible for the slanted post film in figure 3.5. With accentuated geometrical shadowing,

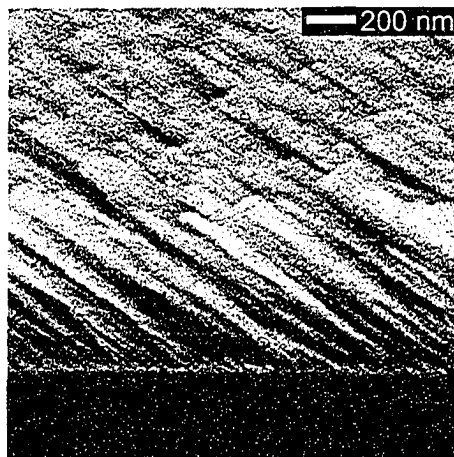


Figure 3.5: Slanted post GLAD film of europium-doped yttrium oxide. The film was deposited at a vapour incidence angle  $\alpha$  of  $85^\circ$  with no substrate rotation. The film structure is seen to be very porous, consisting of columns tilted to an angle of  $56^\circ$  relative to the substrate normal. From [128].

the first nuclei randomly assembling on the substrate (or any preexisting topographical features on the surface) will have long shadows extending behind them, inside which no further impinging vapour can land on the substrate [123, 129]. In the absence of significant surface or bulk diffusion, these voids behind the nuclei cannot be filled in. All subsequently incoming vapour therefore accumulates on top of the initial nuclei, which continue to grow in height and evolve into individual columns [106]. As the growing columns cast still longer shadows behind them, self-shadowing among the columns ensure that a highly voided film structure is maintained throughout the thickness of the film.

Although surface diffusion and bulk diffusion are incapable of overcoming the effects of geometrical shadowing to smoothen out the voided, columnar morphology, diffusion on or inside individual columns impacts the width of the GLAD columns (as well as the shape of the domed column apices), similar to the way in which diffusion affects the grain size in denser, traditional thin films. Consequently, in depositions of materials with large diffusion lengths, the column diameter is generally larger than in depositions of materials with low adatom mobility [123]. Some evaporant materials – such as silicon dioxide – tend to quickly reach a natural column diameter which remains constant through the film. However, for most materials the extreme vapour incidence angles lead to inherent instability in the column diameter,

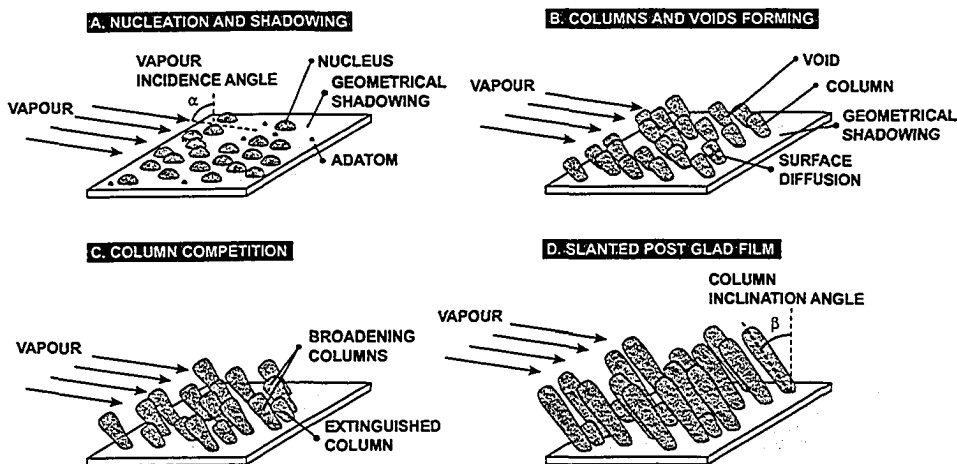


Figure 3.6: The formation of a slanted post GLAD film is achieved by tilting the substrate to a high vapour incidence angle  $\alpha$ . Strong geometrical shadowing among the initial nuclei (a) leads to a columnar, voided film structure with limited adatom diffusion (b), competition among the broadening columns (c), and a final column inclination angle  $\beta$  less than  $\alpha$  (d).

since any random local broadening of a column (caused by the stochastic nature of the vapour impingement) results in irreversible enlargement of its geometrical shadow. This column will now intercept even more incoming vapour, while other columns growing along the edge of its shadow will receive less. The constant competition for vapour among the columns lead to broadening of some columns and extinction of others, as is evident in figure 3.5 and illustrated in figure 3.6 [130, 131].

GLAD is usually performed at moderate to high deposition rates, which in conjunction with the low substrate temperature supports the fact that many GLAD films are amorphous as deposited (cf. section 3.1.1). As would be expected, the properties of the evaporant material – in particular, the melting point – have significant influence on the GLAD film formation. Some materials thus yield poly or monocrystalline GLAD films (e.g., cobalt [132]), with each column segment consisting of one or more crystal grains, columns apices being faceted, and a microstructure featuring characteristics of both structure zones 1 and 2. Careful post deposition annealing of amorphous GLAD films has also resulted in polycrystallinity for some materials [128].

Beyond the macroscopic columns visible in the GLAD film in figure 3.5, which are up to hundreds of nanometres wide, each column in amorphous GLAD films has itself a microstructure of tightly packed nanoscale columns

or fibres, typically with widths less than a few tens of nanometres [129,133]. For some materials (e.g., germanium [134]), it is even possible to discern a grain structure within these fibres. Alongside each level of columnar scale is an associated level of voids, from the large voids in figure 3.5 to nanoscale pores within each column. In general, therefore, the mean density of a GLAD column is not equal to the bulk density of the evaporant material. The sub columnar structure results from the same growth mechanics that are responsible for the macroscopic GLAD morphology, notably geometrical shadowing and limited adatom diffusion [93]. Indeed, Messier has demonstrated that the growth of low mobility thin films – including GLAD films – exhibits self-similar or fractal behaviour [135].

In addition to the film morphology being columnar and voided, another key feature of the GLAD thin film in figure 3.5 – when compared to a traditional, normal incidence zone 1 film – is the fact that the columns are tilted over to one side. Like the high porosity, the column tilt is a result of the vapour incidence angle being highly oblique, with the columns tilting toward the vapour source within the deposition plane. However, perhaps somewhat surprisingly the column inclination angle  $\beta$  is not equal to the vapour incidence angle  $\alpha$ . This fact was the focus of much study in the early days of oblique thin film deposition, and the first empirical attempt to quantify the phenomenon was the so-called ‘Tangent Rule’ by Nieuwenhuizen and Haanstra [136]:

$$\beta = \tan^{-1}(1/2 \tan \alpha). \quad (3.8)$$

This relation (shown as a black dashed line in figure 3.7) works well for  $\alpha$  less than  $60^\circ$  [106], but its prediction of  $\beta$  approaching  $90^\circ$  for  $\alpha$  approaching  $90^\circ$  is clearly not consistent with the real world, as exemplified by the  $\alpha = 85^\circ$  film in figure 3.5.

In fact, closer analysis of the shadowing and adatom diffusion occurring on dome shaped (zone 1) columns under oblique vapour impingement shows that the evaporant is forced to accumulate preferentially at the top of the columns, rather than on their front edge, due to geometrical constraints and a tendency of adatoms to migrate in the direction of the incoming vapour stream to conserve atomic momentum in the plane parallel to the substrate [106,137]. This causes the columns to become more “upright” than the vapour incidence angle would otherwise suggest. Accordingly, Tait *et al.* developed the following expression for the column inclination angle [138]:

$$\beta = \alpha - \sin^{-1}[(1 - \cos \alpha)/2]. \quad (3.9)$$

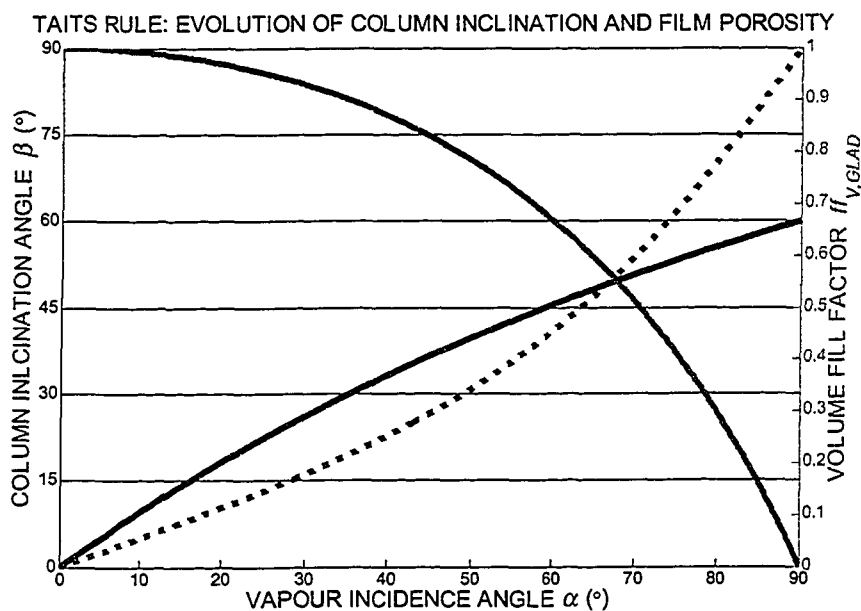


Figure 3.7: Plots of Tait's Rule for the column inclination angle  $\beta$  (black solid curve) and the volume fill factor  $ff_{V,GLAD}$  (red curve) as functions of the vapour incidence angle  $\alpha$ . The Tangent Rule for  $\beta$  (black dashed curve) is shown for reference. According to Tait's Rule, as  $\alpha$  approaches  $90^\circ$ ,  $\beta$  levels out to a maximum of  $60^\circ$  while  $ff_{V,GLAD}$  approaches zero.

This 'Tait's Rule' – plotted as a black solid line in figure 3.7 – does a much better job at predicting  $\beta$  for the high vapour incidence angles common in GLAD, and indeed establishes that  $\beta$  falls behind at higher  $\alpha$  values to a maximum column inclination angle of  $60^\circ$ , in agreement with figure 3.5. Hodgkinson *et al.* made Tait's Rule more general by adding a factor to account for material and deposition specific parameters such as vapour spread and chamber pressure [139].

### Impact of Substrate Rotation

Figure 3.8 illustrates the effect of the second rotation axis in the GLAD method, namely the substrate rotation axis. The columns now have the shape of a square spiral, that is, a helix whose circumference is square rather than round (as viewed along the helix central axis normal to the substrate). As shown schematically in figure 3.9, this film structure is achieved by dis-

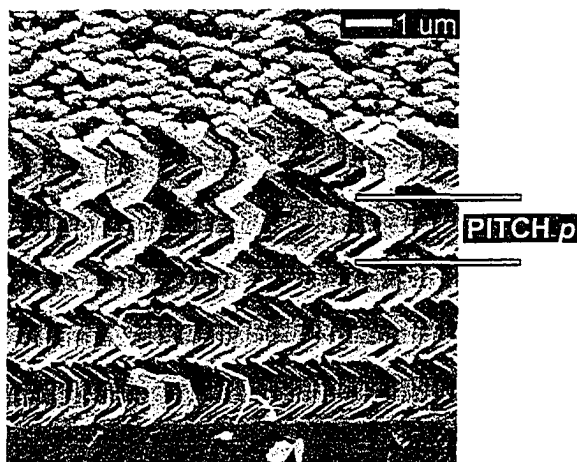


Figure 3.8: Oblique view of a square spiral silicon GLAD film deposited at a vapour incidence angle  $\alpha$  of  $83^\circ$ . The square spiral structure is achieved by rotating the substrate in discrete  $90^\circ$  turn, with four turns for a complete helical winding. The vertical height of a winding defines the pitch  $p$ .

cretely turning the substrate  $90^\circ$  at regular intervals, with four such turns for every complete winding of the square spiral. In effect, this amounts to stacking slanted post GLAD films – as in figure 3.5 – on top of each other, with each layer alternating the orientation of the columns. A range of other columnar film structures can be realized, as will be described later.

The ability to achieve such complex columnar film morphologies relies on the anisotropic vapour distribution inherent in the GLAD method [123, 124]. Being a PVD process, the vapour stream over the substrate is intrinsically collinear (which is necessary to support geometrical shadowing) [98], and the high vapour incidence angles  $\alpha$  make the vapour stream extremely directional with respect to the azimuth angle. As a zone 1 film structure with little adatom diffusion, the GLAD columns will always grow toward this directional vapour stream, even if they are not perfectly aligned with the vapour source, as detailed by Tait's Rule. Rotation of the substrate is equivalent to moving the anisotropic vapour arrival direction about in the hemisphere over the substrate, and the columns simply follow along to become extruded in whichever direction the substrate position dictates.

The science of GLAD thin film growth has been investigated and confirmed by numerous modelling efforts. In particular, oblique thin film studies by Meakin and Krug [108, 109] and by Bales *et al.* [140] have described the evolution of GLAD films, with competition in the voided column structure

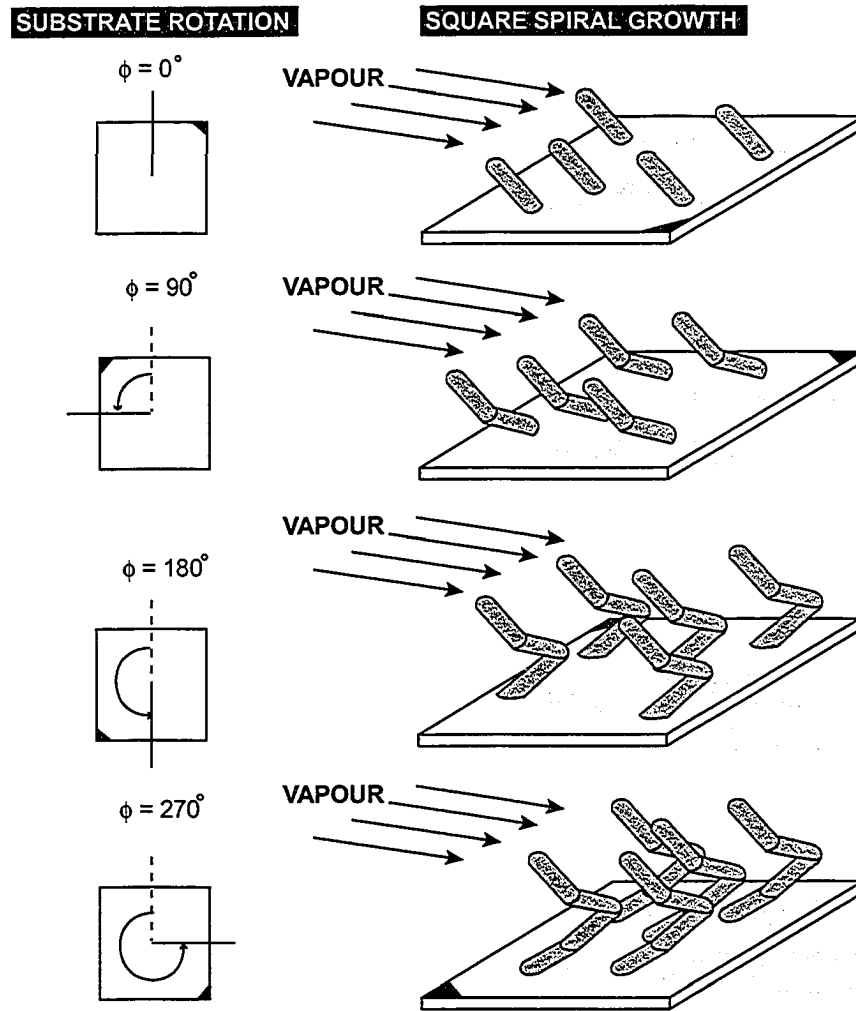


Figure 3.9: In GLAD, the anisotropic vapour stream allows complex columnar shapes to be extruded by discrete or continuous substrate rotation. Regularly spaced  $90^\circ$  turns, for example, deliver a square spiral film structure.

leading to a fractal like scaling behaviour. The best models to take substrate rotation into account have been developed by Smy *et al.* [141] and by Suzuki and Taga [142], whose ballistic deposition simulators rely on all the previously described film growth mechanisms to emulate GLAD film nucleation and growth.

### 3.3.4 The Technology of Glancing Angle Deposition

With vapour anisotropy being a key condition for GLAD thin film growth, only deposition technologies offering a long mean free path  $\lambda_p$  (see equation 3.5) and a high throw-distance  $l$  from the source to the substrate (see equation 3.7 and figure 3.3) are relevant to GLAD. This eliminates chemical vapour deposition as an option altogether, and leaves physical vapour deposition by evaporation or low-pressure, long-throw sputtering as the best methods. Diffusion and cryogenically pumped evaporation systems provide the best GLAD deposition conditions, while sputtering suffers from a wider angular spread  $\Delta\alpha$  of the impinging vapour, caused partly by vapour scattering inside the sputter working gas, and partly by the relatively large angle subtended by the sputter target over the substrate [143, 144]. The angular vapour spread can be reduced somewhat by mechanical collimating grids, but these tend to get clogged with evaporant. In all cases the substrate should be suspended over the centre of the source and the throw-distance maximized, in order to minimize the vapour spread in accordance with equation 3.7 (which, interestingly, shows that tilting of the substrate inherently improves the collinearity of the vapour stream). Using PVD, a very wide range of materials can be deposited as GLAD thin films, including metals, semiconductors, oxide, fluorides, and even some organic materials. Evaporation by electron beam heating generally yields the best results and repeatability, although thermal evaporation works sufficiently well for some materials. Typical deposition parameters are evaporation powers up to a few kilowatts, and pressures below 2 mPa for a mean free path of at least several metres. All GLAD experiments described in this thesis were performed by electron beam evaporation, with a throw-distance of more than 400 mm. One such system is depicted in figure 3.10.

In distinct contrast to the early oblique deposition experiments, in which the substrate tilt angle was fixed before the experiment, and substrate rotation rates were nil or constant, a key aspect of GLAD is dynamic control over both substrate rotation axes during deposition. This is achieved by integrated computer control of the rotation axes, which continuously adjusts the substrate tilt and rotation values  $\alpha$  and  $\phi$  in accordance with a user-defined

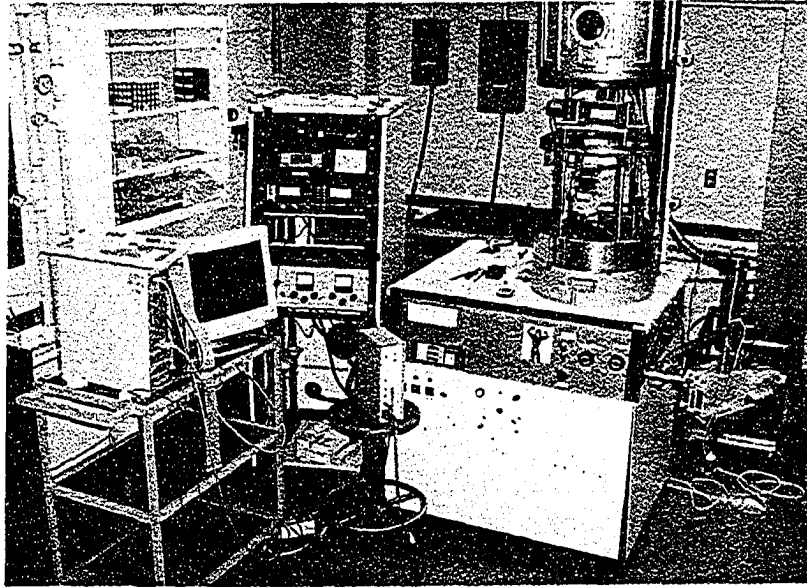


Figure 3.10: GLAD system consisting of a dual-axis substrate mount inside a PVD electron-beam evaporation system. A computer provides dynamic control over both rotation axes, with deposition rate feedback from a crystal thickness monitor.

algorithm for the desired film structure. Furthermore, the control computer is provided with feedback on the deposition rate from a crystal thickness monitor, so that the film structure algorithm can be driven by the actual film thickness without impact from fluctuations in the deposition rate. To make a square spiral as in figure 3.8, for example, the computer ordered the substrate rotation motor to advance by  $90^\circ$  for every 270 nm of film growth. While the crystal thickness monitor measures the deposition rate on a plane normal to the direction to the vapour source, this value is adjusted to reflect that the actual rate of film accumulation on the highly tilted substrate is much lower. From a geometrical point of view the deposition rate  $r$  on the tilted substrate is:

$$r = \cos \alpha \cdot r_{norm}, \quad (3.10)$$

where  $r_{norm}$  is the rate normal to the source. However, material specific effects such as vapour reflection off the substrate means that the adjustment factor for the rate must be determined experimentally.

Dual-axis substrate rotation can be achieved by mounting two vacuum compatible stepper or servo motors inside the deposition chamber (shielded

from the vapour source), with the substrate tilt motor fixed and the substrate rotation motor moving on an arc along with the substrate tilt. A better approach is to mount both motors outside of the chamber, and employ a double-axis mechanical feed-through connected to a platen/planet substrate mount, akin to planetary rotation systems in industrial deposition systems. In both cases the substrate mount must be setup so that the centre of the substrate is immobile in space, i.e., the two rotation axes must intersect in a fixed point in space right over the vapour source. In principle – although relevant only for large scale production – GLAD substrate motion could be replaced by equivalent source motion.

The motion of the substrates makes it difficult to combine GLAD with active substrate temperature control or even measurement. Malac and Egerton used a radiative heater in front of the substrate, and a thermocouple next to it, but the accuracy of this remote approach is questionable [129]. In a better setup, Vick *et al.* mounted thermocouple elements on the back of a substrate, although this still does not provide the temperature on the front surface of the substrate [130].

## 3.4 Characteristics and Applications of GLAD Thin Films

### 3.4.1 Characteristics and Advantages of GLAD Films

Two characteristics combine to make GLAD thin films unique materials, whose consolidated attributes are unattainable by any other thin film or microfabrication method:

- Column structure.
- Extreme porosity.

These characteristics drive the specific properties and applications of GLAD thin films discussed later.

#### Columnar Structure

Perhaps the most striking characteristic of GLAD is the ability to produce intricate, user-defined film microstructures of columns tweaked and turned into a variety of shapes. From a fundamental point of view, the GLAD column structure can be either circular helical or polygonal helical. The *slanted post* column structure shown in figure 3.5 is the most basic structure

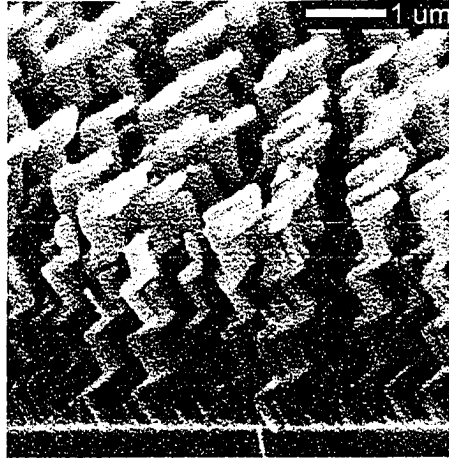


Figure 3.11: Oblique view of a silicon dioxide GLAD film with a chevron or zig-zag column structure, fabricated by discrete  $180^\circ$  substrate rotations. The film consists of eight arm segments, and has a total thickness of  $3.1 \mu\text{m}$ . From [145].

– with no substrate movement during the deposition – and can be considered a ‘one-sided’ polygonal helix. Next comes the *chevron* or zig-zig structure, shown in figure 3.11, which is a ‘two-sided’ polygonal helix made by regular, discrete  $180^\circ$  rotations of the substrate. The previously discussed *square spiral* column structure in figure 3.8 is, amazingly, a four-sided polygonal helix with four  $90^\circ$  substrate rotations per one complete helical revolution. In a similar manner any other kind of polygonal helix can be produced. In both polygonal and circular helices the vertical extension of one complete helical revolution (e.g., two substrate turns in a chevron or four turns in a square spiral) is defined as the helical pitch  $p$ , while the direction of substrate rotation defines whether the helices are left handed or right handed.

For circular helical GLAD column structures the substrate is rotated continuously, rather than in discrete steps, with the only variable being the substrate rotation rate  $d\phi/dz$  (note that the rotation rate is defined relative to the film thickness, not time, in order to permit structures to be designed independently of the deposition rate). For slow substrate rotation rates – typically less than  $3^\circ/\text{nm}$  [147] – *circular helical* columns are produced, with a spiral structure as shown in figure 3.12. The helical pitch  $p$  is a simple function of the substrate rotation rate:

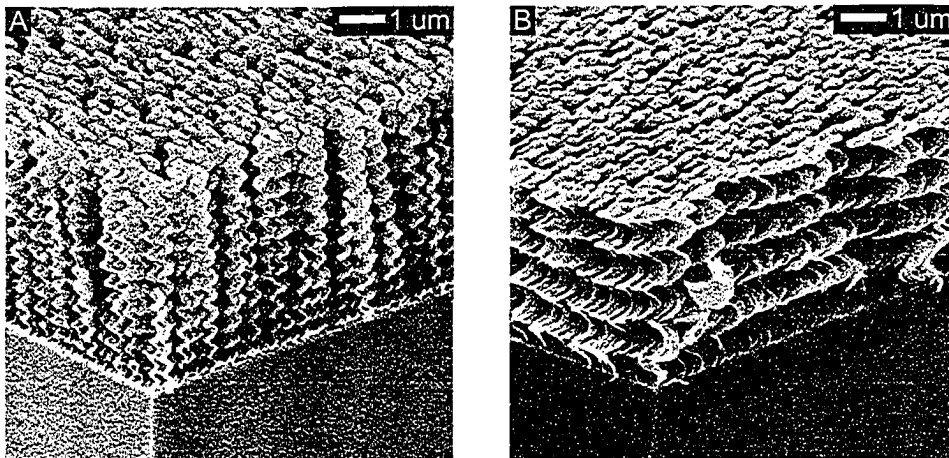


Figure 3.12: Circular helical GLAD films made by continuous substrate rotation at  $\alpha = 85^\circ$ . In (a) the helical pitch is 400 nm (silicon dioxide film), and in (b) the pitch is 905 nm (silicon film). While the overall film thickness is nearly constant (4.4 and 4.5  $\mu\text{m}$ ), the difference in pitch changes the appearance and properties of the films. From [146].

$$p = \frac{2\pi}{d\phi/dz}. \quad (3.11)$$

Thus, the slower the rotation rate, the higher the helical pitch (cf. figure 3.12). A fast substrate rotation rate (typically higher than  $6^\circ/\text{nm}$ ) forces the helical pitch toward zero [148], so that the column structure degenerates from a distinct spiral structure to a smooth *vertical post*, as shown in figure 3.13. In general, this occurs when the pitch approaches or drops below the column width.

It is worth noting that even while the individual linear segments of polygonal helices are tilted, as given by Tait's Rule, the central axis of both circular and polygonal helices is normal to the substrate. This is a consequence of the highly symmetric substrate rotation inherent in helix deposition, which over time evens out the amount of vapour incident from opposing directions. The one exception to this is the slanted post column structure with no substrate rotation at all.

Using combinations and variations of the above basic column structures, and exploiting the ability to dynamically alter the rate and direction of both substrate rotation and tilt, any composite column morphology can be engineered by stacking different structures.

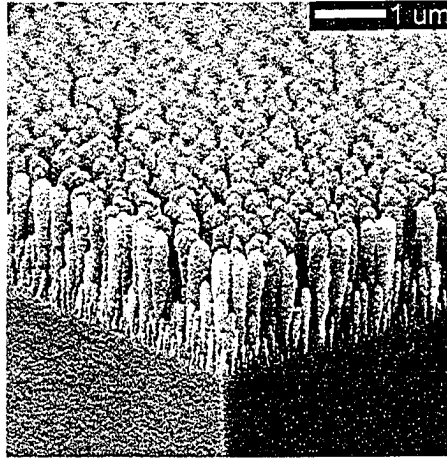


Figure 3.13: Vertical post aluminium oxide GLAD film, achieved by fast, continuous substrate rotation that degenerates circular helices into smooth posts. The vapour incidence angle  $\alpha$  was  $85^\circ$ . From [149].

### Extreme Porosity

As a salient feature of GLAD, the oblique vapour incidence angles cause the individually columns to become completely separated by voids, resulting in extremely high film porosities. In fact, for many GLAD films the mean volume density or packing factor  $\rho_V$  (the volume of solid matter per unit film volume) is only 10 to 40 % [123]:

$$\rho_V = \frac{V(\text{solid film material})}{V(\text{total film} + \text{void})}. \quad (3.12)$$

The high porosity for GLAD films translates into a low mean density  $\rho_{GLAD}$  (average mass per unit film volume), namely an equivalently small fraction of 10 to 40 % of the bulk mean density  $\rho_{bulk}$  of the evaporant material:

$$\rho_{GLAD} = \rho_V \rho_{bulk}. \quad (3.13)$$

A second immediate consequence of the high porosity is a phenomenally high geometrical surface area (total film surface area per unit substrate area or per unit film mass), which is further enhanced by the fact that for most materials each GLAD column itself has a porous, fibrous internal structure and a rough surface. It is difficult to measure and estimate the total surface area, and insufficient to consider just the outer surface area of the columns,

but as detailed in chapter 10, approximate surface area values of GLAD films range from 6 to 70 m<sup>2</sup>/g.

While some applications rely directly on a large surface area, the inner structure of the columns is of little relevance for other applications. It is then more convenient to treat the columns like solid structures with a constant mean density – namely, the effective average density of the voids and solid inside the columns – and instead deal with the volume fill factor  $\overline{ff}_{V,GLAD}$ , which represents the fraction of the volume of the GLAD film that is contained within columns:

$$\overline{ff}_{V,GLAD} = \frac{V(\text{enclosed by columns})}{V(\text{total film + void})}. \quad (3.14)$$

A number of factors influence the porosity of GLAD films. Since bulk and surface diffusion tend to devour voids by rearranging matter to reduce the surface area, low melting point materials and high substrate temperatures tend to yield denser, less porous films [93, 123]. More importantly, the porosity depends profoundly on the GLAD vapour incidence angle  $\alpha$ , which not only dictates the column inclination angle  $\beta$ , but also the column spacing  $a$ . In fact, in deriving Tait's Rule (see equation 3.9) it can be shown that [138]:

$$a(\alpha) = [1 + 1/(\cos \alpha)] / 2, \quad (3.15)$$

with the column spacing expressed in units of the average column width  $w$  for the given substrate tilt  $\alpha$ . The film density, expressed here as the volume fill factor  $\overline{ff}_{V,GLAD}$ , then depends on the substrate tilt as:

$$\overline{ff}_{V,GLAD} = 1/a = 2/[1 + 1/(\cos \alpha)]. \quad (3.16)$$

The last equation – plotted in figure 3.7 – confirms a strong dependence of the film density on  $\alpha$ , and indeed predicts volume fill factors below 30 % for  $\alpha$  higher than 80°, in good agreement with both experimental and modelled data [138]. Both experiments and modelling show that the porosity is maintained constant throughout the thickness of the film, except for aberrations in the initial nucleation layer and in the growing top layer of the film [150].

Given the dependence of film porosity on  $\alpha$ , the GLAD film density can be easily tailored for a given application, and even manipulated dynamically during a deposition. For example, Robbie and Brett demonstrated how a dense capping layer can be deposited right on top of a porous GLAD film by gradually reducing the vapour incidence angle to zero, and thus returning the film structure to that of a compact, normally deposited thin

films. An exponential decrease in  $\alpha$  was found to best alleviate the build-up of mechanical stress in the capping layer [123]. Cyclic but less drastic changes in  $\alpha$  can be used to create GLAD films of multiple layers of varying porosity, which – given the relation between density and refractive index – work as an optical rugate filter [151].

Equations 3.9 (Tait’s Rule) and 3.16 provide one column inclination angle and one film density for each value of the vapour incidence angle  $\alpha$ . However, some applications may require a different combination of film density and column inclination angle. The solution to this problem is the ‘spin-pause’ GLAD growth algorithm developed by Robbie *et al.*, which decouples  $\beta$  from  $\alpha$  while maintaining the film porosity dependence on  $\alpha$  [124]. This is achieved by stacking GLAD film layers of vertical posts (substrate spinning) and slanted posts (substrate paused), with the thickness of each layer being so small that the columns smoothen into uniform slanted posts with an inclination angle  $\beta$  less than that predicted by Tait’s rule. The ratio of spin to pause now dictates  $\beta$ , independently of  $\alpha$  and the film density. The ‘spin-pause’ method can also be used to alter the columnar cross-section, for example by selectively depositing less vapour on those sides of the columns which otherwise naturally broaden [152].

The mechanical characteristics of GLAD films depend on the density. In general, the high porosity relieves mechanical stress in the films, with only capping layers causing potential problems. Seto *et al.* performed nanoindentation experiments on a number of circular helical silicon oxide GLAD films, and found these ‘micro springs’ to exhibit elastic behaviour and possess an area stiffness on the order of 10 to 20 (N/m)/ $\mu\text{m}^2$ . This stiffness is significantly less than that of solid films deposited at normal incidence [153, 154].

GLAD is quite unique in enabling advanced structural thin film engineering on sub micrometre length scales, with free-standing, interwoven columns in complex shapes and less than a few hundred nanometres wide. Although modern lithographic patterning technologies would be able to replicate at least the overall columnar microstructure of GLAD films, this would surely challenge those technologies to their very limit and require tedious processing. No other thin film deposition technique provides the same level of control over the film density and microstructure. GLAD requires only a single deposition step, readily provides large area film coverage, and relies on proven technology that can easily be scaled to industrial mass-production.

### 3.4.2 Properties and Applications of GLAD Films

#### Optical Applications

With the engineerable feature sizes in GLAD thin films being of the same magnitude as the wavelength of visible and near-infrared light, GLAD films constitute an interesting optical material. It was previously mentioned how periodic modulation of the GLAD film porosity can allow a film to be used as a rugate filter for strong reflection in a narrow band of wavelengths, by relying on the correlation between film density and effective refractive index [151]. Index graduation can also be used to produce broadband anti reflection coatings consisting of a Gaussian film density profile in a single GLAD layer (whereas most anti reflection coatings are based on multiple layers). In a report by Kennedy and Brett, less than 1% reflection was observed in silicon dioxide films in bandwidths up to 460 nm for both TE and TM polarized light and for light incidence angles up to 30° [155].

The GLAD column structure itself can also be exploited for optical applications, with circular helical columns as in figure 3.12 constituting a chiral medium that exhibits both circular dichroism (anisotropic absorption of incident light) and circular birefringence (anisotropic refractive index) [122,156]. These effects are a result of the structural chirality of the helices and the index difference caused by the film voids, and thus appear even if the deposited film material itself is isotropic. The circular birefringence gives rise to optical activity – i.e., rotation of the polarization direction of linearly polarized light – with rotatory powers in excess of 3°/μm for aluminium oxide GLAD films [157,158]. The circular dichroism has been evaluated by comparing the selective transmittance of left- and right-circularly polarized light through helical GLAD films, and can be more than 10 % for titanium oxide films up to 2 μm thick. The wavelength dependence of this difference can be tailored simply by adjusting the pitch of the GLAD helices [158].

The optical behaviour of chiral helical GLAD films is not unlike that of birefringent liquid crystals. Indeed, injection of liquid crystals into the porous GLAD films yields a six-fold increase in the magnitude of the optical activity [157]. Furthermore, such hybrid GLAD/liquid crystal devices are a unique way to control the alignment of liquid crystal molecules in thick cells for display applications, as the GLAD helical backbone induces a chiral-nematic phase in the liquid crystal [160]. By sandwiching the GLAD film between transparent and conducting indium tin oxide substrates, the orientation of the polar liquid crystals – and hence the selective transmittance of the cell – can be switched electronically [159]. Figure 3.14 illustrates this

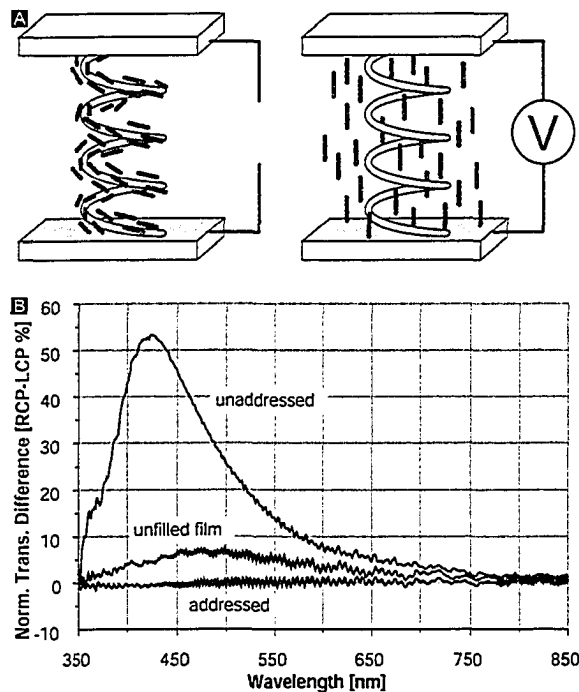


Figure 3.14: a) Helical GLAD columns induce a chiral-nematic phase in liquid crystals, but an external electric field can realign the liquid crystals. b) The selective transmission of circularly polarized light in a dry GLAD film ('unfilled film') increases with the additional of liquid crystals ('unaddressed'), and can be turned off by electronic switching ('addressed'). From [152,159].

principle, and shows a representative plot of both the enhancement of circular dichroism by liquid crystal injection, and the electro-optic switching of a hybrid GLAD/liquid crystal cell.

The two most important, but inevitable, drawbacks of GLAD as an optical material are scattering and environmental sensitivity. Diffuse scattering off the rough, voided structure of GLAD thin films make the films intrinsically lossy, even when non-absorbing materials are employed, and presents some difficulty in finding suitable references for both reflectance and transmittance measurements. Meanwhile, the high film porosity acts as a sponge for absorption of ambient water vapour, while the high surface area is conducive to native oxidation of the film material. Both these effects must be considered when evaluating the effective index of refraction of GLAD films.

### Other Applications

A number of GLAD applications depends on the extreme porosity and surface area of the films. A case in point is their use as catalysts [115], which has been demonstrated for platinum GLAD films in hydrocarbon reactions [161], and for titanium dioxide (titania) GLAD films in photocatalytic decomposition of methylene blue [162]. Along similar lines, titania films are being actively researched for dye sensitized photovoltaic cells (solar cells) [163,164], while manganese GLAD films have been shown to possess record-breaking specific electrochemical capacitances for use in supercapacitors [165].

By capping a porous GLAD film with a dense top layer, as described earlier, the highly voided material can be sandwiched between two rigid boundaries, allowing GLAD to be used for the fabrication of thermal barrier coatings. Harris *et al.* deposited multilayer GLAD films of yttria-stabilized zirconia – a common thermal barrier material – and achieved thermal diffusivity values one order of magnitude better than those attained with traditional thermal barrier coating methods [166]. These results were subsequently corroborated by simulations of the thermal flow in the films [167]. The porosity of GLAD films has also been considered as an option for prosthesis coatings designed to aid bone attachment [123], and as a surface area enhancement coating in microchannels [168].

Whereas the absorption of water vapour is a detriment to the use of GLAD films in optics, the same effect can be exploited to fabricate extremely sensitive humidity and gas sensors [169]. Following work by Wu *et al.* [170] and Harris *et al.* [171], Steele *et al.* recently demonstrated record-setting 40 ms response times for a humidity sensor based on GLAD films deposited onto an inter-digitated capacitor [149]. Another biosensor approach is electrochemical detection via porous electrodes made from carbon GLAD films [172,173].

Single-crystalline GLAD cobalt posts (one of the few cases of non-amorphous GLAD) have been examined both as a high-density magnetic storage medium and as a platform for studying the impact of microstructure on magnetic properties [132,133,174–176]. In another use of the high column densities achievable in GLAD (regularly exceeding  $10^9$  columns per  $\text{cm}^2$ ), ion milling of vertical post silicon and carbon GLAD films was employed to produce field emitter arrays with potential display applications [177].

GLAD films have been found robust to post deposition micromachining, and this has allowed as-deposited GLAD structures to be used as templates for the fabrication of inverted structures consisting of helical holes in a solid background [145,178]. Such ‘perforated thin films’, as shown in figure 3.15,

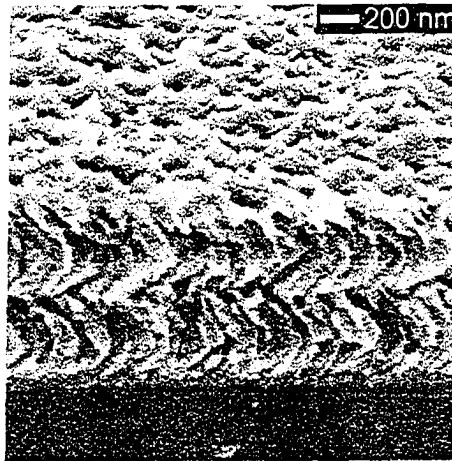


Figure 3.15: This perforated nickel thin film consists of circular helical holes in a dense background. It was fabricated by filling a porous, helical GLAD film with nickel using electro plating, and then etching away the original GLAD film. Micrograph provided by A. Elias.

can be used for many of the same applications mentioned above, including optical and photonic bandgap crystal applications. Added benefits include greater film durability and the ability to use materials (e.g., polymers) that cannot successfully be deposited by physical vapour deposition. Furthermore, in a double-template process, a perforated film can itself be used as a template to produce a new porous, helical film.

## Chapter 4

# The Proposition of PBC Engineering in GLAD Thin Films

The preceding chapters showed how the beneficial properties of photonic bandgap crystals derive from porous dielectric materials with a periodic, sub micrometre structure, and how glancing angle deposition produces thin films with these very characteristics. Theory and practise join together in GLAD fabrication of square spiral PBC architectures, whose concepts and history are surveyed in this chapter. The potential advantages of GLAD based PBCs are significant, but to establish the viability of GLAD as a PBC fabrication technique, the ability of GLAD to engineer bandgaps, pattern defects, and master structural detail must be demonstrated. This sets the stage for the thesis research.

### 4.1 Helical Photonic Crystal Architectures

#### 4.1.1 Circular Helical Architectures

For a 3D PBC architecture to be realizable by GLAD fabrication it must be based on helices, and the first study of such an architecture was provided by Chutinan and Noda in 1998 [179]. Instead of the conventional PBC approach of arranging individual shapes of air or dielectric at FCC or diamond lattice sites, they proposed placing helices in the bottom of a lattice, and letting the upward spiralling helices connect the lattice sites. Plane wave modelling was performed on circular helices with circular cross-sections, which were

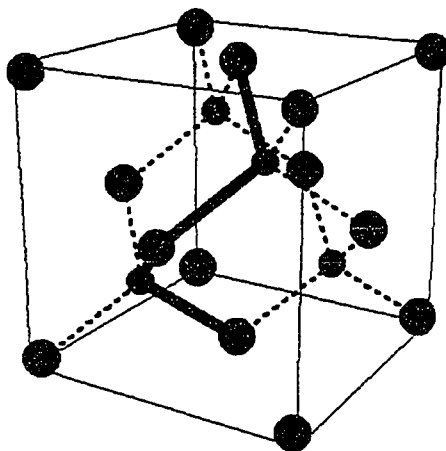


Figure 4.1: The lattice sites of the diamond lattice – which yields the strongest photonic bandgaps – can be traced out by helices winding their way continuously up through the lattice. Chutinan and Noda approximated the trace with a circular helix, whereas Toader and John used the actual square helix. From [179].

arranged in simple cubic, FCC and BCC lattices. The simple cubic case amounts to placing circular helices in a base 2D tetragonal lattice. In this case a small optimized bandgap of only 3% was found for the direct structure of dielectric spirals in an air background, whereas a large bandgap of 17% was found for the inverse structure of air spirals in a dielectric background.

Much better results were obtained by placing the circular helices in an FCC lattice. This is again equivalent to placing helices in a base 2D tetragonal lattice, but with every second helix shifted one half pitch. The direct FCC structure yielded large optimized bandgaps from 17 to 28%, while a 20% bandgap was noted for the inverse structure. Very similar results were obtained for the BCC lattice, since for the helical PBC architecture the BCC lattice is indistinguishable from the FCC lattice when stretching of the spirals along their central axis (the lattice [001] axis) is allowed. By closer scrutiny the success of the FCC helix arrangement is not surprising, for the circular helices then approximately trace out the sites of a diamond lattice, which as previously discussed provides the strongest photonic bandgaps. The helical diamond lattice trace is shown schematically in figure 4.1.

Periodic arrays of circular helices are straightforward to fabricate using GLAD (with periodicity being induced by seed layers, as discussed in chapter 5), but two details prevent Chutinan and Noda's helical architecture from

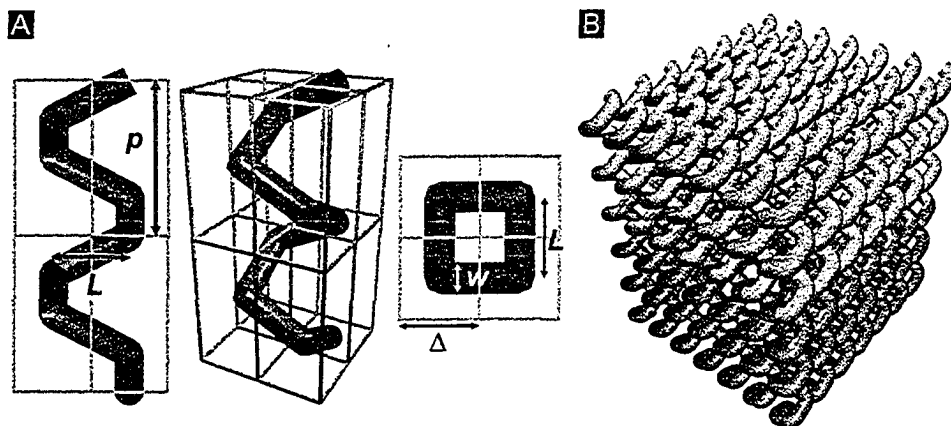


Figure 4.2: a) Definitions of the square helix parameters. The helix pitch  $p$  is also the pitch of the tetragonal lattice making up the photonic crystal. Adapted from [180]. b) Square helix photonic crystal, in which the interleaving helices connect nearest neighbour lattice points in the diamond lattice. From [181].

being GLAD compatible. First of all, GLAD cannot produce films in which adjacent helices have a shift in pitch, as required by the FCC and BCC candidates – all GLAD helices must turn in unison, following the substrate rotation motion. Secondly, the simple cubic arranged helices require that the helices overlap to yield the right dielectric volume fill factors, which is not directly achievable (and not worthwhile trying to achieve for a very small bandgap of 3%).

#### 4.1.2 Polygonal Helical Architectures

Chutinan and Noda limited their study of helical PBCs to circular helices. However, as the schematic in figure 4.1 indicates, the diamond lattice sites actually trace out a *square* helix. In fact, just as the diamond lattice can be considered a FCC lattice with a basis of two sites, it can also be constructed as a tetragonal lattice with a basis of four sites making up a square helix. As these square spirals wind their way through the diamond lattice in the [001] direction, they connect one site in each (001) lattice plane with another site in the next successive plane one quarter unit cell higher. The connected sites can be nearest neighbours (as in figure 4.1), third nearest neighbours, fifth nearest neighbours, and so on, depending on how far each helix arm extends laterally between lattice planes.

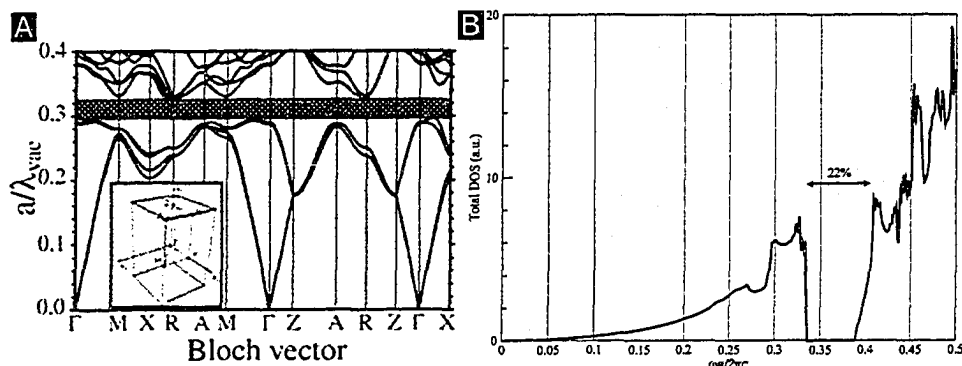


Figure 4.3: a) Band structure for a square spiral photonic bandgap crystal which approximately connects nearest neighbour diamond lattice points. A complete bandgap exists between the fourth and fifth bands. The inset shows the irreducible Brillouin zone with high symmetry points for the tetragonal lattice containing the square spirals. From [182]. b) Density of states for the optimized nearest neighbour square helix architecture, with a complete bandgap of 15% and a pseudo-gap of 22%. The helices have dimensions  $L = 0.70$ ,  $p = 1.35$ , and  $w = 0.4$ . From [181].

Exploiting this representation of the photonically ideal but elusive diamond structure, Toader and John in 2001 proposed a new 3D PBC architecture based on square helices [180, 181]. As shown in figure 4.2a, the helices are arranged in a 2D square lattice with lattice period  $\Delta$ , so that a 3D tetragonal lattice is created with the helix pitch  $p$  being the lattice period in the [001] direction. The helices are further described by their horizontal side length  $L$  and arm width  $w$ . The orientation of the helix arms relative to the base 2D square lattice dictates which diamond lattice points can be connected. For example, to connect nearest or fifth nearest neighbours the helices must be aligned parallel to the square lattice unit vectors (as in figure 4.2b), while for third nearest neighbours to be connected the helices must be turned  $18^\circ$  away from the lattice unit vectors. The helix side length  $L$  must be adjusted accordingly to make the helix arm segments extend all the way from one lattice site to the next, often resulting in interleaving helices. Figure 4.2b illustrates the crystal architecture for the case when nearest neighbour lattice sites are connected.

Using plane wave modelling, Toader and John predicted that the square helix crystal architecture could generate large and complete 3D photonic bandgaps. Figure 4.3a shows the band diagram for a nearest neighbour

square spiral structure, with the complete bandgap located between the fourth and the fifth bands. When optimized, the nearest neighbour structure generates the density of states shown in figure 4.3b, with a relative bandgap of 15%, centered on the relative frequency 0.36, and a pseudo-gap of reduced transmission as large as 22% (assuming silicon as the dielectric). The corresponding optimized helix dimensions are  $L = 0.70$ ,  $p = 1.35$ , and  $w = 0.4$  (all relative to the base lattice period  $\Delta$ , and assuming a circular helix cross-section), for a dielectric volume fill factor  $ff_V$  of 31%. In the case of square spirals connecting third nearest neighbour lattice points the optimized bandgap drops to only 6%, while for fifth nearest neighbours the best bandgap is 16%.

Many variations on the square helix architecture are possible. The cross-section of the helix arm can be changed from circular to square or rectangular, but with very little effect on the bandgap properties. The square helices can also be rearranged to trace out a FCC lattice rather a diamond lattice, simply by rotating each spiral  $45^\circ$  about its own  $[001]$  axis. However, in the FCC configuration the optimum band gap drops to 9%. More radically, one can also cut the diamond and FCC lattices along other lattice planes than the (001) plane to get completely different polygonal helical geometries. A cut through the (111) plane in FCC, for example, would generate trigonal helical PBCs, but Toader and John found the bandgap properties inferior in such structures. Finally, all of the square helix architectures yield larger bandgaps when inverted structures of air helices in a dielectric background are considered. The optimized inverse nearest neighbour diamond configuration, for example, increases the relative bandgap size to 22%, while for the inverse fifth nearest neighbour structure the bandgap size is 24% – the highest computed for any square helix PBC.

By avoiding the half pitch shift between adjacent helices required by Chutinan and Noda, the square helix PBC architecture eliminates the key obstacle to fabrication by GLAD. This comes about by considering the FCC/diamond base (001) lattice plane under a  $45^\circ$  rotation, and interpreting it as constructed from smaller square lattices. Although the square helix PBC architecture is inspired by the diamond and FCC lattices, the square helices are, of course, only approximations, and in the optimized square helix structures the helix corners in fact rarely coincide perfectly with the ideal diamond lattice points.

## 4.2 Square Spiral GLAD Photonic Crystals

### 4.2.1 Matching Architecture and Fabrication

The GLAD technique readily generates porous dielectric films with a sub micrometre square spiral structure – as already shown in figure 3.8 – and thus satisfies the needs of the square spiral PBC architecture. In fact, aside from fabrication via holographic or two-photon lithography, GLAD is the *only* known viable fabrication method for square spiral PBCs. For the direct (dielectric in air) square spiral PBC architectures, interleaving and non-overlapping spirals with dielectric fill factors  $ff_V$  of 30 to 40% are needed, and this is just what is normally obtained in GLAD thin films.

By itself, the match between GLAD and square spiral PBCs is quite unprecedented in 3D PBC fabrication. As discussed below, the architecture and the fabrication method further complement each other with significant benefits that potentially address nearly all the historic challenges of 3D PBCs reviewed in chapter 2.

### 4.2.2 Theoretical and Practical Merits

The bandgaps in square spiral photonic bandgap crystals are large and complete, and are indeed among the strongest reported for any realistic architecture, approaching those of the ideal diamond structure currently established as the ultimate photonic crystal (24% for inverse square spirals vs. 28% for the ideal diamond). Simulations show that 4 to 5 unit cells of square spirals are enough to obtain complete opacity in the bandgap [183]. Just as important, the square spiral PBCs are quite robust to the random variations in helix dimensions that are almost unavoidable across real crystals. For variations up to 10% in the helical pitch  $p$ , Toader and John found virtually no impact on the bandgap, and for the nearest neighbour structure (with an optimized gap size of 15% for  $p = 1.35$ ), the gap remains larger than 10% even for  $p$  ranging as wide as 1.1 to 1.8 (relative to the lattice period  $\Delta$ ). For variations in the helical side length  $L$  and arm width  $w$  the gap size was also found to be intact for variations up to 10%, although the bandgap location shifts quite strongly with both. In a complimentary way of studying the bandgap robustness, the gap size was mapped as a function of the dielectric fill factor  $ff_V$ , and found to be larger than 10% for fill factors from 0.2 to 0.45, closing completely only below 0.12 and above 0.6. This robustness is significantly better than most 3D PBC architectures.

GLAD films are already well understood as optical materials, and many of the attributes of GLAD discussed in chapter 3 translate directly into ben-

efits for PBC architectures. As a PVD process, GLAD is compatible with a large variety of materials, including high permittivity dielectrics such as silicon. The option of annealing GLAD films to obtain mono or polycrystalline helices is important for potentially creating optically active regions, and the ability to micromachine the GLAD films may allow for advanced functionalities to be embedded in the crystals. In particular, the use of GLAD films as a template to create helically perforated thin films – demonstrated so far for nickel and other materials – should allow for realization of inverse square spiral PBC architectures, which not only promise larger bandgaps but also greater mechanical stability. Inverse PBC structures are outside the scope of this thesis, but are currently under research by Summers *et al.* [184] Dense capping layers on top of GLAD films could find use in waveguide engineering.

As mentioned earlier, the interaction between GLAD and liquid crystals is strong, and the infiltration of porous GLAD films with liquid crystals is well studied and relatively straightforward. This will ease the exploitation of LCs for dynamic tuning of GLAD based square spiral PBCs. Other GLAD applications that are or have already been researched, and which might benefit from GLAD PBCs, include bio and gas sensing, electroluminescence, photovoltaic cells, and microfluidics. Last but not least, GLAD has the potential to make thick PBC films with few and small defects on a wafer size scale, with PVD thin film technology already proven for low cost industrial production.

On the downside, the limit in column inclination angles  $\beta$  dictated by Tait's Rule (equation 3.9 and figure 3.7) restricts which square spiral PBC architectures can be immediately realized. Thus, the fifth nearest neighbour direct structure requires  $\beta = 79^\circ$  and is currently unattainable. (Potentially higher column inclination angles might be achieved by bombarding the GLAD films with inert ions during growth [185].)

### 4.2.3 The History of GLAD Square Spirals

The history of GLAD based square spiral photonic crystals is short. Since inverse GLAD films have not yet been realized for silicon, and since fifth nearest neighbour structures are unattainable by way of Tait's Rule, focus has been on the direct, first nearest neighbour architecture. FCC structures and trigonal helical structures have not been considered due to their inferior performance.

The feasibility of fabricating square spiral GLAD films for PBC purposes was reported by Kennedy *et al.* [182] GLAD helices were forced to nucleate

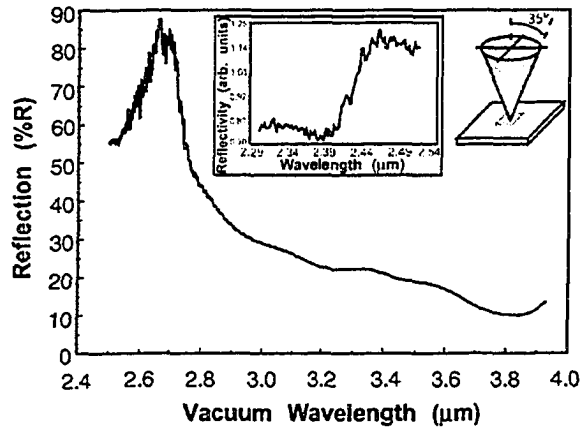


Figure 4.4: The first reflectance spectra for a GLAD film with a square spiral PBC architecture, by Kennedy *et al.* The main spectrum shows the low frequency edge of a high reflectance range from 2.50 to 2.75  $\mu\text{m}$ , whereas the inset (with an abbreviated reflectivity axis) shows the high frequency edge. From [187].

in a periodic lattice – as required for the square spiral PBC architecture – by performing the GLAD deposition on a pattern of substrate seeds fabricated using optical photolithography (thesis research on substrate seed layers is presented in chapter 5). Given the limitations of this lithography system the tetragonal base lattice period  $\Delta$  was fixed to 1  $\mu\text{m}$ . A silicon square spiral film with a thickness of four complete helix turns, or 5.2  $\mu\text{m}$ , was successfully fabricated, but no optical characterization of the film was performed.

Zhao *et al.* deposited silicon GLAD square spirals with a side width  $L$  of 300 nm on self-assembled, close-packed polystyrene spheres [186]. Since colloids pack in hexagonal 2D lattices, and not tetragonal lattices, this column seeding approach is unsuitable for the square spiral PBC architecture. Additionally, the colloidal arrays were hampered by defects limiting the optimum domain size to less than 10  $\mu\text{m}$ , and several GLAD columns nucleated off each sphere. No GLAD films constituting a square spiral PBC structure were presented, and no optical results reported.

The only report on optical probing of a square spiral GLAD film has been provided by Kennedy *et al.* [188] As in the previous report the tetragonal base lattice period was limited to 1  $\mu\text{m}$ , and the 8 turn or 11.2  $\mu\text{m}$  tall deposited silicon square spirals had a pitch  $p$  of 1.4  $\mu\text{m}$ , a side length  $L$  of 0.72  $\mu\text{m}$ , and a width of 0.37  $\mu\text{m}$ , yielding a dielectric volume fill factor  $ff_V$

of approximately 0.3. In theory these square spirals should deliver a 15% large bandgap in the wavelength range from 2.50 to 2.90  $\mu\text{m}$ . Optical and Fourier transform infrared spectroscopy with cone shaped, large numerical aperture beams were employed to investigate the optical properties of the GLAD film, and an increase in reflectivity for several angles of incidence was found for the wavelength range 2.50 to 2.75  $\mu\text{m}$ , corresponding to a 10% relative stop band. One of the reflectivity measurements is reproduced in figure 4.4. The increase in reflectivity was concluded to be suggestive of the presence of a photonic bandgap in the GLAD film, but the authors noted that another possible cause of the high reflectance could be short range localized states of light rather than a true omnidirectional bandgap. The reduction of the gap width relative to the theoretical prediction, as well as the lack of complete reflection inside the gap and zero reflection outside the gap, were attributed to imperfections in the square spiral shape and fluctuations among the spirals across the sample.

### 4.3 Enabling GLAD for Photonic Crystal Engineering

With the inherent advantages of GLAD thin films and the square spiral PBC architecture, GLAD might be the ideal technology for realizing the promise of photonic bandgap crystals. In principle, GLAD fabrication of square spiral 3D PBCs is a straightforward, one-step process – certainly less complicated than most other 3D PBC fabrication schemes – and the theoretical properties of the square spiral architecture are excellent.

However, for GLAD to establish its potential and become a viable PBC technology, a capability to engineer and optimize the square spiral films must be developed. To shift the bandgap to useful frequencies, the GLAD square spirals must be scalable. To introduce functionality, it must be possible to introduce intentional defects. And, as shown by the preliminary results of Kennedy *et al.*, the fine details of the GLAD film morphology must be mastered to achieve the full optical properties. These capabilities are key not only to PBC fabrication by GLAD. Indeed, as discussed in chapter 2, the slow experimental progress for *all* 3D PBC architectures rests on incomplete control over the fine structure and lack of structural engineering capabilities, in particular with respect to the introduction of intentional defects (for which few 3D PBC results exist at all). Advances in photonic crystals cannot be made before better, more flexible fabrication methods are developed.

In pursuit of establishing GLAD for square spiral PBC engineering, this thesis endeavours to achieve the following new capabilities:

- *Enable bandgap engineering* by fabricating periodicity inducing substrate seed layers that are fully scalable to any PBC frequency range, eliminating structural problems found in previous square spiral GLAD films, developing GLAD to cover a wide range of square spiral dimensions, and demonstrating PBCs at useful optical wavelengths.
- *Enable defect engineering* by fabricating seed layers with intentional defects, devising new GLAD growth algorithms for transferring seed defects into film defects, and demonstrating defect patterning in square spiral GLAD films while maintaining overall film uniformity.
- *Develop the fabrication of square spiral PBCs* by improving sample wide film uniformity in periodic GLAD growth, reducing the roughness of individual spirals, and designing new GLAD algorithms that better approach the theoretically ideal square spiral shape and cross-section. This encompasses surmounting structural non-uniformities inherent in GLAD films, and problems exacerbated by efforts to shrink the square spiral morphology for building PBCs at useful optical wavelengths.

Focus will be on the direct, first nearest neighbour square spiral PBC architecture, since this is the most suitable structure for GLAD fabrication. Results for this structure can be easily transferred to inverse, FCC, triangular and other PBC architectures.

## Chapter 5

# Seed Layer Design and Fabrication

The cornerstone of all photonic crystal architectures is structural periodicity, and in square spiral photonic crystals the periodicity must extend in all three dimensions. The GLAD process itself can ensure regularity in the direction perpendicular to the substrate, but in the plane of the substrate the structural periodicity must be enforced by seed layers that precipitate controlled column nucleation. This chapter presents thesis research on the design and fabrication of such seed layers. As the rest of the thesis will demonstrate, substrate seed layers are critical not just to produce GLAD photonic crystals, but also to introduce functional waveguiding defects in the crystals, realize other thin film applications based on periodic columnar structures (such as microfluidic circuits and magnetic storage), and even improve the morphology of GLAD thin films that otherwise do not require a periodic structure.

Thesis research presented in this chapter has been published in the *Journal of Vacuum Science and Technology B* [189] and accepted for publication in the *IEEE Transactions on Nanotechnology* [190].

### 5.1 The Principles of Periodic GLAD Films

In chapter 3 it was discussed that when a GLAD film is deposited on a smooth substrate, the initial nucleation of the thin film occurs stochastically on the substrate surface. Since the nucleation phase dictates where columns will subsequently grow in the GLAD film, random nucleation leads to random column distribution, as well as to column broadening, column

bifurcation, and competition among columns. How can such an intrinsically random film structure be rearranged or patterned to yield a periodic and uniform film structure?

Lithographic processing is routinely performed post deposition to conventional dense and homogeneous thin films (deposited at normal incidence) to create periodic film structures such as two-dimensional photonic crystals. Post deposition processing is applicable to GLAD films as well, since work by Harris *et al.* [145, 168, 178, 191] and Elias *et al.* [192] have shown that GLAD films are resilient to backfilling with photoresist, processing of this resist along with the embedded GLAD, and eventual removal of the resist. Although the cited work did not include attempts to pattern GLAD films, the prerequisites for this are clearly present. However, given the random column distribution that inherently arises in GLAD films during deposition, post deposition patterning would not be able to produce a structure consisting of periodically arranged *individual* columns. Indeed, given the open and inhomogeneous structure of GLAD thin films, post deposition patterning is useful only for applications requiring pattern feature sizes larger than the columnar diameter and spacing of the film. For pattern feature sizes less than a micrometre, the stochastic nature of the GLAD morphology would dominate over any post deposition pattern structure, and the patterned film would become a collection of incongruous column clusters.

Consequently, periodic arrays of GLAD columns can be obtained only by carefully controlling where initial nucleation of the columns takes place, and by ensuring that this *ab initio* film structure is maintained throughout the thickness of the film. That is, to fabricate a periodically structured GLAD film, the individual GLAD columns must be forced to nucleate at periodically spaced sites on the substrate. This is difficult to achieve in traditional thin films deposited at normal evaporant incidence angles, but in the GLAD deposition process, the highly oblique evaporant incidence angle and suppression of adatom diffusion make the film nucleation process very sensitive to any substrate roughness. Even a tiny bump on the substrate will cast an atomic shadow behind it and precipitate the accumulation of incoming evaporant, acting in effect like a stationary adatom cluster. If a substrate is prepared with a periodic topography of bumps, or seeds, prior to performing the GLAD deposition, this effect can be exploited to replace random nucleation with enforced periodic nucleation, yielding a periodically structured GLAD film. This is shown schematically in figure 5.1.

Although the principle of depositing periodic GLAD films on seeded substrates was realized by the original inventors of the GLAD process, only limited research has been carried out on seed layer fabrication and the growth

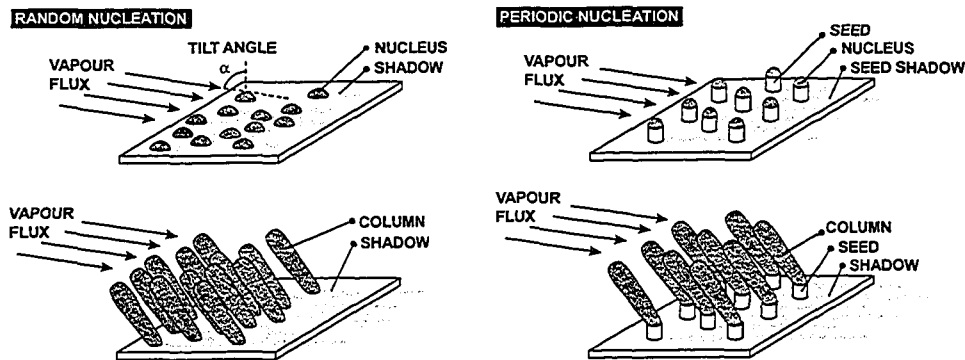


Figure 5.1: For GLAD thin films deposited on smooth substrates, nucleation and subsequent column growth occur randomly. With a topography of seeds on the substrate, enforced nucleation can be exploited to yield a periodic, columnar film structure.

of periodic GLAD films. Malac *et al.* presented some experimental work on periodic GLAD films, but in this work the understanding of seed layer design was inadequate (taking only the seed spacing into account), and the seed layers fabricated were far from ideal [133, 176]. Another report by Dick *et al.* discussed periodic GLAD structures in connection with work on periodic magnetic microstructures [132]. With the prospect of using periodic GLAD thin films for photonic crystals, it has become imperative to thoroughly understand and formalize the design of seed layers, and to make progress in the fabrication of high quality seed arrays.

## 5.2 Design of Seed Layers

Seed layers for periodic GLAD films must be designed to:

- Achieve the geometrical distribution of columns required by the GLAD film application.
- Stimulate the nucleation of one GLAD column per seed (with no film nucleation elsewhere).
- Be compatible with the density and columnar structure of the intended GLAD film.

To attain this, every dimension of the seeds and the seed lattices must be carefully chosen, as formulated in the following paragraphs.

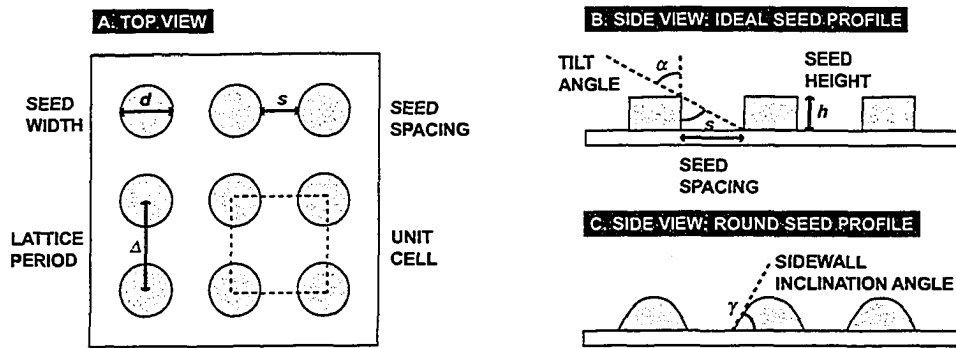


Figure 5.2: Schematic drawings defining the design parameters for GLAD seed layers. a) Top view of a tetragonal seed layer. b) Side view of a seed layer with an ideal seed sidewall inclination angle of  $90^\circ$ . c) Side view of a seed layer with a round seed profile and sidewall inclination angle less than  $90^\circ$ .

**Seed layer lattice geometry** Hexagonal or tetragonal lattices, being highly symmetric two-dimensional lattices with equal magnitude lattice unit vectors and a basis of one seed, are by far the most useful seed layer geometries for practical applications. For example, square spiral photonic crystal GLAD films require a tetragonal seed layer to create a diamond like film structure [181], whereas the use of periodic GLAD films in size exclusion chromatography would benefit from a hexagonal seed layer [193]. In special applications one could also consider one-dimensional lattices (such as gratings consisting of long continuous lines of seeds), two-dimensional oblique or rectangular lattices, or lattices with a multiple seed basis. However, the lower symmetry in such lattice geometries forfeits most of the microstructural benefits of seeded, periodic GLAD films.

**Seed lattice period, seed height, and seed width** A key issue in the use of seed layers for GLAD is to ensure that initial film growth takes place on the seeds only, and not on the exposed bare substrate between seeds. This may sound obvious, but is not a trivial concern. The first consideration in this respect is to ensure that the shadow cast by one seed, as a result of the oblique evaporant incidence angle, reaches all the way to the nearest neighbouring seed. Thus, the distance  $s$  from the backside of one seed to the front side of the nearest seed in the lattice (along the evaporant direction) must fulfil the relation:

$$s \leq \tan \alpha \cdot h, \quad (5.1)$$

where  $h$  is the seed height (all design parameters are defined in figure 5.2). Adding the seed width  $d$  (or diameter for circular seeds), the required seed lattice period  $\Delta$ , defined as the seed centre-to-centre distance, becomes:

$$\Delta = s + d \leq \tan \alpha \cdot h + d. \quad (5.2)$$

The seed width  $d$  cannot always be chosen arbitrarily, since many materials tend to form GLAD columns with fixed diameters given by the material properties and the evaporant incidence angle  $\alpha$ , irrespective of the seed size (one such material is silicon dioxide). The seed width must then be close to the natural GLAD column diameter for the material, in order to prevent several columns from nucleating on the same one seed, or column growth spilling over the sides of the seeds. It must also be emphasized that the seed spacing  $s$  in equation 5.1, and hence the seed lattice period  $\Delta$  in equation 5.2, represent the maximum values allowed for a given substrate tilt angle  $\alpha$ , seed height  $h$ , and seed width  $d$ . As is evident from figure 5.2b, the shadow from one seed never completely covers the front side of the next seed, and some evaporant will therefore always be deposited on the sidewalls of the seeds. To suppress this unwanted sidewall growth, the seed spacing should be designed with some margin below the maximum value.

**Seed layer planar fill factor** The mean density  $\rho_{GLAD}$  of a GLAD film is a material specific function of the substrate tilt angle  $\alpha$ , which has to be determined experimentally [148], and is always less than the bulk density  $\rho_{bulk}$  of the deposited material (due to the porosity induced by the GLAD column self-shadowing). In the planar interface between a seed layer and a GLAD film, the seed layer must match the reduced film density. If this is not ensured, significant column broadening or bifurcation will take place during initial film growth, as the GLAD film converges toward its equilibrium mean density. Thus, the planar fill factor  $ff_{A,seeds}$  of the seed layer (defined as the fraction of a seed lattice unit cell that is covered by actual seed material) must be equal to the volume fill factor  $ff_{V,GLAD}$  of the GLAD film (defined as the fraction of a unit volume of the GLAD film that contains column material):

$$ff_{A,seeds}(\alpha) = ff_{V,GLAD}(\alpha) \geq \frac{\rho_{GLAD}(\alpha)}{\rho_{bulk}}. \quad (5.3)$$

The last inequality reflects that the density of the GLAD columns themselves can be less than or equal to the evaporant bulk density, depending on the

crystallinity and internal porosity of the columns.

The planar fill factor  $ff_{A,seeds}$  can further be related to the seed lattice period  $\Delta$  and the seed width  $d$ . For example, in the case of circular seeds in a tetragonal lattice:

$$ff_{A,seeds}(\Delta, d) = \frac{\pi(d/2)^2}{\Delta^2}. \quad (5.4)$$

Combining equations 5.2 to 5.4, it is now clear that the ideal seed height  $h$  and width  $d$  are not independent, but are inextricably linked to the substrate tilt angle  $\alpha$ :

$$ff_{A,seeds}(\alpha) = \frac{\pi(d/2)^2}{\Delta^2} \geq \frac{\pi(d/2)^2}{(\tan \alpha \cdot h + d)^2}. \quad (5.5)$$

Often, the eventual application of a periodic GLAD film calls for both a specific lattice period  $\Delta$  and a specific volume fill factor  $ff_{V,GLAD}$ . In this case, since the required fill factor is given by the tilt angle  $\alpha$  and determines the seed width  $d$ , only the seed height  $h$  can be adjusted until the required lattice period is achieved:

$$ff_{V,GLAD}(\alpha) = ff_{A,seeds}(\alpha) = \frac{\pi(d/2)^2}{\Delta^2} \geq \frac{\pi((\Delta - \tan \alpha \cdot h)/2)^2}{\Delta^2} \quad (5.6)$$

**Seed shape** From a geometrical point of view, the most natural seed shape for a tetragonal seed lattice is a square, while for hexagonal lattices it is a hexagon. In practise, however, most seed fabrication techniques are unable to maintain sharp corners at sub micrometre length scales, and the actual seed shape tends to degenerate into a circle. Furthermore, the GLAD process naturally tends to produce circular or elliptical column cross-sections, irrespective of the actual seed shape. No difference has been observed in GLAD films grown on, e.g., circular seeds and sharply defined square seeds. The planar seed shape can thus be considered to be of little importance.

**Seed sidewall inclination angle** For GLAD nucleation purposes, the perfect seed should have vertical sidewalls – i.e., a sidewall inclination angle of  $90^\circ$  (see figure 5.2) – and a flat top surface. This seed profile not only provides the longest reaching shadows, but also prevents unintended film growth between seeds from affecting column growth on top of the seeds. For rounded seeds with sidewall inclination angles below  $90^\circ$ , film growth on the sloped sides leads to increased column broadening and sometimes even complete loss of film periodicity. The seed profile is difficult to control in

practise, but experiments with different seed shapes have shown that one should aim for a sidewall inclination angle higher than  $60^\circ$ .

## 5.3 Fabrication of Seed Layers

### 5.3.1 Lithographic Requirements

Once a seed layer has been designed in accordance with the above design rules, the seed pattern must be fabricated on a substrate using suitable lithographic techniques. For many applications of periodic GLAD thin films, the required seed widths are on the order of a few hundred nanometres [132,182]. At the same time, the overall dimensions of the seed layer arrays should be millimetres or more, in order to make it practically feasible to handle and characterize the finished periodic GLAD films. Even over such large areas, the uniformity in seed shape and lattice dimensions must remain very high. While different lithographic technologies allow both sub micrometre resolution and patterning of entire wafers, simultaneously spanning this range of length scales with arrays of billions of highly uniform seeds is a challenging task, even for the most modern lithographic systems. Furthermore, the fabrication techniques employed should possess substantial design flexibility, so that any lattice period or seed size can be implemented quickly and at low cost. In particular, it must be possible to create intentional point and line defects at predetermined sites in a seed layer, with the potential of exploiting such seeded defects in functional GLAD thin films (a subject covered in detail in chapter 9).

With these requirements in mind, the suitability of various lithographic methods for GLAD seed layer fabrication can be evaluated. Interference lithography (or holographic lithography), in which multiple coherent laser beams interfere to create a spatially varying intensity pattern [194], readily produces highly uniform, high resolution periodic patterns over large areas, and even in three dimensions. However, this method intrinsically lacks the ability to create intentional defects, and for the purposes of GLAD seed layer fabrication, the management of details like the seed height and width would require extremely tight control over the laser setup.

Mask based lithography, including traditional UV/VIS photolithography and high resolution X-ray lithography [100], do possess the ability to generate large area, uniform seed patterns with or without intentional defects, even though lengthy process optimization is often required for patterns with sub micrometre feature sizes. Indeed, UV photolithography of silicon nitride, supplemented with post development reactive ion etching to increase

the pattern contrast, has previously been put to use for GLAD seed layer fabrication [182, 184]. The main disadvantage of mask based lithography is that one can only change lattice and seed dimensions, as well as modify any defect patterns, through the expensive acquisition of a new high-quality photomask for every new design, rendering the method impractical for prototype research.

As an alternative to traditional lithography, Zhao *et al.* used close packed monolayers of self-assembled polymer microspheres as a seed layer for periodic GLAD films [186]. This technique is limited to hexagonal lattice geometries (of no immediate interest to GLAD based photonic crystal structures), is prone to disorder in the self-assembled mono layers, is inflexible with respect to lattice period and effective seed size, and is unable to deliver patterns with intentional defects. Another alternative approach suffering from similar drawbacks would be to stamp a soft surface, such as aluminium, along criss-crossing directions with finely ruled gratings, and subsequently etch or otherwise process the imprinted surface to create periodic arrays of tips [195, 196].

Ultimately, direct write lithography – in which patterns are written serially by a high energy particle beam – emerges as the best technology for GLAD seed layer fabrication. With carefully modified and optimized electron beam and laser direct write lithography, the practical and design related challenges of GLAD seed layer fabrication have been successfully addressed. It should be noted, however, that these technologies are for prototype research, and not suitable for mass fabrication of seed layers. Once a useful seed layer has been developed using direct write lithography, it could more effectively serve as a template for high volume seed layer production using hot embossing [197, 198] or nanoimprint technology [199, 200].

### 5.3.2 Electron Beam Lithography

#### Hardware

Electron beam lithography (EBL) uses a focused beam of electrons to photochemically write high-resolution patterns in thin resist films [201–204]. The electrons are emitted either thermally or by field emission from a filament usually made from tungsten or lanthanum hexaboride ( $\text{LaB}_6$ ), and are then focused and collimated by a series of pin hole apertures and electron lenses (cylindrical electromagnets). An extra set of coils inside the final electron lens, or objective lens, is capable of deflecting the electron beam in a cone of directions, in order to scan the beam across a substrate. This setup is

identical to the beam column in a scanning electron microscope (SEM), and most EBL systems are in fact just modified SEMs. The EBL modification consists of additional electronics and software, which take as input a CAD drawing of the pattern to be written, as well as system parameters from the SEM such as beam current and raster size. The EBL software converts the CAD drawing to an exposure bitmap, calculating exactly where the substrate should be exposed by the electron beam and for how long. Since the electron beam scans in a discrete, step-wise fashion, continuous lines or areas in the CAD drawing are converted to strings and arrays of pixels, with each pixel representing a point on the substrate where the electron beam will dwell for a short period of time. Once the electron beam column has been optimized to produce a tightly focused beam, the EBL hardware assumes command of the SEM deflection coils, and scans the electron beam over a resist covered substrate in accordance with the exposure bitmap. More advanced EBL systems also take control of the multi-axis stage on which substrates are mounted inside the SEM chamber, and successively move adjacent sections of the substrate under the objective lens. This allows multiple write fields to be stitched together to form larger patterns. The electron beam size in SEM/EBL systems is normally less than 10 nm, while the typical size of the write field or scan raster is less than  $100 \times 100 \mu\text{m}^2$ . Typical electron energies are 25 to 100 keV, with probe currents on the order of tens of picoamperes. Given their higher brightness (i.e., electron beam current density per solid angle), field emission and LaB<sub>6</sub> electron guns are much preferred over thermionic tungsten guns, providing higher resolution and faster writing [200, 205].

### Chemistry

Electron beam lithography resists consist of thin polymer films, and the chemistry and processing of resists is as important as the EBL hardware. Analogous to photolithography, EBL works by the electron beam inducing local chemical structural changes in the exposed resist compound. In positive EBL resists, the electrons lead to chain scission of the polymer strands, causing a reduction of the molecular weight of the resist. In negative EBL resists, the interaction between electrons and polymers leads to cross-linking of polymer chains, thus raising the molecular weight in the exposed areas. More often than not, the chain scission and cross-linking of polymers are not caused directly by the electrons, but are rather the end result of a sequence of chemical reactions fuelled by the electron bombardment. Subsequent to irradiation the resist is immersed in a suitable developer which selectively

dissolves the lower molecular weight polymer. Positive resists dissolve where exposed, while negative resists dissolve where not exposed. Since the cross-linking in negative resists tends to cause swelling, positive resists generally have higher resolution [100, 206, 207].

Whereas higher electron energies (set by the electron gun accelerating voltage) and smaller beam sizes generally lead to higher lithographic pattern resolution, the actual limiting factor for resolution is usually the interaction volume in the resist and substrate, which represents the spatial extent of primary electron backscattering as well as secondary electron generation [206]. The interaction volume can span several micrometres [205]. In addition to reducing the ultimate resolution of most EBL resist to tens of nanometres (i.e., much worse than the actual e-beam size), electron scattering is also responsible for the so-called proximity effect, in which the exposure of individual features in dense patterns – including GLAD seed layers – may interfere [100, 208]. The proximity effect may necessitate electron exposure dose corrections, since the dose received by each pattern feature depends not just on the its direct irradiation by the electron beam, but also on the additional dose received via scattered electrons from nearby exposure points. This problem is made more complex by the fact that resists respond non-linearly to the exposure dose. More seriously, the proximity effect may be strong enough that the electron dose between exposed features reaches the threshold for developer insolubility. A thin film of resist is then left behind among the pattern features, further reducing the pattern resolution and contrast. For GLAD seed layers in particular, this puts a lower limit on the seed spacing, blurs the seed shape, reduces the seed sidewall inclination angle, and reduces the aspect ratio of the seeds.

### Equipment and Processing

The EBL system used for seed layer fabrication in the course of this thesis research was a LEO 440 digital scanning electron microscope, equipped with the Nano Pattern Generation System (NPGS) from JC Nability Lithography Systems (see figure 5.3). The NPGS hardware and software was installed on a separate personal computer, and as such the EBL functionality was a retrofitted addition to the SEM. The SEM originally had a thermionic tungsten filament, but this was replaced with a higher brightness lanthanum hexaboride filament to reduce the write times. To obtain the best resolution, all experiments used an electron acceleration voltage of 40 kV, a beam aperture diameter of 10  $\mu\text{m}$ , and a beam current of 10 pA (measured using an in-situ Faraday cup). The pixel size was less than 100 Å. Given the

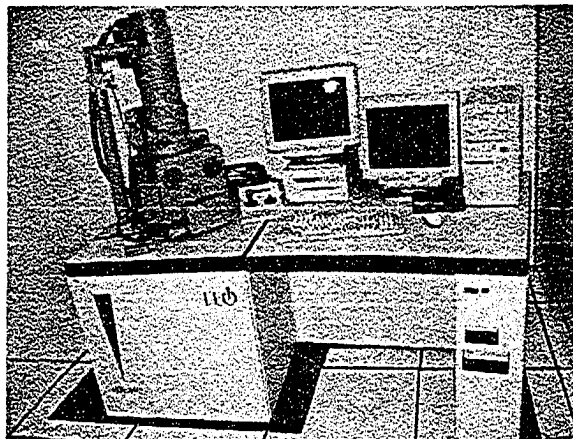


Figure 5.3: Electron beam lithography system consisting of a LEO 440 scanning electron microscope equipped with the NPGS package from JC Nability Lithography Systems.

stringent requirements of GLAD seed layers with respect to resolution and pattern density, extremely careful correction of the tilt, shift, and astigmatism of the electron beam had to be performed prior to every exposure run. In fact, until special vibration dampening equipment was installed for the SEM, seed layers could only be produced after normal laboratory hours, since the presence of trampling colleagues caused unacceptable aberrations.

The details of the resist processing performed pre and post exposure depended on the type of resist, but the following general process sequence was used for all EBL experiments:

- Substrate cleaning in hot piranha (75%  $\text{H}_2\text{SO}_4$  : 25%  $\text{H}_2\text{O}_2$ ).
- Substrate rinse and dehydration on a 200°C hot plate for 5 minutes.
- Resist spin-on application on vacuum spindle, with a low spin speed dispense cycle and constant ramp acceleration to the final spin cycle.
- Soft bake on hot plate.
- Exposure in EBL system.
- Post exposure bake (PEB) on hot plate.
- Development using appropriate developer solution.
- Rinse and hard bake on hot plate.

### 5.3.3 Laser Direct Write Lithography

#### Hardware and Optics

Laser direct write lithography (LDWL) employs some of the same principles as EBL, but now a laser beam is used to expose patterns in a photosensitive resist layer [209, 210]. The laser beam is swept continuously and at constant velocity across the substrate in adjacent stripes up to a few hundred micrometres wide. This sweeping motion is performed by moving the substrate back and forth on a two-axis stage underneath the normally incident laser beam. Simultaneously, a high frequency (35 MHz) acousto-optic (AO) deflector scans the laser beam laterally across the stripe width, while a fast acousto-optic modulator regulates the intensity of the laser beam. This is shown in figure 5.4. The AO deflector is rapid enough that with the combined motion of the substrate stage in one direction and the deflected beam in the perpendicular direction, the beam scans the entire substrate surface. With the substrate thus covered by an  $xy$  raster grid, the AO modulator simply turns the beam on and off where resist exposure is required or not, in accordance with the desired pattern. All parts of the system are controlled by a microcomputer, which also converts CAD drawings of patterns into exposure maps fed to the AO modulator. The AO components are highly accurate, and the substrate stage must likewise employ precision mechanics, with air bearings, water cooled motors, and laser interferometric positioning being the norm. Raster grid resolutions on the order of tens of nanometres are attainable [211, 212].

The resist chemistry is essentially the same for LDWL as for EBL, with both positive and negative resists available. Indeed, many EBL resists double as good LDWL resists. However, given the nature of electrons and photons, the limitations on resolution are distinctly different. The ultimate resolution  $\delta$  in LDWL is given by the diffraction limit of the employed laser light, which for the representative case of a krypton-ion laser emitting at a wavelength  $\lambda$  of 413 nm amounts to [213]:

$$\delta = \frac{\lambda}{2} = \frac{413\text{nm}}{2} = 207\text{nm} \quad (5.7)$$

This diffraction limit usually restricts the resolution before the  $xy$  raster grid or the chemical resolution of the resist does. Yet, the practical resolution of a LDWL system rarely gets as far down as the laser diffraction limit, since aberrations in the laser optics, and in particular electronic and optical limitations in the accuracy of the AO components, put the specified minimum feature size for state-of-the-art LDWL systems at 0.6  $\mu\text{m}$  or

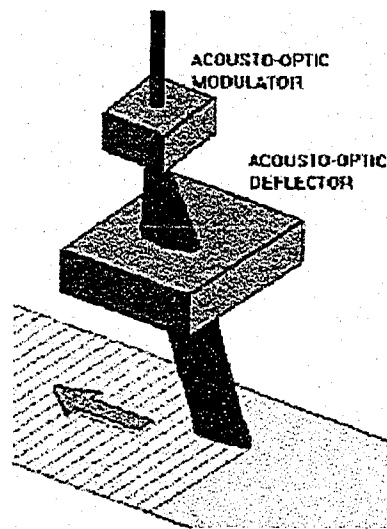


Figure 5.4: Schematic drawing of the acousto-optic modulator and acousto-optic deflector in a laser direct write lithography system.

higher. Another issue is standing waves caused by interference between the incoming, coherent laser beam and light reflected at the resist/substrate interface. The standing waves cause vertical intensity fluctuations inside the resist, which materialize as a rippled roughness in the sidewalls of the developed resist [212]. One way to reduce this impediment to high resolution patterning is to employ a low reflectivity substrate. Proximity effects are rarely a problem in LDWL, as the resist/substrate interaction volume for photons is much smaller than for electrons.

### Equipment and Processing

For LDWL based GLAD seed layer fabrication a Heidelberg Instruments DWL 200 Direct Write Lithography System was used (see figure 5.5 for a picture of the 1,500 kg behemoth). The instrument is located inside its own air flow box, which maintains temperature and humidity (ensuring consistent operation of the laser and optical components), as well as a local class 1 environment. The laser is a 413 nm wavelength water cooled Spectra Physics BeamLok krypton ion laser with a maximum power output of 300 mW. All optics and the substrate  $xy$  stage are mounted on heavy granite slabs to eliminate vibrations. To ensure optimum focus of the laser beam on substrates and resist layers of varying thickness, the system is capable of



Figure 5.5: Heidelberg Instruments DWL 200 Direct Write Lithography System.

moving the entire  $xy$  stage in the  $z$  direction by piezo-electric actuation accurate to 200 nm. Adjustment of the  $z$  height is controlled by an air gauge auto-focus system, which measures the air pressure from an air stream over the substrate. The specified minimum feature size for the system, as delivered, is  $0.6 \mu\text{m}$ , while the maximum write area is  $200 \times 200 \text{ mm}^2$ .

A wide range of UV and wide band resists can be used for LDWL [214], and the pre and post exposure processing steps depend entirely on the chosen resist system. For EBL type resists, such as PMMA, a process sequence as provided in section 5.3.2 must be employed. However, for the LDWL experiments performed here, photomasks blanks with conventional photoresist were used. These were supplied with the photoresist already spin applied to metallized glass substrates, and were mounted directly in the LDWL system with no need for pre exposure processing. The only post exposure processing necessary was development, rinsing, and drying.

#### 5.4 SU-8 as a Negative Electron Beam Resist

The initial experiments with GLAD seed layer fabrication using electron beam lithography employed the positive resist PMMA (polymethylmethacrylate), which is the most widely used and highest resolution (10 nm) EBL resist [206]. However, in order to obtain patterns consisting of individual, isolated seeds with this positive resist, it was necessary to expose all of the resist *between* the seeds. With typical seed layer planar fill factors on

the order of 0.3 to 0.4 – i.e., patterns containing twice as much bare substrate as actual resist – this resulted in large electron doses being pumped into the PMMA layers, and in long write times. The high dose density in turn exacerbated the proximity effect, leading to seed swelling and difficulties in controlling the dose. A possible way to work around this would be to expose only the seed locations in the PMMA and create an inverse image of the seed layer (holes in a thin film), which could then be coated with metal and used as a lift-off template to produce metal seeds. Image reversal in PMMA by hard overexposure has also been reported [144,215], but both of these procedures require additional process steps that degrade the pattern quality.

Clearly, for GLAD seed patterns consisting of arrays of individual dots, negative EBL resists are the better choice. By exposing only the seeds themselves, and not the voids between seeds, less exposure time is required and the adverse proximity effects caused by electron scattering are reduced. Unfortunately, the selection of negative EBL resists has always been limited, and their performance has been much worse than positive resists, with inadequate resolution for GLAD seed layers. In consequence of this, the epoxy novolak SU-8 was developed as a new high performance, negative EBL resist in the course of the thesis research, in collaboration with Dr. Mirwais Aktary (formerly a Research Professional with the University of Alberta NanoFabrication Facility) and MicroChem Corporation.

SU-8 was invented by IBM researchers as a thick, negative photoresist [216], and rapidly gained popularity for high aspect ratio resist applications in MEMS (micro electro mechanical systems). In this role, SU-8 is used in thicknesses from tens to hundreds of micrometres, and patterned using traditional UV/VIS photolithography [217]. Wong and Pun attempted using SU-8 for EBL, but still used rather thick resist layers, and were unable to achieve resolutions better than 100 nm (10 times worse than the resolution of PMMA) [218].

A new formulation of SU-8 was obtained from MicroChem, consisting of bisphenol A novolak epoxy oligomers (the polymer resin building blocks) and triarylsulfonium hexafluoroantimonate (a photoacid generator) dissolved in cyclopentanone. As a negative resist, SU-8 works by chemical amplification. Electron or photon exposure breaks down the photoacid generator into an acid, which protonates the epoxy oligomers. During the post exposure bake step, these protonated oligomers then cross-link to create an insoluble polymer resin network [214,219]. The chemical structure of the SU-8 resin is shown in figure 5.6.

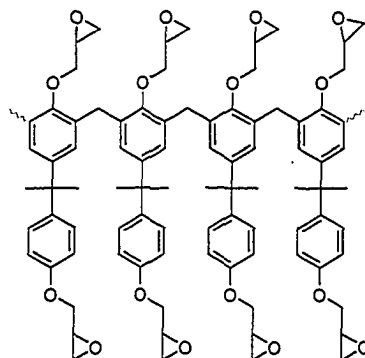
**BISPHENOL A NOVOLAK RESIN**

Figure 5.6: Chemical structure of the bisphenol A novolak polymer network in the negative resist SU-8.

The SU-8 formulation used had a relatively low concentration of oligomers, and hence low viscosity, which allowed very thin resist films to be spun onto substrates. Significant efforts went into optimizing every step of the pre and post exposure processing sequence – outlined in section 5.3.3 – with particular emphasis on the resist spin-on application (which gives the resist thickness and hence the eventual seed height) and the post exposure bake (responsible for the polymer cross-linking). The most uniform resist films were obtained using 30 second long spin cycles at 5000 to 7000 rpm, with relatively slow acceleration and deceleration ramps of 300 rpm/s. Spin cycle rates below 5000 rpm produced non-uniform films. Unlike most other resists, the resist thickness was nearly independent of the spin cycle speed, with a fixed thickness of approximately 150 nm, measured using ellipsometry and stylus profiling (see figure 5.7). The best post exposure bake protocol was found to be a dual hot plate bake at 65°C for 60 seconds and at 95°C for 60 seconds. MicroChem’s standard SU-8 Developer was used for pattern development. Since the sensitivity of SU-8 to irradiation is higher than most EBL resists, the EBL exposure step required some optimization, with the best line doses being in the relatively low range of 0.03 to 0.07 nC/cm.

A number of different test patterns were exposed to evaluate the resolution and characteristics of the resist. Figure 5.8 demonstrates that SU-8 has a resolution of 30 nm, which is three times better than any previously reported negative EBL resist, and close to the 10 nm resolution for the best positive EBL resists. In figure 5.8a, 30 nm wide single pixel lines are shown in a close-up top view. The lines are well-defined and maintain the line

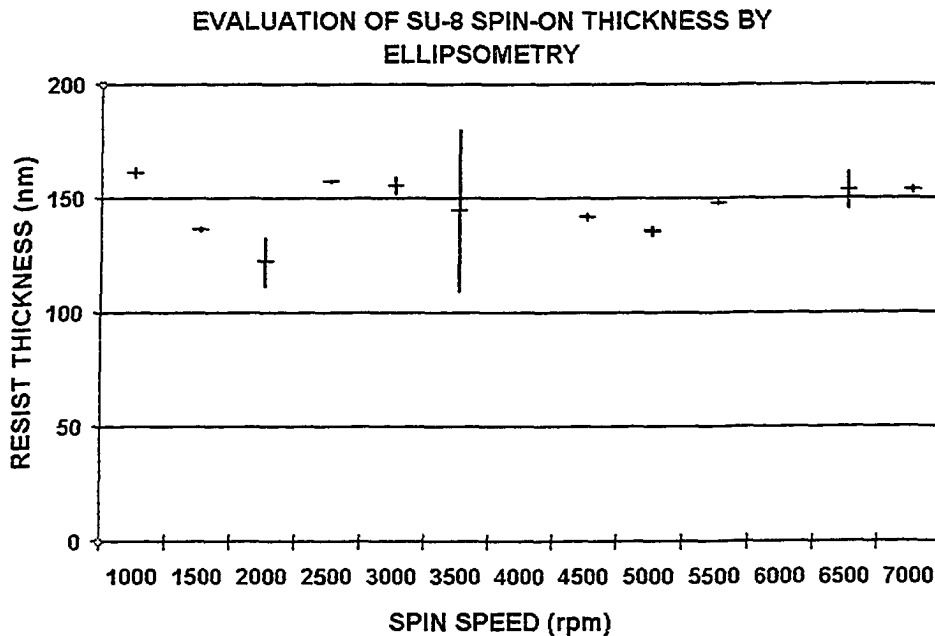


Figure 5.7: When SU-8 resist is spin-on applied to substrates, the thickness is nearly independent of the spin cycle speed. Each data point represents the average value of a series of measurements on several different samples, with the error bar indicating the variance of the data set for each spin speed.

width with a minimal amount of roughness. Figure 5.8b shows an oblique view of a dense linear grating with a pitch of 200 nm, written with a line dose of 0.05 nC/cm. The micrograph was recorded at an angle relative to the grating to show the height of the lines, which both here and in figure 5.8a is 150 nm (the resist thickness after spin-on application), yielding a good aspect ratio. Crucially, the grating in figure 5.8b reveals that dense patterns are achievable in SU-8 without significant proximity effects. The contrast of the resist (i.e., the selectivity of polymer cross-linking to electron exposure) is also observed to be high. Finally, reactive ion etching of the resist was performed using  $\text{CHF}_3$ , confirming that SU-8 has excellent mechanical and thermal stability even as a thin EBL resist. This stability helps SU-8 sustain subsequent thin film deposition and processing [216].

SU-8 has thus been established as the best negative EBL resist to date, and a resist suitable for GLAD seed layer fabrication.

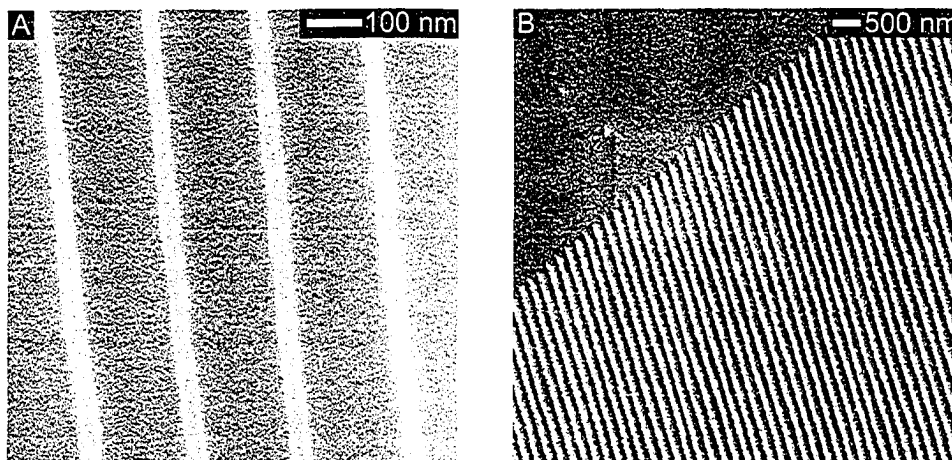


Figure 5.8: SEM micrographs of high resolution EBL lines in 150 nm thick SU-8 resist. a) Close-up image of uniform 30 nm wide single pixel lines. b) Oblique view of dense linear grating, demonstrating high pattern contrast and negligible proximity effects.

## 5.5 Seed Layers Fabricated using Electron Beam Lithography

### 5.5.1 EBL System Optimization

The large area, high resolution lithographic requirements of GLAD seed layer fabrication are not immediately attainable by commercial EBL systems, which normally cannot maintain high resolution patterning over write fields larger than a few hundred  $\mu\text{m}$  (limited by the size of the aforementioned electron beam raster scan). One approach to enlarge the pattern size is write field stitching, in which the resist coated substrate is moved stepwise underneath the electron beam to successively expose adjacent write fields. This requires a motion control stage with extremely high positioning accuracy, i.e., on the order of the EBL resolution, since loss of alignment among write fields inside a periodic GLAD seed array is unacceptable for photonic crystal applications and would cause crystal defects. Additional wiring was installed on the SEM to allow the NPGS system to control the five-axis sample stage, as well as automatically adjust for substrate flatness. However, as shown in figure 5.9, the accuracy and stability of the stage and axis motors were found to be worse than 900 nm, and hence insufficient for the stitching of seed layers with lattice periods as low as 300 nm. Indeed, a

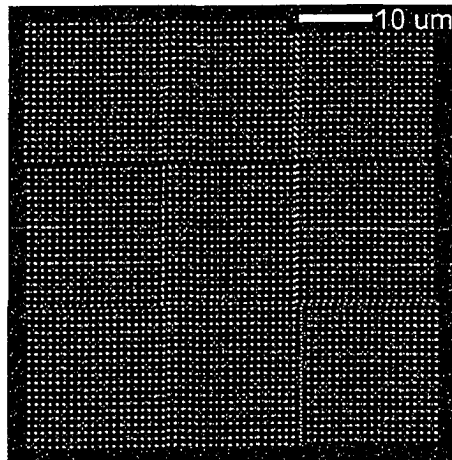


Figure 5.9: Top view SEM micrograph of an attempt to stitch together nine EBL write fields using the five-axis sample stage in the LEO 440 SEM. The accuracy of the stage is worse than 900 nm, which is clearly insufficient for write field stitching.

golden rule in nanoscale lithography is to never have write field boundaries intersect high resolution patterns.

Instead, large area seed patterns were achieved by forcing by EBL system to operate at SEM magnification values of 300x to 400x, which is substantially lower than the 1000x magnification specified for the system. A reduction in the magnification represents an increase in the raster scan size – and hence the write field area – as the electron lenses in the SEM column deflect the e-beam further away from its central axis. At the outer edges of such a large write field the electron beam impinges on the substrate at an oblique angle, which in turn causes distortion of the written pattern. This is the reason why EBL is normally restricted to high SEM magnifications and small write fields. To counter this distortion, the working distance of the SEM (the vertical distance between the SEM objective lens and the substrate) was simultaneously increased from less than 10 mm to a relatively high value of 15 mm. This sacrifices some pattern resolution and makes the EBL system more susceptible to pick up external acoustic and electromagnetic noise, but also lowers the angular deflection of the electron beam, and hence reduces the seed shape distortion at the pattern edges to negligible levels for GLAD seeding purposes. With this approach it was possible to obtain seed arrays larger than 1 mm<sup>2</sup>, or more than 150 times larger than the 80x80 μm<sup>2</sup> originally specified for the LEO 440/NPGS system.

In order to pattern the largest seed patterns, some tweaking of the EBL software was required. Using the conventional EBL approach, in which each seed is individually represented in the CAD design and individually written by the electron beam as a collection of pixels, the write time for arrays containing more than  $10^6$  seeds was several hours. This sluggishness was caused not by the actual pattern writing, but by the time required to calculate the beam position for each pixel and move the beam around. Such slowness is unacceptable not just from a practical point of view, but also creates problems with drift in the SEM column and loss of electron beam alignment. Furthermore, the EBL software simply stalled when trying to handle extremely large CAD files specifying more than  $10^6$  seeds. The solution was to replace the CAD seed array with one CAD rectangle, and manually set the distance between pixels to the lattice constant for the desired seed array. The EBL system thinks that it is writing a single, filled rectangle of connected pixels – which drastically reduces the write time to a few minutes – but in fact the pixel centre-to-centre distance is so large that the “rectangle” develops as a tetragonal array of disconnected dots, i.e., the desired seed array. Clearly, this approach does not work for hexagonal seed arrays, nor for seed patterns with defects or special seed shapes. An exposed single pixel may also be too small to work as a GLAD seed, but this can be corrected by the GLAD process itself, as discussed later.

### 5.5.2 Seed Layers in PMMA

For EBL seed layer fabrication in PMMA, silicon wafers cleaved into  $1 \times 1$  cm<sup>2</sup> dies were used as substrates. These substrates were cleaned in accordance with the process sequence outlined in section 5.3.3, and PMMA was spin-on applied using a Specialty Coating Systems Spincoater Model P6700. PMMA resins with a molecular weight of 950,000 g/mol and dissolved in chlorobenzene were used (supplied by MicroChem under the trade-name NANO 950PMMA C). By varying the PMMA concentration and the spin cycle speeds, any resist thickness – and hence seed height – in the range from 75 nm to 650 nm could be obtained, as evaluated by a Gaertner ellipsometer and a Tencor Alphastep 200 profilometer. Resist thicknesses in the 100 to 200 nm range critical to seed layer fabrication were achieved with a concentration of 2 % PMMA in chlorobenzene, and 30 second spin cycles at 1000 to 4000 rpm, as shown in the spin plot in figure 5.10.

Prior to EBL fabrication of actual seed layer designs for applications, test designs consisting of square and round seeds in various tetragonal and hexagonal lattices were executed to determine the correct electron doses.

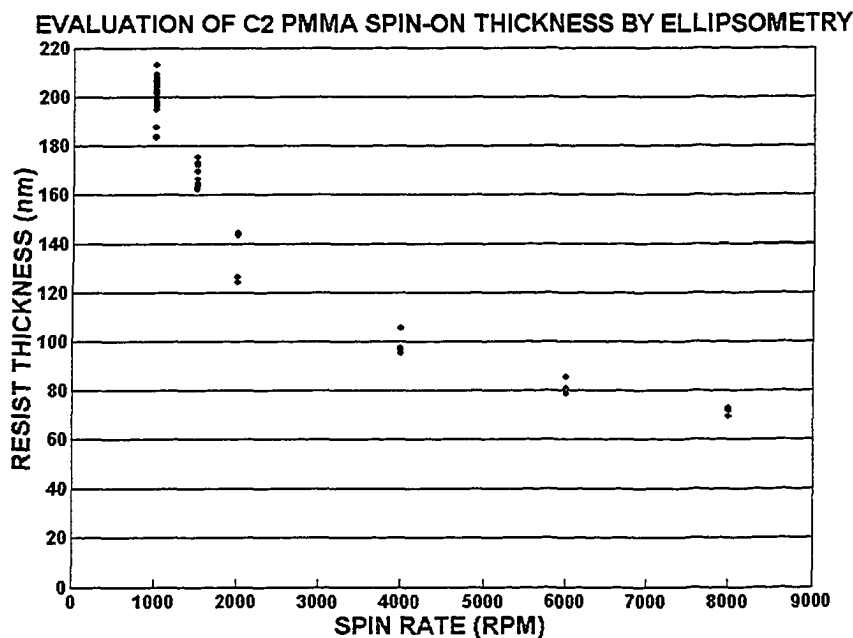


Figure 5.10: Spin curve for 2 % PMMA in chlorobenzene spin-on applied to silicon substrates. Unlike the SU-8 spin curve in figure 5.7, the resist thickness of PMMA depends strongly on the spin speed. Thicknesses were measured using ellipsometry, with five measurements per sample and several samples per spin speed setting.

Due to the aforementioned proximity effect, the electron dose (measured as charge per area) depends strongly on the planar density or fill factor of a seed layer, as well as on the seed size and height and the seed lattice period. Typical electron doses for PMMA were 100 to 600  $\mu\text{C}/\text{cm}^2$ . The remaining SEM settings were set as previously detailed in section 5.3.2.

Figure 5.11 shows a PMMA EBL test pattern with nineteen different potential seed layer designs. The first three rows contain tetragonal seed lattices with square shaped seeds. Except from the three top left sections, the lattice period in these three rows varies from 200 nm to 600 nm from left to right, whereas the seed width varies from 300 nm to 150 nm from top to bottom. For the smallest seed width of 150 nm, the square seed shape has degenerated into a circle. The three top left sections have seed widths of 400 and 500 nm. The bottom row contains two hexagonal seed lattices with circular seeds and periods of 300 and 450 nm, as well as two

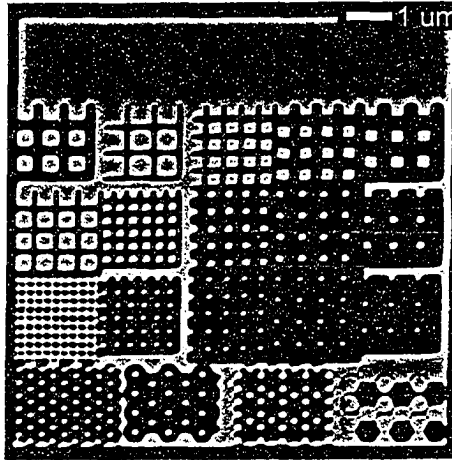


Figure 5.11: SEM micrograph of EBL test pattern in PMMA resist, exposed at an electron dose of  $450 \mu\text{C}/\text{cm}^2$ . Each  $1 \mu\text{m}^2$  section contains a different seed layer geometry, including tetragonal (top) and hexagonal (bottom) lattices, and seed sizes varying from 150 to 500 nm.

experimental honeycomb type lattices with hexagonal seeds and periods of 300 and 450 nm. The entire pattern was written with an electron dose of  $450 \mu\text{C}/\text{cm}^2$ , and this dose is evidently not appropriate for all of the seed test designs. For example, the seeds in the third and fourth design in the top row are overexposed, and so undercut from electron scattering off the silicon substrate that they have partly detached and twisted around. Meanwhile, the dense seed pattern in the first section in the third row is underexposed, with the seeds still being connected by resist. These patterns came out much better with doses of 400 and  $500 \mu\text{C}/\text{cm}^2$ , respectively. It should be noted, however, that test patterns like the  $1 \mu\text{m}^2$  sized ones in figure 5.11 only yield approximate electron doses, since proximity effects can extend over several micrometres. Fine tuning of the dose must be done on full-size patterns. Despite being only 10 by 10 micrometres large, the test pattern took 3 minutes for the EBL system to complete. This is indicative of the long write times required for seed layers in positive EBL resists, and for designs in which each seed is an individual multi-pixel entity, as discussed above.

Details of two full-size GLAD seed layers are illustrated in figure 5.12. Figure 5.12a is a tetragonal seed lattice of square seeds with a lattice period  $\Delta$  of 300 nm and a seed width  $w$  of 125 nm, while figure 5.12b is a hexagonal

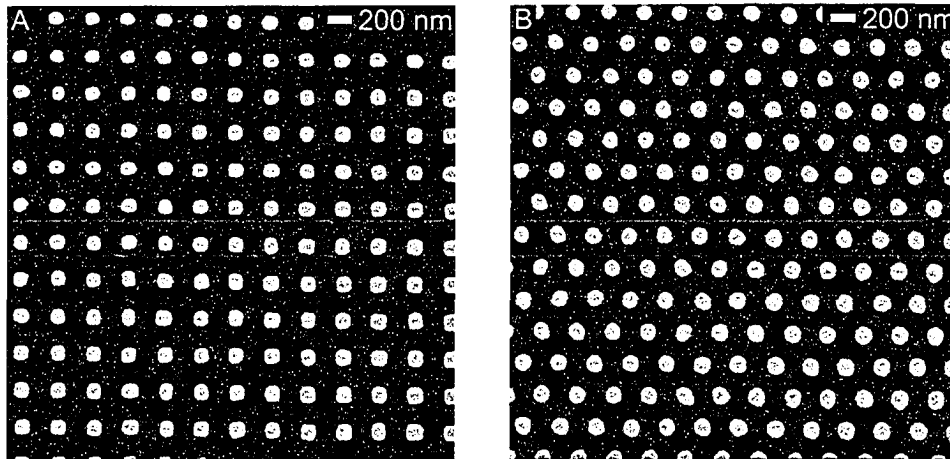


Figure 5.12: Top views of EBL PMMA seed layers for GLAD, both with a lattice period of 300 nm and seed width of 125 nm. The pattern in a) features a tetragonal lattice, whereas b) has a hexagonal lattice.

lattice of circular seeds with the same lattice and seed dimensions. In both cases the EBL electron dose was  $450 \mu\text{C}/\text{cm}^2$ , resulting in complete pattern transfer with high contrast and good uniformity. The square seeds have round corners, likely caused by electron scattering in the resist, whilst some of the circular seeds are slightly deformed, thought to be a result of resist swelling during development. These patterns are directly applicable to use as GLAD seed layers.

Figure 5.13 shows two oblique view SEM micrographs of tetragonal lattice PMMA seed layers. The seed layer in figure 5.13a has a lattice period of 600 nm and seed width of 500 nm, resulting in a high seed planar fill factor of 0.69. The seed height is approximately 180 nm. While the pattern contrast is exceptional, some undercutting of the seeds due to electron scattering is noticeable (the electron dose was  $600 \mu\text{C}/\text{cm}^2$ ). This actually leads to an effective seed sidewall inclination angle higher than  $90^\circ$ , which is perfect for subsequent GLAD deposition. In addition, some swelling of the seed edges has occurred, causing the top surface of the seeds to look slightly concave. Figure 5.13b shows circular seeds with a designed width of 150 nm and a lattice period of 300 nm. With an electron dose of  $400 \mu\text{C}/\text{cm}^2$  the pattern is slightly overexposed, and the actual seed width of approximately 100 nm is lower than designed. Some undercutting of the seeds is observed again, but the seed aspect ratio is high.

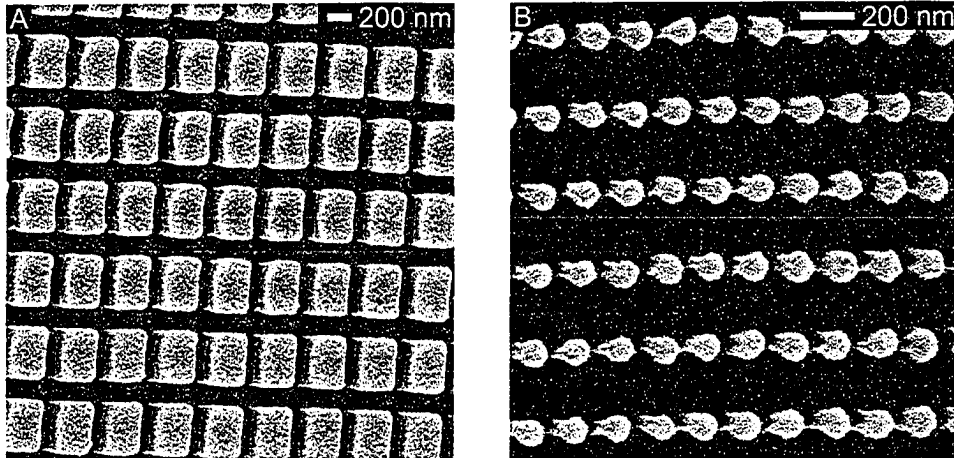


Figure 5.13: Oblique views of EBL PMMA tetragonal seed layers. a) High seed planar fill factor seed layer with 500 nm wide seeds in a 600 nm lattice. b) Low planar fill factor seed layer with 100 nm wide seeds in a 300 nm lattice. Note the undercutting of the seeds in both a) and b).

### 5.5.3 Seed Layers in SU-8

Both silicon and glass substrates were used for EBL seed layer fabrication using SU-8 as resist, with glass substrates allowing transmission measurements of subsequently deposited GLAD photonic crystals. The resist processing pre and post EBL exposure was described in section 5.4, and the same processing steps and EBL settings worked for both types of substrate. The higher sensitivity and different electron scattering characteristics of SU-8 relative to PMMA meant that electron doses had to be adjusted downwards. Typical electron doses for SU-8 seed layers were 10 to 100  $\mu\text{C}/\text{cm}^2$ .

Figure 5.14a depicts a tetragonal seed layer in SU-8 with a lattice period of 600 nm and circular seeds with a width of 200 nm, written with an electron dose of 100  $\mu\text{C}/\text{cm}^2$ . The seeds are almost perfectly round, and the overall pattern has excellent contrast and uniformity. The inset in figure 5.14a shows the outer edge of a similar 1 mm wide seed layer (in this case with a lattice period of 1000 nm and seed size of 400 nm). As previously discussed, this seed layer size – large by EBL standards – was achieved by lowering the SEM magnification and simultaneously raising the working distance. The inset demonstrates that in spite of the pattern area being two orders of magnitude larger than originally specified for the EBL system, there is no distortion at the edges of the seed layer. Figure 5.14b illustrates a hexagonal

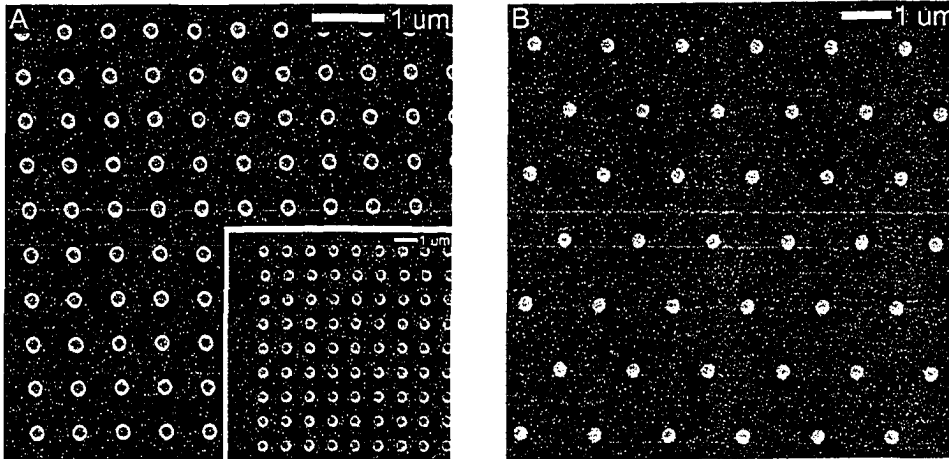


Figure 5.14: Top views of EBL seed layers in SU-8. a) Tetragonal seed layer with a lattice period of 600 nm. The inset shows the absence of pattern distortion even at the edge of a  $1 \times 1 \text{ mm}^2$  large write field. b) Hexagonal seed layer with a lattice period of 1500 nm.

SU-8 seed layer with a lattice period of 1500 nm and a seed width of 250 nm.

Oblique views of SU-8 seed layers are shown in figure 5.15, in the form of tetragonal lattices with a period of 1000 nm, seed widths of 400 nm and 100 nm, and electron doses of  $50$  and  $100 \mu\text{C}/\text{cm}^2$ , respectively. The seed height is just under 150 nm – corresponding to the fixed thickness given by the concentration of the SU-8 used for resist spinning – and the seeds are observed to be very well defined with near vertical sidewalls. The contrast of the patterns is excellent. For the seed layer in figure 5.15a a thin, rough film of exposed resist remains between the seeds, resulting from the increased overall electron exposure and scattering associated with the higher seed planar fill factor in this pattern. The seed layers in the negative resist SU-8 are better defined and more uniform than the seeds in the positive resist PMMA, as expected from the previous discussion on the virtues of a negative resist for EBL patterning of individual, isolated features. Substantially shorter write times was an additional advantage of using SU-8.

Figure 5.16 illustrates the important method described in section 5.5.1 for luring the EBL system into patterning a tetragonal array of seeds by instructing it to write a “filled-in” rectangle with an intentionally high pixel-to-pixel distance. Figure 5.16a shows one of the resulting tetragonal seed layers, with an overall size of  $1 \times 1 \text{ mm}^2$ . The lattice period is 600 nm,

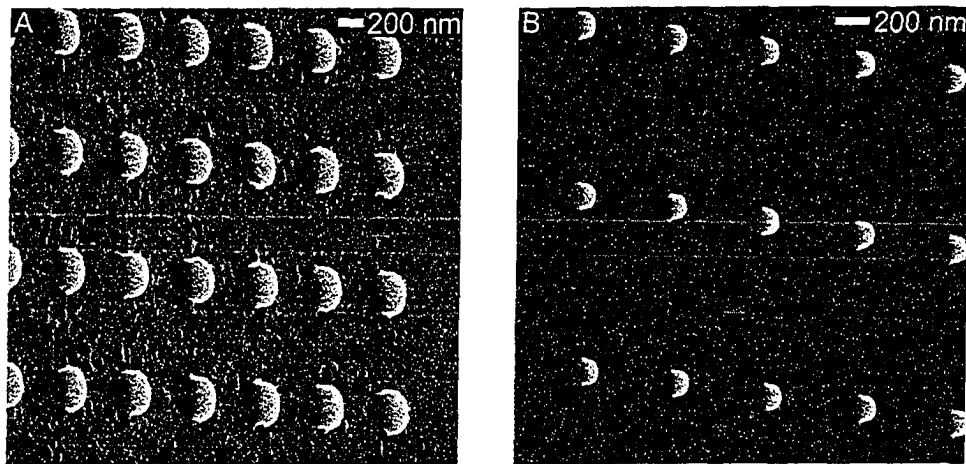


Figure 5.15: Oblique views of EBL seed layers in SU-8. a) In this 1000 nm period tetragonal pattern, written with a dose of  $50 \mu\text{C}/\text{cm}^2$ , some residual resist is observed between the seeds, resulting from the proximity effect. b) Another 1000 nm period pattern written at  $100 \mu\text{C}/\text{cm}^2$ , but with much smaller seeds. No proximity effects can be seen here.

given by the pixel-to-pixel distance, and the electron dose at each pixel or “burst” of exposure was 3 fC. The seeds are smaller and less uniform than those in figures 5.14 and 5.15, which were each composed of a number of pixels and took much longer to write. However, the regularity of the seed lattice is maintained, and as figure 5.16b shows, a short vertical post GLAD deposition can amplify the small EBL seeds to a size suitable for subsequent deposition of a periodic GLAD film. In this example a silicon vertical post deposition of nominal 100 nm thickness increased the seed width from 100 nm to 300 nm, and the effective seed height from 150 nm to 180 nm. The higher the nominal thickness of the vertical post GLAD deposition, the more the seed width increases. This allows for the seed width to be tailored, even if the rapid single-pixel EBL approach itself does not allow the seed size to be set. In general, the nominal thickness of the GLAD seed amplification layer is a compromise between seed contrast improvement and seed broadening, and seed amplification does lead to degradation of the seed sidewall inclination angle, as evidenced by the non-ideal seed shape in figure 5.16b.

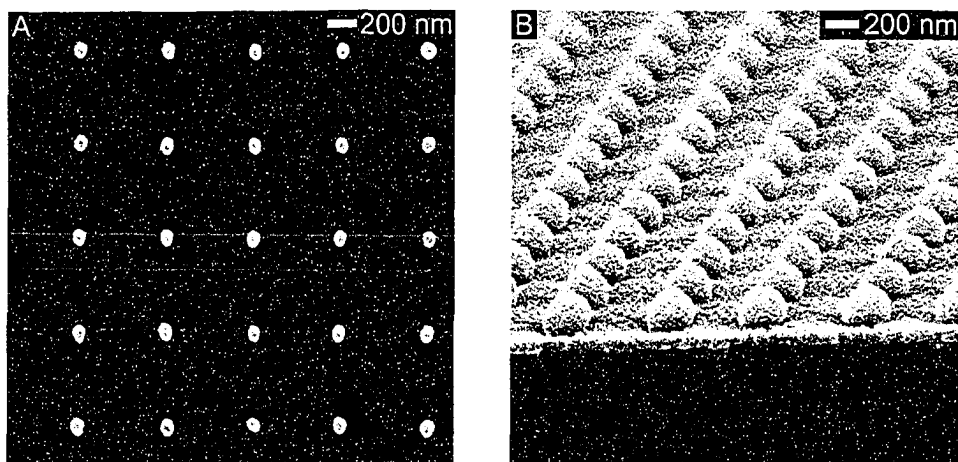


Figure 5.16: a) Top view of a tetragonal EBL seed layer in SU-8, written as a filled-in rectangle with a pixel separation equal to the desired lattice period of 600 nm. The seed width is small and cannot be specified, but as shown in b), a short GLAD deposition can amplify the EBL seeds to a more appropriate size.

## 5.6 Seed Layers Fabricated using Laser Direct Write Lithography

### 5.6.1 Hardware Optimization

Laser direct write lithography is widely used for the fabrication of photomasks for UV/VIS photolithography, with resolutions on the order of 1  $\mu\text{m}$ . However, GLAD seed layer fabrication requires pattern resolution better than even the 0.6  $\mu\text{m}$  specified for the Heidelberg DWL 200 instrument. To achieve an improvement in resolution, substantial effort went into fine tuning and optimizing the settings of the write laser and acousto-optic components. Furthermore, the resist patterns fabricated by LDWL were used directly as GLAD seed layers, rather than as photomasks. This approach eliminated the need for subsequent lithographic pattern transferring and processing, thereby not only reducing processing time and complexity, but also avoiding the inevitable loss of resolution and pattern quality associated with each additional lithography step. The latter was especially important as the LDWL process was being pushed beyond its known limits.

For each new seed layer design, the LDWL laser and optics had to be fine adjusted to a unique, optimum setting. Particular attention had to be given

to the laser beam energy (analogous to the electron dose in EBL), which was tuned to within 10 mW for each pattern design. As the laser energy was found to drift over time (in spite of a feedback loop supposed to maintain constant output), recalibration of the laser energy was required several times daily. Secondly, the focus of the laser beam had to be extremely tight, given that its depth-of-field is less than a micrometre. This was achieved by writing test versions of the seed layers at different foci, stepped in 100 nm increments (given by the piezo actuated height of the LDWL substrate holder), and carefully inspect the developed results to choose the best focused pattern. Great care in mounting substrates flat on the holder had to be taken. Finally, the frequency ramp of the acousto-optic modulator – which is on the order of 750 kHz/s – had to be tuned to within 0.2 kHz/s. Inadequate adjustment of this frequency led to misalignment of the laser sweeps over the substrate, and gaps in the patterns akin to EBL write field stitching errors. The two remaining key LDWL settings were found to be less critical, namely the lateral intensity profile of the laser output and the crystal tilt of the acousto-optic deflector.

### 5.6.2 Seed Layer Fabrication

The substrates used for LDWL seed layer fabrication were dies cut from photomask blanks made specifically for LDWL processing. The Nanofilm Inc. blanks were 2 mm thick, 127 x 127 mm<sup>2</sup> large soda lime glass plates (refractive index  $n$  of 1.52), coated with a dual layer of 100 nm chrome and 530 nm Clariant AZ-1518 positive UV resist. As the blanks were delivered ready to use, the only chemical processing required was development of the resist post exposure. This was performed by immersion and agitation in Microposit 354 developer for 70 seconds, followed by DI water rinsing and nitrogen gas drying.

With AZ-1518 being a positive resist, the LDWL seed layers had to be designed and written in positive tone. That is, as with EBL patterning in PMMA, the laser beam irradiated the resist *around* the designed seeds, rather than the seeds themselves. Unlike EBL in PMMA, however, large area positive tone LDWL seed patterning is practically feasible, given the vastly higher write speed in LDWL. In fact, write times would increase drastically if negative tone LDWL patterning one seed at a time was attempted, since significant time would be required for the laser beam to settle at each seed location. Each LDWL seed layer design was preceded by a number of test designs to optimize the laser and optical settings, as described above.

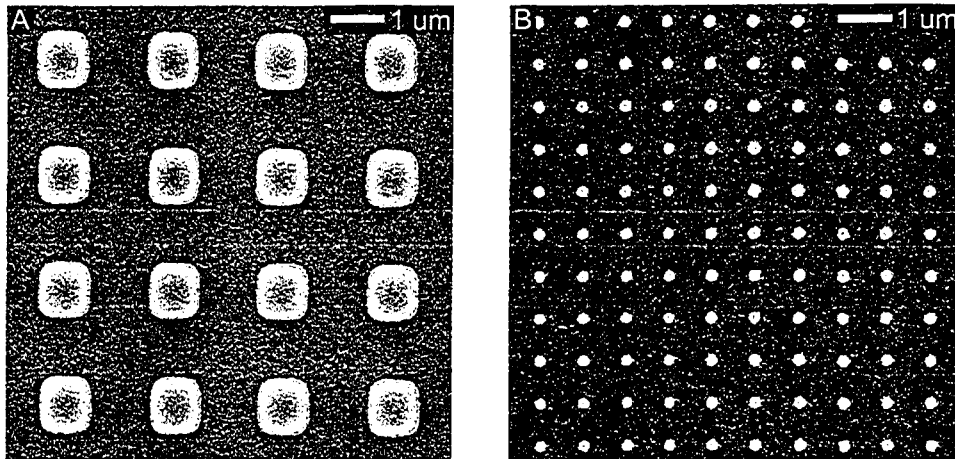


Figure 5.17: Top views of LDWL tetragonal seed layers. a) 900 nm wide square seeds in a 2000 nm lattice. b) 230 nm wide circular seeds in a 800 nm lattice.

Figure 5.17 shows two SEM micrographs of optimized tetragonal seed layers fabricated using LDWL. The design in figure 5.17a has a seed lattice period of 2000 nm and square seeds with a width of 900 nm, and was written with a laser beam energy of 139 mW. The contrast is very high, there is only limited rounding of the square seeds, and as expected for laser based writing there are no signs of proximity exposure of the resist (cf. section 5.3.3). In figure 5.17b – shown at the same magnification as figure 5.17a – the lattice period is 800 nm and the circular seed width 230 nm. Here, too, the seed contrast is excellent.

With a seed size below 250 nm, the LDWL pattern in figure 5.17b represents a significant improvement in resolution over the specified 600 nm for the Heidelberg DWL 200 system. This improvement was realized by the aforementioned careful fine tuning of the write laser and acousto-optic components, and appears to be the highest resolution achieved to date with a commercial LDWL system [220]. Furthermore, this resolution was reproducible and sustainable over large pattern areas, with a potential for patterns as large as a 5" photomask blank.

An oblique view of the LDWL seed pattern from figure 5.17a is shown in figure 5.18a, illustrating that the LDWL seed profile tends to be pyramidal. The seed height is approximately 500 nm, or slightly lower than the nominal resist thickness. The small ripples on the sides of the seeds should also be noted. As discussed before, these ripples are likely the result of standing

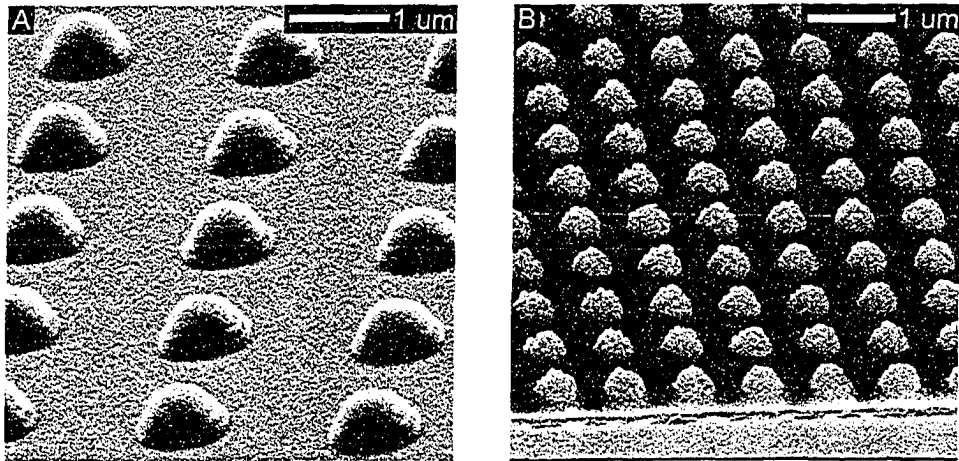


Figure 5.18: Oblique views of LDWL tetragonal seed layers. a) Same seed layer as depicted in figure 5.17a, revealing a pyramidal seed shape. b) 800 nm period seed layer amplified by a short vertical post GLAD deposition to improve the seed contrast and shape.

waves in the resist arising from reflection of the laser beam off the chrome coated substrate. The pyramidal seed shape and associated low sidewall inclination angle are not as ideal as in the EBL produced seeds. This can be rectified by amplifying the LDWL seed with a thin vertical post GLAD film, similar to what was done for rapid SU-8 EBL seeds. An example of this is shown in figure 5.18b for a tetragonal seed pattern with a period of 800 nm and circular seed width prior to amplification of approximately 300 nm. The nominally 100 nm thick GLAD film has broadened the seeds somewhat, but has also improved the sidewall inclination angle.

A photograph of  $5 \times 8 \text{ mm}^2$  large seed patterns is shown in figure 5.19. Even for LDWL patterns this large, representing nearly  $10^8$  seeds and yielding well-sized seed layers for practical GLAD deposition and photonic crystal experimentation, the write time was only 45 minutes. This pattern was the largest achievable with the current LDWL system software, which seized when asked to handle larger patterns. However, since the only hardware limit to pattern size is the 5" substrate holder, better software or more efficient programming of the highly repetitive seed layer designs should allow still bigger seed arrays to be produced.

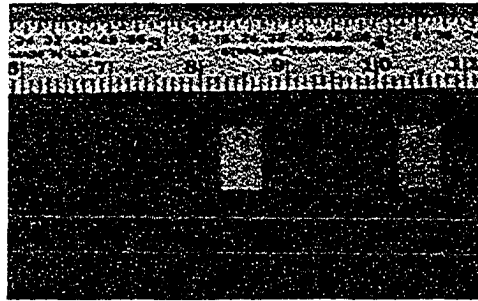


Figure 5.19: Photograph of three complete 5x8 mm<sup>2</sup> large seed layers on a die cut from a photomask blank. The seed patterns diffract visible light like gratings. The lower scale on the ruler is in centimetres.

A brief comparison of EBL and LDWL for seed layer fabrication breaks down as follows:

- Resolution: One order of magnitude better in EBL, making EBL superior for small seeds with non-circular shapes.
- Pattern quality: Generally better contrast and seed sidewall inclination angles in EBL, particularly when using SU-8.
- Pattern size: One to two orders of magnitude larger in LDWL.
- Throughput/write speed: At least one order of magnitude higher in LDWL.

For most GLAD seed layer applications, LDWL is the most appropriate fabrication method.

### 5.6.3 Seed Layers on Transparent Substrates

In order to fabricate LDWL seed layers on transparent substrates, as required for characterization of subsequently deposited photonic crystal thin films, the same photomask blanks as above were used, but with two additional processing steps after development of the seed pattern.

The first process step was a short reactive ion etch (RIE) of the resist pattern, and was required only for dense seed layer designs in which thin residual films of resist were sometimes observed between the developed seeds. This reduction in pattern contrast was not due to proximity effects (as in EBL), but probably caused by incomplete switching of the acousto-optic

modulator, which for small seed lattice periods is required to switch very rapidly. A Plasmalab  $\mu$ Etch apparatus was employed for the resist RIE, using a custom recipe with an O<sub>2</sub> flow of 50 sccm, a RF power setting of 50 W, a process pressure of 150 mTorr, and etch durations of 60 to 90 seconds. The RIE etch was pseudo-isotropic, and effected an overall reduction in the LDWL resist thickness while maintaining the pattern relief, thus causing the seed layer to be exposed to the bare, chrome-coated substrate. In the second process step, the exposed 100 nm thick inter-seed chrome was removed by etching in wet chrome etch for 30 to 40 seconds under agitation.

After these process steps, the seed layers consisted of resist/chrome seeds on transparent glass substrates. To increase the final height of the etched seeds, it was found beneficial to perform seed amplification by a short vertical post GLAD deposition. The optical characteristics of the transparent LDWL substrates will be covered in chapter 8.

## Chapter 6

# Growth and Characteristics of Periodic GLAD Films

The optical characteristics of photonic crystals depend critically on fine details in their physical morphology. Deviations from the ideal theoretical structure may alter the size of the bandgap, and small imperfections can close the bandgap altogether. With the fabrication of substrate seed layers in place, this chapter describes thesis research on the nucleation, growth, and characteristics of periodically structured GLAD films. Such insight is required to refine and optimize the growth of periodic square spiral GLAD films, as in the following chapters, with the dual aim of approaching the ideal photonic crystal architecture and allowing engineering of the bandgap location and waveguides. The experimental focus of the chapter is on periodic square spirals, but the analyses apply to periodic GLAD films in general, and the conclusions reach beyond to all GLAD applications that can benefit from increased structural control and uniformity.

The research results described here have been accepted for publication in the IEEE Transactions on Nanotechnology [190].

## 6.1 The Importance of Periodically Structured GLAD Films

The importance of periodically structured GLAD films goes well beyond photonic crystals, and this chapter is of relevance to many applications and investigations of GLAD. Specifically, GLAD thin films can benefit from a periodic structure in three ways:

- When a periodic film structure is required.
- When a uniform film structure is required.
- When control over the film structure is required.

Photonic bandgap crystals are a notable application of periodic GLAD films, but certainly not the only one. In fact, glancing angle deposition on periodic seed layers is a unique microfabrication technique for many applications that require highly ordered arrays of structured sub micrometre columns. One such application is magnetic storage media consisting of tetragonally or hexagonally ordered ferromagnetic posts, each addressable as a single bit [132, 133, 174–176]. Another application is filtering or chromatographic separation of cells, bacteria, macromolecules, and other biological entities, inside thin film microfluidic channels filled with evenly spaced columns [193, 221].

Even in applications that strictly do not need periodic orientation of the columns, the stochastic nature of non-seeded film nucleation and growth leads to column broadening, competition, and extinction that are often detrimental to the film properties. As described in this chapter, periodically structured GLAD offers much greater uniformity, both in the overall film morphology and in the column shape, which can benefit applications such as optical filters and coatings, liquid crystal/GLAD hybrid cells, field emitter arrays, and photovoltaic cells.

Finally, periodic seed layers offer a direct and precious means to control the microstructure of GLAD films, in particular the column width, the pore size, and the pore distribution. Humidity and biosensors, supercapacitors, and catalysts are among the GLAD applications relying directly on these film characteristics, and whose study and development would benefit tremendously from greater morphological control.

Although this chapter serves as validation of the previous chapter's periodic seed layer design rules, it should be mentioned that in principle any substrate seed topography – including non-periodic ones – can be employed

to induce a certain structure during GLAD film nucleation and growth. Non-periodic seeding, however, forfeits almost all of the structural benefits of seeding presented below.

## 6.2 Growth Evolution of Periodic GLAD Films

### 6.2.1 Experimental Details

In order to study the nucleation and growth evolution of GLAD thin films on periodic substrate seed layers, a number of different seed patterns were fabricated using EBL and DWDL, and GLAD films of various thicknesses were then deposited on the seed patterns using an electron beam PVD evaporation system. In keeping with the overarching research objective of using GLAD for photonic crystal engineering, the geometry of the seed layers was tetragonal, the deposited material was silicon (the most suitable GLAD material for PBCs, as discussed in section 7.2.2), and the column helical structure was square spiral. Since seed enforced nucleation and growth benefits greatly from a high vapour incidence angle – with longer shadows allowing for a wider range of seed lattice periods  $\Delta$ , seed widths  $d$ , and seed heights  $h$  (see equations 5.2 and 5.5) –  $\alpha$  was set to values between  $84^\circ$  and  $86^\circ$ . More experimental details on the GLAD deposition process for silicon are provided in section 7.2.3.

### 6.2.2 Nucleation

Periodic GLAD exploits the fact that highly oblique vapour incidence angles enhance rather than attenuate surface features, with the raised height of each seed precipitating the nucleation of the incident vapour through geometrical shadowing. Figure 6.1 shows the progress of film nucleation on a tetragonal seed pattern with a lattice period  $\Delta$  of 1000 nm and a seed width  $d$  of 400 nm (yielding a fill factor  $ff_{A,seeds}$  of 0.13), fabricated by EBL in SU-8 resist for a seed height  $h$  of 150 nm. Silicon was deposited at a vapour incidence angle  $\alpha$  of  $84^\circ$  and at a rate of  $2.5 \text{ \AA/s}$  (actual rate, adjusted for  $\alpha$ ). As indicated in the figure, the vapour incidence direction  $\phi$  was aligned at  $45^\circ$  relative to the tetragonal seed lattice.

The top row in figure 6.1 shows the GLAD film after 15 nm of silicon has been deposited, while the bottom row depicts the situation with 45 nm of silicon deposited. The extension of a shadow behind each seed is clearly evident. Inside the umbrae slight amounts of silicon have accumulated in an uneven layer a few nanometres thick, however, comparison of figures 6.1b

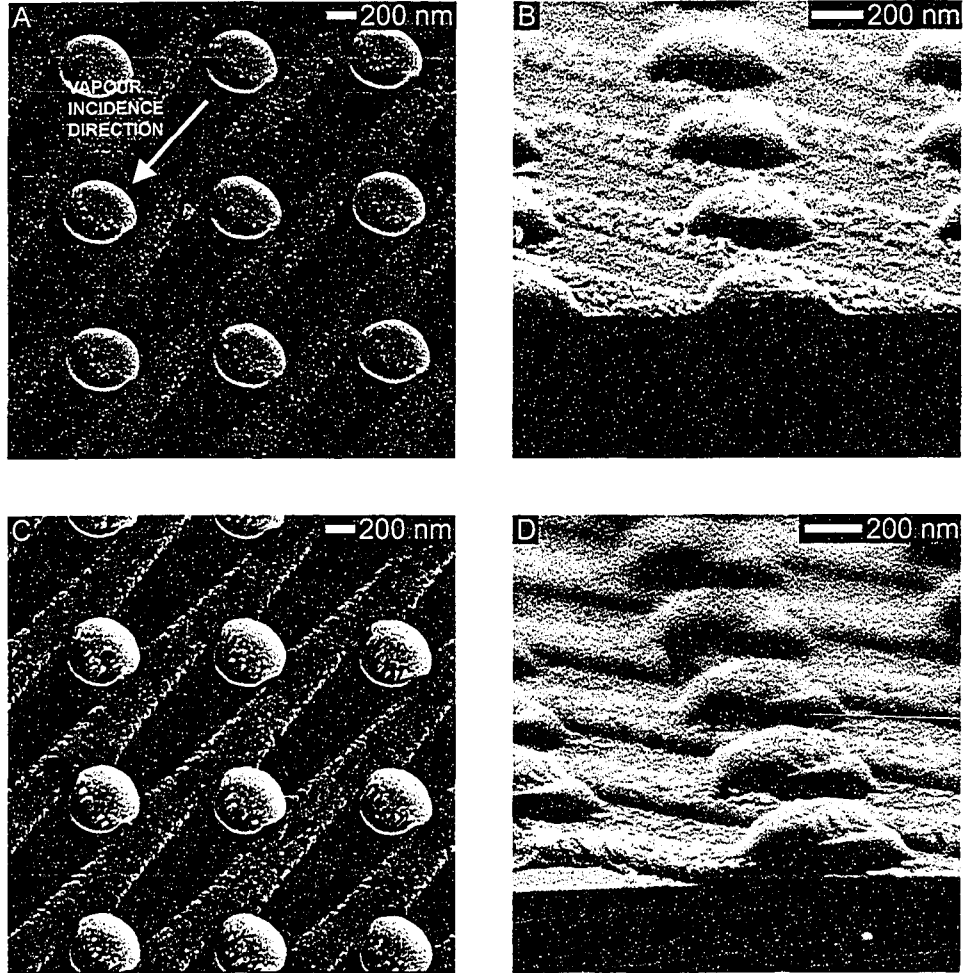


Figure 6.1: Silicon GLAD film grown on an EBL SU-8 seed layer with 1000 nm lattice period and 400 nm seed width. a,b) Top and oblique view of 15 nm film growth. c,d) Top and oblique view of 45 nm film growth.

and 6.1d reveals that this shadow layer grows slower than the unshaded GLAD film on the seeds and between the seed shadows. The 'film' visible inside the shadows may also contain residues of SU-8 resist leaving a rough texture on the substrate. The slight roundness of the EBL SU-8 seeds, along with the small divergence  $\Delta\alpha$  of the vapour incidence angle, is responsible for the shadows behind the seeds being tapered rather than rectangular.

The shadow pattern confirms the ability of the seeds to selectively intercept the impinging vapour, and further confirms that GLAD nucleation and growth are driven by geometrical shadowing and suppression of surface and bulk diffusion. In fact, a voided, columnar zone 1 film structure is visible in the inter-seed film growth even after 15 nm of deposition. The complete absence of a gradual, penumbral region between the shadows and the inter-seed GLAD films further indicates that the adatom diffusion length is very small. This is hardly surprising, as the short deposition times for these very thin GLAD films limit the amount of radiant substrate heating from the hot vapour source.

Apart from having prevented film growth in the shadows behind the seeds, the other immediate effect of the seed layer is that nucleation and initial film growth happens faster on the seeds than on the bare substrate between the seeds, as they capture all the incident vapour that would normally have landed in the umbrae. Consequently, even though the seed layer does not completely prevent film growth on the bare substrate between seeds, a thicker layer of material is deposited on the seeds than on the surrounding bare substrate. This is apparent in figure 6.1 and is the origin of a column on each seed. The faster film accumulation adds to the initial height of the seeds, and the preferential seed-based column growth process thus becomes self-reinforcing. Undesired inter-seed film growth on the bare substrate may continue to accumulate thickness on its own, until being extinguished by shadows cast by the seeded columns.

Figure 6.2 provides a detailed view of one seed from figure 6.1c, i.e., after 45 nm of silicon GLAD growth. The preferential film growth on the seed is prominent, but much silicon has also deposited on the front sidewall of the seed, above the edge of the preceding shadow. For a vapour incidence angle  $\alpha$  of  $84^\circ$ , the SU-8 seeds used were barely tall enough to cast shadows sufficiently long to cover the entire diagonal direction of a 1000 nm period tetragonal lattice, and extensive side wall film accumulation is therefore not surprising. It should also be noted how the deposited film looks denser on the front side of the seeds, where the local vapour incidence angle is less than the substrate tilt angle of  $84^\circ$ . Finally, the silicon film growth on the very top of the seed in figure 6.2 appears to consist of microcolumns or fibres

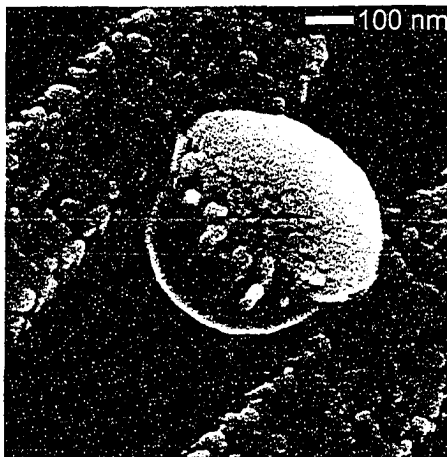


Figure 6.2: Close-up view of the nucleation and initial film growth of silicon on a seed from figure 6.1c. Note the voided, columnar film structure on the top surface of the seed and on the substrate.

approximately 30 nm wide. This fine structure is a general characteristic of GLAD silicon films, and will be exploited to create quite unique film structures in chapter 10.

In similar nucleation experiments performed on substrate seed layers with non-circular seed shapes, no changes in the film nucleation and growth were observed. The exact planar seed shape thus appears to be of little importance.

### 6.2.3 Column Growth

As film growth continues, one column evolves from each seed while growth between seeds is terminated. For the first few hundred nanometres of periodic film growth a transition phase is often seen in which the seeded columns attain a state of equilibrium. This transitional phase lasts at least until inter-seed film growth dies out.

Figure 6.3 visualizes the growth of periodic GLAD columns. While highly undesirable, it depicts what happens when a piece of ‘junk’ – either a large cluster ejected from the melt or contaminant from within the PVD chamber – lands on the substrate before or during growth, leaving large shadowed areas with subdued film growth. For this film the seed layer was a DWDL tetragonal pattern with a lattice period of 800 nm, amplified by a 100 nm vertical post GLAD film to produce a seed width of 440 nm (similar

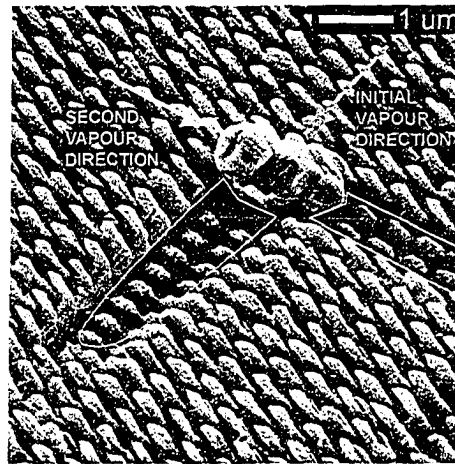


Figure 6.3: Oblique view of a 540 nm thick periodic square spiral GLAD film on an 800 nm period DWDL seed layer. The unintentional contaminant cluster has cast large shadows, leaving a region of bare seeds with no GLAD growth (blue area), and a region of stunted columns equivalent to 270 nm of growth (yellow area).

to figure 5.18 in chapter 5). One half square spiral of pitch 1080 nm was grown, equivalent to a stack of two perpendicular slanted posts of height 270 nm each. In the region enclosed by the blue line, seeds with no noticeable accumulation of silicon are visible. These seeds were deep inside the shadow of the piece of contaminant during the initial film nucleation phase, and received neither incoming vapour nor diffused adatoms (the roughness of the seeds is an artifact of the seed amplification step). Consequently, GLAD columns never evolved off these seeds. Meanwhile, the region enclosed by the yellow line did receive vapour during the initial nucleation and growth phase, but when the substrate was rotated to create the first corner in the square spiral, this region of the substrate fell into the shadow of the piece of junk. Further growth was then stunted, leaving the columns as short slanted posts. The figure thus shows three stages of periodic GLAD growth in one image.

Clearly, the seed layer has managed to enforce a periodic structure in the GLAD film, with one column growing off each seed. There is no significant impact from film growth in-between seeds, but in the yellow region some broadening of the first segment of the square spirals is evident. This is the initial, transitional phase of periodic growth. After the first 90° substrate rotation the second GLAD column segments use the oblong apices of the

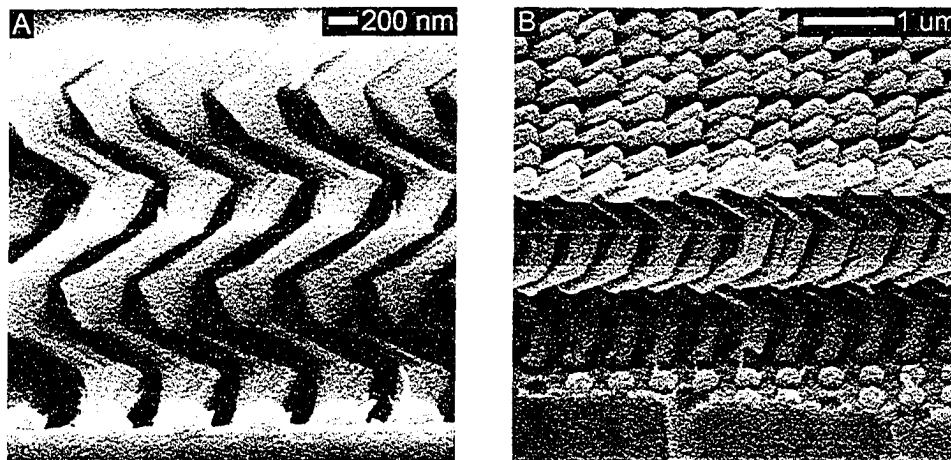


Figure 6.4: a) Side and b) oblique views of a periodic two-turn square spiral GLAD film on a 600 nm period layer of amplified EBL SU-8 seeds. The GLAD film has fully conformed to the seed layer, with limited inter-seed growth visible between the seeds.

first column segments as de facto ‘seeds’ for further column growth, and with the apices being narrower than the initial substrate seeds, the second spiral segments appear slimmer and less broadened. Indeed, since periodic GLAD growth fundamentally amounts to translating and extruding the seed layer pattern from the substrate plane to the third dimension perpendicular to the substrate, shadowing among the growing columns is as important as shadowing among seeds, and impacts the eventual column shape.

Figure 6.4 depicts a thicker, two-turn square spiral periodic GLAD film on a 600 nm period amplified EBL SU-8 seed layer. Again, the columnar microstructure conforms perfectly to the seed layer topography, with the top of the GLAD film in figure 6.4b having the exact same tetragonal geometry and lattice period as the substrate seed layer. The GLAD film initially nucleated preferentially – though not exclusively – on the seeds, and once film growth between the seeds died out, all subsequent growth was in the form of periodically arranged columns with a column width close to the seed width. The inter-seed film growth resulted in a layer of silicon a few tens of nanometres thick, visible where some of the seeds detached during substrate cleaving. In these images, the fibrous sub columnar fine structure of silicon GLAD films (noted already in the nucleation step in figure 6.2) may be discerned. No shadows are visible on the substrate in figure 6.4 (unlike in figure 6.1), since rotation of the substrate gradually filled in the

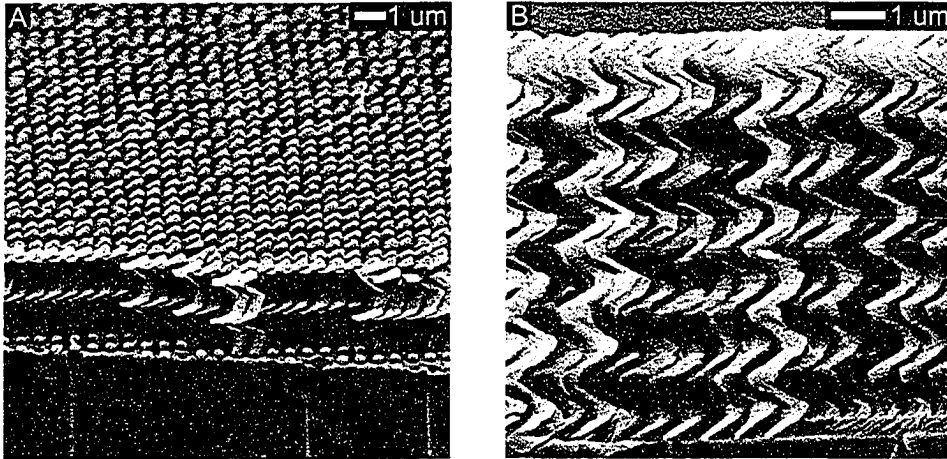


Figure 6.5: a) Oblique view of the GLAD film from figure 6.4, illustrating long-range periodicity. b) Side view of a  $7.9 \mu\text{m}$  thick square spiral GLAD film, whose periodic structure is maintained from the substrate to the top of the film.

initially shaded regions on the substrate. Figure 6.5a illustrates the long range lateral periodicity of the GLAD film shown in figure 6.4.

Periodic film growth can continue indefinitely if a good seed layer that matches the film mean volume density is used. Figure 6.5b shows a  $7.9 \mu\text{m}$  thick film of 6.25 square spiral turns on a  $600 \text{ nm}$  period EBL SU-8 seed layer. Although the large depth-of-field of SEM imaging obscures the figure somewhat, it can be appreciated that the lateral periodicity enforced by the seed layer is maintained all the way from the substrate to the top of the film. At the bottom centre of the image a few SU-8 seeds are visible, with one GLAD column growing off each seed. The regular turning of the substrate adds periodicity normal to the substrate through the square spirals, and with periodicity in all three dimensions, the basis for employing GLAD films as photonic crystals is in place.

#### 6.2.4 Suppression of Inter-Seed Growth

In all examples of periodic GLAD film growth discussed so far, some film growth has occurred on the substrate between the seeds. Rapid quenching of this inter-seed growth is critical to successful evolution of the desired periodic film structure. However, the fact that the seeded columns nucleate and grow faster than the inter-seed film may not in itself be sufficient to suppress the

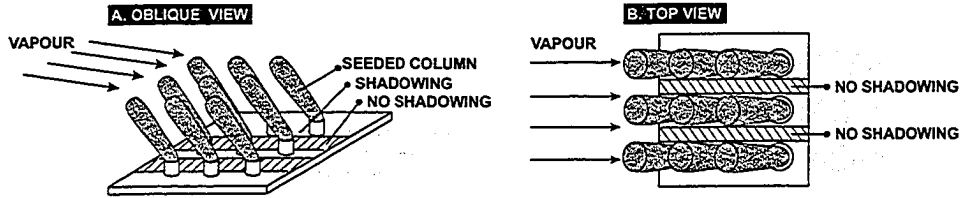


Figure 6.6: Schematic drawings of GLAD growth of slanted posts on a tetragonal lattice. If the vapour incidence direction is parallel to one of the lattice unit vectors, aperiodic film growth can proceed unhindered between the seeds.

inter-seed growth, as one must also consider the match between the seed lattice geometry and the GLAD column structure. For example, consider a slanted post GLAD film deposited on a tetragonal seed layer (i.e., the substrate is kept at a constant  $\phi$  value and is not rotated). If the vapour arrival direction is perfectly aligned with one of the lattice unit vectors in the seed lattice, as shown in figure 6.6, no shadowing occurs between the seeds along lines parallel to the vapour arrival direction. Along these lines, vapour will nucleate randomly and accumulate unhindered, yielding a GLAD film consisting of intermittent periodic and aperiodic growth.

Aperiodic inter-seed film growth may be suppressed in the following four ways:

- Ensuring that the vapour arrival directions  $\phi$  do not coincide with the seed lattice unit vectors.
- Using hexagonal seed layer geometries with seed widths  $d$  larger than the seed edge-to-edge separation  $s$ , ensuring mutual seed overlap in all directions.
- Using advanced growth modes (treated in chapters 7 and 10).
- Using a film column structure for which the substrate is frequently rotated.

Thus, to get a truly periodic slanted post film in figure 6.6, the substrate should be turned away from the tetragonal unit vectors, or a hexagonal lattice geometry should be used instead. The chosen inter-seed suppression mechanisms must be in place at least during the initial nucleation stages of the film deposition.

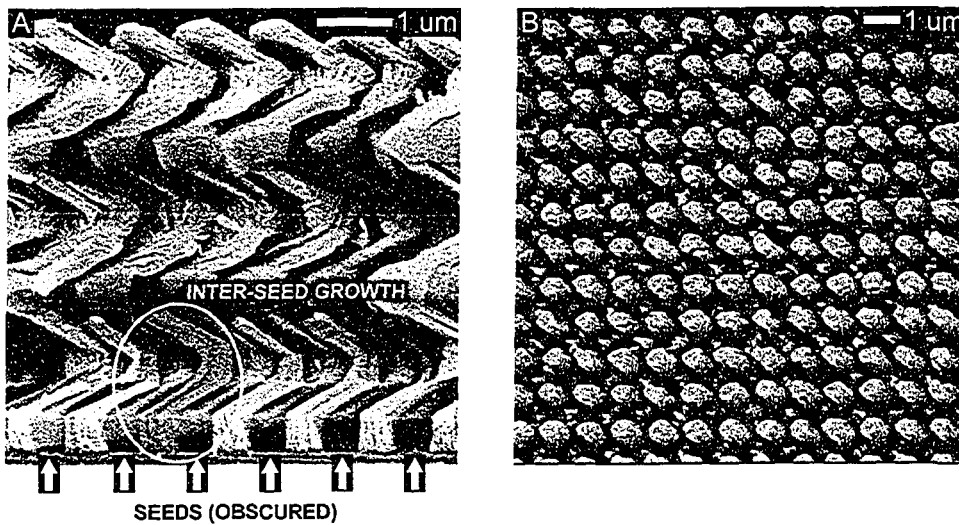


Figure 6.7: a) In this square spiral GLAD film on a tetragonal seed layer, unintentional growth between seeds (one example highlighted) occurred because the initial vapour flux incidence direction was parallel to one of the seed lattice unit vectors. The seeds are obscured by the film, but are indicated by arrows. b) Top view of a similar but only one-turn thick square spiral film, with small inter-seed columns present among the seed-enforced columns.

Figure 6.7a shows a square spiral film on a tetragonal SU-8 seed layer, where the inter-seed growth was terminated after four turns of the substrate. Had the substrate been turned more frequently, the inter-seed growth would have been eliminated earlier. Figure 6.7b is a top down view of an identical square spiral film, which after one spiral turn also shows remaining, but weakening, inter-seed columns between the intended, seed-nucleated columns. GLAD films with vertical post or helical column structures can be expected to maintain periodicity on any seed layer geometry, since they involve continuous rotation.

### 6.2.5 Impact of Seed Layer Design

Satisfactory evolution of periodic GLAD films, as in figure 6.4, depends critically on the seed layer design, and it is essential that the previously derived design rules be adhered to. The seed layer lattice geometry is usually dictated by the eventual application of the periodic GLAD film, but as just mentioned, hexagonal seed geometries are superior for suppressing inter-seed

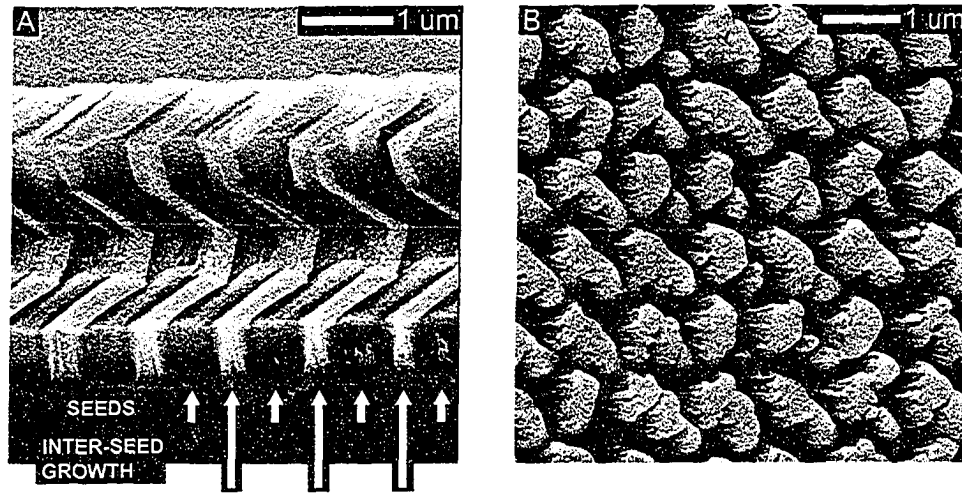


Figure 6.8: a) Side view of a 1.5 turn square spiral GLAD film. The low aspect ratio seeds (visible at lower right) were unable to suppress inter-seed nucleation, leading to growth of inter-seed columns. b) Top view of the same film, showing degradation of film periodicity and uniformity.

film growth. Obviously, if the seed lattice period is too large, the shadow from one seed may not extend all the way to the next seed.

Even more important are the seed height  $h$  and seed sidewall inclination angle (or the aspect ratio of the seeds) because these two parameters determine the selectivity of initial nucleation on the seeds. If the seeds are too shallow or have sloping sides, the ability to extinguish any inter-seed growth is reduced – with the worst case scenario being the incident vapour just smoothly covering the entire substrate – resulting in partial or full loss of film periodicity. The effect of this is shown in figure 6.8, which depicts a 1.5 turn square spiral GLAD film on an EBL SU-8 seed layer with a period of 1000 nm and a seed width of 700 nm. The relatively high seed layer planar fill factor  $ff_{A,seeds}$  of 0.38 is not problematic in itself, but it does amplify the proximity effects in the SU-8 resist during pattern exposure, leading to shallower and rounder seeds. This is evident on the bottom right of figure 6.8a, where the substrate cleave sliced through various segments of a few seeds. The rest of figure 6.8a reveals how these flat, rounded seeds failed to suppress the initial inter-seed film nucleation, which wound up evolving into separate columns growing unimpeded alongside the intended, seed-induced columns. A top view of the film is depicted in figure 6.8b. Some structural periodicity appears present, but as a whole the film is useless.

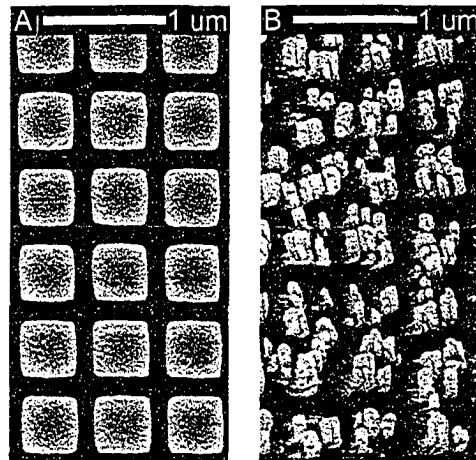


Figure 6.9: a) PMMA seed layer with a large seed layer planar fill factor of 0.6. b) Unsuccessful attempt to grow a periodic GLAD film on this seed layer. Because of the large seed width, several GLAD columns have nucleated on and grown off each seed, resulting in a film morphology that is neither periodic nor uniform. The two images have identical magnification and show the same area of the substrate.

The seed width  $d$  is also an important parameter for successful periodic nucleation. As discussed in chapter 3, at the high vapour incidence angles associated with the GLAD process, some materials tend to form columns with specific diameters in accordance with the mechanical and crystallographic properties of the materials. This is also seen in aperiodic GLAD films on smooth substrates, where the distribution of column diameters becomes constant after a certain film thickness is reached [131,150]. If the seed width is larger than the natural column diameter of the evaporant, multiple columns will originate from each seed. An example of this is shown in figure 6.9, where it was attempted to grow a silicon square spiral GLAD film on a tetragonal seed layer with a large planar fill factor. Conversely, if the planar fill factor of the seed layer is smaller than the planar volume density of the GLAD film, excessive broadening of the seeded columns may occur.

The impact of seed layer design on periodic GLAD growth was further investigated using computer simulations, in collaboration with Dr. T. Smy of Carleton University. His 3D-FILMS simulator models glancing angle deposition (and other thin film deposition processes) by dividing the space above the substrate surface into a fine, three dimensional grid of cubes. Deposition vapour is modelled as filled cubes – each representing a cluster of thousands

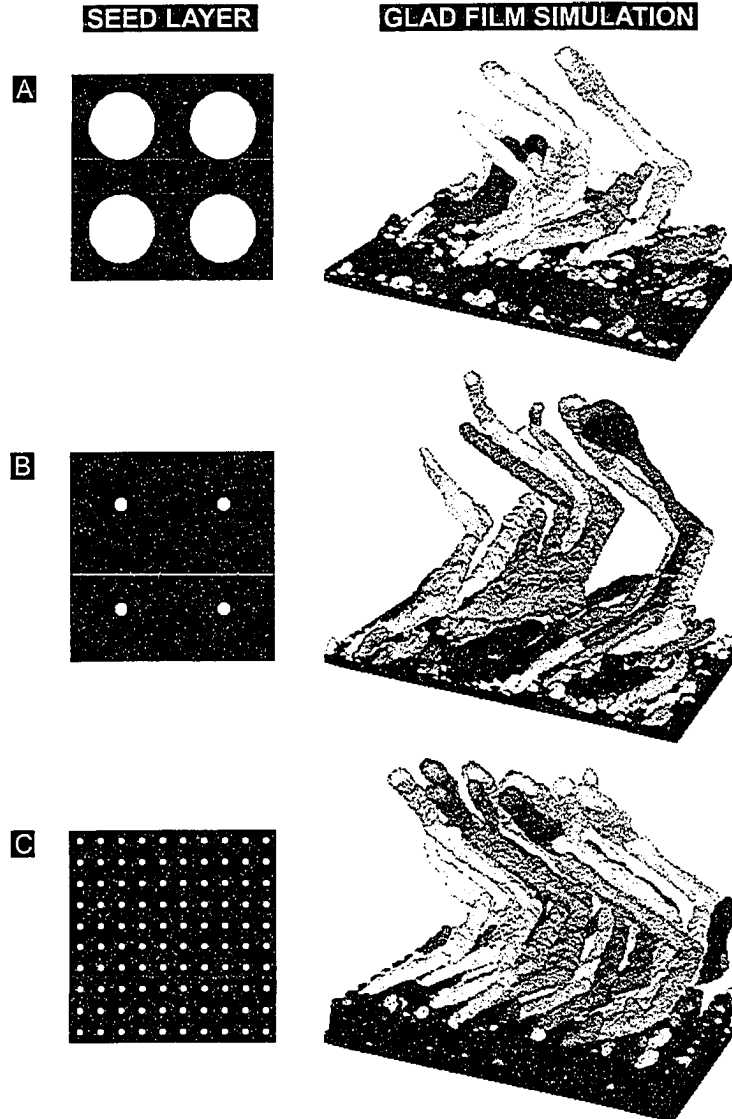


Figure 6.10: 3D-FILMS simulations of periodic square spiral GLAD growth. a) Seed width too large, resulting in several columns nucleating on each seed. b) Seed planar fill factor too small, causing severe inter-seed growth and loss of film periodicity. c) Appropriate seed layer fill factor yielding a uniform film with only modest column broadening.

of vapour atoms – which impinge onto the substrate along straight trajectories, and then settle somewhere in the grid in accordance with the three thin film growth mechanisms. The program accounts for advanced growth effects such as adatom mobility, grain boundary grooving, substrate temperature, and crystal faceting [141].

Figure 6.10 shows three 3D-FILMS simulations of silicon square spiral GLAD film growth on seeded substrates. The vapour incidence angle  $\alpha$  was set to  $85^\circ$  with a angular cone-shaped spread of  $\pm 1^\circ$ , and one complete helical turn with a pitch of 1000 nm was simulated. In figure 6.10a the seed width  $d$  was intentionally set high, at 750 nm, which resulted in several GLAD columns growing off of each seed (note that for clarity not all of the columns near the edges are shown). In figure 6.10b the seed width was reduced to a more reasonable value of 100 nm, but the seed lattice was retained at the previous 750 nm, yielding a low seed planar fill factor  $ff_{A,seeds}$  of 0.014. Not surprisingly, the result is an all but periodic GLAD film, with severe inter-seed growth overwhelming column formation on the actual seeds. Column bifurcation and broadening is also seen. Finally, figure 6.10c shows a simulation using a much better seed planar fill factor of 0.35, based on a lattice period of 150 nm and a seed width of 100 nm. The square spiral film is much more uniform here, with one column on each seed, and only modest column broadening and bifurcation. The simulations thus confirm the previous conclusions on substrate seed layer design.

### 6.3 Characteristics of Periodic GLAD Films

Periodic GLAD films deposited on substrate seed layers have a much more uniform film morphology and significantly better characteristics than randomly nucleated aperiodic GLAD films. Side-by-side comparisons of aperiodic and periodic GLAD film growth are provided in figures 6.11 to 6.13. To ensure that all other variables were kept constant, several GLAD depositions were performed on substrates with both seeded and smooth regions, and sections of both regions were imaged at the same time. In the case of figure 6.11, a  $4.0\ \mu\text{m}$  thick, 3 turn square spiral GLAD film was grown partly on a 1000 nm period SU-8 seed layer; in figures 6.12 and 6.13, a  $2.6\ \mu\text{m}$  thick, 2 turn square spiral film was deposited partly on an amplified SU-8 seed layer with a period of 600 nm.

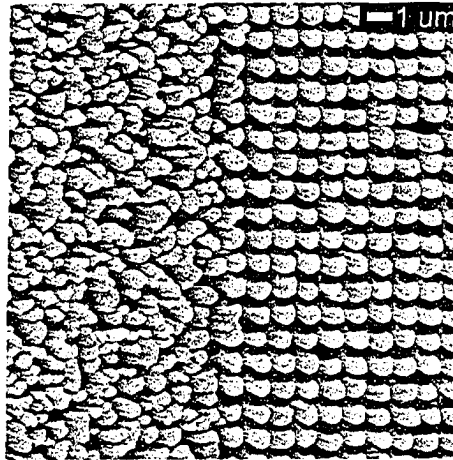


Figure 6.11: Top view image comparing aperiodic and periodic GLAD film growth on the same substrate. The film is a  $4.0 \mu\text{m}$  thick square spiral film on a  $1000 \text{ nm}$  period tetragonal seed layer. The periodically structured GLAD film is much more uniform than the randomly nucleated film, with the columns appearing congruent.

### 6.3.1 Film Uniformity

The first observation to be made from figures 6.11 to 6.13 is the greater overall uniformity of periodic GLAD films compared with aperiodic films. The periodic film structure regularly repeats itself in all directions, both parallel and perpendicular to the substrate, and the seed layer planar fill factor appears to have been appropriate for the given square spiral GLAD depositions. A complete, tetragonal lattice of columns remains intact even after several micrometres of growth, evidencing that no column extinction has occurred, as is otherwise a common occurrence in non-seeded GLAD films (cf. section 3.3.3). The symmetry of the seed layer has been translated into uniformity of the film morphology throughout the periodic films. In consequence, uniformity has been induced in all properties depending on the column spacing, including the local film mean density, the porosity or void size, optical scattering in the plane of the substrate, and transport and absorption of fluids.

Neither periodic nor aperiodic GLAD are isotropic, homogeneous materials, but periodic GLAD is pseudo-isotropic in the sense that any local, micrometre sized region anywhere in the film looks the same and has the

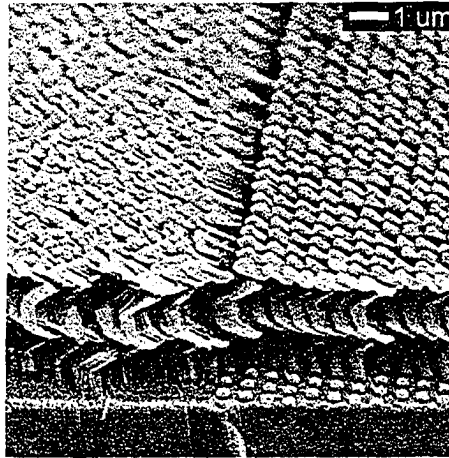


Figure 6.12: Oblique view image of aperiodic and periodic GLAD film growth on the same substrate. The film is a  $2.6 \mu\text{m}$  thick square spiral film deposited on a  $600 \text{ nm}$  period amplified, tetragonal SU-8 seed layer. The periodic film exhibits much less column broadening than the aperiodic film, which consists of more numerous, thinner columns.

same properties, whereas aperiodic GLAD films vary dramatically from close to the substrate to the top of the films, and from one horizontal location to the next. The greater uniformity of periodic GLAD films also manifests itself in the periodic columns being nearly congruent, in contrast to the aperiodic columns possessing a spread in shape and size. Among the seeded GLAD columns in figures 6.11 to 6.13 the column width is nearly constant, whereas the randomly nucleated film contains a wide distribution of different column widths. Coupled with the much higher number of columns on the aperiodic side, this points to the aperiodic columns being more susceptible to competition and extinction. The aperiodic columns come in a variety of anisotropic shapes, and while most of the aperiodic columns are thinner than the periodic columns, some columns have merged to form oblong column clusters.

The film thickness is always observed to be constant over both seeded and smooth regions of a substrate – as in figure 6.13 – and since the same amount of vapour hits the substrate irrespective of the substrate topography, this implies that the overall film mean density  $\rho_{GLAD}$  must be the same in periodic and aperiodic GLAD films.

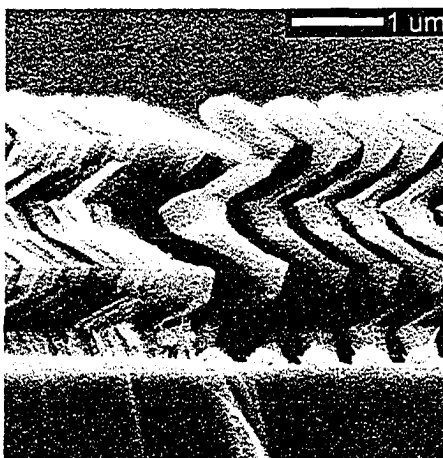


Figure 6.13: Side view image of the same square spiral film as in figure 6.12. The width of the periodic columns is nearly constant from the substrate all the way to the top of the film, and no column bifurcation is seen. Note that the film thickness is the same for both the periodic and the aperiodic film.

### 6.3.2 Column Uniformity

Next to be noticed from comparing periodic and aperiodic GLAD films is the structure of individual periodic columns, and their internal, vertical uniformity as they wind their way from the substrate to the top of the film. The oblique and side views in figures 6.12 and 6.13 reveal that the width of periodic columns remains constant throughout the thickness of the film, from the substrate to the top of the film, whereas the aperiodic GLAD columns change morphology from thin, fibrous columns at the substrate to increasingly fewer and broader columns as the film gets thicker. The more uniform column structure in the periodic GLAD film is a benefit of the absence of column broadening – i.e., general fattening of columns as opposed to cross-sectional fanning – as well as the absence of column bifurcation or merging, which represent the branching of one column into several smaller posts growing in parallel, or the merger of smaller columns into one.

Column broadening was previously discussed in section 3.3.3, and is a familiar phenomenon in aperiodic GLAD films [130, 131]. However, it is generally undesirable, since a wider distribution in pore and column sizes leads to a spread in the optical, electrical, fluidic or other response of the film. While overall column broadening is strongly reduced in periodic GLAD films, it is alleviated only in the sense that it does not lead to column competition.

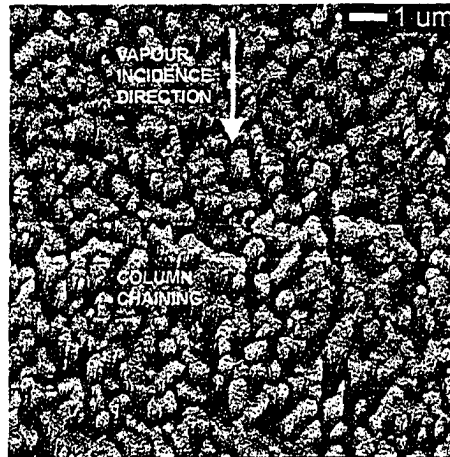


Figure 6.14: Top view of an aperiodic GLAD square spiral film, illustrating column chaining (some examples highlighted) as columns link up preferentially in a direction normal to the deposition plane (represented here by the vapour incidence direction  $\phi$ ). Column chaining is completely eliminated in periodic GLAD films (cf. figure 6.11).

Within each square spiral arm segment some broadening still occurs, as can be noted in both figure 6.12 and 6.13. Each corner in the square spiral resets this broadening process. Arm segment and column broadening will be discussed further in chapters 7 and 10.

Column bifurcation arises either in place of broadening for materials with a small, natural column diameter, or as a distinct side effect of the substrate rotation required to achieve an intended column shape. Column merger can replace broadening for materials with larger, natural column diameters, as in the present case of silicon. In the periodically structured GLAD films in figures 6.11 to 6.13 neither bifurcation or merger are observed.

### 6.3.3 Elimination of Column Chaining

When GLAD is performed on a smooth substrate, and nucleation occurs at random locations to yield a random distribution of columns, the highly anisotropic vapour impingement ensures strong geometrical shadowing along the vapour arrival direction, but only at the expense of a complete lack of shadowing among columns in the direction normal to the deposition plane [106, 131, 187]. This non-uniformity in shadowing leads to two kinds of structural anisotropy, which are much more pronounced in polygonal helical

than circular helical GLAD films, due to the smoother averaging of vapour incidence in circular helical films. First, the individual columns broaden normal to the deposition plane, and assume an oblong or fan shaped cross-section. This is a key issue in using GLAD to fabricate square spiral photonic crystals, and will be covered in the next chapter. Secondly, the randomly oriented columns may chain together normal to the deposition plane to generate a scale or flake-like overall film structure. This effect is highlighted in figure 6.14 for an aperiodic square spiral film.

Column chaining adds another level of structural anisotropy to the inherent non-uniformity of GLAD films already caused by the column tilt and high porosity, and thus plays a role in the resulting anisotropy of the thin film properties, including optical anisotropy [102], magnetic anisotropy [103–105], and electrical anisotropy [222]. For this reason, column chaining has been studied and modelled extensively for oblique vapour deposition [106, 108, 109].

Comparing figure 6.14 with figure 6.11 shows that periodic GLAD completely eliminates column chaining, thus negating many of the anisotropic effects inherent in the characteristics of GLAD films. The stifling of column chaining arises as the seed lattice period imposes a fixed and constant separation of the columns, and works only as long as the lattice period is larger than the natural width of the columns for the given vapour incidence angle  $\alpha$ .

### 6.3.4 Suppression of Column Competition

The uniform overall morphology of periodically structured GLAD films, as well as the absence of column bifurcation and broadening, all derive from suppression of the competition among growing columns that is normally seen in aperiodic GLAD films. As discussed in section 3.3.3, column competition is a result of growth instability associated with the highly oblique vapour incidence angles and extreme geometrical shadowing of GLAD. As columns randomly broaden in one direction, they immediately impact the growth of any downstream columns suddenly falling into the new, larger shadow. Column broadening, competition, and extinction is evident in, for example, figures 3.5 and 3.13.

Growth instability is inherent to the GLAD process, including periodic GLAD. But when random column nucleation is replaced with symmetric, seed layer enforced nucleation, all columns start out with the same width and with the same spacing. Since column competition depends on how unevenly sized the columns are, the seed induced symmetry preempts the onset of

competition to the point where it can be delayed indefinitely, resulting in highly uniform film morphologies and columns.

The structural benefits of periodic GLAD are realized only when the seed layer design rules of chapter 5 are followed, and the best results are achieved when highly symmetric seed patterns such as tetragonal or hexagonal lattices are employed. Of particular importance is matching the seed layer planar fill factor  $ff_{A,seeds}$  to the GLAD film volume fill factor  $ff_{V,GLAD}$ , and accounting for material specific behaviour such as natural column widths and surface diffusion lengths.

Considering the periodic and aperiodic sides of figure 6.11, one might wonder what happens to the vapour incident *between* columns in a periodic, tetragonal array of columns once inter-seed growth has been terminated. In aperiodic GLAD films the random distribution of columns ensures complete interception of all incoming vapour, but in periodic GLAD films the vapour arriving along the empty rows between columns has nowhere useful to go. In fact, some of this ‘excess’ vapour contributes to arm segment broadening and arm cross-sectional fanning, requiring more advanced GLAD growth algorithms to be employed as described in chapter 7. In square spiral structures, some of the vapour also lands on the preceding spiral arm segment, which is now perpendicular to the deposition plane, leading to column bifurcation. Most of the vapour, however, disperses deeper inside the GLAD film.

### 6.3.5 Film Structure Control

Substrate seed layers provide one of the few ways to make the column width, column distribution, and void size *controllable*. In aperiodic GLAD, only the vapour incidence angle  $\alpha$  has influence on the widths of the columns and the size and distribution of the voids between columns, for a given material. However, neither a large spread in column widths nor vertical variation due to broadening can be avoided, the control afforded by  $\alpha$  is weak, and as  $\alpha$  is changed, so is the column inclination angle  $\beta$  and the film density  $\rho_{GLAD}$ .

In periodic GLAD, on the other hand, the column width and the void size can be set by the seed layer and maintained at constant values throughout the film, without affecting the film density given by the vapour incidence angle  $\alpha$ . The use of seed layers therefore not only improves the overall film and column quality, but also provides much needed control and reproducibility of the film morphology. Chapter 10 will present thesis research leading to the development of another approach to film porosity engineering, relying on advanced substrate rotation rather than substrate seeding.

No Text

## Chapter 7

# Bandgap Engineering: Square Spiral PBC Fabrication

Whereas chapter 6 examined the general advantages and challenges of periodic GLAD films, this chapter focuses on periodic square spiral GLAD films for PBC fabrication. The experimental details and design considerations for GLAD PBCs are discussed, and bandgap engineering of high frequency GLAD PBCs is established through down-scaling of the spiral dimensions. Down-scaling, however, compounds the significant structural problems already inherent in square spiral deposition by traditional GLAD growth methods. Following an analysis of these problems, new advanced GLAD growth algorithms are therefore developed to approach the ideal square spiral structure and provide better morphological control over the GLAD films. The new GLAD structures are necessary to facilitate bandgap engineering in smaller structures, reduce disorder and enhance the optical properties, and improve the characteristics of periodic GLAD films for all other applications.

The thesis research presented in this chapter has partly been published in Applied Physics A [223] with further publication in progress.

### 7.1 GLAD PBC Design Considerations

The first step in bandgap engineering of GLAD PBCs is identifying what square spiral dimensions and consequent GLAD deposition parameters are required to achieve a given photonic bandgap, and specifically to achieve a

lower bandgap centre wavelength than the previously published  $2.7 \mu\text{m}$  [188]. The starting point for these design considerations are the theoretical computations discussed in chapter 4, which show that for the direct, first nearest neighbour square spiral PBC structure to generate a complete bandgap at a central wavelength  $\lambda_{\text{centre}}$ , the tetragonal lattice period and dielectric volume fill factor should be [181]:

$$\Delta = 0.36\lambda_{\text{centre}}, \quad (7.1)$$

$$ff_V = 0.31. \quad (7.2)$$

Note that for photonic crystals in general, and square spirals in particular, the dielectric fill factor is as important as the dimensions given by  $\Delta$  in determining the exact bandgap position.

The lattice period  $\Delta$  directly dictates the period of the required tetragonal seed layer, while  $ff_V$  dictates the target volume fill factor  $ff_{V, \text{GLAD}}$  of the GLAD film. Together, and in accordance with equation 5.6 of the seed layer design rules developed in chapter 5,  $\Delta$  and  $ff_V$  also determine the required seed width  $d$  and minimum height  $h$ , as the seed layer planar density must match the volume density of the GLAD film. This fully specifies the necessary seed layer as a function of  $\lambda_{\text{centre}}$ . Further to the computations by Toader and John, the dimensions of the square spiral horizontal side length  $L$ , pitch  $p$ , and arm width  $w$  should scale with the lattice period as follows (for the case of circular cross-section square spirals) [181]:

$$L = 0.70\Delta, \quad (7.3)$$

$$p = 1.35\Delta, \quad (7.4)$$

$$w = 0.40\Delta. \quad (7.5)$$

These dimensions exactly add up to a volume fill factor of 0.31, but as the arm width  $w$  is defined relative to the arm central axis, not the substrate normal,  $w$  is not identical to the required seed width  $d$ .

The required column inclination angle  $\beta$  in the GLAD film can be computed from the square spiral pitch  $p$  and side length  $L$  as:

$$\begin{aligned} \tan(90^\circ - \beta) &= \frac{p}{4L} \Rightarrow \\ \beta &= 90^\circ - \arctan(p/4L) = 90^\circ - \arctan(1.35\Delta/4 \cdot 0.70\Delta) = 64^\circ. \end{aligned} \quad (7.6)$$

With  $\beta$  in turn given by the GLAD substrate tilt  $\alpha$  (in accordance with Tait's Rule, see chapter 3), and the square spiral pitch  $p$  being equal to the

pitch provided by the GLAD substrate rotation axis  $\phi$ , the GLAD deposition parameters  $\alpha$  and  $p$  for a particular bandgap centre wavelength  $\lambda_{centre}$  can now be entirely specified.

In summing up, a bandgap at  $\lambda_{centre}$  requires the following GLAD seed layer and growth algorithm design (for circular cross-section square spirals):

$$\Delta_{seeds} = 0.36\lambda_{centre}, \quad (7.7)$$

$$ff_{A,seeds} = 0.31, \quad (7.8)$$

$$p_{GLAD} = 1.35 \cdot 0.36\lambda_{centre} = 0.49\lambda_{centre}, \quad (7.9)$$

$$\alpha_{GLAD} = \alpha_{GLAD}(\beta = 64^\circ). \quad (7.10)$$

Additionally, the size of the bandgap depends on the dielectric contrast  $n_c$  of the deposited GLAD film, which must be at least 2.15 for a bandgap to exist.

On closer inspection, however, the above design rules contain a hidden inconsistency. As discussed in chapter 3, the vapour incidence angle  $\alpha$  fundamentally defines both the volume fill factor  $ff_{V,GLAD}$  of a GLAD film *and* the column inclination angle  $\beta$ . In fact, Tait's Rule predicts that a column inclination angle of  $64^\circ$  cannot even be achieved! The basic GLAD process therefore cannot simultaneously address the design requirements for the crystal dielectric volume fill factor  $ff_V$  and the  $p/L$  ratio.

Relief from this dilemma is delivered by the robustness of the square spiral PBC architecture to deviations in the fill factor and especially in the spiral pitch  $p$ . Indeed, while the above fill factor and square spiral dimensions describe the *ideal* structure with an optimized bandgap of 14.8%, modelling results predict bandgaps larger than 10% for fill factors less than 0.2 and larger than 0.45, and almost no impact on bandgap location or size when the pitch is varied [181]. The design restrictions on  $p$  and hence  $\beta$  can therefore be relaxed, with focus remaining on optimizing the GLAD algorithms for the spiral side length  $L$  and width  $w$  for the given lattice period  $\Delta$ . Of course, this also means that the ideal square spiral structure is unattainable with GLAD, and that the theoretical bandgap calculations become indicative rather than exact. Even so, the modelled ideal dimensions are a good starting point for crystal design and engineering.

With the limitations of the GLAD process and the challenges of obtaining perfect square spiral structures – especially at the reduced dimensions targeted here for new, higher frequency GLAD PBCs – practical PBC bandgap engineering is best handled by first setting the seed layer lattice period  $\Delta$ , and then adjusting the vapour incidence angle  $\alpha$  and spiral pitch  $p$  through

$\Delta$ (nm)	$L$ ( $\mu\text{m}$ )	$p$ ( $\mu\text{m}$ )	$w$ ( $\mu\text{m}$ )	$\lambda_{ctr}$ ( $\mu\text{m}$ )	$\Delta\lambda$ (nm)
333	0.25	0.48	0.12	0.91	137
600	0.45	0.86	0.21	1.64	247
700	0.53	1.00	0.25	1.92	288
750	0.56	1.07	0.26	2.05	308
800	0.60	1.14	0.28	2.19	329
1000	0.75	1.43	0.35	2.74	411

Table 7.1: For GLAD PBC bandgap engineering, seed layers were designed with lattice periods  $\Delta$  between 333 and 1000 nm. The associated *ideal* square spiral dimensions  $L$ ,  $p$ , and  $w$  are listed, along with the predicted ideal bandgap location and bandgap size.

a number of GLAD deposition iterations until an optimal spiral structure as close to the theoretical ideal is obtained. The three available experimental parameters  $\Delta$ ,  $\alpha$ , and  $p$  then determine the optical properties of the final square spiral photonic crystal via the fill factor and the spiral dimensions.

## 7.2 Fabrication and Materials Considerations

### 7.2.1 Substrate Seed Layers

In pursuit of demonstrating GLAD PBC bandgap engineering by down-scaling the dimensions of square spiral GLAD films, a series of substrate seed layers with lattice periods  $\Delta$  less than 1  $\mu\text{m}$  was fabricated. Table 7.1 lists the lattice periods  $\Delta$  of the designed and fabricated seed layers, along with the associated *ideal* square spiral dimensions for a square spiral cross-section, and the theoretically predicted optimum bandgap centre wavelengths and bandgap widths. Seed layers with  $\Delta = 1000$  nm were fabricated for comparison.

Both EBL and LDWL were employed, with the latter being preferred for its ability to make wider area seed patterns for larger PBCs that are easier to characterize. EBL was performed on SU-8 resist, using the pixel-by-pixel approach described in section 5.5.1. For all seed layer designs tetragonal lattice geometries and circular seeds were used, with transparent substrates facilitating subsequent PBC transmittance measurements. As previously discussed, the seed layer planar fill factor  $ff_{A,seeds}$  need not strictly match that of the intended square spiral GLAD film. For slightly undersized seeds, GLAD growth is able to self-compensate by quickly broadening off the initial seeds.

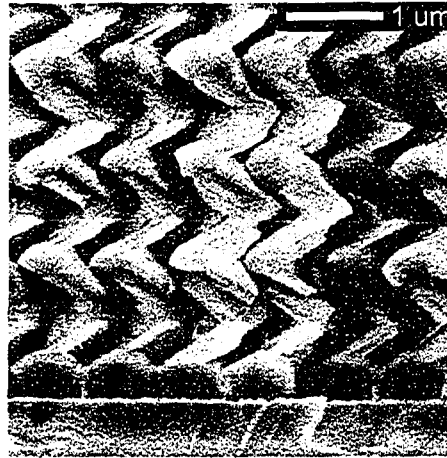


Figure 7.1: Square spiral GLAD film deposited on an 800 nm lattice period seed layer without seed amplification. The low aspect ratio of the seeds causes the GLAD columns to broaden right off the seeds, far from the ideal cylindrical or square shape desired for square spiral PBCs.

Although the intrinsic height of the fabricated EBL and LDWL seeds was sufficient to achieve complete shadowing between seeds, and hence induce periodic GLAD growth, experiments showed that amplified seeds provided better seeding for square spiral GLAD growth than bare seeds. Seed amplification was therefore used throughout. For LDWL seed layers in particular, the benefit derives from the increase in seed aspect ratio provided by the amplification. Figure 7.1 thus shows how square spirals deposited on bare, non-amplified seeds immediately emerge as wide, celery shaped columns, rather than round cylinders. The amplification was performed as short ‘vertical post’ GLAD depositions at  $\alpha \approx 86^\circ$  and with continuous fast substrate rotation, with total nominal thicknesses of 70 to 100 nm depending on the seed width. Thicker seed amplification as well as amplification by slanted posts was also attempted, but was found to be less successful.

### 7.2.2 Materials

Throughout this thesis the material used for GLAD PBC deposition is silicon, which is a superior medium both optically and morphologically. In the wavelength range of interest, i.e., 1.5 to 2.5  $\mu\text{m}$ , it has a large real part of the permittivity of around 11.9 (the listed value for amorphous silicon at 2.0  $\mu\text{m}$ ) [224], which in an air-filled crystal provides a high dielectric contrast:

$$n_c = \frac{n_{\text{dielectric}}}{n_{\text{air}}} = \frac{\sqrt{\epsilon_{\text{Si}}}}{1} = \sqrt{\epsilon_{\text{Si}}} = \sqrt{11.9} = 3.45. \quad (7.11)$$

This contrast is well above the minimum of 2.15 required for a square spiral bandgap, and yields a large gap of 15%. At the same time, silicon has low absorption losses, due to a negligible imaginary part of the permittivity of less than  $10^{-3}$  (making the real expression  $n = \sqrt{\epsilon}$  true) [224]. The absence of absorption is critical for achieving a useful PBC with high transmittance outside the gap.

In the range of interest the permittivity of silicon is almost constant, with only a slight and monotonic increase with frequency. As the wavelength approaches  $1.11 \mu\text{m}$ , however, the imaginary part of the permittivity increases rapidly and silicon becomes absorptive and opaque. This edge is associated with the 1.12 eV electronic bandgap in silicon, which allows for free carrier generation via absorption of photons. Silicon is therefore not relevant as a PBC material for bandgaps located below  $1.11 \mu\text{m}$ . This would include PBCs made on the 333 nm period seed layer in table 7.1, which is included only for studying the scaling behaviour of silicon GLAD films.

In addition to its optical advantages, silicon is a good material for GLAD deposition. It forms a relatively stable evaporant during PVD, and provides high deposition rates. As already seen in chapter 6, silicon generates well-defined film microstructures with column widths spanning sub 100 nm to several hundred nanometres, and with a fibrous sub columnar structure. GLAD deposited silicon is amorphous with no faceting (a TEM crystallographic analysis is provided in chapter 10), but can be annealed to introduce some crystallinity.

One problem with the use of silicon is that oxygen is incorporated during deposition, due to residual ambient gases in the deposition chambers. Further native oxidation occurs as soon as the films are exposed to atmosphere. Rather than pure (amorphous) silicon, the GLAD square spirals thus consist of a mixture of silicon and silicon oxide. This is evident from energy dispersive x-ray spectra, as discussed in chapter 10. While assuming that the oxygen is bound as silicon dioxide, a previous analysis on silicon GLAD films yielded an estimated  $\text{SiO}_2$  content of 8% [188]. Using effective medium theory [225]:

$$\epsilon_{\text{eff}} = \sum_i f_i \epsilon_i, \quad (7.12)$$

where  $f_i$  is the volume fill factor and  $\epsilon_i$  the bulk dielectric constant for each constituent, a more accurate value for the dielectric constant of the silicon/silicon dioxide square spirals can now be calculated:

$$\epsilon_{eff}(\text{GLAD Si}) = f_{SiO_2}\epsilon_{SiO_2} + f_{Si}\epsilon_{Si} = 0.08 \cdot 2.07 + 0.92 \cdot 11.9 = 11.1. \quad (7.13)$$

This reduces the dielectric contrast of the GLAD PBCs from 3.45 to:

$$n_c = \sqrt{\epsilon_{eff}(\text{GLAD Si})} = \sqrt{11.1} = 3.33, \quad (7.14)$$

which in turn reduces the maximum bandgap width from 15% to 14% and blueshifts the bandgap location. Ambient water absorption in the porous GLAD PBC films may further reduce the bandgap width by lowering the dielectric contrast.

Finally, effective medium theory can be used to provide an estimate of the bulk ‘DC’ permittivity of a GLAD PBC, in which the film is merely considered a homogeneous mixture of air and silicon square spirals. This value will prove useful in chapter 8. Assuming a GLAD film volume fill factor of 0.31, and using the SiO<sub>2</sub>-modified effective dielectric constant of the silicon square spirals, the GLAD PBC effective permittivity is:

$$\begin{aligned} \epsilon_{eff}(\text{GLAD PBC}) &= f_{V,GLAD}\epsilon_{eff}(\text{GLAD Si}) + f_{V,air}\epsilon_{air} \\ &= 0.31 \cdot 11.1 + 0.69 \cdot 1.00 = 4.13. \end{aligned} \quad (7.15)$$

### 7.2.3 Square Spiral GLAD Deposition

PBC fabrication was performed in three different but similarly configured electron beam evaporation GLAD PVD systems. In all systems the throw distance from the source melt to the GLAD substrate holder was 420 mm, and 12 mm wide evaporant crucible liners were employed. Assuming a typical substrate tilt angle  $\alpha$  of 85° and a 20 mm large seeded PBC substrate, the worst case angular spread  $\Delta\alpha$  of the evaporant onto the substrate is 0.94°. Although this value ignores small contributions from vapour collisions and reflections off the chamber walls, the spread is quite acceptable.

The deposition rate and accumulated film thickness were measured with a water cooled crystal thickness monitor (CTM) head mounted normal to the vapour source and connected to a Sycom STM-100 controller. For each deposition system a tooling factor accounted for the mismatch in accumulated film thickness between the CTM and the actual GLAD substrate caused by their geometrical separation. The GLAD substrate motion apparatus consisted of two Empire Magnetics vacuum compatible stepper motors mounted on an in-house constructed scaffold above the vapour source. Motor actuation was handled by a custom made controller, which in turn was interfaced to a computer running National Instruments’ LabView software. Film thick-

ness feedback from the CTM was also routed via the custom controller to LabView.

An in-house developed LabView program multiplied the normal incidence CTM deposition rate with an experimentally determined  $\alpha$  and material specific ratio to get the actual GLAD film deposition rate on the tilted substrate. This deposition rate was then used to drive a programmed algorithm of motor rotation commands to create the desired GLAD structure. The samples were aligned and the substrate chucks set to their initial  $\alpha$  and  $\phi$  values prior to the deposition, and since the current GLAD systems do not provide motor position feedback, the angular values were rechecked at the end of each deposition stage to detect any loss of alignment.

The GLAD systems were either diffusion or cryogenically pumped, with base and deposition pressures for the silicon depositions discussed here better than 0.2 and 0.4 mPa, respectively. These low pressures are required to minimize the amount of oxygen incorporation in the silicon. Typical electron beam voltages and currents were 9 kV and 150 to 200 mA, delivering deposition rates between 1 and 2 nm/s (at normal incidence). Other technological considerations pertaining to GLAD deposition were previously treated in chapter 3.

In the most basic form, the GLAD algorithm used to make square spirals consisted of four abrupt 90° turns at regular thickness increments for each complete winding of the square spiral structure. However, as the rest of this chapter will discuss, more advanced growth modes are required to fabricate GLAD square spiral films with a fine structure suitable for photonic crystals.

## 7.3 Scaling of Square Spiral GLAD Films

### 7.3.1 Growth Iterations

As mentioned above, the process of down-scaling the microstructure of square spiral GLAD films for high frequency PBCs involves iteratively adjusting the two relevant GLAD variables – substrate tilt  $\alpha$  and spiral pitch  $p$  – until the spiral side length  $L$  approaches the ideal dimensions for a desired gap centre frequency. The seed layer lattice period  $\Delta$  is chosen in accordance with the bandgap centre frequency but kept fixed during iterations.

Consider now this process for the case of  $\Delta = 700$  nm, which according to table 7.1 corresponds to the bandgap centre ideally being located at 1.92  $\mu\text{m}$  (for a square spiral arm cross-section). Figure 7.2 illustrates three iterations of GLAD square spiral growth on this seed layer. The GLAD parameters  $\alpha$  and  $p$  for each iteration are listed in table 7.2, along with the

Iter	$\alpha$ ( $^\circ$ )	$p$ ( $\mu\text{m}$ )	$p_r$	$L$ ( $\mu\text{m}$ )	$L_r$	$w$ ( $\mu\text{m}$ )	$w_r$
1	$84.0 \pm 0.2$	$0.99 \pm 0.01$	0.99	$0.37 \pm 0.04$	0.70	$0.20 \pm 0.06$	0.81
2	$84.0 \pm 0.2$	$1.07 \pm 0.01$	1.07	$0.40 \pm 0.03$	0.77	$0.19 \pm 0.06$	0.76
3	$86.0 \pm 0.2$	$0.93 \pm 0.01$	0.93	$0.46 \pm 0.03$	0.88	$0.20 \pm 0.06$	0.81

Table 7.2: For the three iterations of GLAD growth on 700 nm period seed layers shown in figure 7.2, this table lists the employed GLAD substrate tilt angle  $\alpha$  and helical growth pitch  $p$ , along with the resulting observed spiral dimensions  $L$  and  $w$ . Each of the three spiral dimensions are also expressed relative to the ideal  $\Delta = 700$  nm dimensions listed in table 7.1 (subscript ‘r’).

spiral dimensions measured off these and other SEM images. The dimensions relative to the ideal spiral arm dimensions in table 7.1 are also listed (denoted by subscript ‘r’). It must be noted that the observed spiral dimensions are somewhat uncertain, even when based on multiple measurements, for as amply displayed by figure 7.2 the spirals are not always well defined. This is especially true for the spiral arm width  $w$ .

The first iteration used the ideal square spiral pitch of  $1.00 \mu\text{m}$  as a starting point for the GLAD helix pitch  $p$ . However, as already discussed, GLAD delivers too small column inclination angles  $\beta$  to rely on  $p$  alone to yield the correct spiral side length  $L$ . Indeed, table 7.2 shows that for this first iteration  $L$  was only 70% of the ideal value. The second GLAD growth iteration attempted to rectify this by increasing the spiral pitch  $p$  to  $1.07 \mu\text{m}$ . This did in fact lead to an improvement in  $L$ , but only to a value that was still more than 20% off the ideal. Thus, the third iteration shifted attention to the substrate tilt angle  $\alpha$  instead, which was increased to  $86.0^\circ$  to force an increase in  $\beta$  and hence  $L$ . This approach proved most successful, with the spiral side length of  $0.46 \mu\text{m}$  now only 10% off the ideal value, and the spiral arm width simultaneously reaching the best value observed.

Apart from optimizing the spiral dimensions, the iterations also appear to lead to an improvement in the morphological quality of the GLAD films. The square spirals thus broaden and bifurcate less in the third iteration film in figure 7.2c than in the first and second iterations in figures 7.2a and b, and the spiral shape and overall film structure is more uniform. However, even in the third iteration, column broadening and bifurcation are still not eliminated, and an outstanding problem is the cross-sectional shape of the spirals which is more crescent shaped than square. For all three iterations the spiral dimensions vary from spiral to spiral and within each spiral.

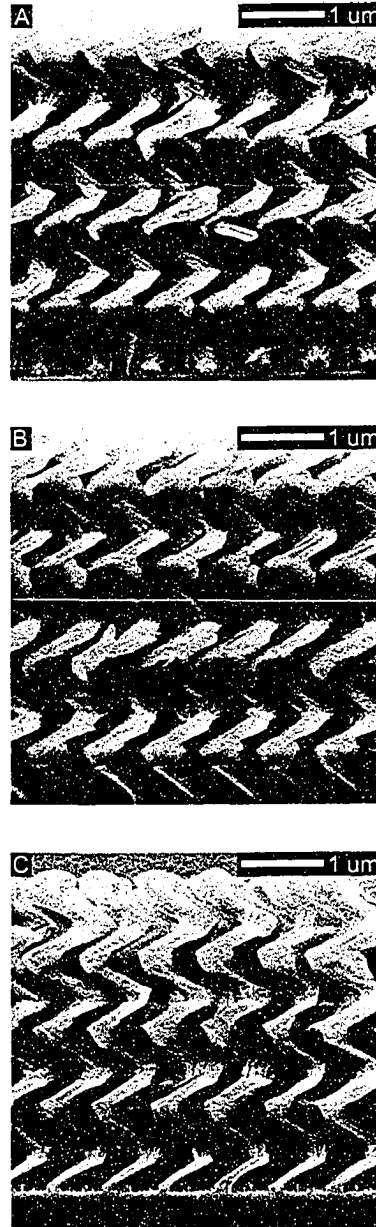


Figure 7.2: SEM edge views of three iterations of GLAD silicon square spiral growth on EBL seed layers with a lattice period  $\Delta$  of 700 nm. The spiral dimensions and GLAD deposition parameters are listed in table 7.2.

$\Delta$	$\alpha$ ( $^\circ$ )	$p$ ( $\mu\text{m}$ )	$p_r$	$L$ ( $\mu\text{m}$ )	$L_r$	$w$ ( $\mu\text{m}$ )	$w_r$
600	$86.0 \pm 0.2$	$1.01 \pm 0.01$	1.17	$0.41 \pm 0.03$	1.00	$0.22 \pm 0.06$	1.05
700	$86.0 \pm 0.2$	$0.93 \pm 0.01$	0.93	$0.46 \pm 0.03$	0.88	$0.20 \pm 0.06$	0.81
800	$85.0 \pm 0.2$	$1.25 \pm 0.01$	1.10	$0.53 \pm 0.04$	0.88	$0.25 \pm 0.05$	0.89

Table 7.3: For best achieved GLAD square spiral dimensions for lattice periods  $\Delta$  from 600 to 800 nm. The optimized GLAD parameters  $\alpha$  and  $p$  for each case are listed, along with the relative dimensions (subscript ‘r’) computed against the ideal PBC dimensions in table 7.1.

### 7.3.2 Scaling Results

A similar approach was applied to downscale and optimize the square spiral GLAD structure for the other seed layer lattice periods investigated. For the  $\Delta$  range of 600 to 800 nm in focus here, the substrate tilt angle was varied between  $84$  and  $86^\circ$ , and the GLAD helical pitch  $p$  was varied from 900 to 1300 nm. The best square spiral structures thus obtained are shown for lattice periods of 600 and 800 nm in figures 7.3b and c, and should be further compared with the 700 nm lattice film in figure 7.2c. For comparison, the best square spiral GLAD film on a 333 nm lattice is displayed in figure 7.3a, while a representative 1000 nm lattice film is shown in figure 7.3d. No optimization was performed for the 333 nm lattice period, given that it represents PBC structures with bandgaps beyond the absorption edge of silicon. 333 nm lattice silicon films might, however, be useful as templates for inverse square spiral PBC structures.

Table 7.3 lists the optimized GLAD parameters and square spiral dimensions for seed lattice periods 600, 700, and 800 nm. For  $\Delta = 600$  nm, both the substrate tilt  $\alpha$  and helix pitch  $p$  had to be increased to obtain a square spiral side length of  $0.41 \mu\text{m}$ , equal to the theoretical ideal. The spiral arm width was also optimized to within 5%. For  $\Delta = 800$  nm, the best square spiral dimensions were obtained with  $\alpha$  raised to  $85.0^\circ$  and  $p$  increased to  $1.25 \mu\text{m}$ , resulting in both  $L$  and  $w$  being within 10% of the ideal.

It emerges from table 7.3 that relatively high substrate tilt angles of  $85.0$  and  $86.0^\circ$  are required to achieve GLAD square spiral films with dimensions approaching the theoretically ideal values. Furthermore, the GLAD pitch must on average be larger than the ideal square spiral pitch to obtain the right spiral side length. This growth behaviour is in full agreement with the fundamental constraints between GLAD substrate tilt and column inclination angle, and between spiral pitch and spiral side length, as discussed earlier.

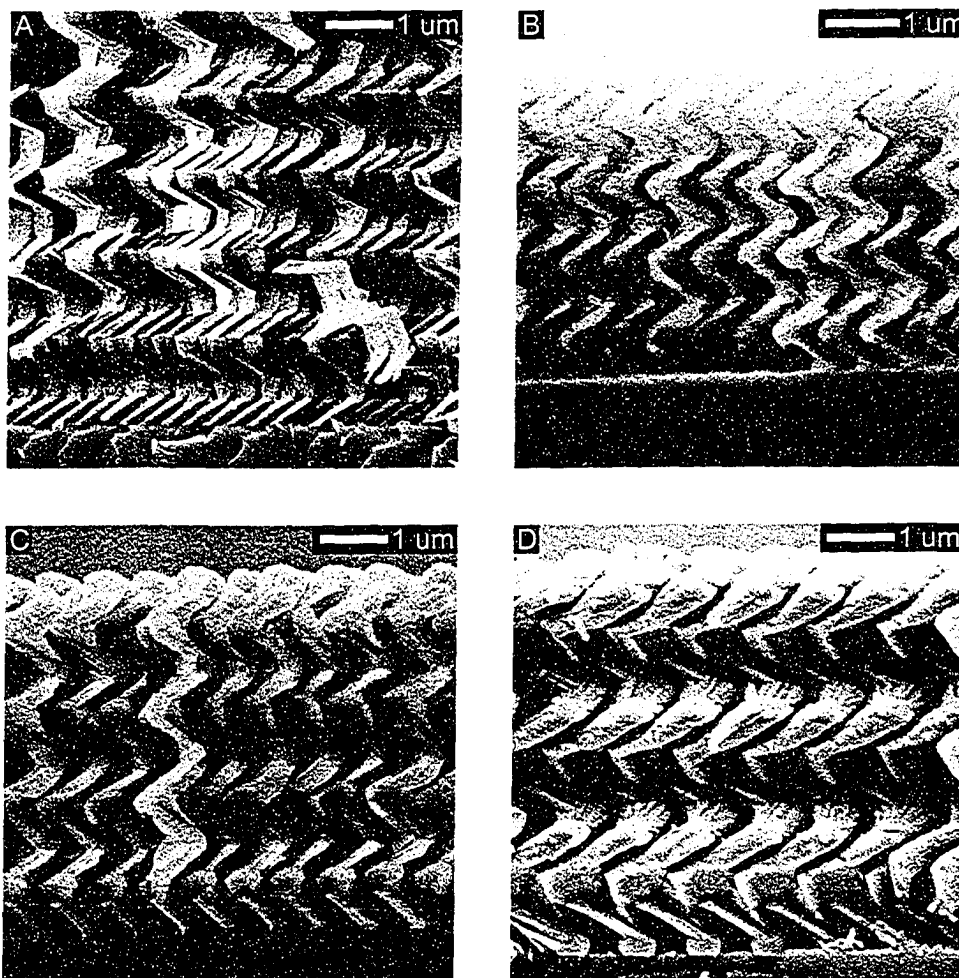


Figure 7.3: GLAD square spiral films on seed layers with lattice periods of a) 333 nm, b) 600 nm, c) 800 nm, and d) 1000 nm. For the lattice periods of 600 and 800 nm the best obtained square spiral structures are shown, while the 333 and 1000 nm films are included for reference. The 333 nm period is too low for periodic square spiral growth in silicon.



Figure 7.4: A single silicon GLAD square spiral, separated from the rest of the film during sample cleaving. The spiral pitch is  $1.7 \mu\text{m}$ . The spiral arm cross-section is elliptical or elongated rectangular, rather than the ideal circular or moderately rectangular shape.

Another important observation from table 7.3 is that the spiral arm width is almost constant, irrespective of the GLAD parameters and the lattice period. Indeed, even for lattice periods down to 333 nm the arm width remains almost the same, and this spells disaster for the  $\Delta = 333$  nm film. As seen in figure 7.3a, the GLAD columns in this film initially nucleate correctly on the seeds and grow a well structured first spiral arm segment. However, after the first spiral corner the arms become so wide that they begin to touch each other, and after several more substrate turns the periodic structure is gradually lost as the spirals merge, broaden further, and begin to compete. Top views of this film show a completely aperiodic structure. The arm width thus presents itself as the square spiral dimension most difficult to control using basic GLAD growth algorithms.

Apart from the less than ideal spiral arm cross-sectional shape, even the optimized 600 to 800 nm period square spiral films (figures 7.2c and 7.3b,c) suffer from the same structural problems as traditional 1000 nm period films (figure 7.3d): Column broadening, some column bifurcation, surface roughness, and non-uniformity in spiral dimensions throughout the films. Many of these effects are illustrated by the separated square spiral in figure 7.4, which was ripped loose during cleaving of one of the substrates.

On the positive side, figure 7.3 indicates that as the lattice period and spiral pitch are reduced, relatively less arm broadening takes place within

each spiral segment between two corners. In fact, the arm width is notably larger in the traditional 1000 nm period film than in any of the down-scaled films. This is hardly surprising, since a lower spiral side length gives the spirals less time to broaden. In this way down-scaling of the GLAD films may actually facilitate a better structure, although – as the 333 nm lattice period films shows – only to a point.

## 7.4 Challenges of Square Spiral GLAD Growth

The challenges of GLAD PBC growth concern enhancing the film fine structure and square spiral shape, and – by extension – improving the film uniformity. Addressing these issues is required for two reasons. First, it is necessary for enabling true bandgap engineering, since some of the morphological problems are exacerbated by down-sizing of the film structures discussed in the preceding sections, and since the size and location of the eventual bandgap depends as much on crystal uniformity and user control over microstructural details as on the spiral dimensions. Secondly, and irrespective of down-scaling, periodic and aperiodic GLAD films possess inherent morphological anisotropies that until now have degraded the optical properties of GLAD PBC films. In the previous report on optical characterization of square spiral films, Kennedy *et al.* reported non-uniformities in the GLAD morphology as the key problem degrading the PBC response [188]. Structural advances are thus required to better approach the ideal PBC architecture and optimize the photonic properties.

While chapter 6 discussed the general structural improvements afforded by periodic GLAD films over aperiodic films, the focus here is on further enhancing the fine structure of periodic GLAD films with a square spiral structure specifically designed for PBC purposes. The main growth issues will first be identified and analyzed, followed by the development of all-new GLAD algorithms designed to provide better square spirals. Although focusing on photonic crystal GLAD, the results are applicable to GLAD films and applications beyond PBCs.

### 7.4.1 Spiral Arm Broadening

The GLAD review in chapter 3 discussed the inherent and monotonic broadening of columns in aperiodic GLAD films, and chapter 6 demonstrated how such broadening is strongly suppressed in periodic GLAD films. Investigated here is the increase in column width  $w$  observed within each individual square spiral arm segment connecting two corners in a spiral. This type of

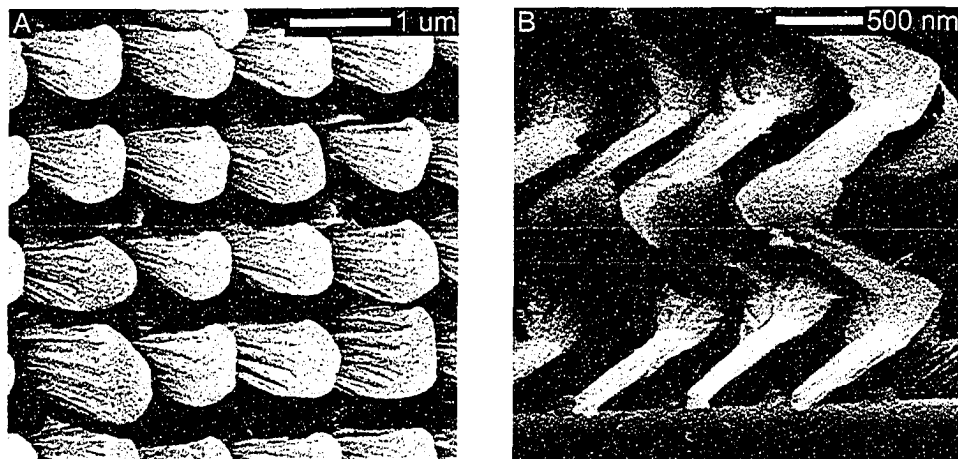


Figure 7.5: a) Top and b) side views of periodic silicon square spiral GLAD films illustrating spiral arm broadening. The broadening process is reset at every spiral corner, but broadening occurs primarily on the outside edge of the spirals.

repetitious column broadening is responsible for the spiral arm cross-section being non-uniform, to the detriment of the photonic properties.

Figure 7.5 shows top and side views of periodic silicon square spiral GLAD films. Broadening of the spiral arm segments is evident, as each segment spreads out quickly from every corner in the spiral. Each corner resets the broadening, however, and there is no cumulative increase in the arm width as the films grow thicker. The rate of broadening in each segment is constant, implying that the segments have not had time to reach equilibrium width in evolving between two corners. From both top and side views it also appears that broadening occurs primarily on the outside edge of each spiral, while the inside edge remains parallel to the vapour arrival direction. The very first arm segments to grow off the seeds, however, broaden isotropically.

Spiral arm broadening is fundamentally driven by the inherent sensitivity at highly oblique vapour incidence angles to vapour randomly impinging on the edge of a growing column and causing irreversible enlargement of the column. (Similarly, the column inclination angle  $\beta$  is always lower than the vapour incidence angle  $\alpha$  because the incident vapour favours the leading edge or underside of a growing column.) The frequent substrate rotations interrupt this natural evolution of the arm segments before they have had time to reach their equilibrium width, so that they have to start broadening anew from each corner. The  $90^\circ$  turns also change the topography of the

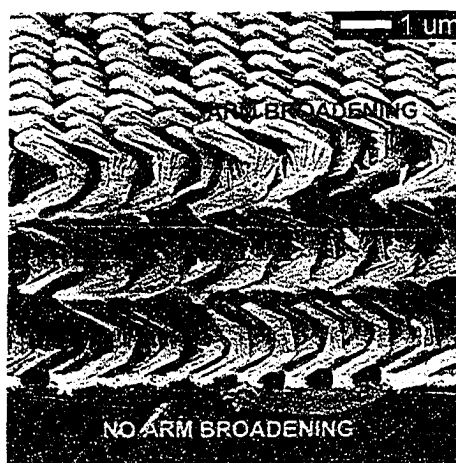


Figure 7.6: Oblique view of a three turn square spiral film on an EBL seed layer with a lattice period of 1000 nm. The seeded square spiral arms broaden strongly after every corner in the film, whereas the deeper lying inter-seed columns are able to evolve with no broadening.

growing spirals as seen from the vapour source, and since the spiral apices look thinner from the side, the broadening process has to start almost from scratch (see also section 6.2.3).

Clues to further understanding spiral arm broadening are found in figure 7.6, which shows an oblique view of a square spiral film. The seeded, periodic spirals, which grow all the way from the substrate to the top of the film, broaden severely after every spiral corner. However, a few inter-seed columns are also observed near the cleaved edge, and until extinguished after four turns, these columns grow with no spiral arm broadening at all. The inter-seed spirals are unique in that they grow at a lower height than the seeded spirals – namely by a height difference given by the height of the seeds – and the surrounding, taller seeded spirals therefore shelter the inter-seed spirals.

Spiral arm broadening thus occurs because the deposition of square spirals with the vapour arrival direction parallel to the tetragonal seed lattice affords no restrictions on random broadening of the columns. Unlike the deeper lying inter-seed columns in figure 7.6, the seeded square spirals have access to a continuous supply of evaporant arriving in-between the tetragonal rows of columns. Any random broadening of the seeded spirals into this adjacent vapour stream is immediately fuelled by more evaporant and reinforced. This also explains why the outer edge of the spiral corners broadens more than the inner edge.

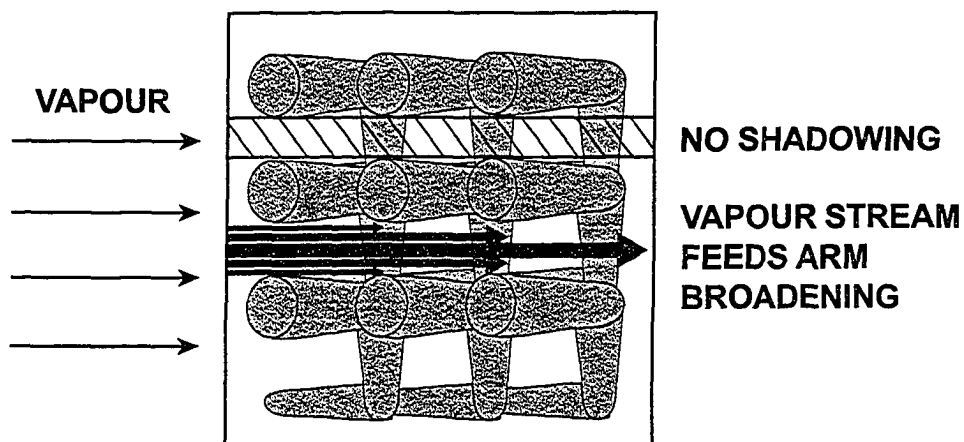


Figure 7.7: Schematic drawing of square spiral deposition with the vapour arrival direction (or deposition plane) aligned parallel to the tetragonal seed lattice unit vectors. The unobstructed vapour stream between the seeded spirals feeds the stochastic spiral arm broadening process.

The alignment of seed lattice and deposition plane and the resulting feeding of the spiral arm broadening is shown in figure 7.7. Comparison with section 6.2.4 reveals that inter-seed column growth and spiral arm broadening are associated GLAD growth effects. It should also be noted that the presence, or at least the extent, of spiral arm broadening is likely related to the tendency of silicon to form GLAD columns with a certain natural width. This is the ‘equilibrium’ width approached in every arm segment before the substrate turns, and in part responsible for the arm widths  $w$  in table 7.3 being similar. Another minor contributor to arm broadening is the slight spread  $\Delta\alpha$  in the vapour incidence angle.

#### 7.4.2 Column Cross-Section and Fanning

Spiral arm broadening might be acceptable if the broadening occurred symmetrically about the spiral arm central axis, so that a circular column cross-section was maintained at all times. However, for conventional square spiral GLAD growth on tetragonal seed geometries, column broadening develops non-uniformly about the spiral axes. This results in asymmetrically shaped column cross-sections that are far from the circular, square, or rectangular cross-sections desired for the square spiral PBC architecture.

Figure 7.8 shows a side view of a square spiral GLAD film with the column cross-section highlighted (see also figure 7.5b). The cross-section is

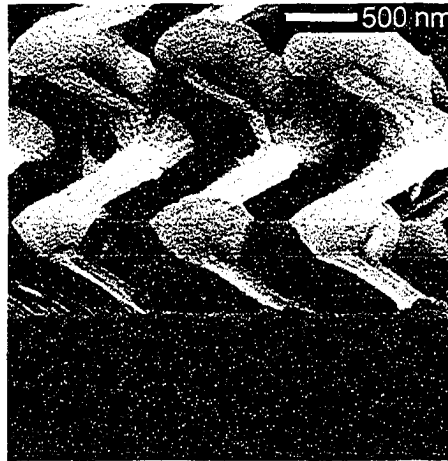


Figure 7.8: The fan shaped column cross-section highlighted in this square spiral GLAD film is far from the ideal circular or square cross-section desired for the square spiral PBC architecture. The fanning is reset at every spiral corner, but does worsen as the films grow thicker.

concave and elongated, and has a fan like shape that almost resembles a celery stalk. The fanning is observed to reset itself at every spiral corner, and then get more pronounced within each arm segment as the segment grows and broadens. It does appear to worsen slightly as the film becomes thicker.

An oblique view SEM image of a square spiral GLAD film, in which the SEM observation axis was aligned to look straight down the axes of the last grown spiral arm segments (i.e., aligned with the column inclination angle  $\beta$ ), is shown in figure 7.9a. The fan shaped cross-section is evident here, resulting in a scale like topography of the tetragonally arranged spirals. Meanwhile, figure 7.9b shows a similar  $\beta$ -aligned oblique view of a square spiral film, but immediately after a  $90^\circ$  spiral corner. Here the spiral cross-section is elliptical, and thus much better. This confirms the observation from figure 7.8 that the spiral cross-section is reset to an acceptable shape at each corner, and then degrades as the next arm segment is grown.

The column cross-section is defined by two effects. First, the elongation or preferential broadening is due to the fact the geometrical shadowing only works within the deposition plane, i.e., the plane spanned by the substrate normal and the unidirectional vapour arrival direction. There is no shadowing perpendicular to the deposition plane, and broadening can thus occur more freely in this direction. This makes an otherwise circular cross-section

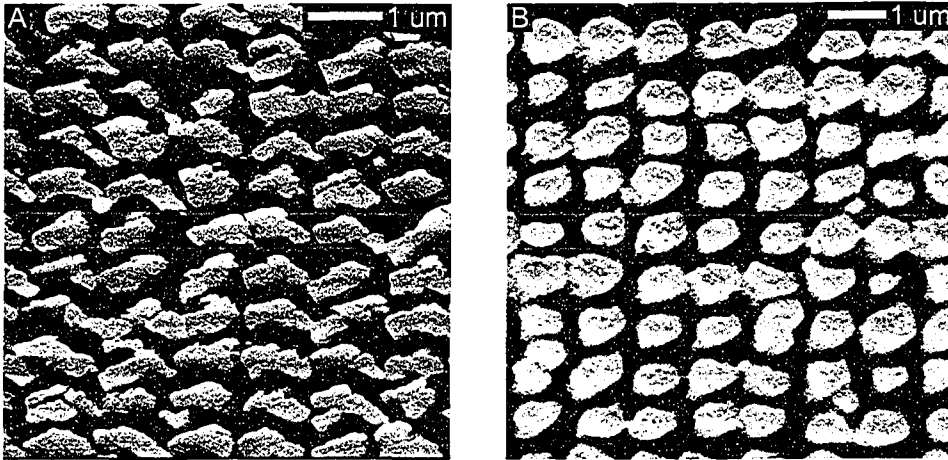


Figure 7.9: Oblique views of square spiral GLAD films aligned with the column inclination angle  $\beta$ , i.e., looking straight down the axes of the spiral arm segments. a) After a full arm segment has been grown, the fan shaped cross-section is prominent. b) Immediately after a spiral corner, however, the fanning is reset and a near-rectangular cross-section is observed.

elliptical, or a square cross-section rectangular, as seen in figure 7.9b.

Second, the elongated cross-section is warped into a fan like shape by shadowing among the columns *within* the deposition plane. Since the column inclination angle  $\beta$  is always less than the vapour incidence direction  $\alpha$ , and since the traditional alignment of the vapour arrival direction with the tetragonal seed lattice causes the spiral arms to be lined up parallel to the deposition plane, the shape of one growing spiral segment casts a concave shadow on the next adjacent spiral segment behind it. This is illustrated in figure 7.10. Although each spiral turn resets this effect by providing a fresh, non-fanned column tip to grow off, the fan shape quickly returns when the next spiral arm segment is grown. Figure 7.11 shows a 3D FILMS simulation of a slanted post GLAD film grown off a tetragonal seed layer, with the direction of observation aligned with the deposition plane and  $\beta$ . The concave shadow effect within the deposition plane is evident here.

To avoid the above two growth effects and improve the column cross-section, Kennedy and Brett recently developed a new GLAD growth mode, named ‘Variable Alpha Post’, in which the vapour arrival direction precesses about the growth direction of the column through continuous adjustment of both the substrate tilt  $\alpha$  and rotation  $\phi$  [187]. This approach results in significantly less column fanning and cross-sectional shapes approaching

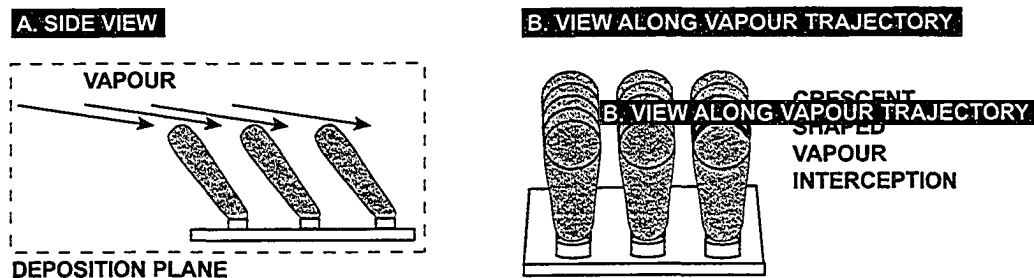


Figure 7.10: a) Schematic of the deposition plane in square spiral growth with the vapour arrival angle aligned with the tetragonal seed lattice. Each column partially shadows the next column behind it. b) Given the initially rounded column tips, this in turn leads to a concave vapour interception pattern being cast from one column to the next, and fanning results.

squares. However, the Variable Alpha Post technique also causes the film volume fill factor to increase to the range of 0.5 to 0.7, making it unsuitable for the fabrication of direct structure square spiral PBCs (but not for the fabrication of inverse PBC templates).

### 7.4.3 Column Bifurcation and Spiral Corners

In the ideal, theoretical square spiral PBC architecture, spiral arm segments connect abruptly in sharp  $90^\circ$  joints. In GLAD film growth, this is equivalent to instantaneous  $90^\circ$  substrate rotations. However, abrupt turning of the substrate exposes the broad sides of the previous arm segments, rather than just their apices, and several new column segments may then grow off each of the existing spirals. Such substrate rotation induced column bifurcation is the only kind of bifurcation normally seen in periodic square spiral GLAD films, where spontaneous branching of columns – prominent in aperiodic films – is rare.

Bifurcation at spiral corners derives from the same origins as spiral arm broadening, namely exposure to vapour arriving between the rows of growing square spirals. This vapour stream has direct access to impinge on the previous arm segments deeper in the film, as illustrated in figure 7.7, and form new column strands. Again, the underlying problem is the alignment of the vapour incidence direction with the tetragonal seed lattice.

A countermeasure to column bifurcation at square spiral corners was introduced by Kennedy and Brett, who proposed turning the substrate gradually rather than abruptly, with a corner turn pitch typically around  $1/30$

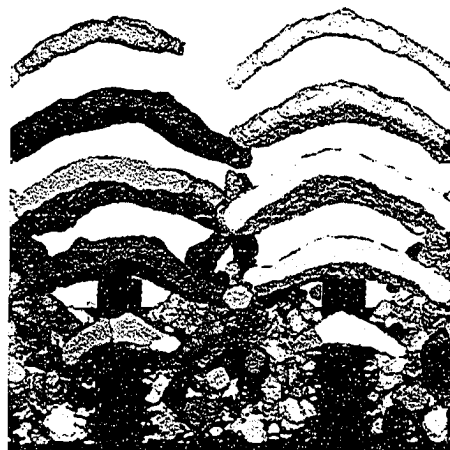


Figure 7.11: 3D FILMS simulation of slanted post GLAD growth on a tetragonal seed lattice. The plane of the image is perpendicular to the column growth direction, and the columns are limited by periodic boundary conditions. When looking straight down the column axes the elongation of columns perpendicular to the deposition plane is evident, and fanning is seen to propagate from one column to the next.

of the full pitch of the square spirals [187]. The compromise of this ‘slow corner’ technique with respect to the ideal abrupt corners in the PBC architecture is negligible, and by softening the transition from one spiral arm segment to the next a significant reduction in corner bifurcation is achieved. The slow corner technique has been used for the majority of square spiral GLAD films fabricated here, including the films analyzed in the preceding sections.

Figures 7.5a and 7.12 show top views of square spiral GLAD film with ‘slow corners’. Some bifurcation is observed even with gradual substrate rotation, but it is much reduced when compared with abrupt rotation, and the few bifurcated columns tend to become extinct rather quickly. However, the same figures also indicate that gradual substrate rotation may promote spiral arm broadening, since the technique appears to facilitate the expansion of the outside edge of the corners (this is particularly evident in figure 7.5a). Since the fibres making up the silicon columns tend to grow straight, the outside edge broadening may be due to the fibres tangentially growing out of the slow corners. This rotation induced broadening of the spiral arms may in fact be partially responsible for the rapid quenching of bifurcated corner growth using ‘slow corners’.

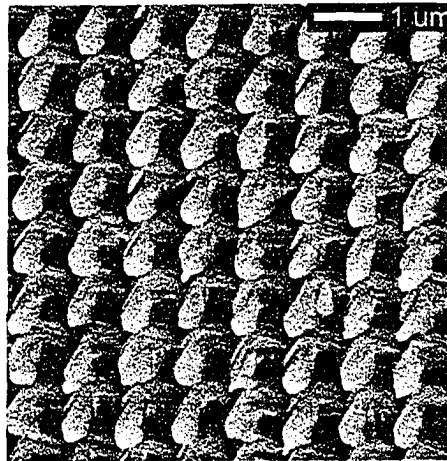


Figure 7.12: Top view of a square spiral GLAD film with ‘slow corners’. Limited column bifurcation is present at the spiral corners, but much less so than in abrupt corner GLAD films. However, it is also evident that broadening of the outer edge of the spirals has taken place at the corners. See also figure 7.5a.

## 7.5 Advanced GLAD Growth Algorithms

The analyses in the preceding sections have established two fundamental causes of spiral arm broadening, bifurcation, and cross-sectional fanning:

- Geometrical shadowing being confined to the deposition plane only.
- The deposition plane coinciding with the tetragonal seed lattice unit vectors.

The former anisotropy is unavoidable in deposition at highly oblique angles. The latter, however, is the more serious of the two root causes, and even amplifies the shadowing anisotropy. It is a direct consequence of the traditional approach to GLAD square spiral PBC deposition, in which the architectural requirement for tetragonally arranged square spirals is achieved by simply aligning the seed layer with the vapour arrival direction.

To overcome the morphological problems in GLAD square spiral films, and improve the PBC fine structure and uniformity, advanced substrate motion algorithms must be developed to replace the existing, conventional growth methods. In addressing the root causes of detrimental growth effects, the new algorithms must specifically:

- Separate the deposition plane from the tetragonal seed lattice unit vectors.
- Minimize the effects of unidirectional geometrical shadowing.

Naturally, this must be achieved while maintaining the square spiral column structure and the seed layer induced periodicity. Two different new GLAD growth algorithms – PhiSweep and Off-Axis – have been developed to this end.

## 7.6 The PhiSweep GLAD Algorithm

### 7.6.1 Definition of the PhiSweep Method

The PhiSweep algorithm is a new method for GLAD film growth, whose principle is to decouple the direction of column growth from the vapour arrival direction  $\phi$ . In contrast to traditional GLAD, where the substrate is kept static for each straight column segment, the new method regularly rotates the substrate from side to side about a central axis defining the direction of the straight column segments. At each outer extreme of the sweep curve, the substrate is paused for a period of time corresponding to a certain, constant thickness of film growth, called the sweep pitch  $q$ . The sweep curve is symmetric about the central axis, and the angle between the central axis and the sweep curve limit is called the sweep angle  $\gamma$ . This is illustrated schematically in figure 7.13. For example, a film with a sweep angle  $\gamma = 45^\circ$  and a sweep pitch  $q = 15\text{nm}$  would have the substrate turn  $45^\circ$  to either side of the central axis (for a full  $90^\circ$  sweep range between the outer extremes), and between these sweeps it would keep the substrate fixed at an outer extreme of the sweep curve for 15 nm worth of thin film growth, measured normal to the substrate.

The  $\phi$  oscillations spread out the incident vapour and prevents vapour from impinging directly along the central sweep axis, but the average direction of film accumulation nevertheless coincides with the very same central axis. When neither the sweep pitch nor the sweep angle are too large, the resulting film therefore consists of straight columns growing in a direction equal to the sweep centre axis, even if vapour never actually arrived along this axis. With current GLAD equipment, and with the sweep pitch values investigated here, the vapour deposited during the time spent in transit as the substrate turns from one end of the sweep curve to the other is negligible. The PhiSweep method can reproduce all known polygonal helical GLAD structures, as long as the polygon side length is not too small. Its

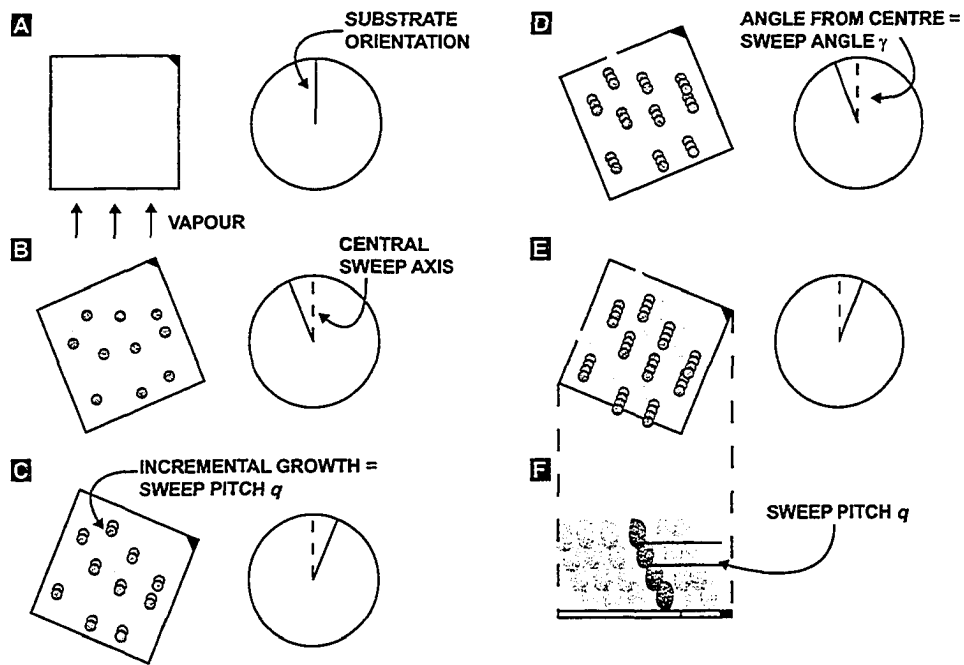


Figure 7.13: Schematic illustration of the novel PhiSweep GLAD growth algorithm. The vapour incidence direction  $\phi$  is decoupled from the column growth direction by rotating  $\phi$  from side to side, and performing incremental deposition at each extreme of the sweep curve. The width of the sweep is given by the sweep angle  $\gamma$ , and the thickness of film deposited between each sweep is the sweep pitch  $q$ .

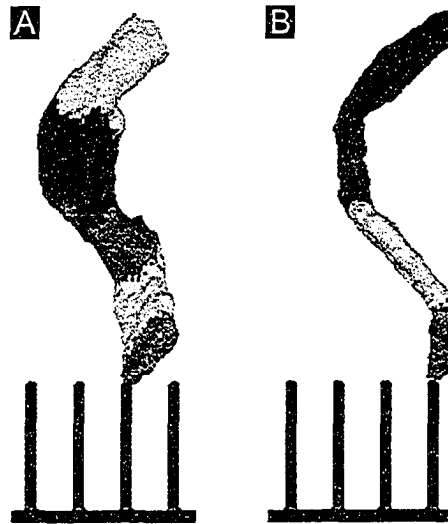


Figure 7.14: 3D FILMS simulations of square spirals grown using a) traditional GLAD and b) the PhiSweep GLAD algorithm. The simulated PhiSweep square spiral has a leaner and more uniform structure with less broadening and bifurcation.

use for high pitch (slow rotation) circular helices, with large helix circumferences divided into linear segments, is a potential future option.

### 7.6.2 PhiSweep GLAD PBC Films

Initial evaluation of the PhiSweep algorithm was performed using the 3D FILMS oblique angle thin film simulator, in collaboration with Dr. T. Smy of Carleton University. Figure 7.14 shows individual square spirals from two 3D FILMS GLAD simulations. In figure 7.14a the deposition was performed as traditional square spiral GLAD with the deposition plane aligned with the tetragonal seed layer and no substrate sweeping. In figure 7.14b a PhiSweep deposition was simulated. The PhiSweep simulation clearly indicates a better and slimmer square spiral structure with less broadening and bifurcation. This warranted proceeding with actual GLAD experiments.

Figure 7.15 shows an array of periodic square spiral PhiSweep GLAD films on tetragonal seed layers. From top to bottom, the sweep angle  $\gamma$  varies from  $15^\circ$  to  $30^\circ$  to  $45^\circ$ , while the sweep pitch is held constant at 15 nm. For the  $\gamma = 15^\circ$  PhiSweep film in figure 7.15a the structure is not unlike that of the traditional non-sweep GLAD investigated earlier, with significant

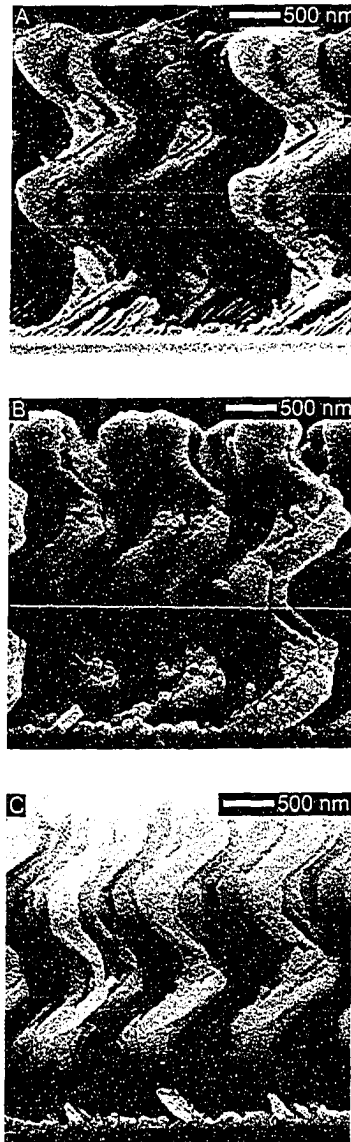


Figure 7.15: Side views of periodic PhiSweep GLAD films with sweep angles  $\gamma$  varying from 15 to 45° and the sweep pitch  $q$  constant at 15 nm. The dimensions of the 30° sweep angle film in b) represent a good fit with the theoretical square spiral PBC architecture, but the column surface roughness is not ideal (note that the side view in b) contains artifacts from excessive chrome coating prior to SEM imaging).

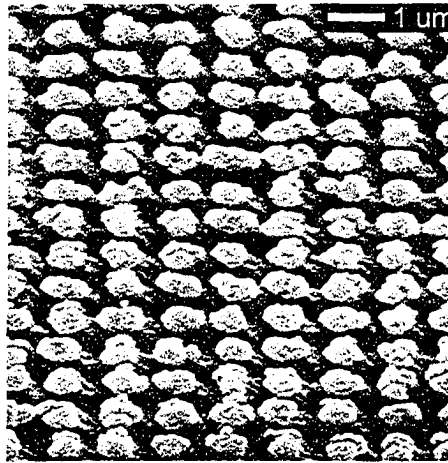


Figure 7.16: Oblique view of the  $\gamma = 30^\circ$  square spiral PhiSweep GLAD film previously shown in figure 7.15c,d. The direction of observation is aligned with the column inclination angle  $\beta$ , i.e., straight down the axes of the spiral arm segments. The column cross-section is elliptical and does not exhibit fanning.

column broadening and a less than ideal column cross-section. This is hardly surprising, given that a  $15^\circ$  sweep angle represents only a modest deviation from the case of conventional GLAD (which can be considered ‘PhiSweep’ with a sweep angle of  $0^\circ$ ). The  $\gamma = 45^\circ$  PhiSweep film in figure 7.15c has an even worse film structure. Each square spiral appears to consist of a loose bundle of smaller spirals, and while there is no fanning and only little broadening within each sub spiral, the structure is useless for PBC purposes. A  $45^\circ$  sweep angle thus appears too large for efficient square spiral growth, and likely causes the sub columns to develop and grow independently on opposite sides of the sweep curve.

Meanwhile, the PhiSweep square spirals with a sweep angle of  $30^\circ$ , in figure 7.15b, have better dimensions. The spiral surface is rather rough (although this roughness is amplified by an erroneously thick chrome coating prior to SEM imaging), but spiral arm broadening and cross-sectional fanning are all but eliminated, and there is little column bifurcation. An intermediate sweep angle of  $30^\circ$  thus yields the best PhiSweep periodic square spirals. A column axis or  $\beta$  aligned view of the spiral arm cross-section for  $\gamma = 30^\circ$  PhiSweep square spirals is shown in figure 7.16.

Variation of the sweep pitch  $q$  has less impact on the overall square spiral structure, although at higher pitch values small ripples appear on the spiral

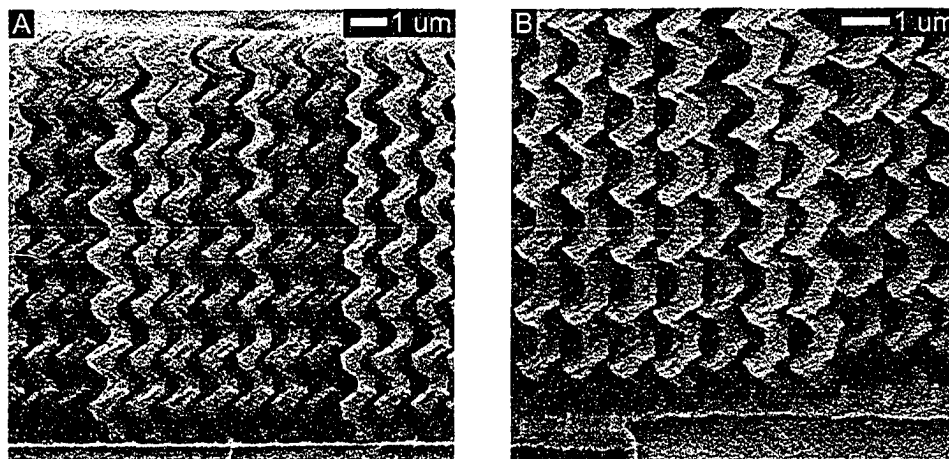


Figure 7.17: a) Side view of an eight turn thick PhiSweep square spiral PBC GLAD film with  $\gamma = 30^\circ$  and  $q = 45$  nm. b) Close up oblique view of the same film as it evolves off the tetragonal seed layer with very little inter-seed film growth. The film structure is highly uniform.

surface as artifacts of the changing vapour incidence variation (at small pitch values the ripples are entirely smoothed out, just as in vertical post GLAD films with a low helical pitch). In  $\gamma = 45^\circ$  PhiSweep films a reduction of the pitch to 10 nm provided some improvement over the structure from figure 7.15c, presumably as a result of the more frequent sweeping offering better dispersion of the vapour and hence limiting the tendency to form individual sub columns. Figure 7.17 shows a full size, eight turn ( $10.8 \mu\text{m}$  thick) PhiSweep square spiral GLAD PBC film. This film has a sweep angle  $\gamma$  of  $30^\circ$ , as in figure 7.15b, but a pitch of 45 nm, which yields optimal results for the  $\gamma = 30^\circ$  range.

### 7.6.3 Evaluation of PhiSweep GLAD

In closer examination of the  $30^\circ$  sweep angle PhiSweep square spiral films, in particular the optimized film in figure 7.17, it is observed that inter-seed column nucleation and growth is almost completely suppressed. In the oblique view in figure 7.17b, for example, only small vertical spikes of silicon are observed among the seeded spirals. This is the first benefit of the vapour arrival direction in PhiSweep being non-parallel with the unit vectors of the tetragonal seed lattice. In fact, the inter-seed growth suppression is especially strong at  $\gamma = 30^\circ$ , where even diagonal vapour arrival between

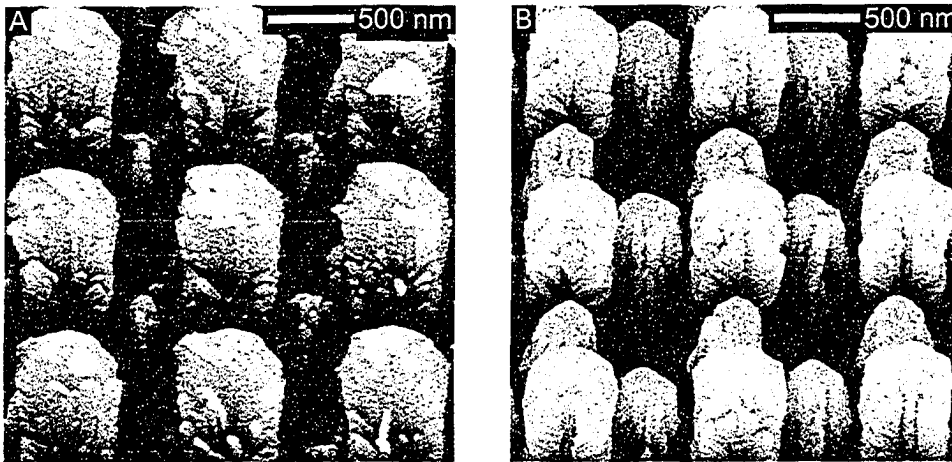


Figure 7.18: Top views of the initial growth of PhiSweep GLAD films on tetragonal seed layers, prior to the first square spiral corner. In a) the sweep angle  $\gamma$  is  $30^\circ$ , while in b)  $\gamma$  is  $45^\circ$ . The  $30^\circ$  sweep angle film provides superior suppression of inter-seed growth by eliminating column nucleation along the tetragonal lattice diagonal, and also minimizes column broadening.

the tetragonally arranged seeds is prohibited. This is illustrated in figure 7.18, which compares interseed growth at sweep angles of  $30^\circ$  and  $45^\circ$ . At  $\gamma = 45^\circ$  (figure 7.18b) vapour can get access along the tetragonal diagonals, and there is significant accumulation of inter-seed growth. At  $\gamma = 30^\circ$  (figure 7.18a), meanwhile, the substrate is more completely covered by the seed shadows, and very little inter-seed nucleation occurs. (Compare also with figure 6.7b.)

As the spiral arms continue to grow off the seeds, the frequent sweeping back and forth of the vapour arrival angle helps break the shadow anisotropy prevalent in traditional GLAD films. Figure 7.18a thus illustrates how spiral arm broadening is eliminated by the sweeping vapour stream ‘filling in’ the growing columns so that they completely match the width given by the seeds. Indeed, as is evident from figures 7.15b and 7.17a, the amount of spiral arm broadening is negligible in  $\gamma = 30^\circ$  PhiSweep films – both within each spiral segment and from the bottom to the top of the films – and the correct spiral width is obtained right off the seeds.

The combination of sweeping the vapour stream and breaking the seed lattice/deposition plane alignment is also responsible for the square spiral arm cross-section being better in PhiSweep GLAD films than in traditional GLAD films. Figure 7.16 shows that although the cross-section is still not

ideal – being neither circular, square, or slightly rectangular – its low eccentricity elliptical shape is vastly improved over the celery shaped cross-section examined earlier in figure 7.9a. Fanning has thus largely been disposed of.

The PhiSweep algorithm does not incorporate ‘slow corners’, since substrate rotation is already broken down into small segments equal to the sweep pitch. A corner is simply created by incrementing by  $90^\circ$  the central axis about which the vapour is swept. The vapour being swept away from the lattice unit vectors, however, is itself capable of eliminating column bifurcation both at the corners and in the spiral segments, as is evident in figure 7.17.

One drawback of PhiSweep square spiral GLAD films is the surface roughness of the spirals. The traditional GLAD algorithm produces columns with a smooth surface, striated only by the individual silicon fibres making up the columns. The PhiSweep process, however, creates small ripples in the column surface from the frequent changes in vapour direction, and further clutters the surface by continuing to bombard the spiral arms from both sides for some time after they have first been formed. The extent of these effects depend on the sweep pitch  $q$ , but in no cases are a fibrous column structure observable in periodic PhiSweep films. (It is a completely different matter for *aperiodic* PhiSweep films, however, as discussed in chapter 10.)

The uniformity of the  $\gamma = 30^\circ$  PhiSweep PBC GLAD film in figure 7.17 is notable, with the initial periodic square spiral structure emerging off the seed layer being maintained through the thickness of the film. There is little variation in the dimensions or fine structure laterally among spirals and vertically within spirals, and the film uniformity – crucial to the eventual PBC properties – is much better in these PhiSweep films than in traditional GLAD square spiral films.

By decoupling the spiral growth direction from the vapour arrival direction, moving the deposition plane away from alignment with the tetragonal seed lattice, and sweeping the vapour stream symmetrically from side to side to break the deposition plane shadow anisotropy, the PhiSweep algorithm addresses many of the structural problems in traditional GLAD film growth. The sweep angle  $\gamma$  predominantly determines the overall square spiral shape and amount of inter-seed growth, while the sweep pitch  $q$  determines the fine structure and surface roughness. In essence, the dispersion of the vapour shifts the impinging vapour from where it damages the square spiral structure (via fanning and bifurcation) to where it benefits the structure (filling in columns to reduce broadening and improve the cross-section). PhiSweep thus offers several advantages for the fabrication of GLAD square spiral PBC films, although the surface roughness must be expected to affect the

photonic properties. (A short anneal in forming gas might be able to remove some of this roughness while maintaining the overall column shape [226].)

The PhiSweep technique has other advantages and applications, and will be further discussed in connection with defect engineering in chapter 9 and porosity engineering in chapter 10.

## 7.7 The Off-Axis GLAD Algorithm

### 7.7.1 Definition of the Off-Axis Method

The Off-Axis algorithm is a second new GLAD growth method, independent of the PhiSweep algorithm. The principle of Off-Axis is to perform the square spiral deposition with the vapour arrival direction *statically* misaligned with the unit cell vectors in the seed lattice (i.e., the [100] and [010] lattice unit vectors in the PBC tetragonal lattice). The angular deviation between the seed lattice and the vapour arrival direction is labelled  $\psi$ . As discussed above and exploited in the PhiSweep algorithm, breaking the alignment between the seed lattice and the vapour arrival angle is critical to countering the detrimental growth effects in traditional GLAD films, with the first benefit being the suppression of inter-seed column nucleation and growth. However, by maintaining the off-axis alignment throughout the entire deposition, the Off-Axis technique becomes more subtle than just providing the simple protection against inter-seed growth already mentioned in chapter 6.

GLAD films – including square spirals – can be grown with either a right handed (RH) or a left handed (LH) helical rotational orientation, depending on whether the substrate is rotated clockwise (CW) or counter-clockwise (CCW), respectively, during the deposition. The rotational handedness is hence defined with the origin on the substrate. In the Off-Axis GLAD algorithm the off-axis deviation  $\Psi$  of the vapour arrival angle relative to the seed lattice must be *contrary* to the substrate rotation required for the given helical handedness. For example, for the Off-Axis technique to work for a *RH* square spiral, which requires *CW* substrate rotation, the vapour arrival angle must be skewed in the *CCW* direction. This is shown schematically in figure 7.19a–c. For *LH* square spirals, the substrate must be turned off-axis in the *CW* direction.

The salient feature of the Off-Axis technique is that with the above orientation in place, square spirals in a tetragonal arrangement mutually cover each other with staggered geometrical shadows. As illustrated in figure 7.19d, one square spiral partially covers the previously grown arm segments

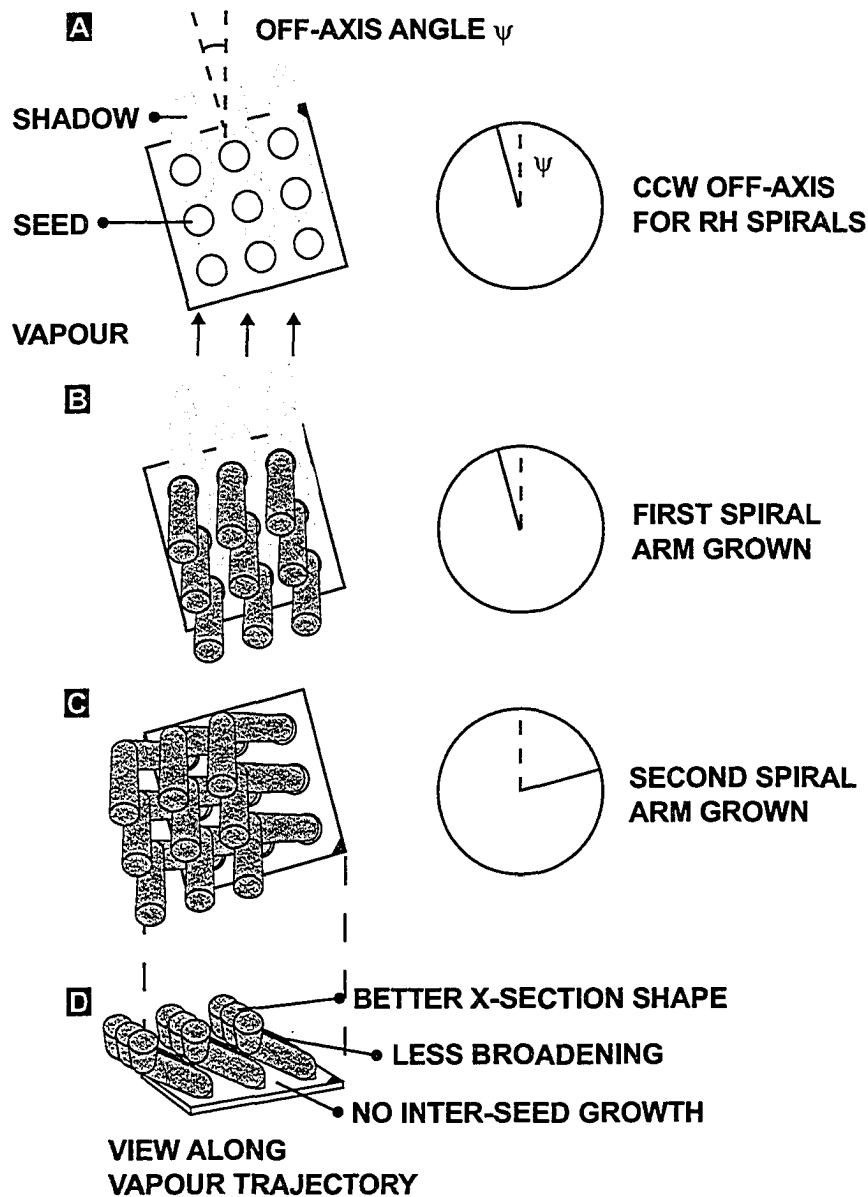


Figure 7.19: Schematic of the principles of the Off-Axis GLAD growth algorithm for square spirals. By moving the vapour arrival direction away from the lattice unit vectors of the tetragonal seed lattice – by an angle  $\psi$  opposite the spiral turn orientation – the spirals become staggered so that they shadow the previously grown segments of each other and intercept the vapour more uniformly.

of the next spiral behind it to prevent broadening and bifurcation. Simultaneously, and unlike the traditional GLAD method illustrated in figure 7.10, the shadow cast by one spiral no longer covers the tip of the currently growing arm segment of the next neighbouring spiral. This permits uniform rather than crescent shaped column growth.

With the apices of the growing square spirals staggered to more uniformly intercept the vapour stream, the Off-Axis algorithm manages to break the shadow anisotropy, in addition to shifting the deposition plane away from the seed lattice. This qualifies the technique as a contender for eliminating the traditional GLAD growth problems. However, if the substrate is mistakenly rotated off the seed lattice to the wrong side (e.g., CW rotation for RH spirals), the benefits will be limited as the full broadsides of the neighbouring spirals become exposed to the vapour stream and hence prone to bifurcation and broadening.

Twisting the square spirals relative to the tetragonal lattice does represent a distortion of the ideal PBC architecture (which itself is a distortion of the diamond lattice). The off-axis vapour arrival angle  $\psi$  should therefore be kept as small as possible. Indeed, a large  $\psi$  value would be counterproductive since staggering the spirals too strongly would expose the deeper lying, previously grown arm segments anew. After some initial experimentation an off-axis angle  $\psi$  of  $10^\circ$  was found to be a good compromise.

### 7.7.2 Off-Axis GLAD PBC Films

Figure 7.20 shows two Off-Axis square spiral GLAD PBC films on tetragonal seed lattices with an 800 nm lattice period. For the film shown in figure 7.20b, a problem with the GLAD substrate rotation apparatus ruined the periodic film structure after four turns. However, both the surviving  $5.5 \mu\text{m}$  thickness of this film and the film in figure 7.20a have a remarkably uniform structure, with lean and smooth square spirals that broaden only modestly, and with no column bifurcation or fanning.

The structural characteristics are confirmed by the close-up oblique views of interleaving,  $\psi = 10^\circ$  Off-Axis square spirals in figure 7.21. No interseed growth is observed at all, and the square spiral shape is maintained almost constant up through the film. The column surface is smooth and fibrous, but some broadening is observed within each arm segment. The same broadening is seen in the top views in figure 7.22, but the spiral arm cross-section appears to be almost circular, with no traces of column fanning, and certainly more uniform than in traditional GLAD.

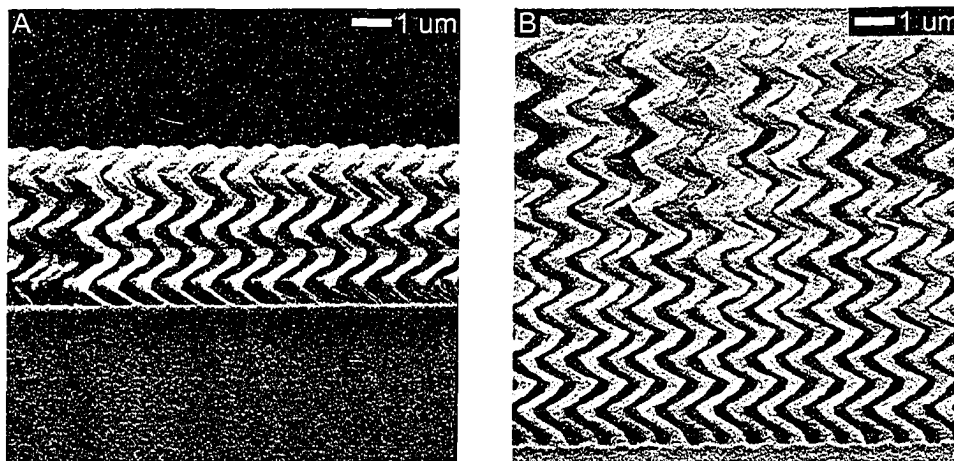


Figure 7.20: Side views of Off-Axis square spiral GLAD films. The off-axis angular spread is lower in a) than in b), causing some inter-seed column growth in a). In b) a problem with the GLAD substrate rotation apparatus caused the  $10.6 \mu\text{m}$  thick film to lose its periodicity about halfway through the deposition.

Finally, figure 7.23 shows an individual square spiral broken off from the Off-Axis film in figure 7.20b. In comparison with the traditional GLAD square spiral previously shown in figure 7.4, the morphological uniformity, surface smoothness, and lack of bifurcation in the Off-Axis spiral is notable.

### 7.7.3 Evaluation of Off-Axis GLAD

The elimination of inter-seed column nucleation and growth in Off-Axis square spiral GLAD films is complete, as evident in all the Off-Axis films shown (except in figure 7.20a, where the off-axis angle  $\psi$  was too low). This clearly derives from shifting the vapour arrival angle away from the seed lattice unit vectors, and is an improvement not only over traditional GLAD films, but also over PhiSweep films (in which the bare substrate between the seeds is exposed for every sweep from one side to the other). It is further evident that the Off-Axis square spirals evolve evenly off the seeds, with the initial column width closely matching the seed width.

Contrary to PhiSweep square spirals the arm segments in Off-Axis films do broaden, although not as severely as in traditional GLAD films. The broadening can be explained by the fact that even though the square spiral shadows overlap to cover each other, the tips of the growing arm segments

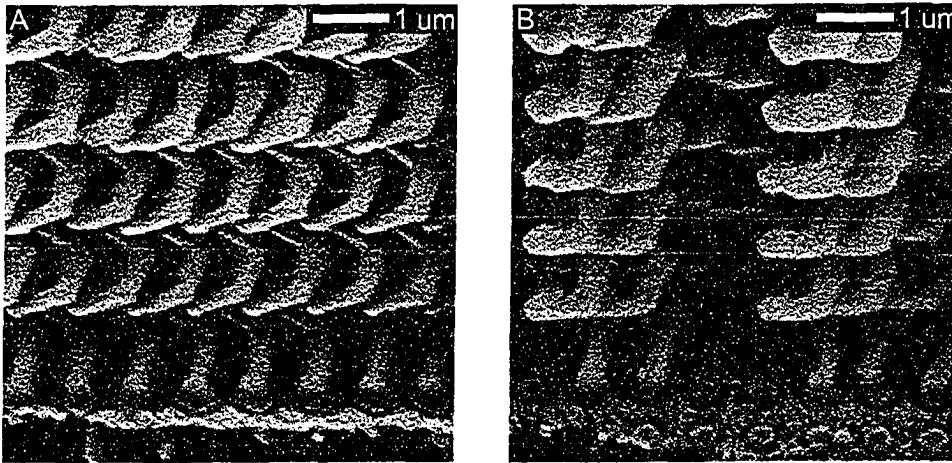


Figure 7.21: Oblique views of Off-Axis GLAD square spirals, deposited with an off-axis angular spread  $\psi$  of  $10^\circ$ . No inter-seed growth or column bifurcation is observed, but some arm segment broadening is present.

are at all times statically exposed to the vapour source. Without the frequent sweeping substrate motion in the PhiSweep algorithm, this allows random broadening of the growing arm segments to develop. However, the reduction in the shadow anisotropy also provided by the Off-Axis technique limits the severity of the arm segment broadening by limiting the amount of vapour incident between the growing spiral arms.

The spiral cross-section is better in Off-Axis square spirals than in any other square spiral GLAD growth algorithms, with reduced elongation and no fanning at all. First, the staggered Off-Axis arrangement of the growing spirals eliminates the crescent shaped shadows found in traditional GLAD films, where the deposition plane is fully aligned with the seed lattice. Secondly, the staggering of the growing spiral tips, as seen from the vapour source, exposes the tips more fully and uniformly to the vapour stream, so that the cross-section automatically becomes more regular and attains a lower aspect ratio, to the benefit of the eventual PBC properties. In essence, the Off-Axis algorithm collapses the fan shaped columns into tighter, circular columns. Thus, in spite of the arm segment broadening the Off-Axis columns come out with a lower width than in traditional GLAD.

Similarly, the overlapping shadows of the Off-Axis square spirals – combined with the use of ‘slow corners’ in all Off-Axis films – entirely eliminate column bifurcation. The inter-column vapour stream, which as illustrated in figure 7.7 allows evaporant to impinge on previously grown spiral

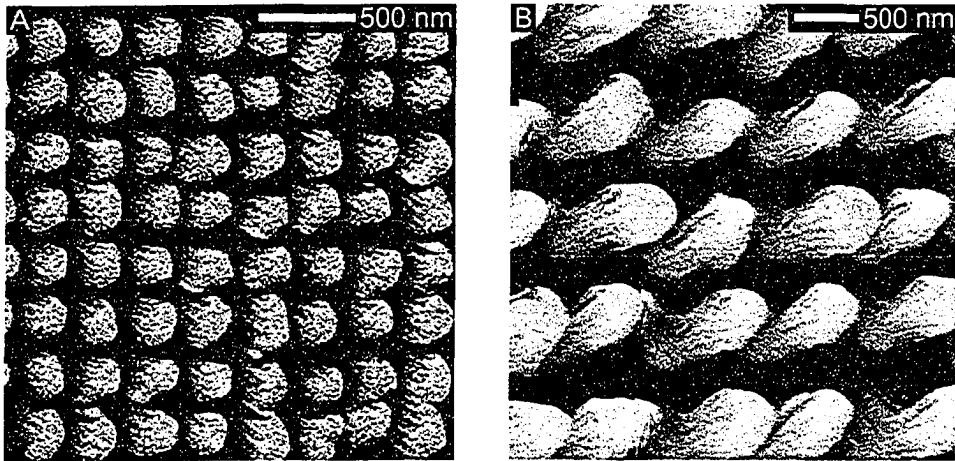


Figure 7.22: Top views of Off-Axis GLAD square spirals with off-axis angular spreads  $\psi$  of 10 and 30°, respectively. The column cross-section is more round than in traditional GLAD films, and no column fanning is seen.

arm segments deep inside traditional GLAD films, is in Off-Axis GLAD redistributed to hit the growing spiral tips instead. Furthermore, the lack of side-to-side vapour sweeping prevents the development of independent sub columns on opposite sides of the square spirals, as seen in some high sweep angle PhiSweep films. Without the sweeping action, the surface of the Off-Axis square spirals is much smoother and without the ripples found in PhiSweep GLAD films. The only remaining roughness is the inevitable fibrous structure of the silicon columns themselves, which could conceivably be smoothed by soft annealing.

In moving the vapour arrival angle off the tetragonal lattice unit cell vectors and partially breaking the shadow anisotropy perpendicular to the deposition plane, the Off-Axis algorithm provides a much better geometrical shadow pattern within the growing film than other GLAD growth algorithms. This forces the square spirals to assist shadowing those segments of each other that should not be exposed to the vapour source, and disperses the growing spiral tips to intercept more vapour rather than compete for it. Almost all of the detrimental growth effects in traditional GLAD are thereby removed.

Morphologically, the Off-Axis GLAD algorithm delivers the best square spirals fabricated to date. The fine structure of the square spirals is close to the theoretically ideal shape given by the PBC architecture, and the uniformity is greater than in any other square spiral films, both locally within the

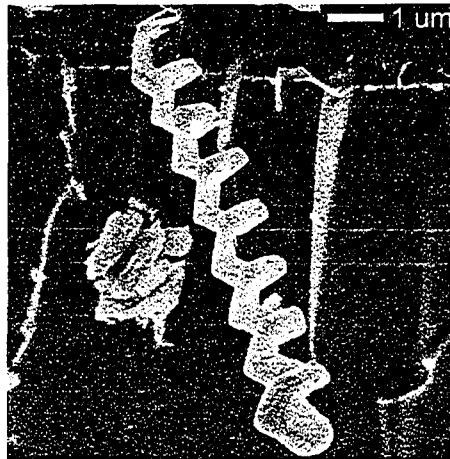


Figure 7.23: A single square spiral released from the square spiral Off-Axis GLAD film previously shown in figure 7.20b. In comparison with the traditional GLAD square spiral in figure 7.4, the Off-Axis spiral is a much better representation of the ideal PBC architecture.

spiral arm segments and globally throughout the films. Significant improvements have consequently been attained over traditional GLAD films, while in comparison with the PhiSweep technique the main structural drawback of Off-Axis GLAD is the slight spiral arm broadening.

The key outstanding issue with respect to Off-Axis square spiral GLAD films is the impact of the tetragonal lattice distortion on the potential PBC properties. No PBC modelling data exists to evaluate this effect. However, given the superior structural quality of the films, they will become the prime suspects in the optical characterization of GLAD square spiral PBCs in the next chapter.

No Text

## Chapter 8

# Bandgap Engineering: Optical Characterization

Following the development of scalable substrate seed layers and new square spiral GLAD structures, the objective of this chapter is to characterize the optical properties of the new GLAD films and evaluate the photonic crystal engineering potential. It must first be shown that bandgaps do exist and are complete in all three dimensions, with more comprehensive experimental evidence than what has previously been published for square spiral PBCs. The bandgap engineering capability must then be assessed by investigating photonic bandgaps at higher and more useful frequencies in down-scaled square spiral GLAD PBC films. Finally, the success of efforts to create square spiral films with better uniformity and tighter controlled, more ideal structures must be judged by comparison of the bandgap properties with theoretical expectations and earlier experimental data.

The thesis research presented in this chapter is under preparation for publication.

### 8.1 Methodology

#### 8.1.1 Transmittance and Reflectance

As discussed in chapter 2, the characteristics of a photonic bandgap are evaluated by examining the transmission through and reflection off a candidate crystal structure as a function of the frequency of the impinging electromagnetic waves. In ideal crystals the reflection becomes complete and the transmission nil at bandgap frequencies, with the opposite true outside the

bandgaps. For the bandgap to be complete and three-dimensional, this behaviour must be maintained for all light incidence angles and polarizations. Complementary evaluation of both reflection and transmission is required to eliminate simple absorption or surface scattering effects as sources of low transmission or abnormal reflection, respectively.

In practise, optical transmission and reflection is measured as transmittance  $T$  and reflectance  $R$ , i.e., the optical power transmitted  $P_t$  or reflected  $P_r$  relative to the incident power  $P_i$ :

$$T(\lambda) = \frac{P_t(\lambda)}{P_i(\lambda)}, \quad (8.1)$$

$$R(\lambda) = \frac{P_r(\lambda)}{P_i(\lambda)}. \quad (8.2)$$

Many optical instruments cannot simultaneously measure the incident and outgoing power, especially in reflectance setups. The absolute transmittance and reflectance 8.1-8.2 must then be replaced with a 'relative' transmittance and reflectance, defined against references that approach 'ideal' transmitters and reflectors (e.g., air and gold):

$$\%T(\lambda) = \frac{T_{abs}}{T_{ref}} = \frac{P_t/P_i}{P_{t,ref}/P_i} = \frac{P_t}{P_{t,ref}}, \quad (8.3)$$

$$\%R(\lambda) = \frac{R_{abs}}{R_{ref}} = \frac{P_r/P_i}{P_{r,ref}/P_i} = \frac{P_r}{P_{r,ref}}. \quad (8.4)$$

The same approach is used with suitable references to isolate the spectral response of PBCs in situations where the PBCs cannot be physically isolated from, for example, the substrates that they are mounted on. The challenges and impact of choosing the right reference will be discussed in detail later.

### 8.1.2 Instrumentation Requirements

Practical transmittance and reflectance measurements on photonic crystals are non-trivial. Contrary to traditional integrated and fibre optics, which concentrate on narrow frequency bands, PBC measurements must be broadband to cover both the full bandgap and surrounding frequency ranges. Often the exact position of the bandgap cannot be safely predicted in advance, which calls for even higher spectral width. For square spiral GLAD PBCs the bandgaps can be expected to fall in a NIR range of wavelengths from 1 and 4  $\mu\text{m}$ , which straddles the useful spectral ranges of various optical components and instruments without being perfectly covered by any of them.

PBC characterization also requires high spectral resolution to pick up band edges and transmission spectrum fringes. As bandgaps must sometimes be identified amidst scattered light from crystal disorder and inherent material absorption in, e.g., the substrate, one should aim to employ high output sources, high throughput optical paths, and sensitive detectors.

Not only must both transmittance and reflectance measurements be possible, but the instruments should allow these measurements to be performed at variable angles of incidence on the PBC, and with variable polarizations. In order to ensure specular probing of one crystal direction at a time, the numerical aperture of the source and detector – as seen from the PBC – should be small, so that the incident light beam has a small angular spread and approaches a collimated plane wave. A low numerical aperture, however, also reduces the energy throughput and limits how small the beam spot size can be made.

### 8.1.3 FTIR Spectrometry

No optical instrument perfectly addresses all of the above requirements, but Fourier transform infrared (FTIR) spectroscopy delivers on many of the key issues. It was used here as the primary measurement tool. In FTIR spectroscopy the output from a broadband infrared source is first sent through a Michelson interferometer with one fixed and one moving mirror, which creates an interference signal whose power depends on the path difference between the mirrors. The signal is then modulated by the sample under analysis, and registered by a detector as an interferogram (i.e., power as a function of the mirror path difference). In accordance with Fourier theory, Fourier transformation of the interferogram now yields a spectrogram, i.e., the desired optical power as a function of spatial frequency [213].

The key advantage (the so-called Fellgett advantage) of FTIR spectrometry is that every point in the interferogram contains information about every frequency emitted by the source. In contrast to traditional dispersive spectrometers, every frequency in the spectrum is therefore being detected simultaneously (some spectrometers do measure all frequencies at once using CCD arrays). A second advantage (the Jacquinot advantage) is that this allows the full intensity of the source to be employed at all times, whereas in dispersive instruments the output is cropped by a narrow slit that mechanically filters out one frequency as a time. The time to obtain a spectrum is given by the mirror scan cycle, and is typically a few seconds. It is thus feasible to repeat each scan multiple times to eliminate random noise, and in

combination with the high optical throughput provide good signal to noise ratios and high sensitivity. The resolution of FTIR spectrometry is high, and depends on the extent of the mirror movement. It can be sub nanometre for even a 1 cm mirror movement [213].

The FTIR spectrometer used here was a Thermo Nicolet Nexus 670, with a broadband EverGlo source and liquid nitrogen cooled mercury cadmium telluride detector. The Nexus 670 has a built-in HeNe laser for internal calibration and visual sample alignment in the beam, while an attached computer performs real-time Fourier transformation of the spectra. To remove atmospheric spectral artifacts, the sample chamber is continuously purged with nitrogen. While delivering a usable wavelength range from 1.3 to 16  $\mu\text{m}$ , the instrument was limited to the 1.3 to 4  $\mu\text{m}$  range relevant here, with a resolution of 1 nm and a beam spot size of approximately 1 mm. Typically, 32 to 64 scans were recorded for each spectrum. For each sample the detector gain and source aperture were adjusted to optimize the energy throughput, while at the same time ensuring that the detector did not saturate, and that the aperture was small enough to maintain the desired resolution.

For reflectance measurements a Pike Technologies VeeMAX II variable angle specular reflectance accessory was used. It is mounted inside the main sample chamber and uses a series of mirrors to direct the beam to the surface of the sample. The sample must be positioned in the accessory with the PBC surface facing down, with some risk of damaging the edges of the fragile GLAD films. For polarization dependent measurements a wire grid polarizer with variable orientation is inserted. In both transmittance and reflectance measurements the beam is nearly collimated with a low numerical aperture.

Since only one beam is used in FTIR spectrometry, a background spectrum must be recorded for every sample spectrum to eliminate instrument effects such as frequency dependent behaviour of the source, detector, and beam steering mirrors. The sample spectrum is divided by the background. New background or reference spectra must also be obtained when the light incidence angle or polarization is changed, or when the instrument settings are altered.

#### 8.1.4 Spectrophotometry

Spectrophotometry was used as a secondary technology for GLAD PBC characterization. Although for the present purposes the performance of spectrophotometers does not match that of FTIR spectrometers, it is still

important to verify the FTIR spectral response on a different platform to ensure that the spectral characteristics are not just an artifact of, for example, the FTIR instrument or the Fourier transformation. As a dispersive technique, spectrophotometry is based on diffracting the light from a broadband source off of a moving grating and using a slit to filter out narrow frequency bands one at a time. The nearly monochromatic light is next split into two constant-length beam paths, with one being empty and the other containing the sample under analysis. For each frequency band a detector first measures the power in the sample beam, and then divides it by the power measured from the empty reference beam to eliminate fluctuations and frequency dependence in source, detector, and components. The monochromator grating is then advanced and the process repeated until a full spectrum is obtained. To remove substrate effects, reference samples can be placed in the reference beam, or background spectra can be recorded separately and divided into the sample spectra.

A Perkin Elmer Lambda 900 spectrophotometer was used, with a tungsten-halogen source, two monochromators, and a thermo-electrically cooled lead sulfide detector. Of its maximum spectral range of 175 to 3300 nm, the 900 to 3300 nm range was employed. The slit width determines the spectral resolution and energy throughput, and was set to yield 2 nm resolution or better. It is automatically adjusted to maximize the throughput for a better signal to noise ratio, while simultaneously preventing detector saturation and maintaining the set resolution. Random noise was minimized by integrating the detected signal over at least 0.25 seconds for each frequency step.

Compared with FTIR spectrometry the main drawbacks of spectrophotometry are a larger and less collimated beam (the typical spot size is 10 mm<sup>2</sup>), and a smaller energy throughput causing weaker and more noisy signals. To reduce the spot size and increase the power hitting the actual GLAD PBC, additional focusing optics were mounted on high precision *xyz*-stages and placed in the beam path. With the *xyz*-stages the optimum focal lengths could be found, and the receiving post-PBC optics aligned with the pre-PBC delivery optics. The pre-PBC lens was a Thor Labs calcium fluoride plano-convex lens with a numerical aperture of 0.30, while the post-PBC lens was an ISP Optics calcium fluoride hemi spherical lens with a NA of 0.66. Calcium fluoride lenses are nearly achromatic in a wide range from UV to mid-IR. For better achromatic performance and lower losses, reflective optics – such as Cassegrain objectives – could be used. Reflective objectives do suffer from high numerical apertures and central obscuration of the beam, but through systematic measurements at several different angles, both of these detriments can be calculated out of the spectra [227].

## 8.2 GLAD PBC Bandgap Verification

### 8.2.1 Initial Spectral Response

Reflectance spectra for four different GLAD square spiral films are shown in figure 8.1. The spectra were all obtained using FTIR spectrometry, but are depicted individually as they were recorded under different conditions and instrument settings. From figure 8.1a to 8.1d the square spiral dimensions gradually decrease, with the pitch  $p$  falling from  $1.40\ \mu\text{m}$  to  $1.26\ \mu\text{m}$ . Concurrently, the tetragonal lattice period  $\Delta$  drops from  $1.0\ \mu\text{m}$  to  $0.74\ \mu\text{m}$ .

The spectra contain one or more high reflectance bands of different widths, as well as low amplitude fringes between some of the high-reflectance bands. In each of the spectra one high-reflectance band dominates in intensity, and the wavelength of peak reflectance is found to decrease from  $3.3\ \mu\text{m}$  in figure 8.1a over  $2.6\ \mu\text{m}$  and  $2.1\ \mu\text{m}$  to  $1.65\ \mu\text{m}$  in figure 8.1d. Thus, the high reflectance bands qualitatively scale in wavelength in accordance with the gradual down-scaling of the square spiral dimensions. The fact that some of the spectra exhibit reflectances larger than 100% stems from the use of partly transparent glass/seed substrates as background references. This will be further discussed below in section 8.2.4.

Since high reflectance is one indication of the presence of a photonic bandgap, the spectra in figure 8.1 are consistent with photonic bandgap engineering through successful scaling of the square spiral GLAD films. However, a single spectrum is far from sufficient evidence of a photonic bandgap. To ascertain the bandgap engineering capability and the GLAD film structure optimization, the following sections will provide the most exhaustive investigation yet of the existence of complete bandgaps and the interpretation of the optical response for GLAD square spiral PBCs. Focus will be on GLAD films with the optimized square spiral structure developed in chapter 7, and with bandgaps near the attractive third telecommunications window, as represented by figure 8.1d. Not only is this wavelength range the most useful, but by being the lowest attempted for any GLAD PBC candidate, and requiring the smallest square spiral dimensions, successful results here should translate well to larger structures with more relaxed dimensions. For completeness, square spiral films with potential bandgaps at other wavelengths will be considered as well.

### 8.2.2 Confirming the Bandgap: Reflectance

The first task is to ensure that the spectral features of a candidate bandgap derive from the actual photonic crystal structure, and are not simply inher-

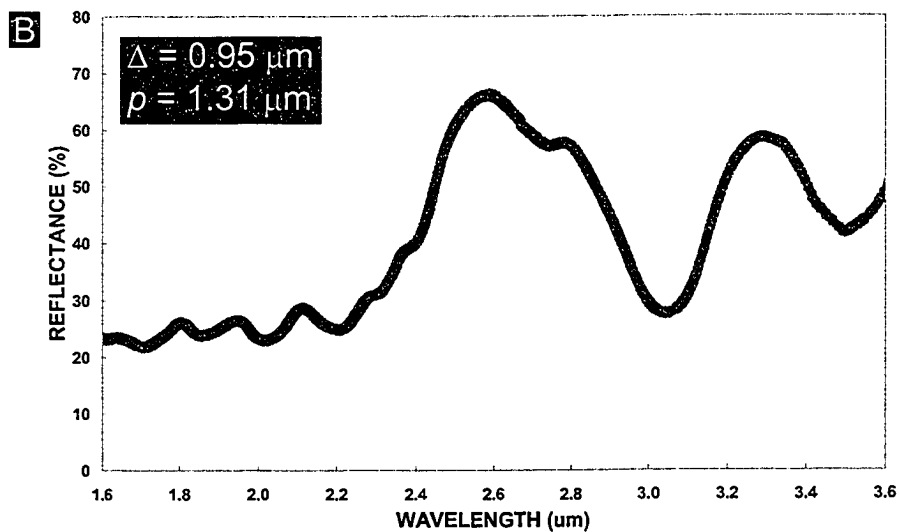
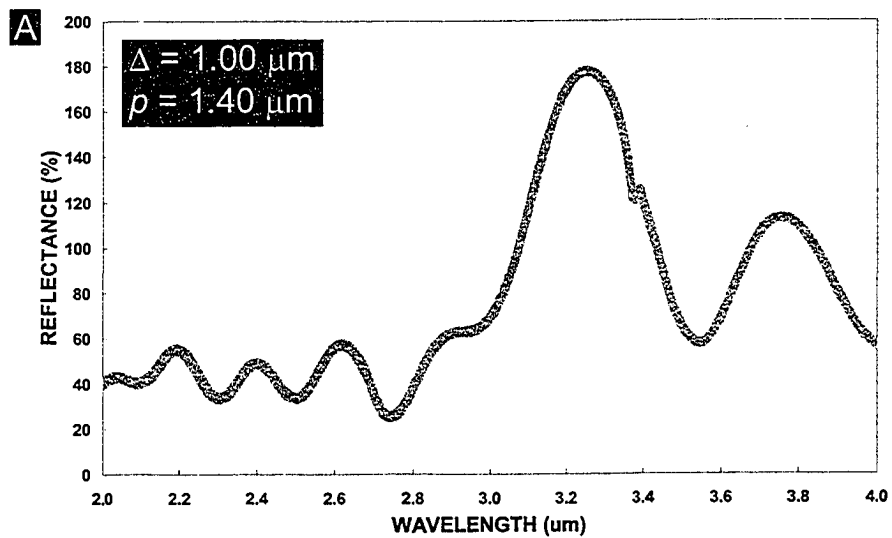
ent to the substrate, the seed layer, or the materials making up the crystal. This is a key analysis, which has not previously been performed for GLAD PBC films. To rule out interference effects from the optically thin layers, the sample constituents must be evaluated not just individually, but – since the PBCs have to be mounted on substrates – also as composite layers. Any optical instrument taints measurements with its own spectral characteristics, but for FTIR and spectrophotometry these effects are eliminated with the use of background scans and reference beams, respectively.

Performing reflectance measurements on GLAD PBCs on glass substrates from the backside, i.e., letting the light penetrate through the glass and seed layer into the GLAD film, is beneficial for accessing the highest quality part of the films, and for not damaging the fragile films by otherwise having to mount them upside down in the FTIR reflectance accessory. However, backside measurements also present the most complex sample system for reflectance measurements. A series of FTIR reflectance measurements was therefore performed on all the elements included in the complete GLAD photonic crystal sample:

- Bulk soda lime glass from stripped LDWL photo mask.
- Chrome layer on LDWL photo mask.
- Bulk silicon.
- Patterned chrome seed layer on soda lime glass.
- Dense silicon film on chrome seed layer on soda lime glass (with the optical thickness of the silicon film similar to that of the GLAD square spiral film).
- Aperiodic GLAD square spiral film on unpatterned chrome layer on soda lime glass (with the aperiodic GLAD film having the same thickness and structure as the periodic GLAD film).

All the measurements were performed with gold as the reference, which was assumed to yield a near-ideal reflectance response (flat and  $\sim 100\%$ ) in the frequency range of interest, and thus ensure a correct qualitative and quantitative evaluation of the materials above.

In figure 8.2 the black and grey curves show the reflectance of the soda lime glass, chrome, and silicon at an incidence angle of  $45^\circ$ . As expected, these three materials exhibit spectrally flat reflectance with no noteworthy features, except for a drop in the reflectance of the glass above  $2.7 \mu\text{m}$



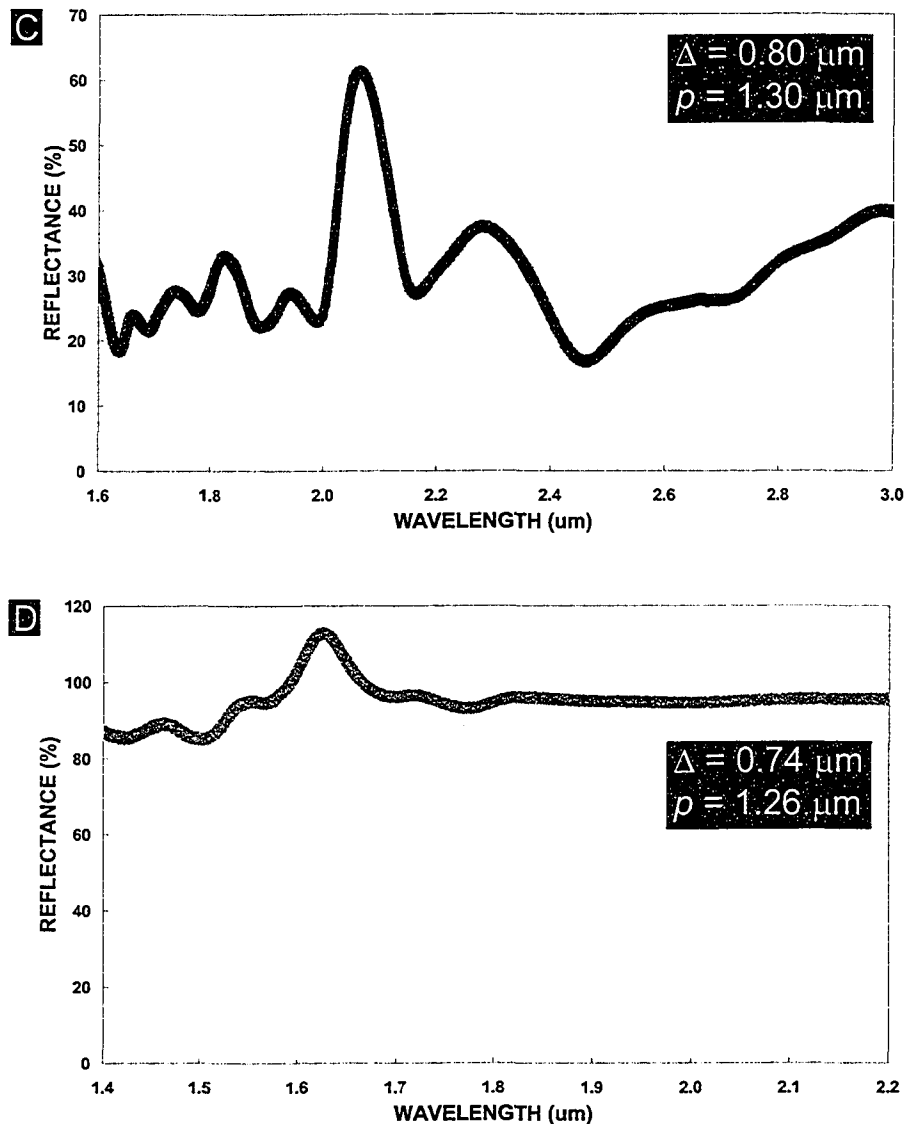


Figure 8.1: Reflectance of four different GLAD square spiral films whose dimensions shrink from a) through d). As the square spirals decrease in size – represented by the pitch  $p$  and the tetragonal lattice period  $\Delta$  – so does the wavelength of the dominant high-reflectance band in each spectrum. Some of the spectra were obtained by probing the films through the substrates, and exhibit reflectances larger than 100% due to the use of partly transparent glass/seed substrates as background references.

associated with increased absorption. The bulk silicon sample was an unpolished single crystalline silicon wafer surface, whose observed reflectance is in good agreement with published data [224, 228]. For the amorphous silicon in GLAD films the reflectance is slightly lower but still flat.

The chrome seed layer could potentially act as a diffraction grating, but as the green curve in figure 8.2 shows there is no spectral response from the seeds patterned on the LDWL soda lime glass substrate (the dip in reflectance above  $2.7 \mu\text{m}$  is still due to absorption in the glass). Indeed, the spectrum for the seeded substrate is as flat as that of non-patterned chrome on glass (not shown). The blue curves in figure 8.2 show the spectral response of thin silicon films on LDWL soda lime substrates. The dark blue curve is a square spiral GLAD film deposited simultaneously with a PBC GLAD film, but on an *unseeded* part of the glass substrate. The light blue curve is a dense, non-GLAD silicon film, deposited at normal vapour incidence angles on an unseeded glass substrate, and with the *same* amount of silicon deposited per unit substrate area as the square spiral GLAD film in the dark blue curve (i.e., with the film thickness corrected for the vapour incidence angle). This dense silicon thin film thus has an optical thickness similar to that of the GLAD films, when the latter are regarded as linear effective media consisting of silicon and air.

The aperiodic GLAD film shows no distinct spectral features, but does have a higher overall reflectance than the seed layer alone. Since this aperiodic GLAD film has the same effective refractive index as the periodic candidate PBC film, the presence of PBC-like spectral features arising from effective medium theory can also be ruled out. Meanwhile, the dense thin film exhibits a strong interference pattern with its reflectance oscillating between that of the bare glass and that of the aperiodic GLAD film for different wavelengths of light. This interference pattern derives from multiple reflection off the outer surfaces of the dense silicon film, in accordance with thin film calculations based on the Fresnel equations [213]. Although the aperiodic square spiral GLAD film has the same optical thickness as the dense silicon film, the random internal boundaries between silicon and air in the porous microstructure scramble the light in a non-coherent manner, and no interference fringes arise.

Apart from the interference pattern in the dense silicon thin film, no distinct spectral features that could falsely indicate a photonic bandgap are present in any of the samples in figure 8.2. Now compare this with the reflectance spectrum of the candidate GLAD PBC structure of periodic square spirals shown in figure 8.1d. The reflectance peak at  $1.65 \mu\text{m}$  nearly coincides with one of the interference fringe maxima of the dense silicon film,

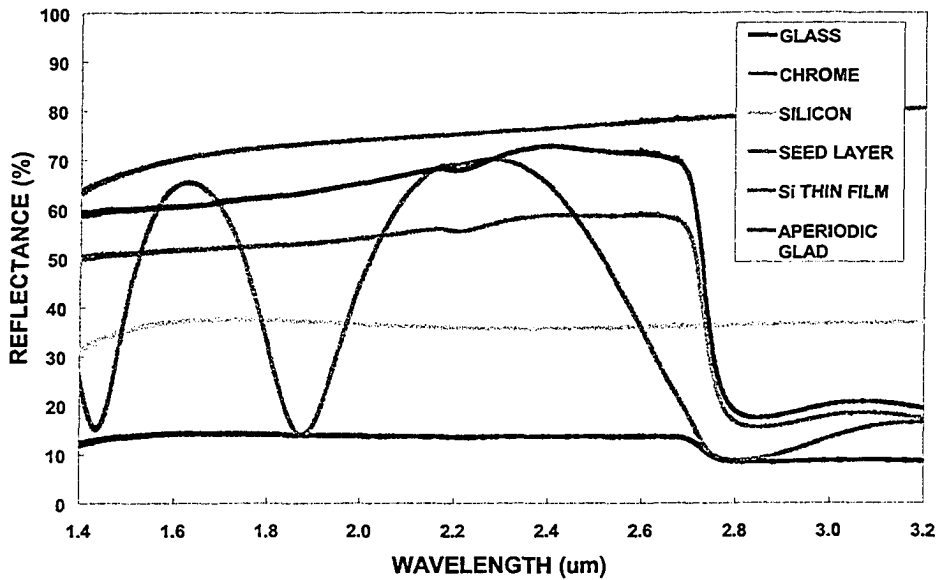


Figure 8.2: Reflectance spectra of the constituent materials in GLAD PBC samples (soda lime glass, chrome, and silicon), as well as chrome seed layers on soda lime glass, a dense silicon thin film on soda lime glass, and an aperiodic GLAD silicon film on unpatterned soda lime glass. All spectra were obtained at an incidence angle of  $45^\circ$  with a gold mirror as reference.

but the periodic GLAD film does not contain the other interference maxima of the dense silicon film, nor are the smaller fringes around the reflectance peak in the periodic GLAD film consistent with external surface interference. Also, whereas the wavelength dependence of the interference pattern in figure 8.2 is very sensitive to the angle of incidence, the high-reflectance region in the candidate GLAD PBC structure is largely independent of the incidence angle – a key requirement of 3D photonic bandgap crystals to be discussed below.

Thus, neither the individual constituent materials nor combinations of these are able to account for the reflectance spectra of the candidate GLAD PBC films. In particular, neither the seed layer, the optical thickness of the silicon, the porosity of the GLAD films, or the presence of a square spiral microstructure explain by themselves the observed high-reflectance regions. As would be expected for a true photonic bandgap crystal, only the *periodic* arrangement of silicon square spirals induces the observed candidate PBC reflectance spectrum.

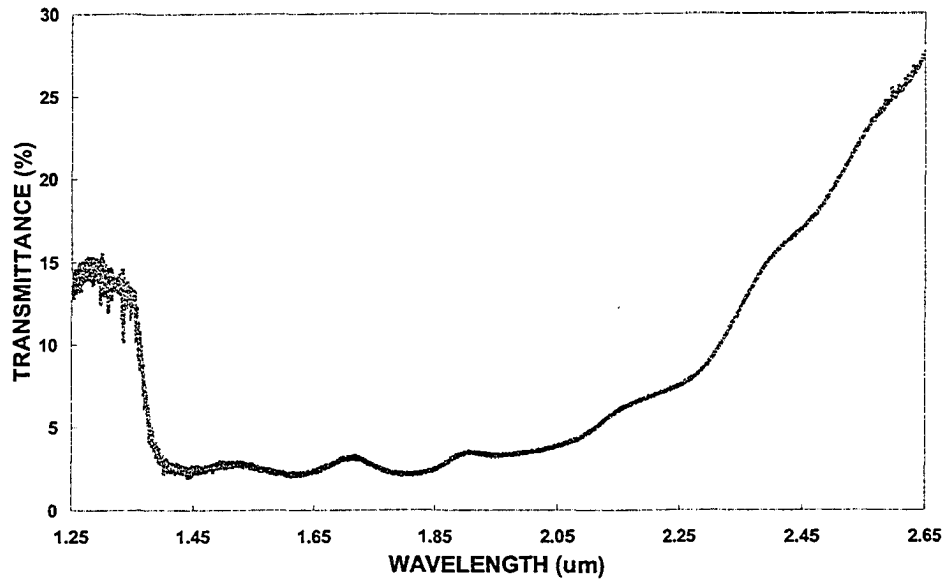


Figure 8.3: Transmittance spectrum of the periodic square spiral GLAD film previously characterized for reflectance in figure 8.1d. The low-transmittance band from  $1.4 \mu\text{m}$  to  $2.1 \mu\text{m}$  overlaps with the high-reflectance band, and is indicative of the presence of a photonic bandgap.

### 8.2.3 Confirming the Bandgap: Transmittance

A crucial requirement for the presence of a photonic bandgap is that high reflectance is accompanied by low transmittance, but transmittance measurements have never previously been performed for a GLAD square spiral film. Figure 8.3 shows a normal incidence FTIR transmittance spectrum for the same GLAD PBC candidate studied in the preceding section. A low-transmittance band is observed for the wavelength range  $1.4 \mu\text{m}$  to  $2.1 \mu\text{m}$ , with small fringes in the bottom of the stop band. At the low frequency edge of the stop band the transmittance rises toward 100%, while at the high frequency edge the transmittance increases even faster but only to a limited transmission value. The latter effect is commonly seen in 3D PBC structures [41, 46, 229].

The low-transmittance band includes – and is wider than – the high-reflectance band of the reflectance spectrum in figure 8.1d. Although the reflectance and transmittance do not add to 100% (due to differences in measurement references), the complimentary spectra strongly indicate the

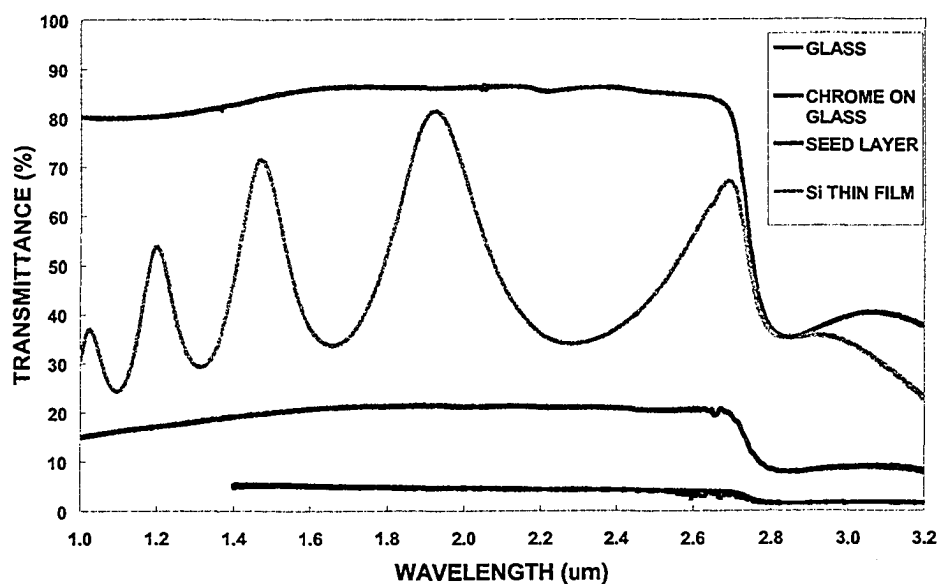


Figure 8.4: Normal incidence transmittance spectra of the constituent materials in GLAD PBC samples, including chrome seed layers on soda lime glass, and a dense silicon thin film on unpatterned soda lime glass.

presence of a photonic bandgap. However, as for the case of the reflectance spectra it must be verified that the low-transmittance band in figure 8.3 is indeed caused by the periodic GLAD square spirals. Normal incidence transmittance spectra for the various elements of the GLAD PBC sample are shown in figure 8.4, all with air as reference (i.e., an empty sample compartment). The spectra were obtained using spectrophotometry, except for the 'Chrome on glass' spectrum recorded by FTIR spectrometry. The transmittance spectrum of the soda lime substrate glass (red curve) agrees fully with the reflectance spectrum in figure 8.2, with a drop-off due to absorption above  $2.7 \mu\text{m}$ . Both the glass and the chrome on glass spectra (black curve) are otherwise featureless. The transmittance response of the periodic chrome seed layer (blue curve) also do not contain any spectral features reminiscent of the stop-band seen in figure 8.3, but the transmittance is roughly four times higher than that of the continuous chrome layer, which agrees well with a seed layer planar density of 25%. Finally, the previously investigated dense silicon thin film (green curve) has an interference pattern similar to the reflectance spectrum, which is incompatible with the wider stop band in the periodic GLAD square spiral film.

With a stop band now observed in both reflectance and transmission spectra, and this stop band caused by the presence of a periodically structured square spiral GLAD film, strong evidence for the existence of a photonic bandgap has been established. The bandgap investigated is furthermore located at the highest and most useful frequency yet seen for the square spiral PBC architecture.

#### 8.2.4 Optical References

An important aspect of relative optical power measurements is the choice of references against which the transmittance and reflectance spectra are quantified. This is frequently neglected by researchers, with published spectra being in ‘arbitrary units’ or relative to unspecified background spectra. Yet, without a judicious reference the interpretation of relative optical spectra becomes questionable. While not previously discussed in the literature, the nature of GLAD films presents special challenges with respect to references, since the desired optical properties (photonic bandgaps or otherwise) result from a complex interplay between material characteristics, structure, effective index, and porosity.

No direct structure GLAD photonic crystal can exist without being attached to a substrate and a seed layer, and although the previous sections showed that no bandgap-like spectral features are induced by the substrate materials or structure, substrate absorption and reflection will affect the GLAD film spectra both quantitatively and qualitatively. The ideal reference should eliminate these substrate effects.

Beyond the substrate issue, the purest references for transmission and reflectance measurements are vacuum (in practise air) and an ideal mirror (exhibiting flat, omni directional, and complete reflection of light), respectively. Potentially, the most ideal mirrors are none less than photonic bandgap crystals, but for practical purposes specular metal surfaces provide flat and high – though not constant – reflectance for broad angles of incidence and over wide frequency ranges. Substrate corrected spectra referenced against air or gold thus provide the closest approximations to ‘absolute’ reflectance spectra for GLAD films.

However, for applications purposes it may be equally relevant to reference the silicon GLAD PBC spectra against a silicon background, in order to eliminate spectral features of the *material* (e.g., absorption) and isolate the optical response of the periodic square spiral *structure*. A dense silicon reference might be an option, but as illustrated in figure 8.2 the resulting interference fringes make this approach amount to referencing a 3D PBC

against a 1D PBC. A porous silicon reference with a density similar to that of the GLAD film under investigation would more accurately account for the effective refractive index, but porous materials inherently have microstructures which themselves affect the optical properties. The ideal porous reference would then be a granular sample of randomly oriented silicon square spirals with the same effective index as the GLAD PBC candidate. This is not a readily achievable reference, though, and the best practical reference for eliminating material and density effects is the aperiodic GLAD square spiral films growing on an unseeded substrate.

For the GLAD PBC transmittance spectra presented in this chapter, empty seed layers on soda lime glass were used to reference out the substrate effects. As documented in figure 8.4, the seed layer reference accounts for the loss of transmittance through the substrate without adding unintended spectral features. Backside reflectance spectra of GLAD PBCs were referenced against either a gold covered seed layer on glass substrate, or aperiodic square spiral GLAD films. As verified by figure 8.2, both the seed layers and the aperiodic GLAD films have flat responses. Aperiodic GLAD films generally have a lower reflectance than PBC GLAD films at bandgap frequencies, and the obtained PBC spectra will therefore often exhibit *relative* bandgap reflectance values larger than 100%. Of course, the *absolute* PBC reflectance is always less than 100%.

It is important that instrument settings are maintained constant for corresponding reference and sample spectra, and that a new reference is used for every change in light incidence direction or polarization, given that no practical reference has constant, omni directional transmittance and reflectance. Furthermore, since no two seed layers develop exactly the same – particularly with respect to chrome etching of LDWL patterns – seed layers used for referencing should be from the same batch as the seed layer used for the GLAD film. Only spectra with the same type of reference can be compared.

### 8.3 GLAD PBC Bandgap Characterization

Having established strong evidence for the presence of high frequency photonic bandgaps in square spiral GLAD films, the next task is to determine whether the bandgaps are complete, i.e., are maintained for all crystal or light incidence directions and for all polarizations of the light. Previous optical measurements on GLAD PBCs were performed with Cassegrain objectives and hence wide angle cones of incident light that blur the directional characteristics of the bandgaps, both latitudinally (half cone angles of 20 to

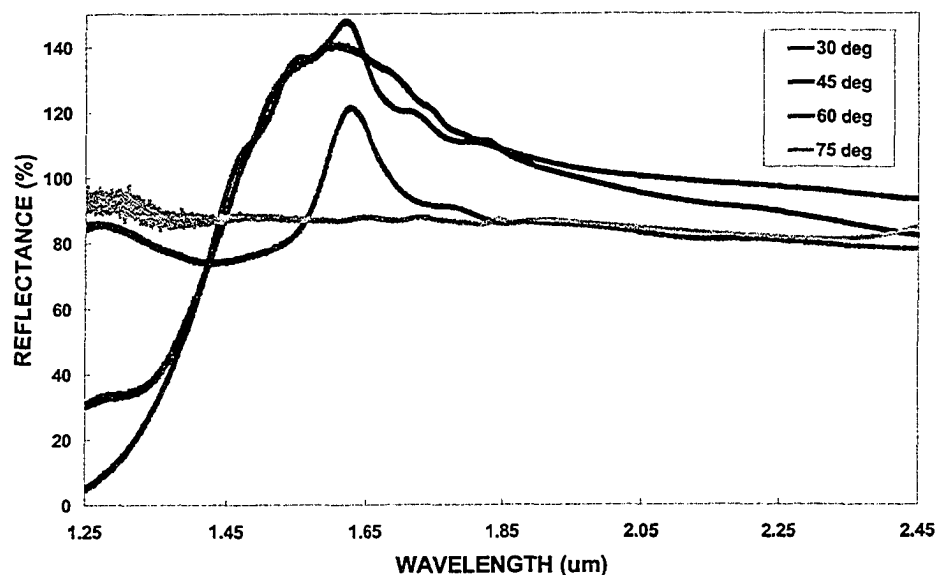


Figure 8.5: Reflectance spectra for a square spiral GLAD PBC at various external light incidence angles (referenced against an equivalent aperiodic square spiral GLAD film). The photonic bandgap position remains constant, indicating that the bandgap is complete with respect to crystal direction. At  $75^\circ$  most of the light is reflected off the glass substrate before hitting the PBC.

$35^\circ$ ) and longitudinally (over the full  $360^\circ$ ). Here, specular reflectance measurements were employed to probe individual directions in the new GLAD PBCs, complemented by the first directional transmittance measurements.

### 8.3.1 Directional Invariance of the Bandgap: Reflectance

Figure 8.5 shows FTIR backside reflectance spectra with external angles of incidence from  $30$  to  $75^\circ$  for the high frequency GLAD PBC previously investigated in figures 8.1d and 8.3. Each measurement was performed with a matching reference of aperiodic square spirals. It is first noted that the reflectance spectrum for  $75^\circ$  incidence is almost completely flat and also quite noisy. This is due to the fact that the reflection coefficient for the glass substrate, through which the light passes en route to the PBC, rapidly increases for incidence angles higher than  $70^\circ$ , as described by the Fresnel equations [213]. Almost no light then hits the actual PBC.

For external incidence angles of 30 to 60° a distinct high-reflectance band is observed. Critically, these bandgaps overlap and maintain their position even as the angle of incidence is altered. This is fundamental and required new evidence in support of GLAD square spiral PBCs exhibiting complete bandgaps. It also rules out simple, one dimensional thin film interference as being responsible for the stop bands.

The high frequency bandgap edges for the 45 and 60° spectra in figure 8.5 coincide perfectly with the normal incidence transmittance spectrum for the same PBC in figure 8.3. At all angles both the transmittance and reflectance spectra exhibit a more gradual tapering of the low frequency bandgap edge, with the exact edge harder to define. Yet, even at the low frequency edges the similarities between the 45 and 60° reflectance spectra and the 0° transmittance spectra are striking. The 30° reflectance spectrum appears to have a pinched high frequency edge, even while the low frequency edge matches those of the higher incidence angles.

In chapter 2 it was discussed that Snell's law of refraction is invalid in photonic crystals. This makes it difficult to translate the direction of an externally incident beam of light to an exact propagation direction inside the crystal. Ideally, refraction can be eliminated by cutting the photonic crystal along planes perpendicular to each of the crystal directions of interest, and letting the beam impinge normal to these facets. This, however, is not feasible for GLAD films. Using Snell's law with the 'DC' effective refractive index of the GLAD PBC calculated in equation 7.15 in chapter 7:

$$\sin \theta_{crystal} = \frac{n_{air}}{n_{eff}(\text{GLAD PBC})} \sin \theta_{air}, \quad (8.5)$$

provides a crude estimate of the actual crystal direction. Although the stated crystal directions should not be considered rigorous, the external light incidence angles in figure 8.5 thus correspond to internal propagation angles of 14, 20, 25, and 28°, relative to the substrate normal. The substrate normal corresponds to the  $\Gamma$ -Z direction in the tetragonal lattice of the PBC, in accordance with the irreducible Brillouin zone shown in figure 4.3. All the reflectance measurements were performed with the tetragonal lattice aligned parallel to the light incidence plane, so that the crystal directions or  $\mathbf{k}$  vectors all lie in the  $\Gamma$ -Z-R-X plane of the Brillouin zone. Thus, while normal incidence corresponds to the  $\Gamma$ -Z direction, an increase in the angle of light incidence corresponds to moving toward the  $\Gamma$ -R direction.

Inspection of the generic square spiral PBC band structure in figure 4.3 shows that the local bandgap in the  $\Gamma$ -Z direction – equivalent to normal

light incidence here – is particularly large, in agreement with the wide stop band noted in figure 8.3. Meanwhile, the R point in the Brillouin zone – which is approached as the angle of incidence is increased – limits the high frequency edge. This indicates that in crystal directions closer to  $\Gamma$ -R the local bandgaps are inclined toward lower frequencies and smaller bandgaps. As the  $\Gamma$ -X direction is approached, the local bandgap shifts to higher frequencies again.

It is thus possible that the  $30^\circ$  spectrum in figure 8.5 results from a high frequency pinch in the PBC dispersion relation in the  $\Gamma$ -R like crystal direction, and that the  $45^\circ$  and  $60^\circ$  bandgaps are likewise slightly narrower than the normal incidence bandgap. However, the generic square spiral band structure in figure 4.3 may not be applicable to the particular GLAD square spiral structure investigated here, since the higher frequency air bands in particular (including the R point limit) vary significantly with the detailed fine structure. Also, band structures for 3D PBCs normally only cover the high symmetry points in the Brillouin zone, and cannot be used to interpret local bandgaps at all intermediate crystal directions. The band structure in figure 4.3, for example, does not explicitly detail the size of the bandgap in the  $\Gamma$ -R direction. For one-to-one comparison of the spectra in figure 8.5 with theory, significant modelling outside the scope of this thesis has to be performed. Additionally, given the oddly high reflectance of the  $30^\circ$  spectrum below the air band edge of the other spectra, the low wavelength part of this particular measurement might be unreliable for comparison with theory.

Figure 8.6 shows the effect of rotating the above analyzed GLAD square spiral PBC so that the light incidence plane is  $45^\circ$  off the  $[100]$  and  $[010]$  base vectors of the tetragonal lattice. This corresponds to light propagation in the  $\Gamma$ -Z-A-M crystal direction plane in the Brillouin zone. Although the low frequency delineation of the FTIR reflectance spectrum is rather weak, the high-reflectance bands of the off-axis and on-axis planes overlap very well. The photonic bandgap is hence maintained for both longitudinal and latitudinal crystal direction variations. In continuing the interpretation of the PBC spectral data in terms of the square spiral band structure in figure 4.3, with the off-axis direction being  $\Gamma$ -A like and the on-axis direction being  $\Gamma$ -Z like, the  $\Gamma$ -A direction does indeed tend toward a smaller, higher frequency local bandgap, in agreement with the observed.

Angular reflectance spectra for a different, lower frequency GLAD square spiral PBC are shown in figure 8.7. This GLAD film was of worse quality than the ones investigated above, resulting in rather narrow high-reflectance bands that just barely overlap as the angle of incidence is varied. The nar-

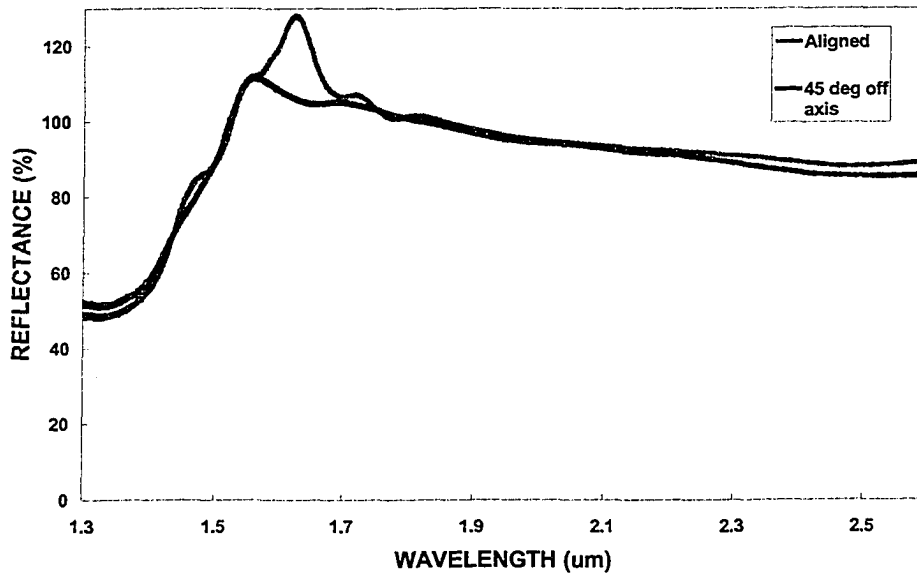


Figure 8.6: Reflectance spectra for the square spiral GLAD PBC analyzed in figure 8.5 (aperiodic GLAD reference), with light incident at  $45^\circ$  relative to the crystal  $\Gamma$ -Z direction, and either in the  $\Gamma$ -Z-R-X (aligned) or  $\Gamma$ -Z-A-M (off-axis) plane of the tetragonal lattice Brillouin zone.

rower local bandgaps and the smaller incremental changes in crystal propagation direction provide confirmation that the local square spiral bandgap does shift toward lower frequencies as the crystal direction move from  $\Gamma$ -Z toward  $\Gamma$ -R.

### 8.3.2 Directional Invariance of the Bandgap: Transmittance

For transmittance verification of the directional invariance of GLAD PBCs, consider first the FTIR spectra in figure 8.8 for the same square spiral GLAD film analyzed earlier in this section. The green curve is the transmittance spectrum at normal light incidence previously shown in figure 8.3, while the blue curve is the transmittance at an external light incidence direction of  $30^\circ$  and aligned with the tetragonal lattice (for a  $\Gamma$ -R like crystal direction). Although noise obscures the high frequency edge, the bandgap at  $30^\circ$  overlaps the one at normal incidence with nearly the same shape and size. The transmittance spectra are also complimentary to the reflectance spectra in figures 8.5 and 8.6, as expected and required for a complete bandgap. In-

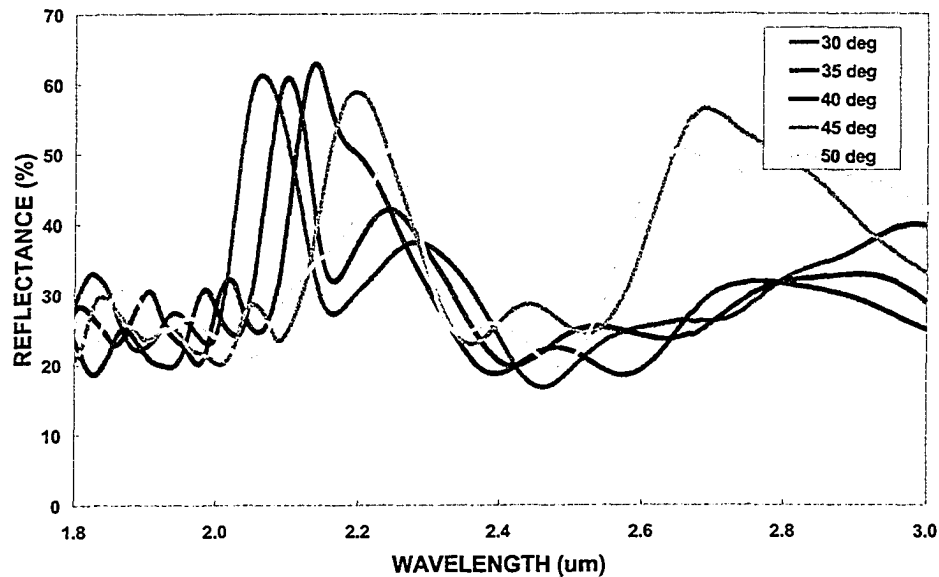


Figure 8.7: Reflectance spectra for a lower frequency square spiral GLAD PBC at various external light incidence angles (referenced against gold on glass). The local bandgaps in this lower quality film are too narrow to overlap, but a downward trend in frequency for higher incidence angles is evident.

deed, the bandgap exhibited in this 30° transmission spectrum fits the rest of the spectra and the theoretical expectations better than the 30° reflectance spectrum in figure 8.5.

Less noisy transmittance data for a different high frequency square spiral GLAD PBC are illustrated in figure 8.9, again for 0 and 30° angles of incidence. The overlap of the bandgaps remains excellent, with a distinct low-transmittance band that hardly changes with the crystal propagation direction. Aside from the smoother air band edge, the similarities between the GLAD PBC transmittance spectra in figures 8.8 and 8.9 are pronounced.

### 8.3.3 Polarization Invariance of the Bandgap

In addition to being maintained in all crystal directions, a complete photonic bandgap must sustain all polarizations of the impinging light. Indeed, the spectra analyzed so far in this chapter were obtained with unpolarized light, and hence *could* represent bandgaps that only exist for certain polarizations.

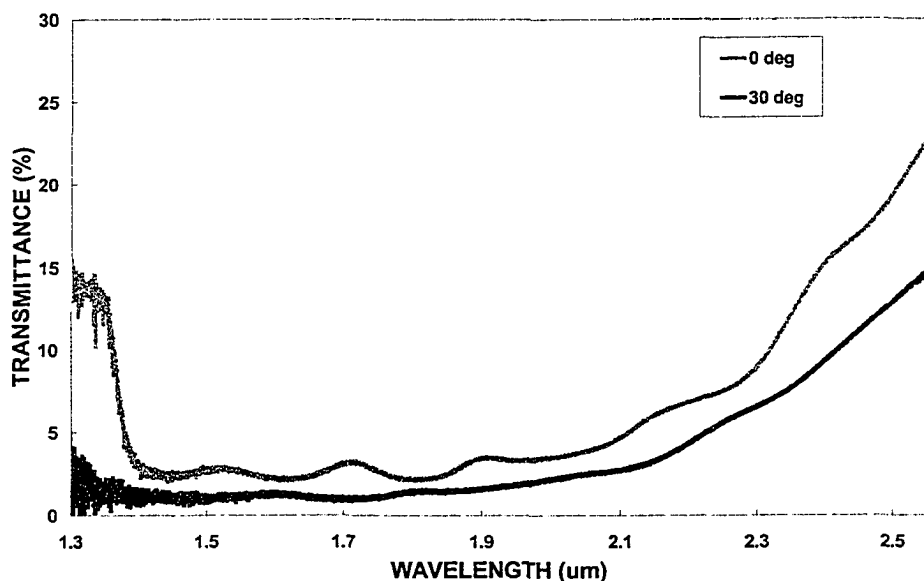


Figure 8.8: Transmittance spectra for a square spiral GLAD PBC at external light incidence angles of 0 and 30° (referenced against seeds on glass). The photonic bandgap position and size are constant.

Figure 8.10 shows reflectance spectra for a GLAD square spiral PBC at an external light incidence angle of 30°. The red spectrum shows the PBC reflectance for unpolarized light, and is similar to the red curve in figure 8.5. The blue spectrum shows the PBC reflectance for *s* linearly polarized (or TE polarized) light, i.e., for electromagnetic radiation in which the electric field is perpendicular to the plane of incidence. The orange spectrum in figure 8.10 shows the PBC reflectance for the case of *p* polarized (or TM polarized) light, with the electric field parallel to the plane of incidence. The black and green spectra represent intermediate linear polarization directions, with the angular label indicating the setting of the rotating wire grid polarizer in the FTIR spectrometer ('30 deg' being predominantly *s* type and '60 deg' being predominantly *p* type).

A high reflectance region is maintained for both *s* and *p* and the intermediate polarization directions in figure 8.10, and the position of this stop band is invariant to the polarization direction. Since all polarization types can be constructed from linear combinations of *s* and *p* polarized light, the spectra shown fully detail the polarization dependent behaviour of the photonic bandgap for the particular crystal direction. This is the first experimental

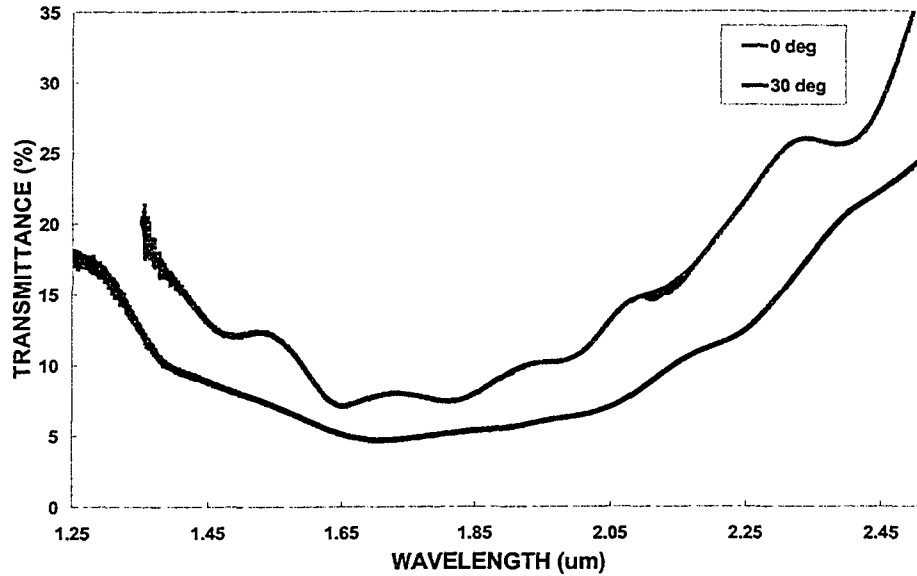


Figure 8.9: Transmittance spectra for a square spiral GLAD PBC at external light incidence angles of 0 and 30° (referenced against seeds on glass). The photonic bandgap position and size are constant with respect to the crystal propagation direction.

verification of a GLAD square spiral photonic bandgap being complete for all polarization directions, and emphasizes the advantage of 3D PBCs over 2D PBCs, which in many cases yield bandgaps only for *s* or *p* polarization.

As would be expected, the reflectance spectrum for unpolarized light in figure 8.10 resembles an average of the spectra for the four linearly polarized spectra. The one exception is the reflectance of pure *p* polarized light (the orange curve), which appears to be abnormally low. Indeed, even while a high-reflectance band exists at the bandgap frequencies, a still larger and stronger high-reflectance region appears at around 1.47  $\mu\text{m}$ . This anomaly is likely caused by the polarization selective reflectance of light through the sample and instrument system, where every boundary between two media work as a partial polarizer that reflects *p* polarized light weaker than *s* polarized light [213]. Indeed, reflectance measurements on an aperiodic GLAD square spiral film on glass under the same settings as used for the spectra in figure 8.10 showed the throughput of *p* polarized light through the FTIR instrument to be only 25% of the throughput of unpolarized light. (The wire grid polarizer itself lets through approximately one half of the intensity of

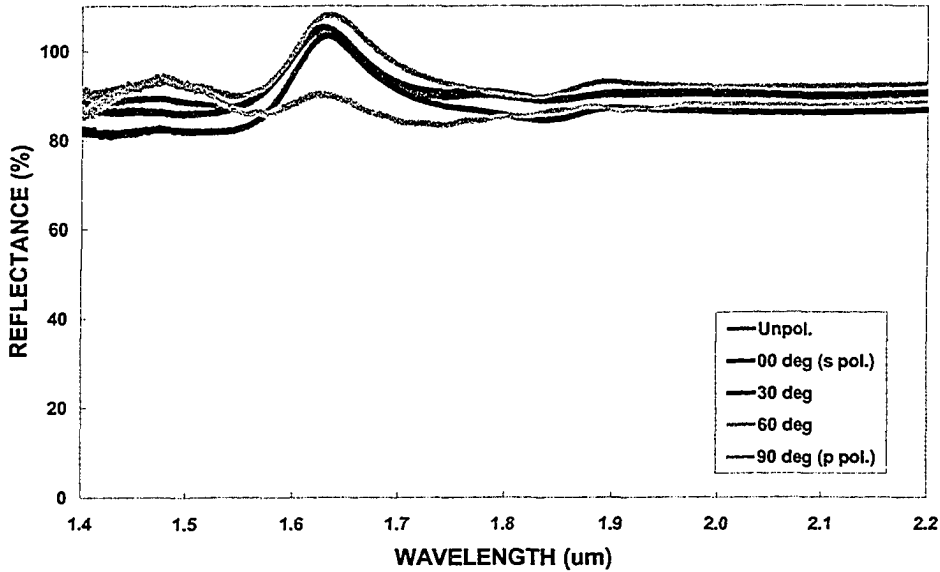


Figure 8.10: Reflectance spectra for a square spiral GLAD PBC for different linear polarizations of the impinging light ( $s$ ,  $p$ , and intermediate polarizations). The measurements were performed at an external light incidence angle of  $30^\circ$  and referenced against an aperiodic GLAD film. The photonic bandgap remains in place for all polarizations, indicating that it is a complete bandgap.

unpolarized light.) Thus, for pure  $p$  polarized light the sample and instrument are more lossy than for pure  $s$  polarized light, and less light hits the actual photonic crystal. In analogy with the poor spectra for high angles of incidence (see the  $75^\circ$  spectrum in figure 8.5), this leads to a weaker and noisier signal for pure  $p$  spectra, as is evident in figure 8.10.

The impact of light polarization was investigated at other angles of light incidence/crystal directions, with the bandgap location invariably found to remain constant irrespective of the polarization direction. However, as the angle of incidence is increased and approaches the Brewster angles for the various materials boundaries in the system, the selective transmission of  $s$  and  $p$  polarized light becomes more pronounced, and the spectra for  $p$  like polarized light become more noisy.

Having verified that the bandgaps of square spiral GLAD PBCs support all light polarizations not only provides required evidence for the bandgaps being complete, but also confirms the validity of the unpolarized spectra

discussed earlier in this chapter. The polarization analysis in figure 8.10 also reveals the impact of the materials system and measurement methodology on the polarization response of the PBC spectra.

## 8.4 Interpretation and Evaluation

### 8.4.1 A Real and Complete Photonic Bandgap

In summing up the optical characterization described so far, the following new results have been achieved for square spiral GLAD PBCs:

- A photonic stop band exists for *both reflection and transmission*.
- The photonic stop band genuinely stems from the *periodic arrangement of square spirals in a tetragonal lattice*, and not simply from the square spiral film microstructure, the seed layer geometry, the substrate, or intrinsic or composite properties of any of the constituent materials.
- The photonic stop bands overlap with little variation in frequency for all analyzed *specular crystal directions*.
- The photonic stop bands are maintained for *all polarizations*.

Additionally, the behaviour of the GLAD PBCs has been qualitatively rationalized with the available theoretical models previously published for square spiral PBCs.

In principle the above analyses should be repeated for every single crystal direction in a PBC. Yet, the optical data presented here are the most conclusive evidence to date of a real, complete, and three dimensional photonic bandgap in tetragonal square spiral GLAD thin films, corroborated by the previous diffuse reflectance measurements of Kennedy *et al.* [188] on low frequency GLAD PBCs. The quality of the bandgap data will be discussed below in section 8.4.3.

### 8.4.2 Bandgap Engineering

Figure 8.1 at the beginning of this chapter presented spectra for four different square spiral GLAD films fabricated with the growth algorithms developed in chapter 7. These spectra indicated potential bandgaps in a range of gap centre wavelengths from  $3.2 \mu\text{m}$  to  $1.7 \mu\text{m}$ . With the above optical characterization of the  $1.7 \mu\text{m}$  film – the most interesting and challenging case –

the presence of a complete 3D photonic bandgap has been demonstrated at a definitively higher frequency than the only previously reported GLAD PBC at  $2.7 \mu\text{m}$ . By extension, the remaining films in figure 8.1, and any other square spiral GLAD films with dimensions attainable by the new growth algorithms, can be expected to deliver bandgap properties at the designed frequencies.

The objective of establishing a new capability to engineer the bandgap position of GLAD PBCs has thus been achieved. In turn, this verifies the efforts of previous chapters to provide scalable seed layers, improve the fine structure of periodic GLAD films, and use new algorithms to down-size square spiral GLAD films. The close proximity of the  $1.7 \mu\text{m}$  GLAD film to the third telecommunications window further addresses the goal of extending the bandgap engineering flexibility to frequencies useful for optical applications.

### 8.4.3 Bandgap Enhancement and Comparison with Theory

Last but not least, the photonic bandgaps must be evaluated quantitatively to find the size of the bandgaps and judge the quality of the square spiral GLAD films. Focus will again be directed toward the  $1.7 \mu\text{m}$  crystals with an optimized square spiral structure.

In ideal photonic crystals (i.e., those existing in computer simulations), bandgaps are delineated by near-vertical, 0 to 100% increases in reflectance and drops in transmittance. However, in the real world the bandgaps are characterized by more gradual changes in reflectance and transmittance between finite values, and it is non-trivial to determine the bandgap edges. This is particularly so at the low frequency edge – as seen both in the spectra here and throughout the experimental literature – where the lower wavelength of the light makes the periodic crystal appear more homogeneous. The established experimental approach is to estimate the full width of the bandgap from half the relative maximum of each edge, which is a reasonably conservative way of discarding the trailing parts of the stop band. Where the tapering of the low frequency edge extends over a long range (as in many transmittance spectra), a more cautious measure is to cut off the bandgap width at the lowest ordinate value defined by the sharpest edge.

Based on this approach, the resulting bandgap edges, centres, and widths for the  $1.7 \mu\text{m}$  GLAD PBC for a number of external light incidence angles are shown in table 8.1. While shown as vacuum wavelengths, as per convention, the bandgap widths and centres were calculated using the frequencies of the bandgap edges. Where several experimental spectra were available for

Angle ( $^{\circ}$ )	$\lambda_{low}$ ( $\mu\text{m}$ )	$\lambda_{high}$ ( $\mu\text{m}$ )	$\lambda_{centre}$ ( $\mu\text{m}$ )	$\Delta\lambda/\lambda_{centre}$ (%)
0	1.37	2.18	1.68	45.6
30	1.56	1.75	1.65	11.5
45	1.50	1.74	1.61	14.8
45off	1.47	1.74	1.59	16.8
60	1.45	1.77	1.59	19.9
Complete	1.56	1.74	1.65	10.9

Table 8.1: Bandgap wavelength edges, centres, and relative widths as a function of the external light incidence angle (relative to the  $\Gamma$ -Z crystal direction) for the square spiral GLAD PBC structure studied in detail in this chapter. The ‘Complete’ bandgap is the smallest overlapping bandgap shared by all the different crystal directions.

the same incidence angle, the most well-defined edges have been used. The ‘45off’ bandgap is for the case of light incident in a plane  $45^{\circ}$  off the [100] and [010] square base vectors of the tetragonal lattice. The local bandgaps in different directions vary slightly in size and location – as discussed above in comparison with the theoretical band structure – but the ‘Complete’ bandgap data denote the all-angles bandgap, i.e., the *narrowest* frequency range shared by the bandgaps in *all* the probed directions. This bandgap, extending between the wavelengths of  $1.56 \mu\text{m}$  and  $1.74 \mu\text{m}$ , centred at  $1.65 \mu\text{m}$ , and with a width of  $180 \text{ nm}$  or  $10.9\%$ , is the true, complete bandgap of the photonic crystal.

### Bandgap Position

Certainly, the  $1.65 \mu\text{m}$  central wavelength position represents the highest bandgap frequency achieved for a square spiral PBC, but how does it compare with theoretical predictions? For the *optimized* direct structure, first nearest neighbour square spiral PBC, the bandgap centre is located at a vacuum wavelength given by [181]:

$$\lambda = \frac{\Delta}{0.36}, \quad (8.6)$$

where  $\Delta$  is the lattice period of the base (001) plane in the tetragonal lattice. For the GLAD PBC structure under analysis here, the lattice period of  $0.74 \mu\text{m}$  yields a prediction of:

$$\lambda = \frac{0.74 \mu\text{m}}{0.36} = 2.06 \mu\text{m}. \quad (8.7)$$

Clearly, the experimental bandgap is located at a much higher frequency than predicted. This discrepancy is caused by the dimensions of the GLAD square spiral film deviating from the ideal, optimized structure. Although strict comparison with theory requires a unique band structure to be computed for the actual dimensions of the GLAD film, existing published models on square spiral PBCs by Toader and John [181] provide a strong basis for explaining the blue shift of the GLAD PBC.

For the ideal square spiral PBC with the predicted gap centre at  $2.06 \mu\text{m}$ , the optimized volume fill factor  $ff_{V,ideal}$  of dielectric in air is 0.31. However, for the GLAD films examined here the dielectric volume fill factor is significantly lower. The eight helix turn GLAD films were measured with SEM imagery to have a thickness of  $11.8 \mu\text{m}$ , while during their deposition a cumulative silicon thickness of  $36.25 \mu\text{m}$  was recorded at normal incidence. Taking the substrate tilt  $\alpha$  of  $86^\circ$  into account, this amounts to a GLAD film volume fill factor of:

$$ff_{V,GLAD} = \frac{z(\alpha = 86^\circ)}{\sin(90^\circ - 86^\circ) \cdot z(\alpha = 0^\circ)} = \frac{11.8 \mu\text{m}}{\sin(4^\circ) 36.25 \mu\text{m}} = 0.214. \quad (8.8)$$

As discussed in chapter 2, and noted in numerous experimental PBC studies, a reduction in the dielectric content of a PBC leads to a blue shift of the bandgap. This is exactly what is observed here. Critically, and as one of the great advantages of the square spiral PBC architecture, this relatively large change in gap centre frequency can be achieved without closing the bandgap.

It is instructive to study in greater detail how the reduction in dielectric volume fill factor manifests itself in the GLAD square spiral PBC. Using SEM imagery the following dimensions were derived for the square spirals:

$$\begin{aligned} L &= 0.57 \mu\text{m} = 0.77\Delta, \\ p &= 1.26 \mu\text{m} = 1.70\Delta, \\ w/2 &= 0.13 \mu\text{m} = 0.17\Delta, \end{aligned}$$

where the last column denotes the dimensions relative to the tetragonal lattice period  $\Delta$  of  $0.74 \mu\text{m}$ . In the ideal optimized square spiral structure, on the other hand, the relative dimensions are [181]:

$$\begin{aligned} L &= 0.70\Delta, \\ p &= 1.35\Delta, \\ w/2 &= 0.20\Delta. \end{aligned}$$

Thus, for  $L$ ,  $p$ , and  $w/2$  deviations of +10%, +26%, and -15% are observed for the actual GLAD square spiral film. Assuming a circular spiral arm cross section, Toader and John derived from computer simulations that variations in the spiral pitch  $p$  would have almost no impact on the bandgap, while a 10% increase in the spiral arm horizontal length would slightly redshift and lower the gap. For a decrease in the spiral arm radius  $w/2$ , however, they found a significant blue shift [181], in full accordance with the experimental data above. Consequently, while the overall decrease in volume fill factor for the GLAD films is borne both by an increase in the spiral pitch and a decrease in the column radius, it is primarily the latter which is responsible for shifting the GLAD PBC bandgap centre down to  $1.65 \mu\text{m}$ . This shows that the bandgap engineering capability in square spiral GLAD PBCs depends not only on seed layer and film structure scaling, but also on the tighter control over the spiral dimensions and volume fill factor afforded by the new square spiral growth algorithms.

Finally, the modelled gap centre prediction is based on square spirals consisting of pure silicon ( $\epsilon_{Si} = 11.9$ ), whereas the actual silicon GLAD square spirals contains trace amounts of oxygen incorporated during the deposition process (an EDX compositional analysis is provided in chapter 10). The oxygen impurities lower the effective permittivity of the silicon, which in turn leads to a higher frequency but smaller bandgap. This effect will further contribute to raising the gap frequency of the analyzed GLAD PBC, although much less so than the dielectric fill factor.

### Bandgap Size

Consider now the width or size of the GLAD PBC bandgap. From table 8.1 the local bandgap width of 46% at normal incidence is unreasonably large, even when taking into account that the  $\Gamma$ -Z crystal direction delivers the largest local bandgap in the square spiral PBC architecture, with widths up to twice that of the complete, omnidirectional bandgap [181]. For the normal light incidence direction only transmittance data was obtained, and the local bandgap width was most likely inflated by the gradual tapering of the low frequency edge in these measurements. However, the  $\Gamma$ -Z direction does not limit the global bandgap in square spiral PBCs, and as evident from table 8.1 the normal incidence data has not inflated the final, complete bandgap

width. Much more important is that the R and A points in the tetragonal lattice Brillouin zone were probed, namely via the 30 to 60° aligned incidence and 45° off-lattice incidence measurements. These lattice points do limit the high and low frequency edges of the square spiral bandgaps, and their inclusion is therefore critical in any complete PBC characterization. Clearly, in the analyzed GLAD PBC the complete bandgap width of 10.9% or 180 nm is delimited by these very measurements.

For the ideal, optimized square spiral PBC with a dielectric volume fill factor of 31%, the bandgap width is 14.8%. However, when the volume fill factor drops to 21%, as for the GLAD film in question here, the optimized bandgap width is 12.4% [181]. Thus, the GLAD PBC bandgap of 10.9% represents not just a large gap for an experimental 3D PBC near optical telecommunications frequencies, but fits well with the theoretically predicted optimized bandgap width for the given fill factor. As mentioned above, it is a cardinal feature of the square spiral architecture that a large bandgap width can be maintained even as the square spiral dimensions are significantly altered to engineer a higher frequency gap position.

Two effects may have assisted the GLAD PBC in achieving a large gap width. First, the experimental data may reflect not just the true bandgap but also the additional pseudo-bandgap, which expands the ideal, theoretical square spiral PBC stop band from 15% to 22% (for a 31% fill factor – no theoretical data exists for a 21% fill factor) [181]. This is especially true at the low frequency edge, where the gradual tapering of the experimentally observed stop bands could be due in part to the pseudo-gap. Yet, most of the square spiral pseudo-gap width is on the high frequency edge, where the experimental data in fact exhibited sharper edges. While some pseudo-gap inflation of the experimental gap width must be assumed, the pseudo-gap is therefore unlikely to have manifested itself to the fullest theoretical extent. The other, much smaller effect is that the cross-section of the fabricated GLAD square spirals is elliptical rather than circular. As discussed in chapter 4, modelling has shown that a slightly rectangular cross-section squeezes another 1 percentage point of bandgap width out of the square spiral architecture, compared with circular or square cross-sections. Approaching an oblong shape with the elliptical cross-section may thus have increased the experimental gap width slightly.

When the same ‘full width half maximum’ approach used to find the 10.9% bandgap above is applied to the previously published optical data for a square spiral GLAD PBC [188], a bandgap width of 6.4% is found for the latter (with the gap centred at 2.66  $\mu\text{m}$ ). The GLAD square spiral PBC fabricated and analyzed here thus represents a 70% increase in

the available bandgap width. Since the same methodology was employed both in the present case and in the earlier reports, the improved photonic bandgap properties derive from a better square spiral GLAD film structure. The substrate seed layers designed and fabricated in chapter 5, and the improvements in film fine structure resulting from the new GLAD growth algorithms in chapter 7, have enabled the fabrication of GLAD square spirals whose shape and dimensions remain more uniform throughout the film by elimination of column bifurcation, broadening, fanning, and surface roughness, as well as inter-seed growth. The PBC films based on LDWL seed layers and the Off-Axis GLAD growth algorithm – which were the focus here – have been especially well suited to address these challenges.

### Bandgap Quality

In spite of the above results, square spiral GLAD PBCs are hardly ready to roll onto the shelves at Photon-Mart. In particular, the photonic stop bands do not yield ideal 100% reflection and 0% transmission in the full width of the bandgap, even if some of the experimental spectra have peaks of high reflectance and bandgap transmittances close to zero (such as in figure 8.8 with 20 dB attenuation). Furthermore, the predicted transmission band edge resonance fringes discussed in chapter 2 are all but absent here. These are indeed general problems for experimental 3D PBCs, caused by the quality issues imparted by the real world as compared to the theoretical world in computer models.

The first and inescapable detractor of experimental bandgap quality is the fact that real PBCs have finite rather than infinite dimensions, which immediately lead to more gradual stop band transitions. Real PBCs also have real surfaces, whose roughness invariably reduce the specular reflectance from 100% [230]. For GLAD PBCs, substrates are necessary to support the interleaving but non-interconnecting square spirals, and even though the seeds and substrate can be referenced out in relative measurements, they still cause directional scattering of the probing light waves. This in turn causes the spectral characteristics to blur. More scattering is caused by the thin silicon layer accumulating on the substrate for all GLAD algorithms.

Disorder within photonic crystals is well known to degrade the optical characteristics, especially at higher frequencies where the wavelength tends to approach the feature size of the imperfections. Disorder effects have been noted in almost all experimental PBC work [41], and modelling of square spiral PBCs have confirmed that the high frequency air bands change a lot when disorder among the square spiral dimensions is present [181,

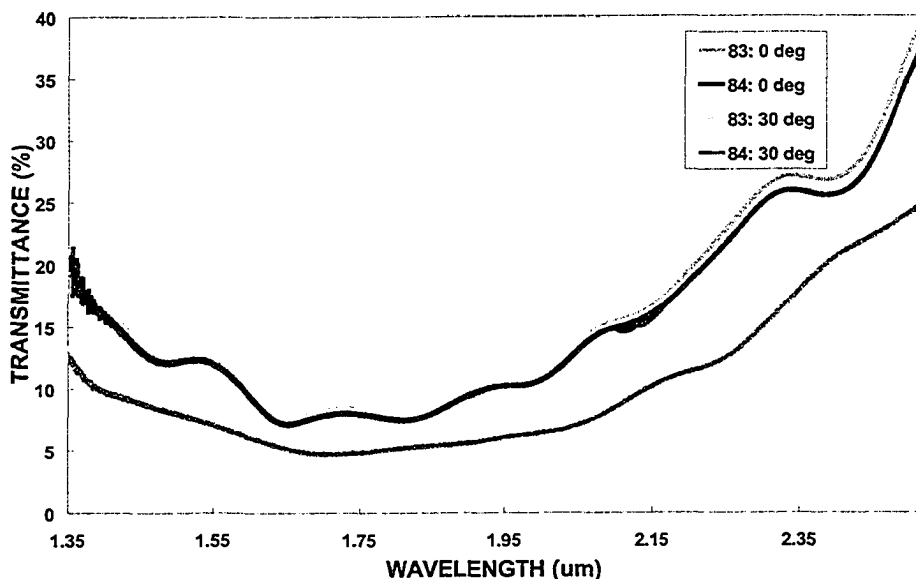


Figure 8.11: FTIR transmittance spectra for two different square spiral PBCs ('83' and '84') from the same GLAD batch. At each of the external light incidence angles of 0 and 30°, the spectra for the two crystals are nearly identical. This indicates good intra-batch structural and spectral consistency. ('84' data previously shown in figure 8.9).

188]. It is important here to distinguish between 'disorder', which represents variation in the square spiral dimensions inside one GLAD film without necessarily affecting the volume fill factor (via column broadening, fanning, etc.), and 'structural deviation', which represents the case in which the square spiral dimensions are *constant* throughout the film but not equal to the optimized, theoretical dimensions (as was just exploited to force a higher bandgap frequency at a lower dielectric fill factor). In both cases the square spiral PBC architecture is generally more robust than most other 3D PBC designs, but the bandgap quality is much more sensitive to 'disorder' than 'structural deviation'. Thus, in the previous GLAD PBC report by Kennedy *et al.*, the non-ideal bandgap properties were explained by disorder fluctuations up to 10% in the square spiral dimensions [188].

Both optical data and SEM imagery confirm that there is less disorder in the new square spiral GLAD films studied here than in those previously reported, hence yielding a stronger bandgap. Yet, despite the higher film uniformity, imperfections still cause undesired light scattering inside the

new GLAD films. One problem is ejection of micrometre sized chunks of silicon from the evaporant melt during deposition. These ejected particles not only embed themselves in the PBC as nodular defects, but also prevent further growth in their shadows to cause additional air defects. Another problem is that thick PBCs require several successive GLAD depositions to be performed. With current GLAD technology the deposition chamber must be reconfigured for each deposition stage, and it is difficult to maintain the exact same conditions for all stages. Thick GLAD PBCs thus become a multilayer structure of slightly different PBCs, which may be part of the reason why the transmittance stop bands appear broader and more blurred than the reflectance stop bands. Addressing these problems would require the development of new GLAD hardware with tighter substrate rotation control.

Apart from reducing the depth and obscuring the edges of stop bands, the above PBC quality issues tend to lower the width of the bandgaps, and may affect the bandgap frequency position. But in spite of these remaining quality problems, the uniformity and repeatability of the optical characteristics across individual crystals and between crystals in the same batch is good. Figure 8.11 shows transmittance spectra for two square spiral PBCs (labelled '83' and '84') deposited simultaneously on two different substrates. At both angles of incidence, the spectral consistency among the crystals is strong.

## Chapter 9

# Defect Engineering in GLAD Films

Photonic bandgap crystals are an interesting new class of optical materials in their own right, but they become truly useful only when defects are introduced to localize light or exploit the modification of radiative emission. Yet, the fabrication of designed defects in intricate 3D PBC structures has traditionally been an experimental challenge. This chapter presents thesis research on GLAD film defect engineering that avoids the complexity of post deposition film processing. In addition to the potential for waveguide fabrication in GLAD square spiral 3D PBCs, the defect engineering capability has sparked new GLAD applications and promises to serve existing ones.

The research presented here has been accepted for publication in the *Journal of Nanoscience and Nanotechnology* [231], with further publication in progress.

### 9.1 Defect Engineering in GLAD PBCs

Photonic bandgap crystals are made into functional devices by introducing defects that locally perturb the crystal symmetry. As discussed in chapter 2, electromagnetic radiation with frequencies within the bandgap can be localized at such defects, making point defects in 3D PBCs into optical cavities, and making line or plane defects waveguides for the propagation of light.

For waveguiding PBC defects in particular, a number of requirements must be addressed to achieve their full potential compared with traditional optical waveguides based on total internal reflection. The defects should

preferably have an air core, both in order to reduce absorption and maximize transmission, and in order to secure single-mode propagation (which is generally beneficial to optical information processing). Dielectric core PBC waveguides, meanwhile, tend to be multi-mode and to be less robust to scattering losses from structural imperfections [232].

Furthermore, the size of the waveguiding defect determines the frequencies and modal characteristics of the guided light. If the defect width is too small it may cut off propagation altogether, whereas large defect widths lead to multi-mode propagation. To facilitate propagation of the lowest (single) order mode, the defect width should be approximately one half of the gap centre wavelength [15]. For the ideal, optimized square spiral PBC this calls for a defect width  $s$  of:

$$s = \frac{\lambda_{centre}}{2} = \frac{\Delta/0.36}{2} = 1.39\Delta, \quad (9.1)$$

i.e., close to the lattice period  $\Delta$ .

As alluded to earlier, only a minimum of cavity and waveguiding fabrication has been demonstrated in 3D PBCs, with the main obstacle being experimental complexity. Almost all PBC waveguiding research has been performed in less complicated 2D PBC slabs, which suffer from diffraction losses and light leakage and really do not exploit the true potential of PBCs. In square spiral 3D PBCs the incorporation of intentional defects is also non-trivial. However, the GLAD technique does offer methods for defect engineering that are not readily available in other 3D PBC architectures. As illustrated in figure 9.1, three types of defect engineering can be envisioned for GLAD films:

- Seed layer induced defects.
- Multilayer defects.
- Micromachined defects.

*Seed layer induced* defect engineering is developed in this chapter as a new capability for patterning any GLAD film grown on a seed layer. By transferring defects initially defined in the seed layer directly to the GLAD film – without the need for any other pre or post deposition processing steps – it represents a unique method for defect engineering, not just for square spiral PBCs but also a number of other GLAD applications. Given the planar nature of GLAD films, however, seed layer induced defects remain open at the substrate and at the top of the film, and this requires additional

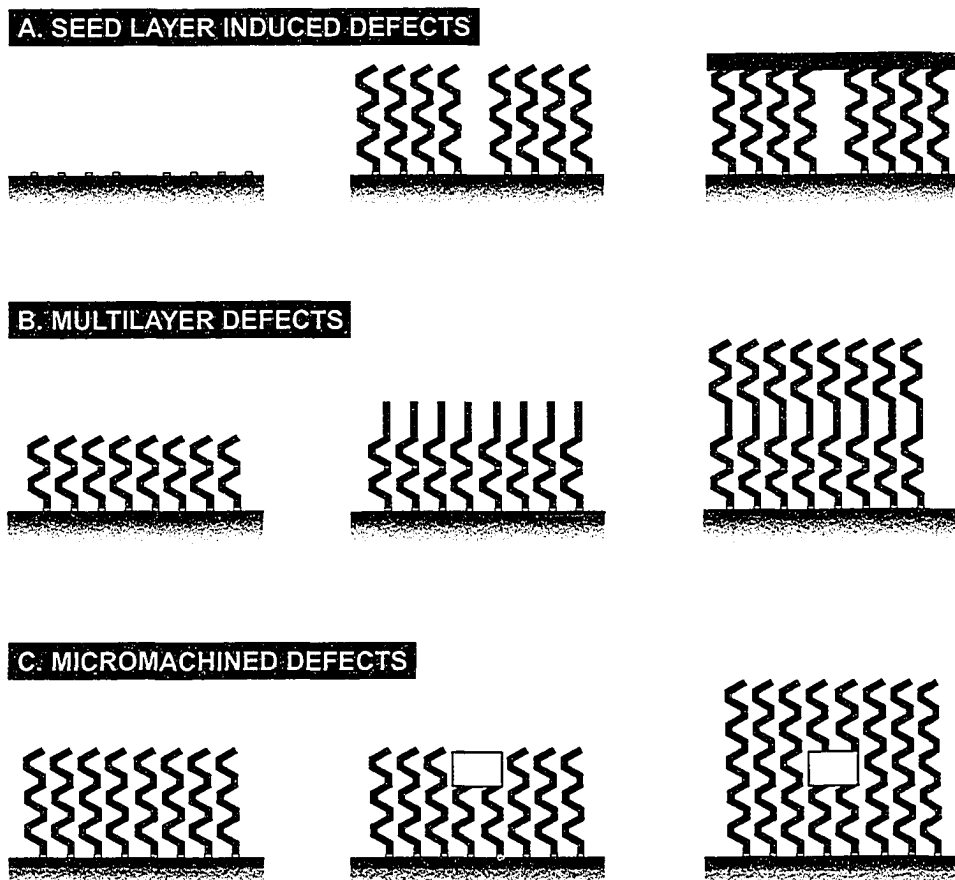


Figure 9.1: Schematic illustration of the three classes of defect engineering in GLAD square spiral films. Seed layer induced and multilayer defects are unique to GLAD and will be developed further in this chapter. Micromachined defects are the most suitable for point and line defects, but require complex post deposition processing.

wave bounding capping layers to be applied before such defects can be used to guide light.

*Multilayer* defects are engineered by stacking thin film layers with different microstructures. The method is highly amenable to implementation in GLAD, where a mid-deposition adjustment of the substrate rotation rate  $d\phi/dz$  and/or the vapour incidence angle  $\alpha$  immediately and smoothly creates a new film layer on top of the existing one, while preserving the film structure periodicity. In a square spiral GLAD film, a planar and potentially waveguiding horizontal defect can thus be inserted between two 3D PBCs, e.g., as a high density layer or by changing the spiral geometry or dimensions. This is discussed at the end of the chapter.

*Micromachined* defects are the most ideal for waveguides in square spiral GLAD PBCs, and the only way to build truly embedded point and line defects. It involves depositing a square spiral GLAD film, performing post deposition processing to leave a real or latent defect pattern in the film or in a dense capping layer on top of the film, and then continuing with a second square spiral deposition to clad the defect with PBC material on all sides. Post deposition lithographic patterning of GLAD films backfilled with photoresist has already been successfully demonstrated, along with the deposition of dense capping layers that could serve as the defect medium (see chapter 3). Apart from wet chemical etching, air defects could also be defined by laser ablation, ion beam milling, or dopant implantation, or even three-dimensional holographic lithography. Dielectric defects could be created using CVD on films masked with patterned sacrificial resist. There is thus every reason to believe that micromachining of defects in GLAD PBCs is feasible using existing microelectronic silicon processing technology, but implementing such defects will require a significant research effort – outside the scope of the thesis – with focus on optimizing post deposition processing without damage to the square spiral fine structure, and on enabling periodic GLAD films to be aligned with and grown on top of previously machined GLAD layers.

Modelling of waveguiding defects in direct structure, first nearest neighbour square spiral PBCs has been performed only for micromachined defects, by Chutinan and John [232,233]. They investigated the case of linear defects in a thin 2D PBC layer embedded inside a 3D square spiral PBC, obtainable in GLAD by depositing a dense capping layer on top of a square spiral film, etching cylinders and linear defects in the capping layer, and depositing a second square film off a seed layer on top of the patterned capping layer (see figure 9.2a). While a full and complete 3D bandgap remains in the square spiral PBC films now capping the 2D PBC, a reduced but still complete

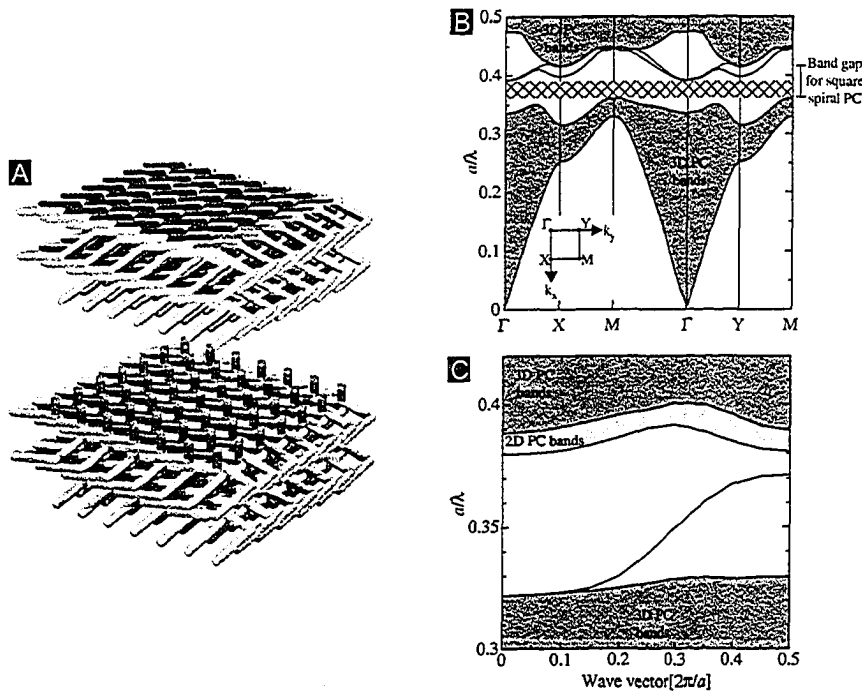


Figure 9.2: a) A 3D-2D-3D heterostructure for embedding 2D PBC waveguides inside square spiral 3D PBCs. b) In-plane 2D PBC band diagram for the structure in a). The cross-hatched complete bandgap arises from overlap of the square spiral 3D bandgap and the embedded 2D bandgap. c) Dispersion relation for a linear waveguiding defect in the embedded 2D layer. From [232].

3D bandgap exists inside the 2D PBC layer. As illustrated in figure 9.2b, this bandgap arises as a result of frequency overlap between the bandgap of the surrounding 3D PBCs (preventing all light propagation out of the 2D PBC plane), and the in-plane bandgap created by the periodic dielectric structure of the tetragonally arranged cylinders in the 2D PBC layer. In other words, the capping 3D PBCs completely eliminate the light leakage normally impeding 2D PBC slabs. Point and line defects can then be defined to effect light localization inside the consolidated bandgap. The simulations by Chutinan and John demonstrated single-mode waveguiding with bandwidths up to 180 nm (for a 3D PBC bandgap centred at 1.55  $\mu\text{m}$ ), with a large tolerance to the exact alignment and dimensions of the 2D PBC layer within the 3D square spiral PBC. They also documented that a trade-off

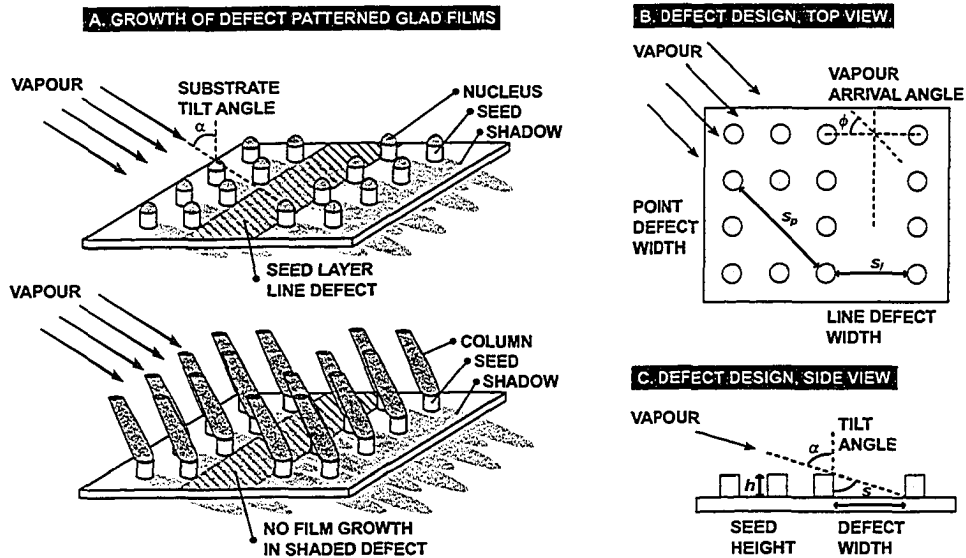


Figure 9.3: a) Schematic of the principle of seed layer induced bottom-up defect engineering in GLAD films. When geometrical shadowing extends over a seed layer defect, the defect transfers to the film. b) Top and c) side views defining the parameters for periodic seed layer defect design, including the maximum point and line defect widths  $s$ .

exists between the single-mode waveguide bandwidth and the size of the consolidated heterostructure 3D bandgap. The dispersion relation for a 3D-2D-3D waveguide is shown in figure 9.2c. Simulations have also shown that waveguiding in the square spiral PBC architecture is robust to microstructural roughness and fluctuations in defect dimensions, with inhomogeneities up to 50 nm causing scattering losses of not more than 5% [183].

## 9.2 Seed Layer Induced Defect Engineering

### 9.2.1 The Principles of Seed Layer Induced Defects

Whereas multilayer and micromachined defect engineering in GLAD films rely on existing knowledge, the main focus of this chapter is on enabling seed layer induced defect patterning as a new capability for GLAD films. This is an all-new approach to thin film patterning, which not only avoids complicated micromachining of the fragile porous films, but also has importance as an independent technique with applications well beyond PBC waveguides.

The principle of seed layer induced defect engineering is that modestly sized non-seeded areas on the substrate will remain free of film growth as long as they are covered by the geometrical vapour shadows cast by the surrounding seeds. Since GLAD conforms to seed layer topographies with each seed enforcing the growth of one column, as previously detailed in chapters 5 and 6, the non-seeded areas will then transfer directly from the substrate to the deposited GLAD film and create embedded voids in the film. As the seed nucleated columns continue to grow taller, the shadowing effect reinforces itself, and the void defects can be maintained throughout the thickness of the film irrespective of the film microstructure. This is illustrated in figure 9.3a.

In effect, the deposition of a GLAD film on a seed layer with intentional defects extrudes the defect patterns from the two dimensional substrate into the three dimensional film. A point defect in the seed layer thus becomes a line defect in the film, whereas a line defect in the seed layer becomes a planar defect in the film. In the context of square spiral GLAD PBCs only defects in a uniform tetragonal seed lattices are relevant, but in principle non-periodic seed layers can be employed for defects engineering too. In fact, even substrate topographies consisting of patterned slabs or gratings, rather than individual seeds, can be used to enforce a defect structure in GLAD films. This was previously reported by Horn *et al.* In their approach, however, aperiodic GLAD films were deposited over large-scale grooves with substantial excess film growth inside and adjacent to the grooves, and without the pattern induced control over the film microstructure required for functional applications [234].

As a bottom-up like approach, in which desired patterns automatically transfer from the seed layer to the GLAD film right as the film is deposited, the key advantage of seed layer induced defect engineering is the complete elimination of the need for complex and potentially detrimental post deposition film processing. Only a single pre deposition seed layer fabrication step is required.

### 9.2.2 Seed Layer Defect Design Rules

The design rules for periodic seed layers were derived and described in section 5.2, and only the additional requirements pertaining to seed layer based defect engineering will be considered here.

A point defect can consist of one or several clustered missing seeds, while a line defect can consist of one or several rows of missing seeds. Since the objective is to transfer these seed defects to the GLAD film as regions

free of growth, the defects must be covered by shadows extending from the surrounding seeds in order to prevent vapour from impinging and nucleating in the defects. Hence, for a *point defect* the maximum allowed defect width  $s_p$  – defined as the maximum seed edge to seed edge distance along any direction in the substrate plane in which vapour will arrive – depends on the seed height  $h$  and the substrate tilt angle  $\alpha$  (see figures 9.3b and 9.3c):

$$s_p = \tan(\alpha) \cdot h. \quad (9.2)$$

This defect width must not be exceeded along any of the vapour arrival directions  $\phi$  required by the GLAD growth algorithm. Clearly, taller seeds and more oblique vapour incidence angles permit larger defects.

For a *line defect* the perpendicular defect width is defined as  $s_l$ , and the above relation is true only when the vapour arrival direction is perpendicular to the longitudinal direction of the defect. If the vapour arrives at an angle  $\phi$  relative to the line defect normal (see figure 9.3b), the maximum defect width is limited to:

$$s_l = \cos(\phi) \cdot \tan(\alpha) \cdot h. \quad (9.3)$$

Thus, for line defects in particular the maximum permitted defect width depends strongly on the vapour arrival direction.

### 9.2.3 Seed Layer Defect Fabrication

In fabricating seed layers with defects in the form of intentionally missing seeds, direct write lithography excels as the most suitable prototype technology. Both of the mask-less EBL and LDWL technologies previously described in chapter 5 readily deliver seed layers with customized, arbitrary defect patterns at very short turn-around times. In contrast, the prototyping of seed layer defect patterns is costly and cumbersome using traditional mask based UV and X-ray lithography, and nearly impossible when based on self-assembly of microspheres or interference lithography (even if unintentional defects often arise).

Seed layers with a variety of point and line defects of different sizes were fabricated. Figure 9.4a shows a two-row or  $2.6 \mu\text{m}$  wide line defect in a tetragonal, periodic EBL SU-8 seed layer with a lattice period of  $1 \mu\text{m}$ . The seed layer quality is maintained even in the presence of the defect. Figure 9.4b illustrates a seed layer with an array of line defects, designed with defect widths  $s_l$  varying from  $1.6$  to  $4.6 \mu\text{m}$  (one to four rows).

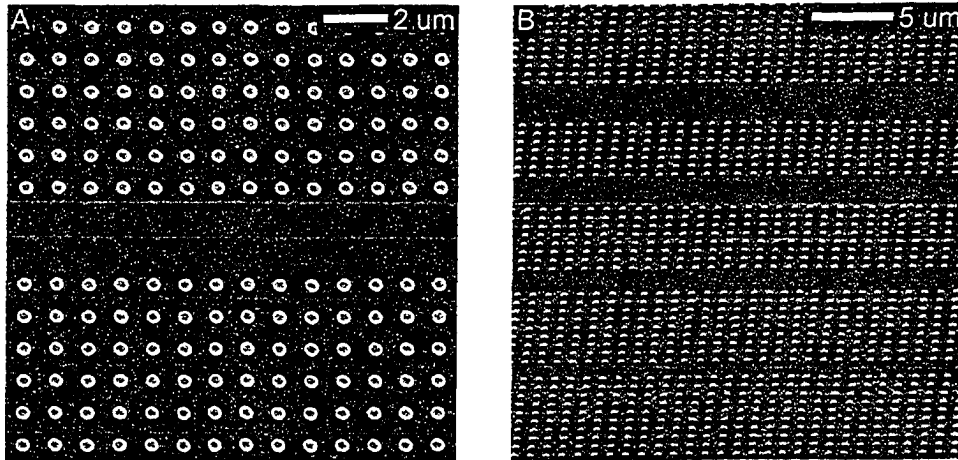


Figure 9.4: a) Top view of a tetragonal seed layer with a  $2.6 \mu\text{m}$  wide linear defect, fabricated in SU-8 using EBL. b) Oblique view of a tetragonal seed layer with a series of linear defects, varying in width from one to four rows.

### 9.3 Traditional GLAD Defect Engineering

Seed layer induced GLAD film defect engineering was first investigated with traditional GLAD square spiral growth modes, i.e., with the tetragonal seed layer precisely aligned with the vapour arrival direction  $\phi$ . The experimental details pertaining to the depositions were as previously described in section 7.2.3.

Figure 9.5a shows a top view of a traditional silicon square spiral film deposited on a seed layer with intersecting one to four-row wide linear defects. The one-row wide defects are observed to be entirely clear of film growth (except where they intersect wider defects), and thus represent successful air filled planar film defects. In the horizontal direction in figure 9.5a, the two-row wide defects are also void, whereas in the vertical direction these defects contain some film growth. The three and four-row wide defects are full of aperiodic film growth, and clearly have not been fully shaded by the surrounding seeds and periodic spirals.

After seed amplification, the one to four-row wide line defects in the seed layer used for the GLAD film in figure 9.5 yielded effective seed edge to seed edge defects widths of  $1.0$  to  $4.0 \mu\text{m}$ . Meanwhile, with a seed height of  $150 \text{ nm}$  and a vapour incidence angle  $\alpha$  of  $85^\circ$ , the maximum acceptable line defect width  $s_l$  given by equation 9.3 is:

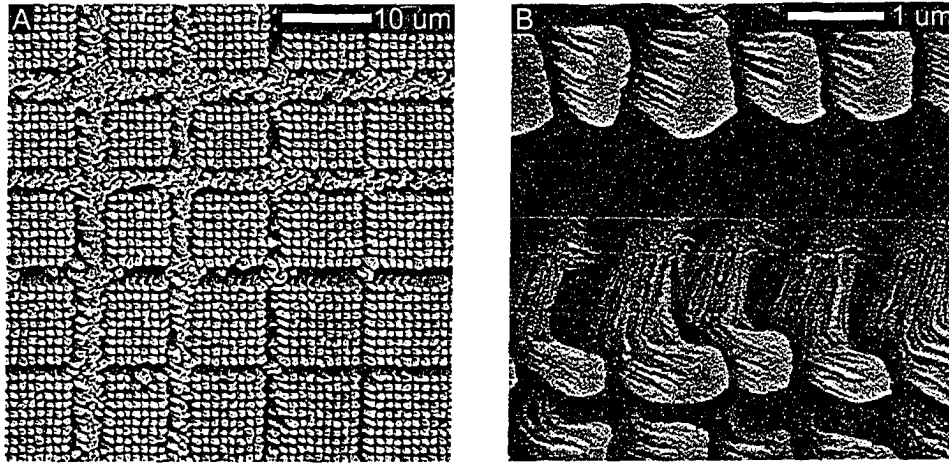


Figure 9.5: a) Top view of a square spiral GLAD film deposited on a tetragonal seed layer with one to four row wide line defects. The one-row wide defects and the horizontal two-row wide defect have transferred well from the seed layer to the film. b) Magnified view of the square spirals adjacent to a two-row wide defect. Only minor perturbation of the spiral fine structure is observed.

$$s_l = \cos(\phi) \cdot \tan(\alpha) \cdot h = \cos(0^\circ) \cdot \tan(85^\circ) \cdot 150 \text{ nm} = 1.7 \mu\text{m}. \quad (9.4)$$

Thus, the one-row or  $1.0 \mu\text{m}$  wide line defects should be fully covered by geometrical shadows and transfer well to the GLAD film. This is indeed observed in the actual film in figure 9.5a. Transfer of the two-row or  $2.0 \mu\text{m}$  wide line defects is a borderline case, but evidently any initial growth in these slightly too large defects did become extinct, resulting in successful void defects. Both the three and four-row wide defects are clearly too large to be fully covered by the  $1.7 \mu\text{m}$  long shadows, exposing them to random, aperiodic film nucleation and growth.

From figure 9.5a it is also seen that, remarkably, the periodic square spirals growing next to the planar defects have maintained their uniformity and are almost unperturbed by the presence of the defect. The periodicity, shape, and height of the seeded columns are intact, and the only observable perturbation is a slight broadening of the columns immediately adjacent to the defect. Wider film defect patterns lead to increased broadening of only the closest columns, and a few rows away from the defects the periodic columns remain completely undisturbed. Figure 9.5b shows a magnified view of a section of the two-row wide defect. The square spiral corners right

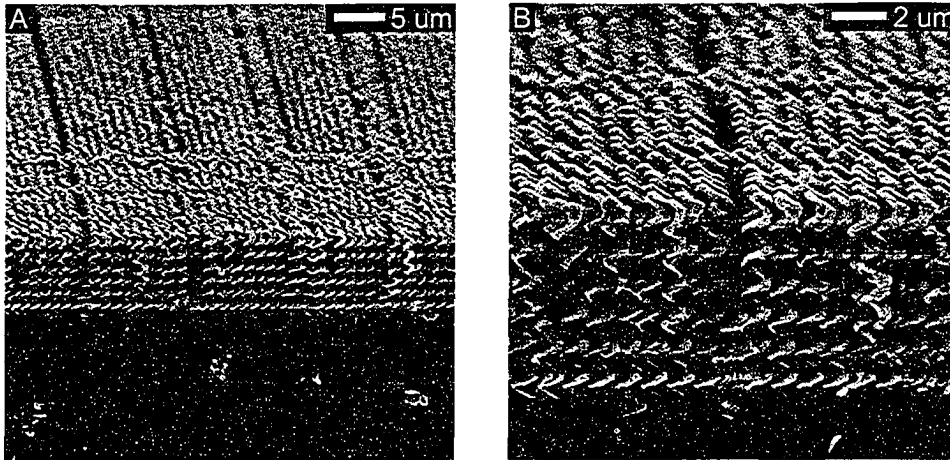


Figure 9.6: a) Oblique view of a square spiral GLAD film defect engineered via the seed layer. In this case only the one-row wide defect on the left transferred to the film as a planar air defect. b) Magnified view of the one-row wide defect, extending from the substrate to the top of the film. No significant alteration of the neighbouring periodic spirals is seen.

adjacent to the defect void appear to have received some additional vapour, but otherwise no modification of the square spiral fine structure is noted in comparison with the defect-free morphologies studied in chapter 7.

This ability of the periodic square spiral film to maintain its structural integrity is a major and critical characteristic of seed layer induced defect engineering. If the introduction of defects was to destroy the neighbouring square spiral morphology and film uniformity, the method would clearly be unsuitable for the fabrication of waveguides or even other types of functional patterns. One might expect the vapour that normally would land inside the defect patterns to amass quickly on the neighbouring seeds, but as soon as initial column nucleation has occurred on these seeds, the excess flux is dispersed evenly among the growing columns. The ability of the GLAD process to distribute and absorb the excess flux is a direct benefit of the high porosity and anisotropic growth behaviour of the films.

Figure 9.6 shows oblique views of one to four-row wide seed layer induced planar defects in a square spiral GLAD film (different from the film studied in figure 9.5). In this case with a vapour incidence angle  $\alpha$  of  $84^\circ$ , only the one-row wide seeded line defect was successfully transferred to the GLAD film. The remaining two to four-row wide defects were too large and consequently subject to aperiodic film nucleation and growth.

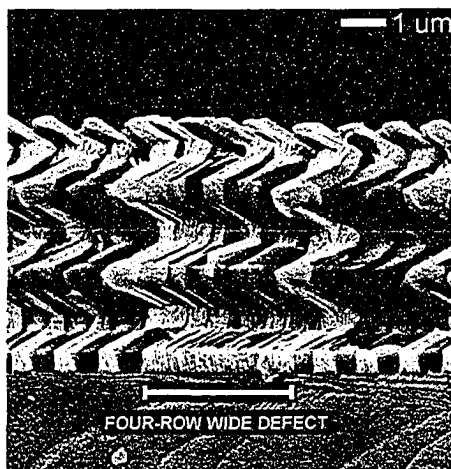


Figure 9.7: Side view of a four-row wide defect in a square spiral GLAD film. With the seed layer line defect being too wide for full geometrical shadowing, the defect has been filled with aperiodic film growth.

The close-up view of the one-row wide defect in figure 9.6b confirms that, apart from some spurious debris right in the foreground, the seeded line defect has created a planar defect in the GLAD film extending all the way from the substrate to the top of the film. Furthermore, it is again observed that the square spirals adjacent to this defect have maintained their uniformity and morphological integrity.

Finally, a side view of GLAD square spiral growth on a four-row wide defect is shown in figure 9.7. Film growth inside the defect is random and aperiodic, as a result of the insufficient geometrical shadowing afforded by the surrounding seeds and periodic square spirals. However, the presence of this aperiodic film growth has not adversely affected the neighbouring seeded square spirals.

Thus, seed layer induced defect engineering does work for appropriately small defect widths, with one column growing off each seed, no film growth occurring inside the defects, and the excess vapour being dispersed among the columns. As the GLAD film conforms to the defect patterned seed layer, the uniformity and porosity of the thin films is maintained with minimal impact on the film morphology adjacent to the patterns. On the downside, the ‘appropriately small’ defects that the method appears able to engineer are in fact rather small. For GLAD parameters typical of square spiral PBCs, even two-row wide defects are barely achievable. Another serious

problem with the use of traditional GLAD growth algorithms – with the vapour arrival angle  $\phi$  statically aligned with the seed layer lattice – is that even the narrow seeded line defects produce truly void defects only when the defects are perpendicular to  $\phi$ . In figure 9.5a it was previously noted that the vertical two-row defects (relative to the image orientation) contained more unwanted film growth than the horizontal two-row defects. Indeed, the initial vapour arrival direction for this deposition was in the vertical orientation on the image, meaning that at the beginning of the deposition no geometrical shadows covered the vertically oriented seed defects. For the ‘vertical’ one-row wide defects the inter-seed growth accumulated during the initial square spiral growth step was subsequently quenched, but for the vertical two-row wide defects the aperiodic growth inside the defects persisted all the way to the top of the film.

Since meaningful PBC waveguides (and other applications in patterned thin films) require defects going around corners and propagating in different directions, the restriction of the traditional GLAD growth mode to defect engineering in only one direction is a liability. To address this problem it is necessary to switch to a GLAD algorithm in which the column growth direction is decoupled from the vapour arrival direction.

## 9.4 PhiSweep GLAD Defect Engineering

The principles of seed layer induced defect engineering employing the PhiSweep GLAD algorithm – which was previously introduced and described in section 7.6.1 – are the same as for traditional GLAD algorithms, and the same seed layers with point and line defects are used. However, given the rotation of the vapour arrival angle  $\phi$  away from the column growth direction, the above equation 9.3 for the maximum allowed line defect width must be modified for PhiSweep GLAD. For square spiral growth on a tetragonal seed lattice in particular, two separate situations must be considered, depending on whether the column growth direction is parallel or perpendicular to the line defect.

As illustrated in figure 9.8a, when the seed layer line defect is perpendicular to the column growth direction, the maximum line defect width  $s_{l,\perp}$  is:

$$s_{l,\perp} = \cos(\gamma) \cdot \tan(\alpha) \cdot h, \quad (9.5)$$

where  $\gamma$  is the PhiSweep sweep angle. Compared with the case of traditional GLAD, in which the vapour arrives perpendicularly to the defect (equivalent to  $\gamma = 0^\circ$ ), the PhiSweep algorithm results in a  $\cos(\gamma)$  reduction in the

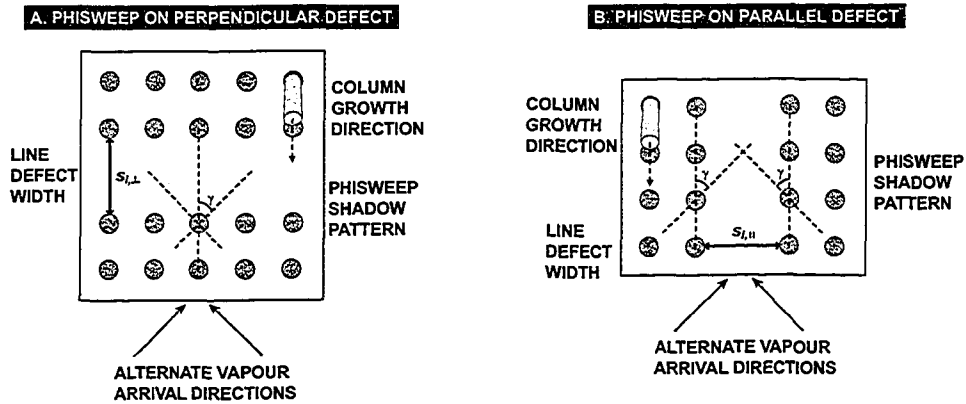


Figure 9.8: Schematics defining the maximum allowed defect widths  $s_l$  in seed layer line defects a) perpendicular and b) parallel to the column growth direction for the PhiSweep GLAD growth algorithm. The PhiSweep sweep angle  $\gamma$  determines the extent of geometrical shadowing inside the defects.

maximum defect width. The maximum sweep angle used, however, is  $45^\circ$ , leading to a relatively modest worst-case defect width reduction of  $\sqrt{1/2}$ .

When the column growth direction is parallel to a line defect, as in figure 9.8b, the sweeping of the vapour arrival direction in PhiSweep allows for even wider line defects, since alternating geometrical shadows now extend from both sides of the defects. Thus, provided that the inter-seed growth in the defect is rapidly quenched (requiring a low PhiSweep sweep pitch  $q$ ), the maximum PhiSweep parallel line defect width is:

$$s_{l,\parallel} = 2 \sin \gamma \cdot \tan(\alpha) \cdot h. \quad (9.6)$$

In this case, higher sweep angles  $\gamma$  yield better defect shadowing, with a factor  $\sqrt{2}$  gain at  $\gamma = 45^\circ$ . Not only is the allowed parallel defect width larger than the maximum perpendicular defect width, but compared with the use of traditional GLAD algorithms there is now geometrical shadowing even in parallel line defects where before there was no shadowing at all (causing a maximum allowed defect width of zero, as in equation 9.3).

Using PhiSweep rather than traditional GLAD for seed layer induced defect engineering in square spiral GLAD films consequently promises to offer two benefits:

- More complete geometrical shadow coverage of the seed layer defects, expected to cause less spurious growth inside the defects.

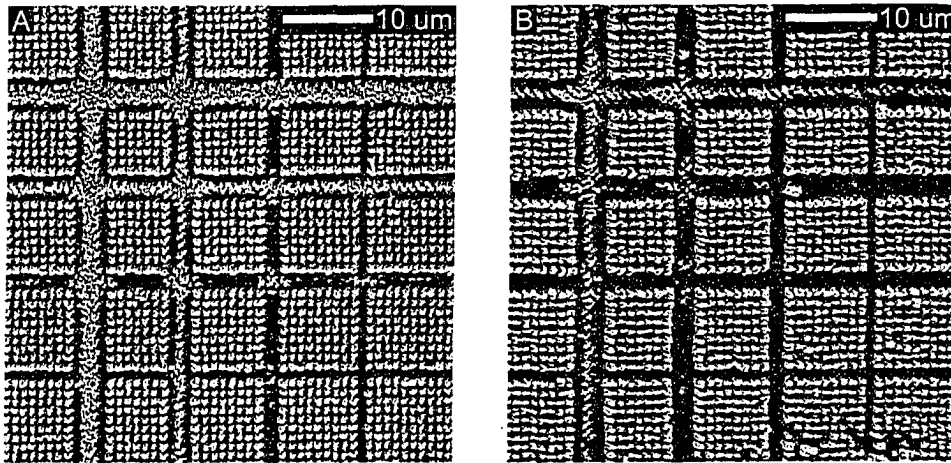


Figure 9.9: Top views of defect engineered PhiSweep GLAD films with a sweep pitch  $q$  of 15 nm. In a) the sweep angle  $\gamma$  was  $30^\circ$ , whereas in b) it was  $45^\circ$ . In both PhiSweep films the vertical and horizontal defects are nearly identical, but the higher sweep angle in b) is superior for keeping even the larger defects free of aperiodic film growth.

- Concurrent coverage of all defect orientations, allowing complex defect patterns to be realized.

The first advantage results from the more uniform dispersion of the vapour associated with the PhiSweep GLAD algorithms, whereas the second derives from the decoupling of the vapour arrival and column growth directions. Although some vapour is going to impinge down the centre of the seed layer defects every time the vapour arrival angle is swept from side to side, no part of the defect patterns is going to receive a continuous supply of flux.

#### 9.4.1 Air Filled PhiSweep GLAD Defects

Two defect engineered PhiSweep square spiral GLAD films with a sweep pitch  $q$  of 15 nm are shown in figure 9.9. The film in figure 9.9a was deposited with a sweep angle  $\gamma$  of  $30^\circ$ , and exhibits air filled defects devoid of film growth for both the one- and two-row wide seed layer line defects. Perturbation of the adjacent seed square spirals remains negligible. Furthermore, unlike the traditional GLAD film in figure 9.5a, vertically and horizontally oriented defects now appear identical, indicating that independence of defect engineering from the vapour arrival direction or defect orientation has indeed been achieved.

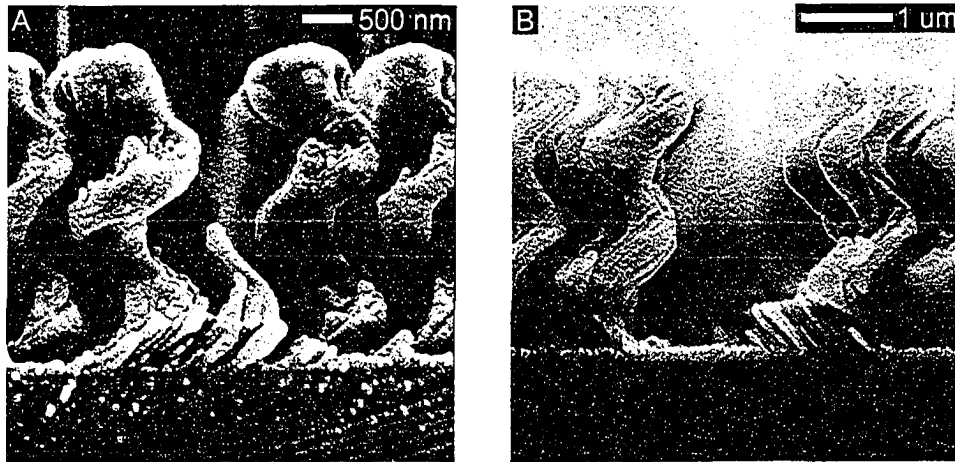


Figure 9.10: Side views of a) one-row wide and b) two-row wide defects from the PhiSweep square spiral GLAD films previously shown in figure 9.9. The  $\gamma = 45^\circ$  film in b) exhibits less spurious film growth inside the defect than the  $\gamma = 30^\circ$  film in a), but also more pronounced broadening of the adjacent periodic square spirals.

Yet, the three- and four-row wide defects in the PhiSweep film in figure 9.9a continue to be full of aperiodic GLAD growth. With a larger sweep angle  $\gamma$  of  $45^\circ$ , the PhiSweep square spiral film in figure 9.9b ought to keep wider defects free of film growth, in accordance with equation 9.6. This is indeed observed. As figure 9.9b shows, not only are the one- and two-row wide defects in this film completely clear of aperiodic growth (much more so than in any of the previously studied films), but now also the three-row wide defects are close to being free of growth. Even inside the four-row wide defects is the aperiodic growth suppressed. Hence, for an appropriate choice of sweep angle the PhiSweep GLAD algorithm provides much better air filled film defects.

It is evident from figure 9.9 that broadening of the periodic square spirals adjacent to defects is more pronounced in the  $\gamma = 45^\circ$  PhiSweep film, and more so for the wider defects. This is hardly surprising, given that emptier and larger line defects invariably create a greater excess of vapour that must accumulate somewhere else. The side views in figure 9.10 confirm this moderate broadening, and also show how some initial aperiodic growth in the defects quickly gets quenched. The two-row wide defect in the  $45^\circ$  sweep angle PhiSweep film in figure 9.10b exhibits superior extinction of aperiodic defect growth, which leads to a more ideal, air filled defect, but

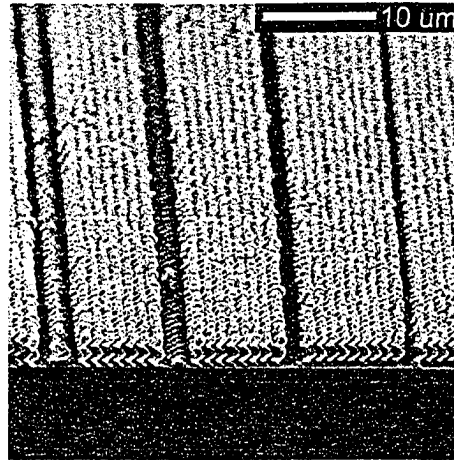


Figure 9.11: Oblique view of one- to four-row wide defects in a PhiSweep square spiral GLAD film with a sweep pitch of 15 nm and a sweep angle of  $45^\circ$ . The one- and two-row wide defects are devoid of film growth, whereas some film material is present in the three- and four-row wide defects.

also to greater broadening of the neighbouring spirals than in the  $\gamma = 30^\circ$  PhiSweep film in figure 9.10a.

Figure 9.11 shows an oblique view of an array of defects in a  $45^\circ$  sweep angle PhiSweep film. The one- and two-row wide defects are almost perfect air filled planar defects, while some film growth has accumulated in the centre of the three-row defect. Due to the differential film growth rates on the neighbouring seeds and on the exposed substrate inside the pattern, the film growth in the centre of the three-row wide pattern (where the shadows from either side of the defect were unable to reach) eventually terminated at a thickness of approximately  $2 \mu\text{m}$ . The four-row pattern was altogether too wide for efficient coverage at the given seed height and vapour incidence angle, with substantial aperiodic film growth.

#### 9.4.2 Evaporant Filled PhiSweep GLAD Defects

The PhiSweep GLAD films analyzed above behaved as expected in enhancing the engineering of air filled defects. Figure 9.12 shows another two PhiSweep square spiral GLAD films on tetragonal seed layers with one to four row wide defects, and deposited under the same conditions and using the same GLAD parameters as in figure 9.9, except for one change: an increase in the sweep pitch  $q$  from 15 nm to 45 nm. In a surprising turn of

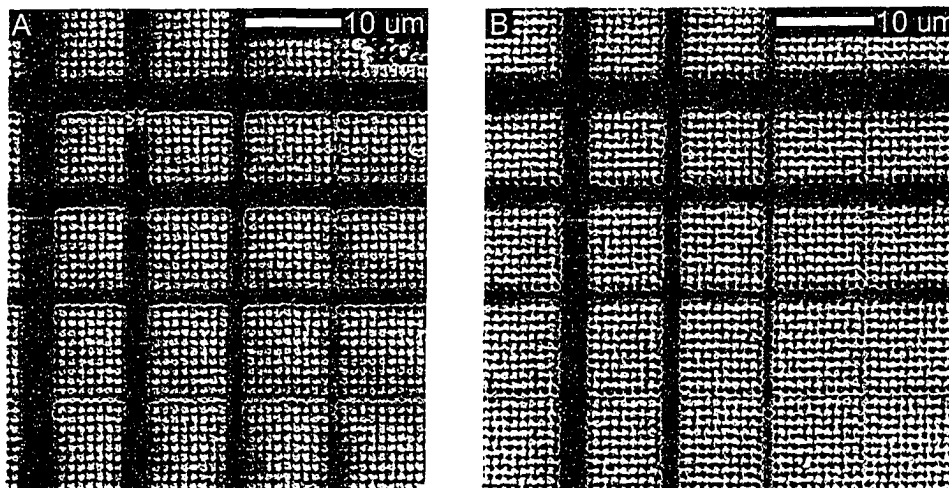


Figure 9.12: Top views of defect engineered PhiSweep square spiral GLAD films with a sweep pitch  $q$  of 45 nm and sweep angles  $\gamma$  of a)  $30^\circ$  and b)  $45^\circ$ . Changing the sweep pitch from 15 nm to 45 nm has dramatically altered the film defects from being air filled (as in figure 9.9) to being filled with compact looking evaporant material.

events, the defects delivered by these PhiSweep films are no longer void of evaporant, but instead filled from top to bottom and wall to wall with dense looking film material. Rather incredibly, a simple change of the sweep pitch has inverted the defects from air filled to evaporant filled, while preserving the background of tetragonally arranged square spirals!

Closer examination of figure 9.12 reveals that even the one-row wide line defects, which were void in all previous GLAD films, are now filled with evaporant. The filled defects are slightly wider for a sweep angle  $\gamma$  of  $30^\circ$  (figure 9.12a) than for  $\gamma = 45^\circ$  (figure 9.12b), but the structure and appearance of the defect filling is similar for both sweep angles. Also, as would be expected for the PhiSweep algorithm, the filled defects look the same in all directions, irrespective of the initial column growth direction.

The magnified view in figure 9.13a of a two-row evaporant filled defect is consistent with figure 9.12 in showing no broadening or perturbation of the fine structure of the periodic square spirals adjacent to the defects. The dense looking evaporant filling extends across the full width of the defect, with small ripples on the edges apparently being artifacts of the geometrical shadowing from the surrounding periodic square spirals. The side view of a two-row defect in figure 9.13b shows that the defect filling has the

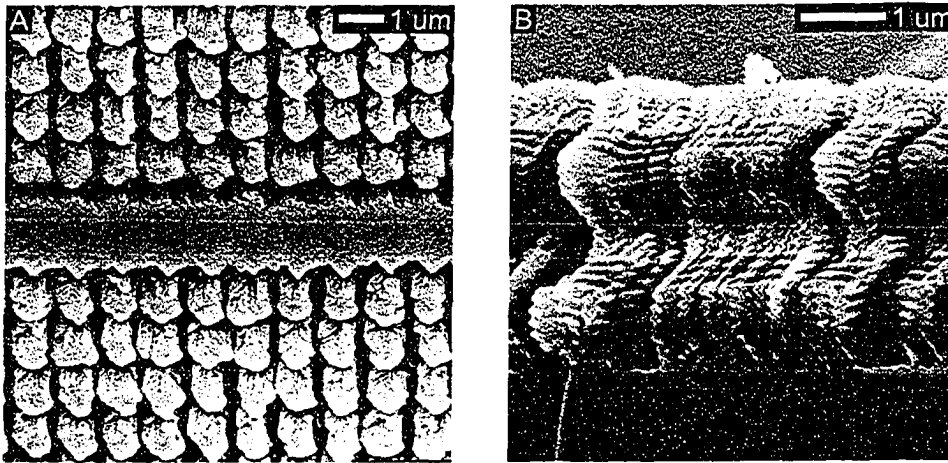


Figure 9.13: a) Top view and b) side view of two-row wide defects in 45 nm sweep pitch PhiSweep square spiral GLAD films. The compact defect fillings extend across the full width and height of the defects, with no broadening or alteration of the surrounding periodic square spirals.

same height as the periodic, seeded spiral. It also appears that the dense-looking aperiodic film growth inside the defect consists of small silicon fibres extending all the way from the substrate to the top of the film. The origin, nature, and significance of this aperiodic film structure will be studied in detail in chapter 10.

Figure 9.14 shows an oblique view of a defect engineered PhiSweep GLAD film with a sweep pitch  $q$  of 45 nm and a sweep angle  $\gamma$  of  $30^\circ$ . In comparison with the 15 nm sweep pitch GLAD film in figure 9.11, the sweep pitch driven transformation from air filled to evaporant filled defects is striking.

### 9.4.3 The Mechanisms of PhiSweep Defect Engineering

The previous sections have shown that the PhiSweep sweep pitch  $q$  is the one parameter deciding whether a seed layer defect gets filled with evaporant or is left empty, whereas the sweep angle  $\gamma$  only plays a role in determining the extent of the filling, and in particular how much undesired evaporant accumulates in the empty low sweep pitch defects.

To explain the presence of evaporant filled defects and understand the dependence of this phenomenon on the sweep pitch, consider the SEM images in figure 9.15 of the first 135 nm of PhiSweep GLAD film growth for

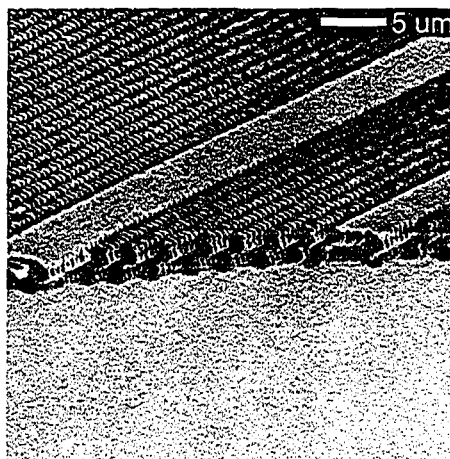


Figure 9.14: Oblique view of a PhiSweep square spiral GLAD film deposited on a tetragonal seed layer with three and four row wide line defects. The sweep pitch  $q$  was 45 nm while the sweep angle  $\gamma$  was  $30^\circ$ .

two different sweep pitch values. The left column depicts a 15 nm sweep pitch film, both on a one-row wide seed layer line defect and on a uniform tetragonal seed lattice, while the right column illustrates the same for a 45 nm sweep pitch film. The sweep angle was  $45^\circ$ , and the initial column growth direction was vertically downwards as oriented on the images. All other GLAD deposition parameters were kept identical, so that the only difference between the two columns is the sweep pitch. Under-sized EBL SU-8 seeds with no seed amplification were employed to clarify interpretation of the geometrical shadow patterns.

Two key observations describe how the 45 nm sweep pitch film on the right hand side of figure 9.15 differs from the 15 nm sweep pitch film on the left hand side at this early stage of PhiSweep film growth:

- In the 45 nm sweep pitch film the shadows inside the seed layer line defect appear not to extend as far, resulting in more aperiodic growth being present near the bottom of the defect.
- In the 45 nm sweep pitch film the height contrast between the seed-based periodic column growth and the substrate-based aperiodic inter-seed film growth is lower, resulting in the film topography being more blurred and diffuse.

In other words, the 15 nm sweep pitch film exhibits more bare substrate and more pronounced seeded column growth.

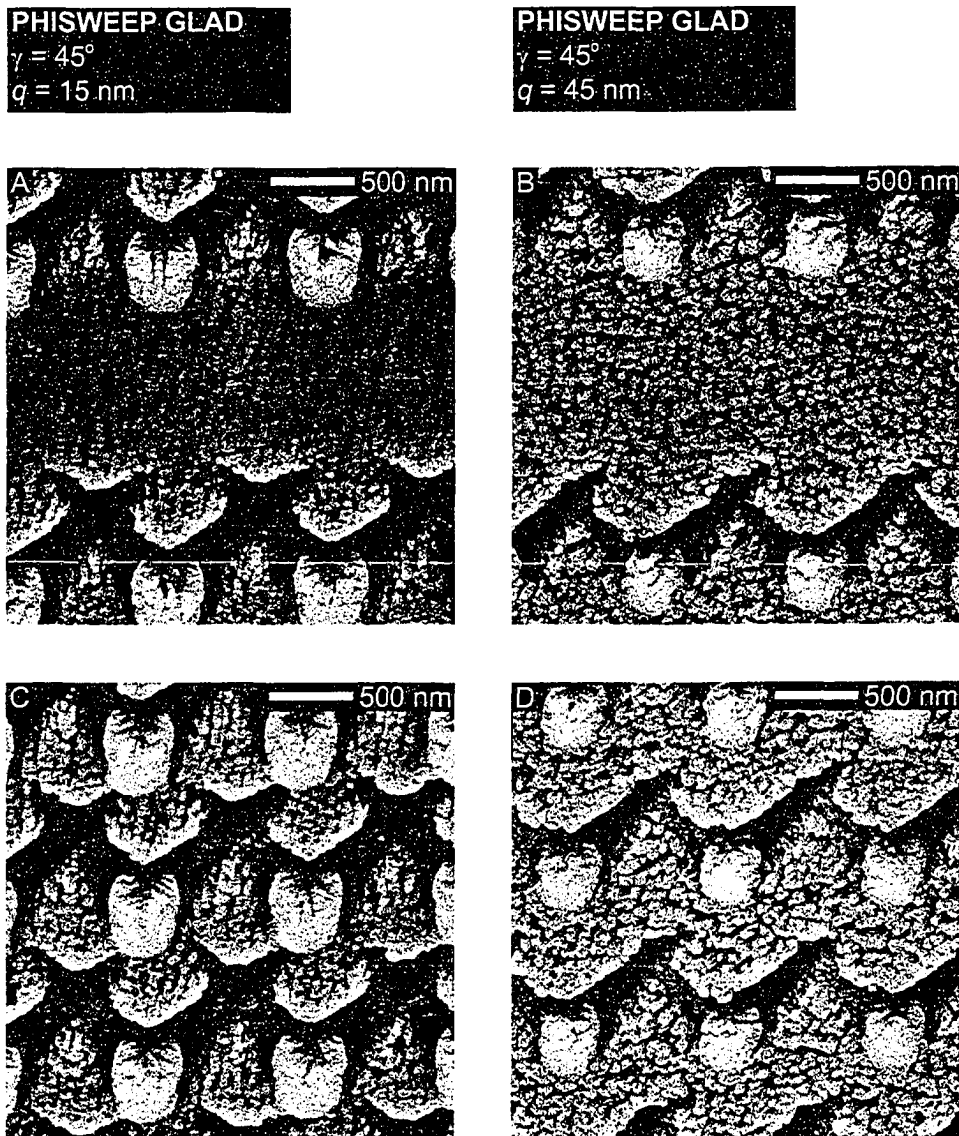


Figure 9.15: Top views of 135 nm thick PhiSweep GLAD growth on one-row wide seed layer line defects and uniform tetragonal seed lattices. In the left column the sweep pitch  $q$  was 15 nm, while in the right column it was 45 nm. The sweep angle  $\gamma$  was  $45^\circ$ .

How does this divergence in the film structure come about after only 135 nm of GLAD film growth? The shorter the sweep pitch, the more often the substrate rotates from one side to the other. This frequent rotation favours growth on the seeds, and later growth of the columns emerging from the seeds, for they are quite literally raised above all shadowing effects, and gobble up all the vapour incoming from both ends of the sweep curve. Meanwhile, the pattern of shadows down on the substrate between the seeds dramatically changes whenever the substrate is rotated. Some areas fall into the shade and new areas are suddenly exposed to the vapour stream. A low sweep pitch and frequent rotation thereby impede the accumulation of inter-seed, substrate-based film growth, and encourage greater disparity between growth on top of seeds and growth on the substrate between seeds. Indeed, in the extreme case of continuous substrate rotation, a large ball of material builds up on each seed with almost no film growth between the seeds (such as when seeds are amplified with short vertical GLAD posts, as in figure 5.16b).

When the sweep pitch is high, the opposite effect sets in. Less frequent sweeping of the vapour arrival angle means that the inter-seed film growth can keep up with film accumulation on top of the seeds, and the height contrast between film accumulation on the seeds and on the bare substrate remains so low that the seeded periodic columns are almost overwhelmed by aperiodic inter-seed growth. This is observed in figure 9.15b,d.

Critically, the process of either pronounced or suppressed seeded column growth for low and high sweep pitches, respectively, is self reinforcing. As the seeded columns grow larger and the height contrast to the inter-seed aperiodic growth increases, the geometrical shadows behind the seeded columns deepen and further help extinguish the inter-seed growth, causing still more vapour to be intercepted by the columns. This is why the shadows in the line defect in the 15 nm sweep pitch film in figure 9.15a appear longer than those in the 45 nm sweep pitch film in figure 9.15b.

The defect engineering behaviour of the PhiSweep GLAD algorithm can now be understood. For a relatively low sweep pitch of 15 nm, the self reinforcing height contrast between seeded column growth and inter-seed aperiodic film growth quickly quenches further accumulation of film growth inside moderately sized defects (as is in progress in figure 9.15a). As the defect width increases, it takes still thicker films to reach the point where growth inside the defect dies out, resulting in more evaporant being left at the bottom of the defect. This is clearly seen among the one to four row wide line defects in figure 9.11.

For a relatively high sweep pitch of 45 nm, the column to substrate film height contrast remains low, and only short shadows extend into the defects. In the absence of seed-induced shadowing a line defect is no different than a bare substrate, and aperiodic film growth can continue unimpeded inside the defect, all the way from the substrate to the top of the film. In essence, the low contrast between seeded and non-seeded substrate growth corresponds to reducing the effective seed height  $h$  in equations 9.3 and 9.5, so that the maximum allowed defect width tends toward zero. The low sweep pitch is also responsible for the compact but curious fine structure of the aperiodic film, as explained in chapter 10.

Raising the sweep pitch  $q$  slightly beyond the maximum 45 nm investigated here will not lead to any further change in the defect engineering response, but will affect the structure of the aperiodic film growth inside the defects. (Of course, if the sweep pitch is very large the algorithm approaches traditional GLAD.) Lowering the sweep pitch  $q$  below 15 nm may add some improvement in the maximum acceptable defect width. Equally important, however, is the vapour incidence angle  $\alpha$  and the initial seed height  $h$ . The higher the seeds or steeper the vapour incidence angle, the wider defects can be kept free of film growth *regardless* of the sweep pitch, although at the expense of more broadening of the adjacent periodic columns. Conversely, only relatively short seeds allow evaporant filled defects to be engineered.

Finally, it is noted that a higher sweep angle  $\gamma$  leads to more complete elimination of growth in empty defects (figure 9.9), as well as narrower stripes of compact evaporant growth in filled defects (figure 9.13), simply because higher sweep angles make the geometrical shadows from the seeds and the seeded columns extend further into the defects.

By sweeping the vapour stream and decoupling the vapour arrival and column growth directions, the PhiSweep algorithm significantly enhances seed layer induced defect engineering of GLAD films. In comparison with traditional GLAD algorithms, PhiSweep provides both wider and emptier air filled defects, and enables entirely new evaporant filled, solid looking defects. For any use in GLAD PBCs, the PhiSweep parameters used must of course be appropriate for obtaining a good square spiral structure. In this respect it is advantageous that the square spiral fine structure depends only modestly on the sweep pitch  $q$ , as discussed in chapter 7. The high quality square spiral PBC structures achievable with the PhiSweep algorithm can then conveniently be engineered with both void and filled defects.

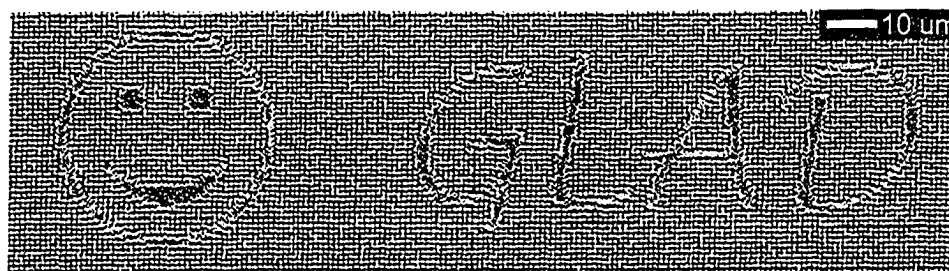


Figure 9.16: Advanced GLAD film defects, consisting of silicon filled patterns in a background of tetragonally arranged square spirals. The GLAD algorithm was PhiSweep with a sweep pitch of 45 nm. Efforts to turn these patterns into photonic crystal neon signs are not underway.

## 9.5 Applications and Advanced Defects

Defect engineering based on the transfer of two-dimensional seed layer designs to three-dimensional air or evaporant filled defects is a new capability enabling the fabrication of embedded functional patterns in GLAD thin films. It allows a periodic film geometry, the chiral structure of the columns, and empty or filled defects to be created concurrently in a single deposition step that maintains film uniformity. If similar film structures were to be achieved using conventional semiconductor microfabrication techniques based on dense film deposition, three-dimensional lithography, and etching, it would involve a considerable number of process steps. Being a bottom-up process, seed based defect engineering intrinsically ensures perfect alignment of the film defects according to the design and relative to the background seed lattice. Furthermore, the integrity of the GLAD columns is maintained, whereas bulk lithography would slice across columns. High aspect ratio defects are readily achievable, and in narrow air filled defects only small amounts of unwanted film growth are left on the substrate. Post deposition patterning and etching, on the other hand, would leave debris scattered throughout the entire porous film.

With the fundamentals of GLAD defects engineering established, it is straightforward to proceed to more advanced patterns consisting of angled linear segments, linear corners and intersections, curved segments, and even text and bitmap images. Any circuitry that can be designed in a two-dimensional seed layer is transferable to a GLAD film, provided that the pattern dimensions remain within the limitations given by the seed height and vapour incidence angle. Examples of complex GLAD film patterns are

shown in figure 9.16, using evaporant filled defects based on a 45 nm sweep pitch PhiSweep deposition.

In the defect engineering approach discussed so far, missing seeds in a seed lattice have been used to generate empty or filled defects in a periodic film background. An alternative approach is to invert the seed layer, so that the intended patterns consist of isolated seeded areas on an otherwise bare substrate. After GLAD deposition, this will create patterns of locally periodic GLAD columns in an aperiodic background. A key advantage is that unlimited pattern widths can then be achieved.

In addition to the potential for PBC waveguiding discussed in the next section, seed layer induced defect engineering enables the introduction of thin film functional patterns, benefiting numerous existing and novel GLAD applications. Air filled defects, for example, could delineate partitions in field emitter arrays or magnetic storage devices, while solid defects could be used to enclose individual cells in GLAD/liquid crystal hybrids or photovoltaic elements. During prototype development of many applications it would simply be advantageous to confine the effects being studied, such as catalysis or capacitance, to well-defined areas.

A particularly important instance of functional pattern engineering is fluid transport, where linear periodic or air filled patterns in compact GLAD film backgrounds can act as flow channels. Analytical microfluidics based on this concept will be explored as a new GLAD application in chapter 11. Another potential application is embedded gas conduits in GLAD humidity sensors, aiding the absorption and release of vapour in the film.

## 9.6 Toward GLAD PBC Waveguides

### 9.6.1 Seed Layer Induced Waveguides

With seed layer induced GLAD film defect engineering now in place, how can such defects address the original objective of creating waveguides in square spiral PBCs? A seed layer point defect leads to a vertically aligned GLAD film line defect, which could potentially guide light. However, even though the general direction of such a line defect is vertical, its actual morphology is one of numerous linear segments joined together in a square spiral, as it follows the surrounding square spiral GLAD columns winding their way up through the film. This would give the defect complicated and lossy multi-mode waveguide characteristics [183]. Furthermore, the only propagation direction of such linear defects is from the substrate to the top of the film, which is not useful for waveguiding circuits.

A far better way to exploit seed layer induced defect engineering for potential PBC waveguides is to employ seed layer line defects to create vertically aligned planar film defects. By appropriately capping such a planar defect at the substrate and at the top of the film, the defect could be turned into a pseudo-linear waveguide for directed propagation parallel to the substrate. This was shown schematically in figure 9.1a, and has previously been used by Temelkuran and Ozbay to demonstrate waveguiding in woodpile 3D PBCs (although at microwave frequencies) [76]. While this waveguide architecture is certainly not as ideal as truly embedded, micromachined defects (as in figure 9.1c), capped planar 3D PBC defects would still perform better than traditional line defects in planar 2D PBCs. In the latter approach, PBC confinement is provided *only* in the plane of the 2D PBC slab, while in all other directions one must rely on refractive index confinement or capping. In the capped 3D PBC approach, meanwhile, PBC confinement is potentially provided in *all* directions, except for the one vertical plane of the defect bounded on two sides by capping layers. As such, the capped planar defects approximate the ideal multilayer square spiral waveguide structure proposed by Chutinan and John [232, 233], but tilted onto its side.

Since seed layer induced planar defects based on the PhiSweep algorithm can produce both air filled and dielectric filled defects, refractive index guiding inside the dielectric defects might be a way to avoid capping layers altogether. However, analyses in chapter 10 will show that in spite of the dense-looking appearance of the defect filling in figures 9.12 to 9.14, the film structure inside the defects is in fact highly porous. This would lead to high losses if the dielectric defects were to be used as waveguides, in addition to the previously discussed general disadvantages of dielectric PBC waveguides over air filled waveguides. In air filled defects, a separate problem leading to optical scattering could be the small amounts of inter-seed growth always present at the bottom of the defects.

The most feasible way of capping a vertical, planar defect in a GLAD PBC, without resorting to advanced multilayer processing, would be to clamp the defect engineered film between metallic reflectors. This architecture is essentially a superposition of a 3D PBC planar waveguide and a parallel plate hollow metallic waveguide, with the perpendicular confinement of the PBC and metallic plate components providing full guidance of electromagnetic radiation down the defect. The same approach has also been used for 2D PBC waveguides [15]. The key requirement is that the metallic waveguide supports guided modes within the bandgap of the 3D PBC. Thus, the metallic waveguide must have a cut-off frequency below the lower edge of the photonic bandgap. The exact modal characteristics of the

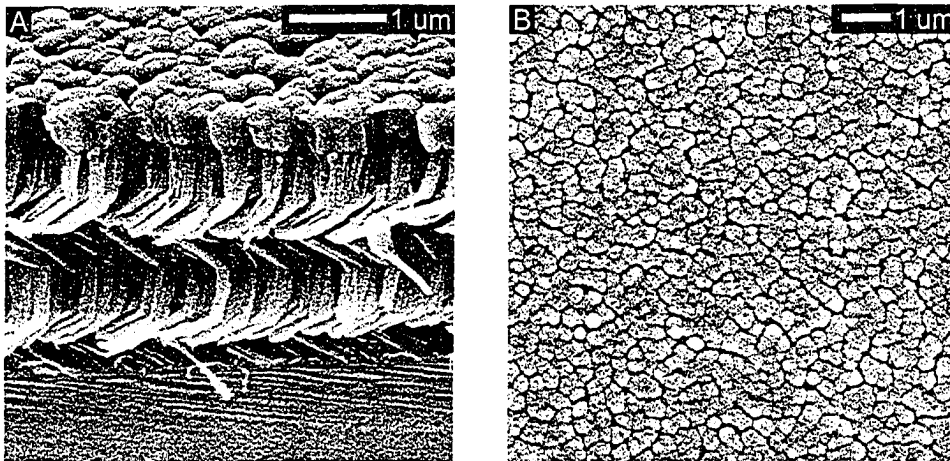


Figure 9.17: a) Oblique and b) top views of an aperiodic silicon square spiral GLAD film with a 260 nm thick intermediate capping layer. The capping layer, created by gradually reducing the vapour incidence angle  $\alpha$  to zero, is designed to increase the density of the GLAD film (as evident in b)), so that a gold layer can subsequently be deposited without contaminating the underlying square spirals.

hybrid waveguide geometry are complicated, however, and require modelling to properly evaluate.

No perfect, lossless metallic reflectors exist, and in fact metallic waveguides are generally avoided at optical frequencies given their relatively high losses (compared with much lower energy dissipation at microwave frequencies). Yet, analyses by Vermeulen *et al.* [235, 236] of hollow metallic waveguides [237] have shown that micrometre sized gold coated parallel plate metallic waveguides can transmit light at near infrared frequencies with losses as low as 0.3 dB/cm. This level of signal attenuation is much lower than what is seen in current PBC waveguides, and acceptable over the short distances relevant for PBC waveguiding applications. Other potential metals for the waveguides are silver and aluminium.

Cut-off for the metallic waveguides occur at roughly  $\lambda/2$  [235], so to assure that guided modes in the PBC bandgap can propagate, the vertical height of the capped planar defect should be approximately the same as the horizontal width given by equation 9.1. Wider or higher defects will lead to multi-mode propagation, but also facilitate easier coupling of light into the waveguides [71]. Any waveguide bends and circuitry can be defined by linear defects in the original seed layer.

Two methods can be envisioned for capping GLAD films with metallic thin films. First, dense GLAD capping layers can be created by adjusting the vapour incidence angle  $\alpha$  to zero at the end of the square spiral film deposition (a technique discussed in chapter 3, and regularly used in, for example, thermal barrier GLAD films). The capping layer could be deposited directly with gold, but this would lead to gold contamination deep inside the square spiral GLAD film. A better approach would therefore be to first deposit a thin intermediate GLAD capping layer of silicon that matches the underlying square spirals, and then use this denser layer as a platform for a gold cap. Figure 9.17 shows oblique and top views of such an intermediate silicon cap on an aperiodic square spiral GLAD film.

Unfortunately GLAD capping layers tend to have a rough surface, as evident in figure 9.17, and the resulting scattering would be detrimental to the modal characteristics and transmission efficiency of a hollow waveguide [238]. Furthermore, any asymmetry between the substrate and the GLAD capping layer (the two plates in the waveguide) will itself induce mode mixing [75]. Perhaps the best approach is therefore to use a gold coated, seeded substrate, and mount a second, bare gold coated substrate on top of the defect engineered square spiral GLAD film. The top substrate could be attached by low-temperature (363°C) eutectic gold-silicon bonding [239–241], or – with less stringent requirements for cleanliness – simply be glued on using a thin layer of adhesive applied to the edges of the substrate, far away from any defect pattern [242, 243].

### 9.6.2 Multilayer Waveguides

As mentioned at the beginning of this chapter, a second GLAD PBC defect engineering method is the insertion of a horizontal defect plane by mid-deposition adjustment of the GLAD parameters. Such a defect plane sandwiched between identical, periodic square spiral GLAD film layers can serve as a 2D planar waveguide for electromagnetic radiation, namely for light whose frequencies fall within the bandgap of the surrounding 3D PBCs and which is therefore prohibited from leaking out of the defect plane. By not relying on defect patterned seed layers or post deposition film processing, the approach is the most simple for defect engineering.

The defect plane can be realized in several different ways. The square spiral pitch  $p$  can be temporarily changed to create a 3D-3D-3D PBC multilayer with different bandgap characteristics in the central PBC layer. This is shown in principle in figure 9.18a, although only for an aperiodic square spiral GLAD film. In this case the highlighted central square spiral layer

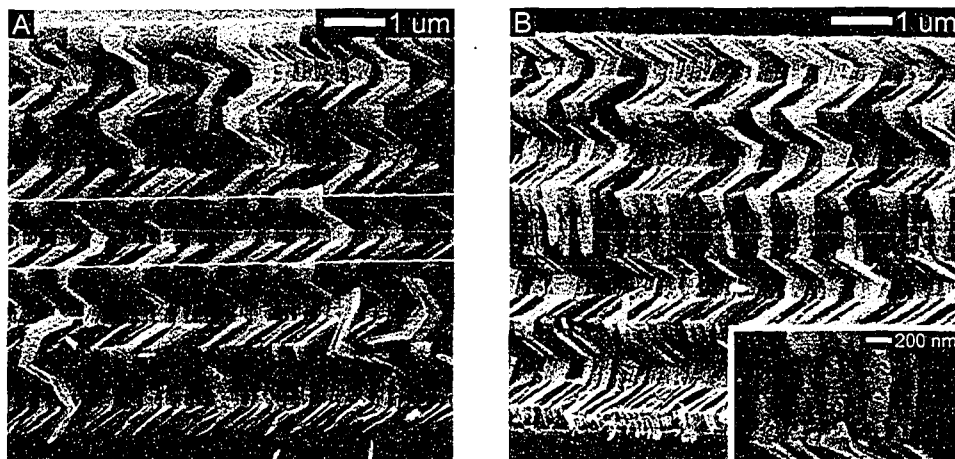


Figure 9.18: a) Side view of an aperiodic multilayer square spiral GLAD film. The highlighted central square spiral layer has a pitch  $p$  of  $1.0\ \mu\text{m}$ , whereas the surrounding square spirals on either side have a pitch of  $1.3\ \mu\text{m}$ . b) Side view of an aperiodic square spiral GLAD film with an intercalating  $0.7\ \mu\text{m}$  thick vertical post layer. The inset shows that broadening of the short vertical posts is modest.

has a pitch  $p$  of only  $1.0\ \mu\text{m}$ , compared with  $1.3\ \mu\text{m}$  for the surrounding top and bottom square spiral layers. Rather than adjusting the spiral pitch, the central layer could also be deposited with a second dielectric material having a different optical response. Simply changing the handedness of the square spirals would create an infinitely thin defect plane.

Another approach is to alter the GLAD microstructure altogether. A particularly useful structure is vertical posts, which then creates a 3D-2D-3D PBC heterostructure. An aperiodic demonstration of this architecture is shown in figure 9.18b, where the central vertical posts are  $0.7\ \mu\text{m}$  tall, or one half the pitch of the surrounding square spirals. As shown in the inset, only modest broadening of the vertical posts takes place – even for aperiodic columns – as long as the posts are kept short. Although waveguiding in a 2D plane is not nearly as useful as waveguiding in 1D along a directed linear defect, this architecture is a starting point for obtaining the more advanced micromachined heterostructures proposed and modelled by Chutinan and John as ideal 3D PBC waveguides [232,233]. The remaining, but significant, challenge is to carve linear defects out of the planar defect planes.

No Text

## Chapter 10

# Porosity Engineering and Nanofibrous GLAD Films

Earlier chapters described how the PhiSweep GLAD growth method was developed to improve the structure of periodic square spiral GLAD films for photonic crystals, and to prevent the accumulation of aperiodic film growth inside seed based defect patterns. During this research a third capability of PhiSweep GLAD emerged: The ability to engineer the pore size and distribution of aperiodic GLAD films, leading to the discovery of a new class of compact, helical, nanoporous thin films. Although not directly related to square spiral photonic crystals, porosity engineering is perhaps the most powerful aspect of PhiSweep GLAD. As an adjunct thesis research area it is the subject of the present chapter. GLAD porosity engineering not only represents an innovation in thin film engineering, but also has immediate applications, such as in microfluidics as covered in the next chapter.

The thesis research results presented in this chapter have been published in Applied Physics A [223].

### 10.1 The Context of Porosity Engineering

High porosity is one of the main attributes of GLAD thin films, and the direct driver of many GLAD applications. The development and understanding of these applications – humidity sensors, catalysts, and supercapacitors, for example – would benefit greatly from an ability to engineer a specific nanoscale structure in the GLAD film, independently of both the overall film density and the helical columnar microstructure.

Yet, in its basic form the GLAD process offers few means to control the film porosity. For a given material the vapour incidence angle  $\alpha$  dictates both the column inclination angle  $\beta$  and film porosity, and a fixed relationship exists between  $\beta$  and the film mean density  $\rho_{GLAD}$  (mass per unit film volume) or volume density  $\rho_V$  (volume solid material per unit film volume) [123]. Variation of  $\alpha$  does allow control over the film structure and pore distribution, but not without simultaneously affecting the overall film density. With the advent of the ‘spin-pause’ method  $\alpha$  and  $\beta$  were partially decoupled (see section 3.4.1), so that a range of different column inclination angles could be obtained for a given film density [124]. However, the column inclination angle is of little relevance to most high porosity/high surface area applications of GLAD, and offers only modest control over the film void distribution.

What is really needed for true porosity engineering is control over the spatial distribution, size, and shape of voids in the film. These are the structural attributes that determine nearly all properties of GLAD films: The surface area, the transport of fluids, the absorption of gases, the thermal diffusivity, the scattering of light, and so on. Furthermore, the ability to engineer the film porosity must remain independent of the overall film density – which itself is an important driver of GLAD film properties – and the helical structure of the film, which drives especially the optical properties. Since the film mean density  $\rho_{GLAD}$  is inextricably linked via geometrical shadowing to the vapour incidence angle  $\alpha$  (at least as long as film depositions are performed without substrate heating or ion bombardment), this implies that any porosity engineering method should be independent of  $\alpha$ . To maintain independence from the helical structure, porosity engineering must be separate from the column growth direction as well.

To achieve all of the above, porosity engineering has to exploit the fine details of growth and evolution of GLAD columns, since this is exactly where the porous microstructure arises. With its decoupling of the vapour arrival direction  $\phi$  from the column growth direction, PhiSweep GLAD turns out to successfully meet the challenges of thin film porosity engineering.

## 10.2 Aperiodic PhiSweep GLAD Films

A number of PhiSweep GLAD depositions were performed on bare silicon substrates with a range of different combinations of sweep angle  $\gamma$  and sweep pitch  $q$  (for more details on the PhiSweep method see section 7.6.1). In all cases the film material was silicon, and the GLAD helical structure was

square spiral. Except where explicitly stated otherwise the deposition pressure was kept at  $2$  to  $4 \times 10^{-4}$  Pa, while the deposition rate was set at  $15$ - $20$  Å/s. The vapour incidence angle  $\alpha$  was  $84^\circ$ .

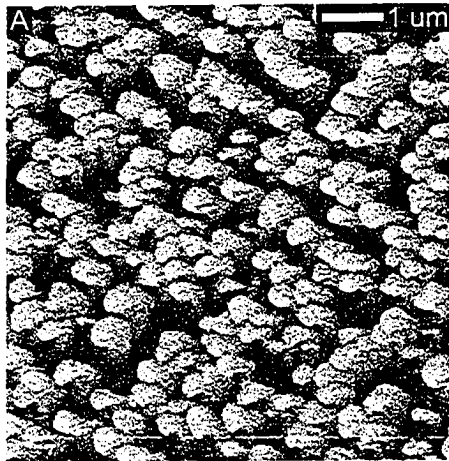
Figure 10.1 shows three PhiSweep GLAD films deposited with a sweep angle  $\gamma$  of  $45^\circ$  and sweep pitches  $q$  from  $15$  to  $45$  nm. For reference, a traditional (i.e., non-PhiSweep) square spiral GLAD film is also shown. In the absence of  $\phi$  oscillation the traditional GLAD film can be considered a 'PhiSweep film' with a sweep angle of  $0^\circ$  and an infinite sweep pitch. In both the top and side view images of the PhiSweep films a striking evolution of the film microstructure is observed. The  $q = 15$  nm PhiSweep film has a finer microstructure than the traditional GLAD film, but the film characteristics are otherwise similar: both exhibit widely separated free-standing columns that broaden as they grow, leading to significant column competition and extinction, and eventually an open structure of fat columns and large voids. In the  $q = 30$  nm film, column broadening and competition is still seen, but it is less pronounced than in the  $15$  nm pitch film, and the top view reveals a tighter packed structure of intermediate sized columns and smaller voids. The real surprise, though, is the  $q = 45$  nm film. Unlike any previously seen GLAD or obliquely deposited thin film, this PhiSweep film experiences no column broadening, competition or extinction at all. The film appears to have an extremely compact structure of narrow fibres growing all the way from the substrate to the top of the film with constant width, and no voids are visible at all in the two SEM micrographs. This novel film structure has been named '*nanofibrous*'.

For further comparison, figure 10.2 shows another two PhiSweep GLAD films with sweep pitches  $q$  of  $15$  and  $45$  nm, but now with a sweep angle  $\gamma$  of  $30^\circ$ . The change in sweep angle has had little impact on the morphology of the films, which is identical to the  $\gamma = 45^\circ$  films in figure 10.1. That is, the  $q = 15$  nm film has an open structure similar to traditional GLAD films, while the  $q = 45$  nm film has a compact, fibrous structure.

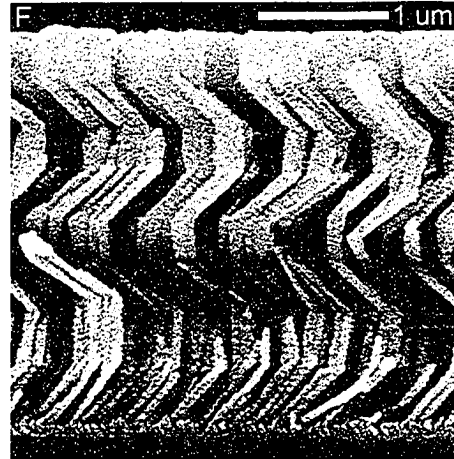
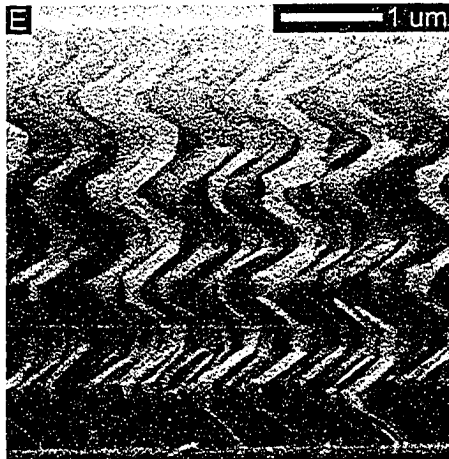
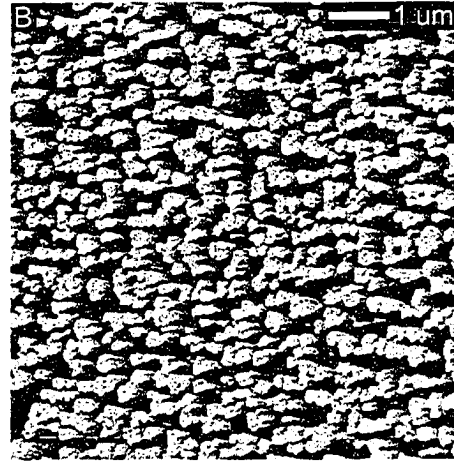
The nanofibrous film structure in figures 10.1d,h and 10.2b,d is the same as what was observed as a solid looking fill inside certain seed layer based defect patterns for similar deposition conditions in chapter 9. Also, as was the case for the periodic, seed-nucleated PhiSweep square spirals discussed in chapter 7, small ripples resulting from the  $\phi$  sweeping action are evident on the columns and fibres in figures 10.1 and 10.2. Nor surprisingly, the ripples are more pronounced in the higher  $q$  films.

Figures 10.1 and 10.2 demonstrate that the PhiSweep GLAD process is able to manipulate the film fine structure, independently of the vapour incidence angle  $\alpha$  and the helical structure, and to the point of even creating

**TRADITIONAL GLAD**  
( $\gamma = 0^\circ$ )  
( $q = \infty$ )



**PHISWEEP GLAD**  
 $\gamma = 45^\circ$   
 $q = 15 \text{ nm}$



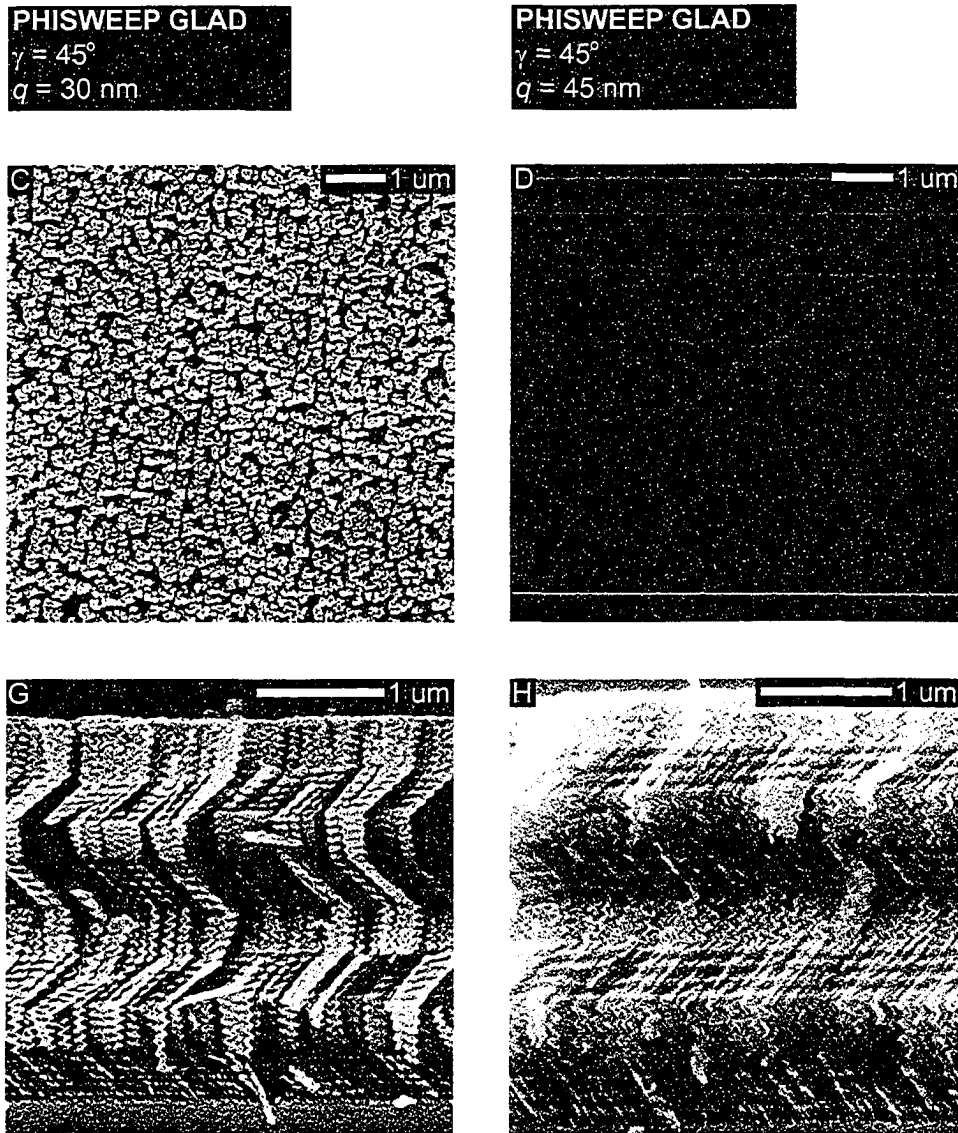


Figure 10.1: Top views (top row) and side views (bottom row) of one traditional GLAD film and three PhiSweep GLAD films with a sweep angle  $\gamma$  of  $45^\circ$ . As the sweep pitch  $q$  is varied from 15 nm to 45 nm, the PhiSweep films change from an open structure of separate, broadening columns – similar to the structure of traditional GLAD films – to an increasingly compact structure of non-broadening fibres.

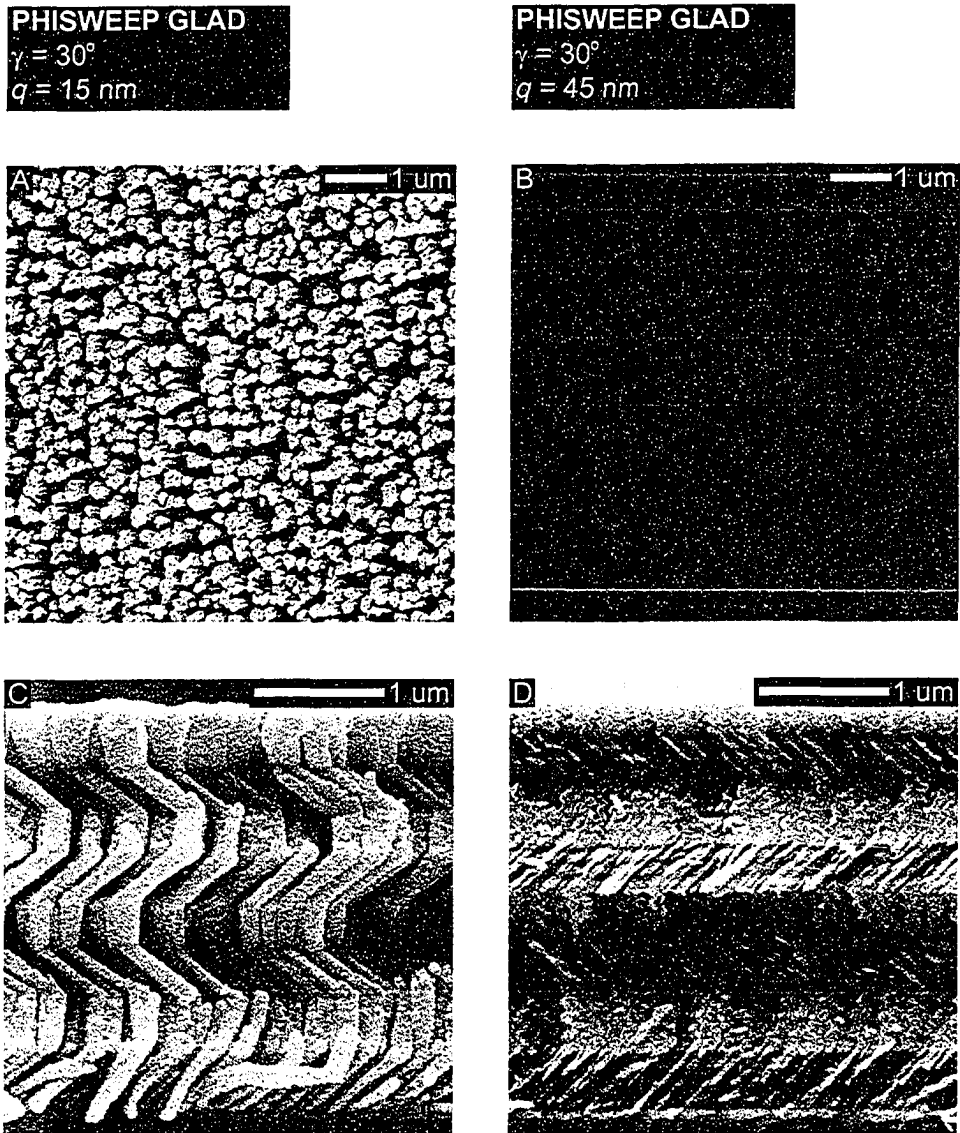


Figure 10.2: Top views (top row) and side views (bottom row) of two PhiSweep GLAD films deposited with a sweep angle  $\gamma$  of  $30^\circ$  and sweep pitches  $q$  of 15 and 45 nm. (The film structure in c) appears 'swollen' due to excessive chrome coating prior to SEM imaging.) In spite of the change in sweep angle, the film structures are identical to the 15 and 45 nm pitch PhiSweep films in figure 10.1.

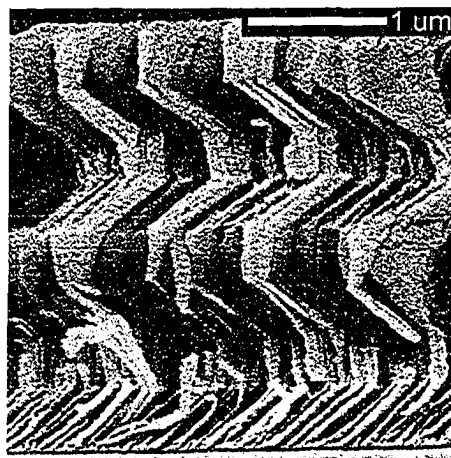


Figure 10.3: Side view of a PhiSweep GLAD films deposited with a sweep angle  $\gamma$  of  $15^\circ$  and a sweep pitch  $q$  of 15 nm. This structure is similar to the  $q = 15$  nm films in figures 10.1 and 10.2, confirming that the sweep angle is of little importance in determining the structure of aperiodic PhiSweep films over the range of parameters analyzed here.

a new nanofibrous film structure. Crucially, the figures also reveal that the morphology of aperiodic PhiSweep GLAD films depends solely on the sweep pitch  $q$ , whereas it is independent of the sweep angle  $\gamma$  within the range of pitch values investigated here. For completeness, a side view of a  $\gamma = 15^\circ$ ,  $q = 15$  nm PhiSweep film is shown in figure 10.3. This film looks like the  $q = 15$  nm PhiSweep films in figures 10.1 and 10.2 – i.e., much like a traditional, open GLAD film structure – confirming that the sweep angle has little impact on the film structure.

## 10.3 Analysis of PhiSweep and Nanofibrous GLAD Films

### 10.3.1 SEM Analysis and Film Density

The nanofibrous PhiSweep films immediately look much more ‘dense’ than the traditional, open GLAD films, calling for an evaluation of the film mean density  $\rho_{GLAD}$ . The fact that all the films were deposited at the same vapour incidence angle ( $\alpha = 84^\circ$ ) allowed the density to be analyzed by using SEM images of cleaved edges of the films to accurately measure the thickness of each film, and then normalize this thickness with the actual amount of film

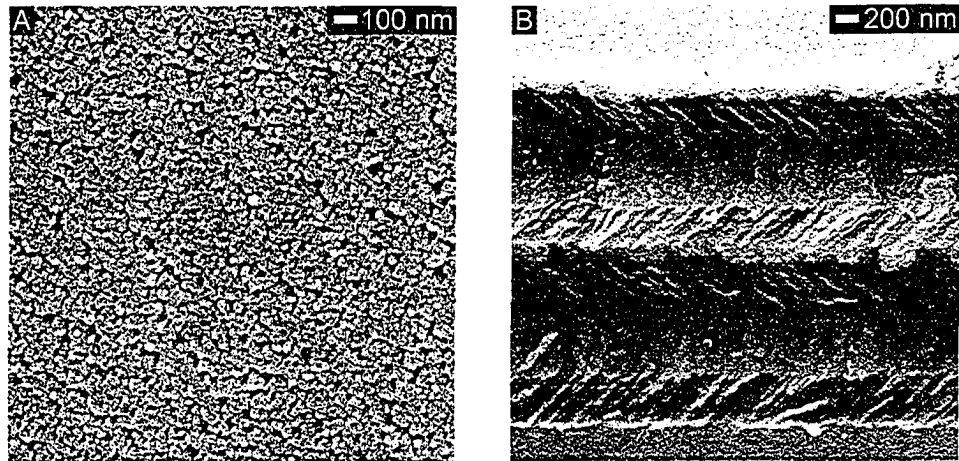


Figure 10.4: a) High magnification SEM image of the top surface of a PhiSweep nanofibrous GLAD films, deposited with a sweep angle  $\gamma = 45^\circ$  and a sweep pitch  $q = 45$  nm. Small voids are discernible. b) Oblique SEM image of a square spiral nanofibrous PhiSweep GLAD film with  $\gamma = 30^\circ$  and  $q = 45$  nm. The film appears to consist of tightly packed fibres.

material deposited on each substrate as recorded by the independent crystal thickness monitor inside the PVD system.

Strikingly, the analysis showed that the traditional and PhiSweep GLAD films have the *same* thickness per unit mass of material deposited per unit substrate area, irrespective of the sweep pitch  $q$  and the sweep angle  $\gamma$ . In consequence, even the ‘dense-looking’ nanofibrous PhiSweep films have the same mean density  $\rho_{GLAD}$  as traditional, open GLAD films. This has important repercussions for the interpretation of the structural characteristics of the PhiSweep GLAD films, and especially for the nanofibrous films.

While the nanofibrous PhiSweep films are not denser than regular GLAD films, they do indeed have a very different structure, with a fibrous texture and none of the large voids seen in regular films. Two high magnification images of nanofibrous PhiSweep films are shown in figure 10.4, confirming that in comparison with the lower sweep pitch PhiSweep films and traditional GLAD films, the voids in the nanofibrous PhiSweep films are significantly smaller. In fact, given the charging effects and high depth of field in SEM imaging, hardly any voids are visible at all in the oblique view in figure 10.4b.

To maintain the overall film density, either the individual fibres of the nanofibrous PhiSweep film have a lower density than the columns in a regu-

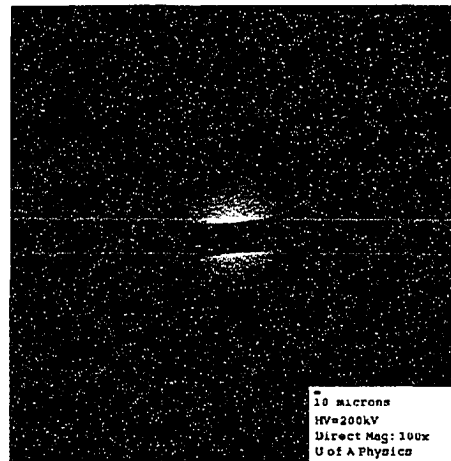


Figure 10.5: Transmission electron microscope (TEM) diffraction pattern of a single silicon fibre/column from a nanofibrous PhiSweep GLAD film. The uniform, smeared out diffraction pattern reveals that the fibres are amorphous.

lar GLAD film, or else the nanofibrous PhiSweep films contain a vast number of smaller, finer pores between the individual fibres to match the larger, less numerous voids in the traditional GLAD films. Transmission electron microscopy (TEM), performed in collaboration with B. Djurfors, was employed to investigate these two possibilities.

### 10.3.2 TEM and EDX Analyses

If the nanofibrous PhiSweep films maintained a low film mean density by way of a lower than normal internal density of the slim, fibrous columns, these fibres should either have internal voids, or else a different crystal structure than normal GLAD columns.

The TEM diffraction pattern in figure 10.5 of a single nanofibre shows that the crystal structure is amorphous. This is the case for all silicon GLAD films, and therefore rules out crystallography as a possible explanation for any anomaly in the density of PhiSweep silicon nanofibres. In fact, since all known silicon GLAD films have been found to be amorphous, and since the amorphous configuration already yields the lowest possible material density, the nanofibrous columns could not possibly lower their density by rearranging themselves in any other higher order poly or monocrystalline configuration.

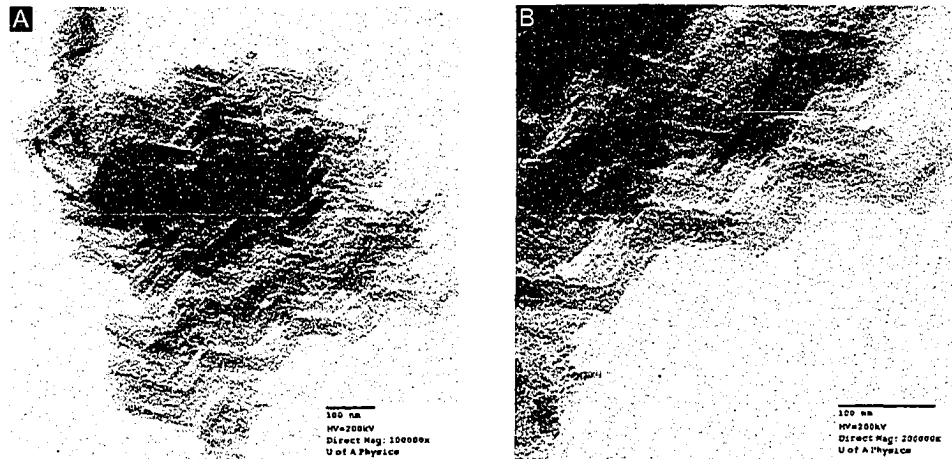


Figure 10.6: Bright field TEM images of a) a cluster of silicon fibres from a nanofibrous PhiSweep GLAD film, and b) a few individual fibres. The outer surface of the fibres is rough, but there is no evidence of internal voids in the fibres.

Consider next the TEM bright field images of nanofibres in figure 10.6. The width of each fibre is 20 – 30 nm, and the fibres have a rather rough surface, which would support voids between them. However, even the close-up view in figure 10.6b reveals no internal voids inside the fibres. Indeed, as discussed in chapter 3, the internal structure of the grains or columns in thin films depends principally on the fundamental properties of the film material – in particular its surface and bulk diffusion lengths – rather than on any substrate motion. Since the traditional GLAD columns and the fibre strands in nanofibrous PhiSweep film were deposited from the same material, on identical substrates, and under identical deposition conditions, it is unlikely that the sub columnar structure would be different in the two cases. This is exactly what the TEM analysis shows.

Energy dispersive X-ray analysis (EDX) was also performed, as shown in figure 10.7, confirming that the nanofibrous films contain silicon and some oxygen. The oxygen content can be attributed to residual gas present in the deposition chamber and to native oxidation post deposition, and is seen in all silicon GLAD films. The trace amounts of carbon and copper derive from the EDX support grid. Again, there is no discrepancy between the material composition of nanofibrous PhiSweep films and tradition, open GLAD films.

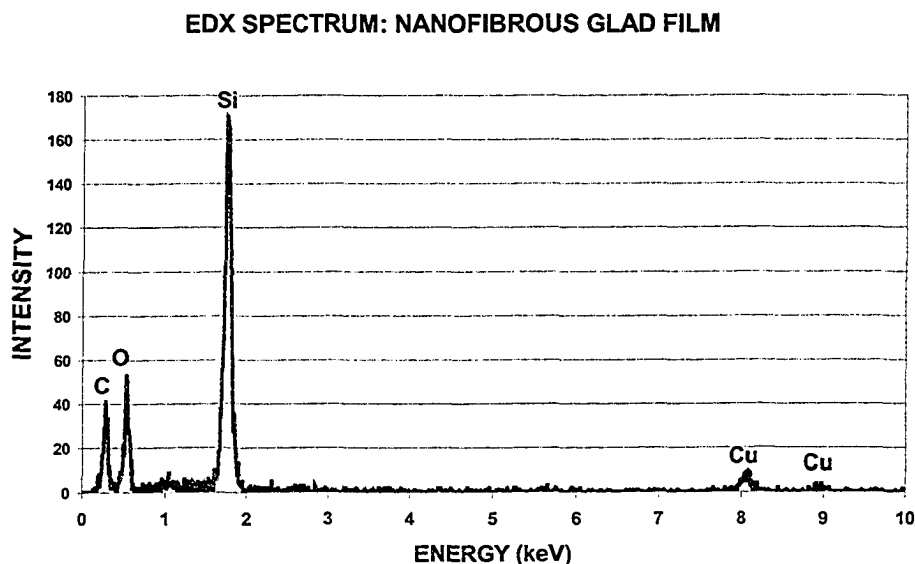


Figure 10.7: Electron dispersive X-ray analysis (EDX) spectrum of a silicon nanofibrous PhiSweep GLAD film. The material composition is identical to what is usually found in silicon GLAD films, with some oxygen incorporated during deposition or by post deposition native oxidation. The carbon and copper signals are from the EDX support grid.

### 10.3.3 The Realization of Porosity Engineering

The TEM analysis has shown that on the sub columnar level there is no difference between traditional GLAD films and nanofibrous PhiSweep films. Consequently, the film mean density  $\rho_{GLAD}$  can be maintained across the PhiSweep films, irrespective of the sweep pitch and sweep angle, only because the *total* volume of voids between the columns or fibres is constant. Thus, what really distinguishes PhiSweep films from traditional GLAD films are the size, number and distribution of the microstructural columns and pores, not the overall density. As the sweep pitch  $q$  is increased from 15 nm to 45 nm, the PhiSweep method is able to change the film structure from few, large pores between fat, broadening columns, to much smaller – but correspondingly more numerous – microscopic pores between thinner, rough fibres.

This establishes the PhiSweep method as the first true method for porosity engineering of GLAD films, where the pore distribution and surface area

can be manipulated independently of the overall film density  $\rho_{GLAD}$  (given by the vapour incidence angle  $\alpha$ ), and without affecting the base helical shape (as long as the helical shape is compatible with the PhiSweep process).

Figure 10.1 succinctly demonstrates the ability of the PhiSweep method to engineer the porosity of GLAD thin films, with a full range of available film textures, highlighted by the discovery of nanofibrous GLAD as a new type of thin film with a very high number of extremely small pores.

## 10.4 The Mechanisms of PhiSweep and Nanofibrous GLAD

The obvious next questions are how the PhiSweep film structures arise – in particular the nanofibrous structure – and why the sweep pitch is the singular parameter determining the film pore distribution. TEM and EDX analyses have already shown that neither crystallographic effects nor material composition can explain the PhiSweep film structures. Thermal effects are likely not the drivers of the PhiSweep growth process either, since growth at different deposition rates – and hence substrate heating rates – produce no change in the structure, and since the film mean density and crystalline structure are the same for both traditional and PhiSweep GLAD films.

For the case of silicon the film microstructure can best be explained by the magnitude of the sweep pitch relative to the width of the silicon fibres. This hypothesis is inspired by the initial observation that a sweep pitch  $q$  of 15 nm is below the average silicon fibre width of 20-30 nm, and gives an open GLAD film, whereas when the sweep pitch is raised to 45 nm, and hence slightly above the average fibre width, the compact, nanofibrous film unique to the PhiSweep method is obtained.

To understand the importance of this observation, one must first compare nanofibrous film growth with the column growth processes seen in traditional GLAD films. Once GLAD nucleation and agglomeration has taken place, the highly oblique incidence angle leads to a compact forest of fine columns. The columns are very thin and closely packed, since the columns grow off equally small and close packed nuclei. Hence, for the first nanometres of growth there is no difference in the film structure of traditional GLAD films and nanofibrous PhiSweep GLAD films. However, the inherent instability in the columnar self-shadowing process at oblique vapour incidence angles gradually leads to structural anisotropy among the columns in traditional GLAD films [109, 131, 150, 244], and the columns evolve from an

initially finely stranded or nanofibrous film structure into an open, non-uniform structure with broadening and competing columns. This has been seen in numerous periodic and aperiodic traditional GLAD films in the preceding chapters, and is evident in figure 10.1e.

If the sweep pitch in the PhiSweep films is smaller than the natural fibre width of the deposited silicon, alternation of the vapour incidence direction  $\phi$  occurs so frequently that – by definition – the impinging vapour cannot fully form a new fibre segment in the short time available between sweeps. Instead, vapour accumulates rather haphazardly on two opposite sides of the nucleated fibres, and thereby degenerates the fibres into lumps. This is shown schematically in figure 10.8a. These lumps are equivalent to the beginnings of broadening columns in traditional vertical post GLAD films, in which continuous or nearly continuous substrate rotation leads to preferential vapour deposition on the periphery of growing columns. The lumps therefore evolve to become regular, broadening GLAD columns and yield an open GLAD film, although the broadening per unit thickness of film does appear to be decreased in PhiSweep films relative to traditional, non-PhiSweep GLAD films (compare figure 10.1b with a, and figure 10.1f with e).

On the other hand, when the sweep pitch  $q$  is slightly larger than the fibre width, the fibres have enough time to redirect and rebuild their cylindrical shape between sweeps, as shown in figure 10.8b. In this case, each sweep essentially starts a new column and resets the column nucleation, hence postponing indefinitely the column broadening and competition otherwise inherent in GLAD. The nanofibrous film structure is then obtained, in which closely packed fine strands of deposited material can grow continuously with no observable column broadening. The elimination of broadening can be attributed directly to the frequent changes of the vapour incidence direction, since this oscillation of the vapour prevents the build-up of a structural anisotropy in the shadowing pattern among the growing columns, and thereby removes the precondition for column broadening. By neutralizing the structural anisotropy effect of traditional GLAD, PhiSweep GLAD allows the initial off-the-substrate film structure to keep growing throughout the film, without column competition, extinction, or broadening, as evident in figure 10.1d and h.

Finally, if the sweep pitch is much larger than the fibre width, the structural anisotropy has enough time to impact the film topography between sweeps, and one reverts to the case of traditional GLAD films ( $q = \infty$ ) with each column broadening between substrate rotations. Thus, for silicon the PhiSweep algorithm delivers distinct new film structures only within the

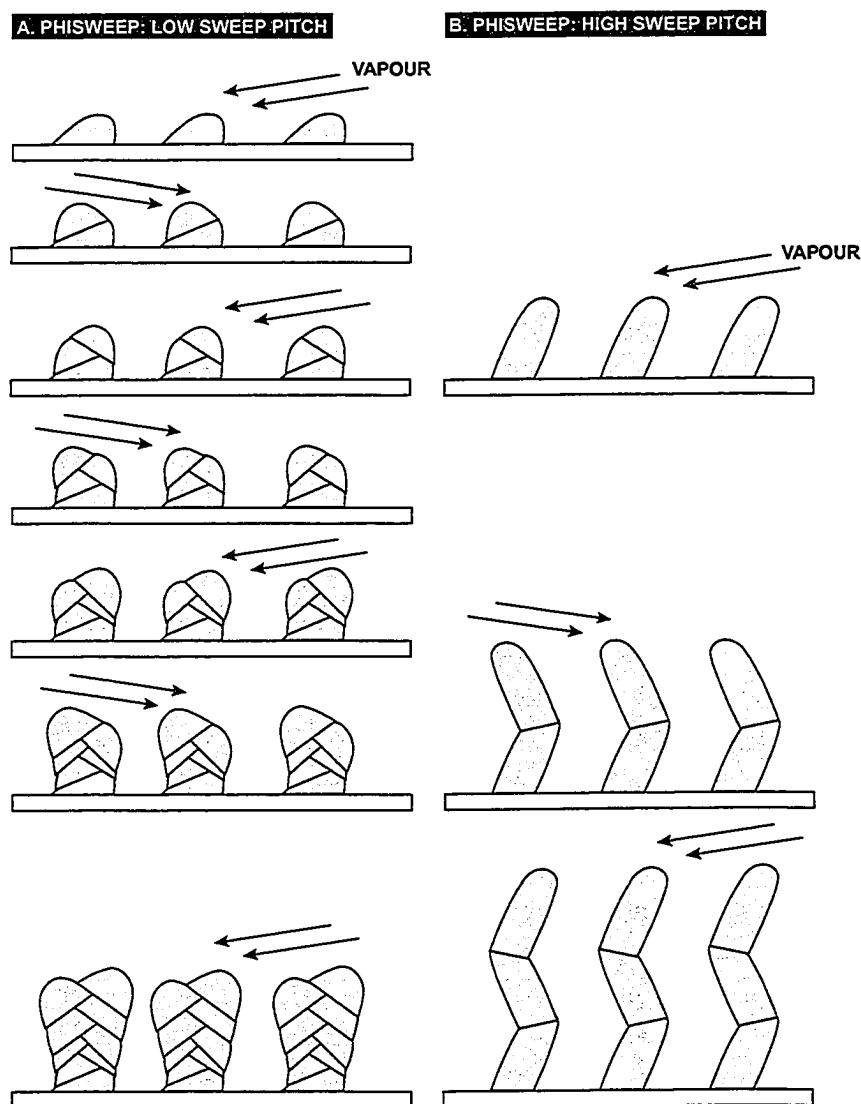


Figure 10.8: Schematic illustration of the growth of aperiodic PhiSweep GLAD films and the impact of the sweep pitch  $q$ . a) When  $q$  is smaller than or equal to the column/fibre width, the fibres degenerate into lumps and broadening sets in to yield an open film structure. b) When  $q$  is slightly larger than the fibre width, the fibre structure can re-form fully between sweeps, and each sweep resets the nucleation process. Column competition is then delayed indefinitely, leading to a compact film structure.

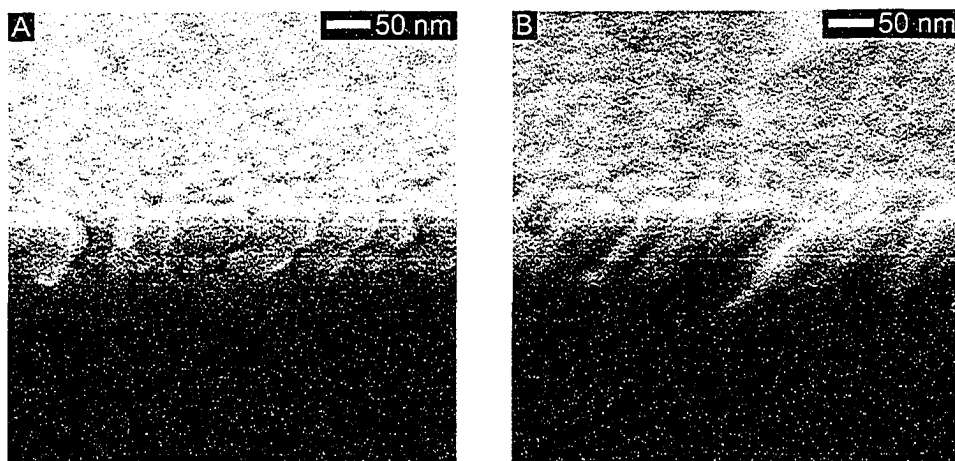


Figure 10.9: Initial film growth of two 45 nm thick PhiSweep GLAD films with different sweep pitches. In a) the 15 nm pitch is less than the fibrous column width, leading to silicon lumping on the tips of the columns and hence subsequent column broadening. In b) the pitch of 45 nm is slightly higher than the fibre width, and the fibrous column structure is maintained without lumping or broadening.

sweep pitch range of 15 to 45 nm discussed here. The case of a sweep pitch  $q$  of 30 nm represents a growth evolution situation with elements of both traditional column broadening and infinite fibrous growth. The structure of the  $q = 30$  nm PhiSweep film, shown in figure 10.1c and g, is therefore intermediate to the open  $q = 15$  nm structure and the nanofibrous  $q = 45$  structure.

For experimental evidence in support of the above geometrical explanation of PhiSweep and nanofibrous GLAD film growth, consider first figure 10.9 of two PhiSweep films with a thickness of 45 nm. In figure 10.9a the sweep pitch  $q$  was 15 nm, meaning that three  $\phi$  sweeps were performed to attain the thickness of 45 nm, while in figure 10.9b the sweep pitch  $q$  was 45 nm, so that only one  $\phi$  sweep was done. After only 45 nm of growth the  $q = 15$  nm PhiSweep columns in figure 10.9a already show a tendency to clump, with gobs of silicon forming on the tips of the columns. This is a direct consequence of the frequent substrate sweeping. Meanwhile, such clumping is absent in figure 10.9b, where the  $q = 45$  nm PhiSweep columns manage to grow more uniformly. Here the fibrous morphology is maintained without broadening, even though the film contains many small voids between the columns.

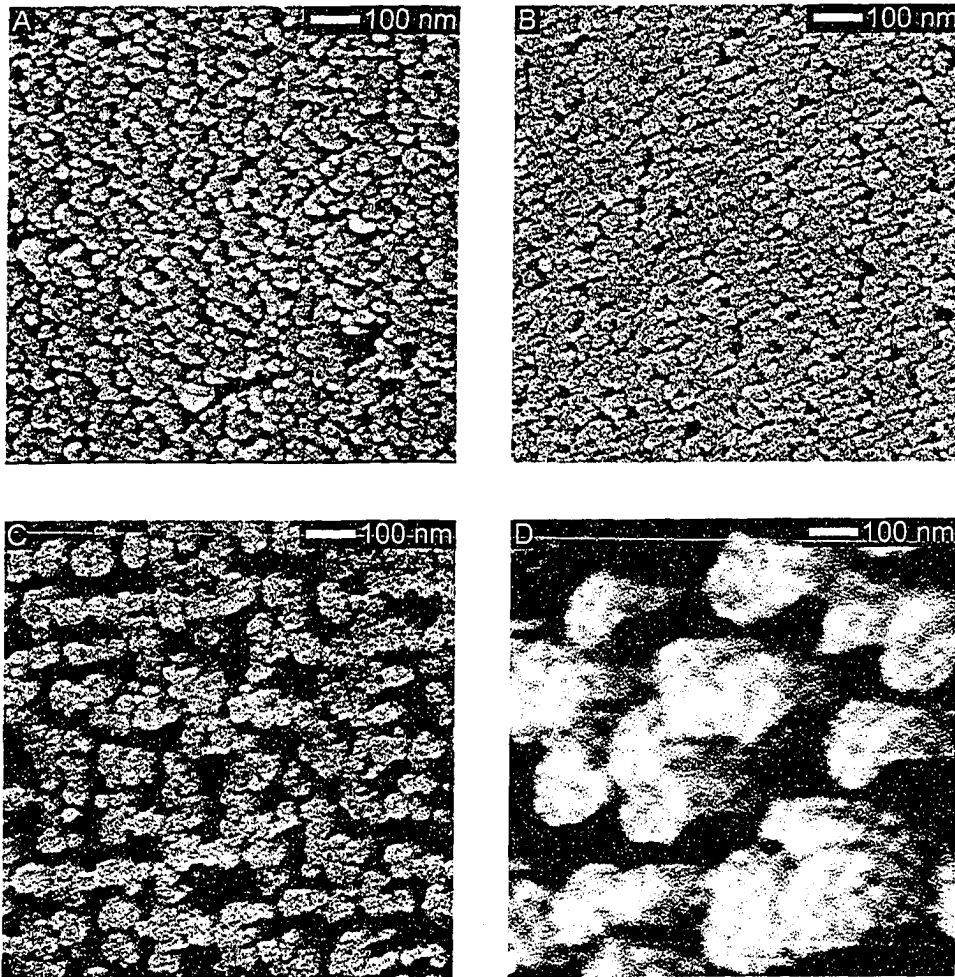


Figure 10.10: a,b) Top views of PhiSweep GLAD films with a sweep pitch  $q$  of 45 nm, shown after 15 nm and 2645 nm of growth, respectively. Column competition is completely suppressed. c,d) Top views of PhiSweep films with a sweep pitch of 15 nm, shown after 270 nm and 2730 nm of growth, respectively. For this sweep pitch value column competition and broadening are evident even after 270 nm of growth, and dominant after 2730 nm of growth.

Consider next figure 10.10. The top row shows top views of PhiSweep GLAD films with a sweep pitch of 45 nm, after 15 nm of growth (i.e., right after substrate nucleation) and after 2645 nm of growth (equivalent to  $58 \phi$  sweeps). The film morphology is all but identical in the two cases, demonstrating that column competition has been completely suppressed by the PhiSweep method. Meanwhile, the bottom row in figure 10.10 shows top views of two PhiSweep GLAD films with a sweep pitch of 15 nm, this time after 270 nm of growth and after 2730 nm of growth. Comparing figure 10.10c with 10.10a reveals that after only 270 nm of growth, significant column competition has set in for the case of  $q = 15$  nm. At the full film thickness of 2730 nm (figure 10.10d) severe column competition and broadening has taken place. The absence of column competition in  $q = 45$  nm PhiSweep films, and its strong presence in  $q = 15$  nm films, is in full agreement with the geometrical explanation of PhiSweep growth.

It must be emphasized that the nanofibrous PhiSweep film structure arises only in aperiodic films. Indeed, the periodically seeded PhiSweep columns discussed in chapter 7 did not exhibit a nanofibrous structure for sweep pitches of 45 nm, but rather had a smooth outer surface. It is possible, however, that these periodic square spiral columns do have a nanofibrous internal structure, and that the outer structure has been smoothed by vapour dispersing between the widely separated seeded columns. This is corroborated by the fact that the apices of the periodic columns – where no dispersed vapour has yet arrived – exhibit a rougher structure more akin to the aperiodic nanofibrous films.

Recent research by colleagues P. Hrudey and D. Gish has extended the fabrication of nanofibrous PhiSweep GLAD films to titanium and titanium dioxide, although for these materials the full dependence of the film structure on the sweep pitch has not yet been investigated [245, 246]. Since the fibre or column width of a film material depend on the characteristics of that material, the absolute sweep pitch values required to obtain a given PhiSweep film structure must be determined experimentally for each material. The sweep pitch range discussed above is therefore valid only for silicon. Indeed, materials which do not yield a stranded fine structure during initial nucleation might be indifferent to the sweep pitch altogether.

## 10.5 The Impact of Porosity Engineering in GLAD Film

In addition to its usefulness to square spiral photonic crystals and waveguides, the development of the PhiSweep GLAD method represents two important achievements:

- Porosity engineering in GLAD films.
- Nanofibrous GLAD films as a new thin film structure.

PhiSweep addresses the challenges for porosity engineering outlined previously, with its ability to achieve a certain size, shape, and spatial distribution of the voids present in obliquely deposited thin films – or, conversely, engineer the diameter and spacing of the constituent columns – and hence obtain a given surface area independently of the vapour incidence angle and helical shape. Apart from being useful to many existing GLAD applications, this provides significant thin film fabrication flexibility, broadens the scope of future GLAD applications, and aids the understanding of the growth of GLAD films.

With their extremely small and numerous pores, nanofibrous GLAD films are an innovation on their own. In chapter 6 it was detailed how periodic, traditional GLAD films offer a more uniform film structure than aperiodic GLAD, and now nanofibrous GLAD provides yet another level of improvement in film uniformity. Indeed, for applications where the nanoscale fibre roughness is of little importance, nanofibrous GLAD films are for all intents and purposes a homogeneous and isotropic, but nevertheless highly porous, material.

The last sections of this chapter describe some of the properties of nanofibrous GLAD films, while the next chapter deals with nanofibrous GLAD films in columnar microfluidic channels as a new GLAD application unique to this kind of thin film structure. Another application of nanofibrous GLAD films under current investigation is dye sensitized solar cells in titanium dioxide PhiSweep films [246].

## 10.6 Characteristics of Nanofibrous GLAD Films

### 10.6.1 Surface Area Estimates

Based on the measured fibre width of 20 - 30 nm, taking into account that the nanofibrous GLAD films have the same density as traditional GLAD films

(i.e., 40% of bulk density), and approximating the nanofibres to smooth cylinders, the geometrical surface area of a 3.2  $\mu\text{m}$  thick nanofibrous film can be estimated to 180  $\text{cm}^2/\text{cm}^2$ , or 68  $\text{m}^2/\text{g}$ . Since the nanofibres do in fact have a rough surface texture, rather than a smooth one (see figure 10.6), the actual surface area will be substantially higher than this conservative estimate. In addition, more surface area can be added simply by growing thicker PhiSweep films.

Even so, the geometrical surface area estimate for the nanofibrous films is much higher than the surface areas in traditional GLAD films, which have been measured to 13.2  $\text{cm}^2/\text{cm}^2$  or 6.6  $\text{m}^2/\text{g}$  for GLAD nickel films [165], and 119.5  $\text{cm}^2/\text{cm}^2$  for silicon dioxide films [168] (in both cases measured using porosimetry). In another approach, the surface area was found to be 42  $\text{cm}^2/\text{cm}^2$  based on a 3D-FILMS simulation that did not account for columnar micro roughness [168]. The higher surface area of the nanofibrous films is a direct consequence of these films consisting of more numerous and thinner columns/fibres than traditional GLAD films. Interestingly, although nanofibrous PhiSweep films were not known at the time, the 3D-FILMS simulation presented in [168] showed that the surface area of GLAD films is very high in the initial film structure close to the substrate. Nanofibrous films attain a high surface area exactly by maintaining this initial structure throughout the thickness of the film.

The estimated nanofibrous film surface area is only one order of magnitude lower than that of activated carbon, whose surface area of  $\sim 1000 \text{ m}^2/\text{g}$  is generally considered the highest available for any material today.

### 10.6.2 Mechanical Properties

To evaluate the mechanical properties of the nanofibrous films, a number of nanoindentation experiments were performed and compared with the response of traditional GLAD films. The nanoindentation experiments were carried out in collaboration with M. Seto. In the instrument an indenter tip is pressed down ten to several hundred nanometres onto the top of a film, and the relation between the applied load and the depth of the indentation into the film is recorded. For each film several nanoindentations were made at various locations on the film surface, and each indentation was repeated several times to test for permanent deformation. Also, the magnitude of the applied load was varied among the indentation experiments.

Figure 10.11 shows a nanoindentation plot in which a maximum force of 200  $\mu\text{N}$  was applied to a nanofibrous GLAD film. Each of the curves represent a separate indentation with varying applied load, and the fact that

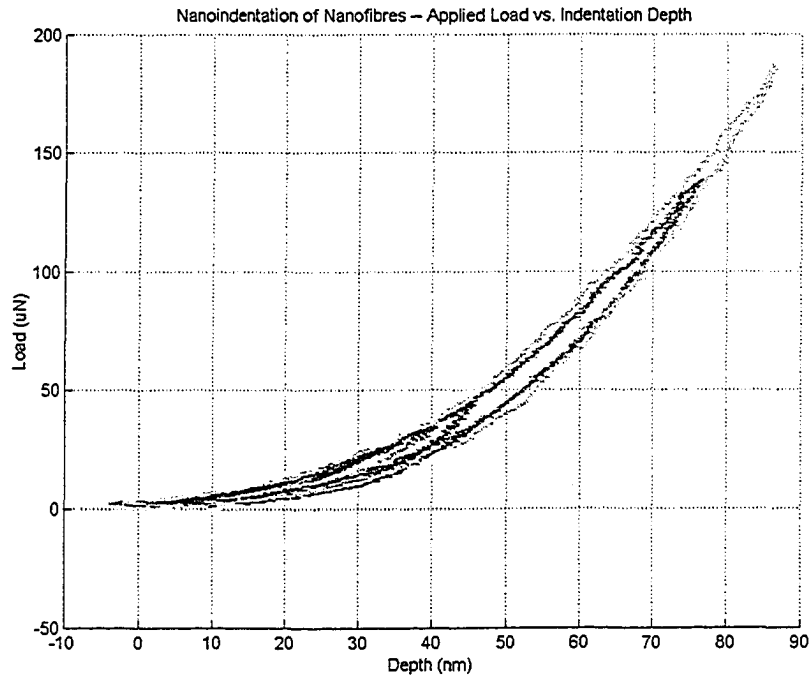


Figure 10.11: Nanoindentation plot of a silicon nanofibrous PhiSweep GLAD film. A number of indentations were carried out with a maximum applied load of 200  $\mu\text{N}$ .

all curves are on top of each other with only little deviation demonstrate that the indentations are reproducible and non-destructive. By fitting the indentation curves from this and sixteen other locations to a power law function, and in each case relating the indentation depth to the contact area of the indentation tip, the average area stiffness  $S_A$  of the nanofibrous film was found to be:

$$S_A(\text{nanofibrous}) = 120 \text{ N/m}/\mu\text{m}^2.$$

Assuming a volume density  $\rho_V$  of the film of 0.4 – in accordance with the discussion on film density earlier in the chapter – and an average column or fibre diameter of 25 nm, the number of nanofibres per  $\mu\text{m}^2$  of film is:

$$N = \frac{\rho_V \cdot 1 \mu\text{m}^2}{A_{\text{cross-section}}(\text{fibre})} = \frac{0.4 \cdot 1 \mu\text{m}^2}{\pi(25/2 \text{ nm})^2} = 815 \text{ fibres}/\mu\text{m}^2. \quad (10.1)$$

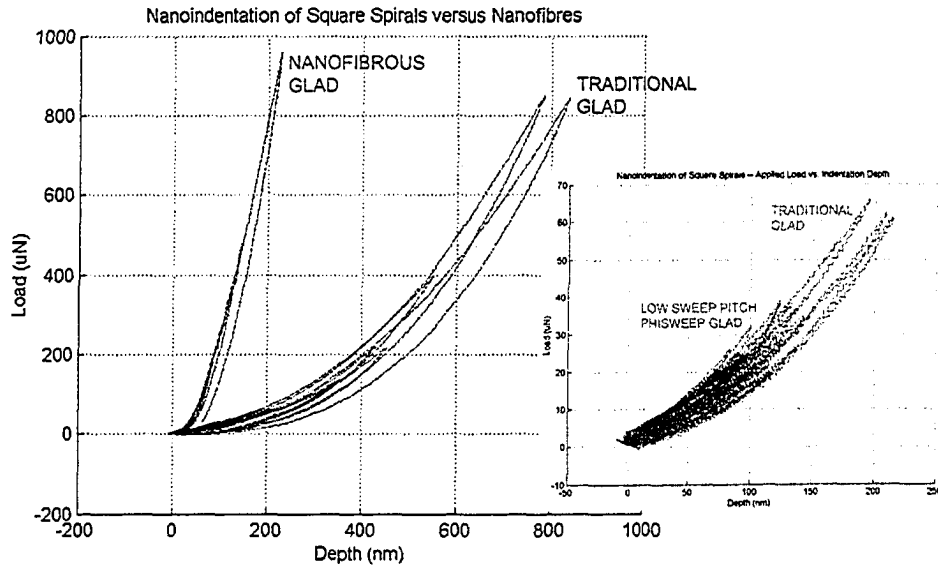


Figure 10.12: Composite nanoindentation plots of a nanofibrous PhiSweep film (red) and a traditional square spiral GLAD film with an open structure (blue). The stiffness of the nanofibrous film is one order of magnitude higher. The inset shows that the mechanical responses of a traditional square spiral film (blue) and an open PhiSweep film with a sweep pitch  $q$  of 15 nm (red) are nearly identical.

Thus, the approximate stiffness per fibre is:

$$S_{fibre} = \frac{S_A(\text{nanofibrous})}{N} = \frac{120 \text{ N/m}/\mu\text{m}^2}{815 \text{ fibres}/\mu\text{m}^2} = 0.14 \text{ N/m/fibre}. \quad (10.2)$$

Earlier nanoindentation experiments on circular helical GLAD films of silicon monoxide, titanium and chromium yielded areal stiffnesses  $S_A$  of 10 to 21 N/m/ $\mu\text{m}^2$  for films with 10 columns per  $\mu\text{m}^2$ , or a stiffness per column of 1.1 N/m [153, 154, 247]. However, for more relevant comparison with the nanofibrous PhiSweep GLAD films, a new series of nanoindentation experiments was performed on a silicon square spiral film deposited using traditional GLAD (no  $\phi$  sweeps) to give an open, aperiodic film structure (similar to figure 10.1a and e). Figure 10.12 shows overlaid nanoindentation plots of the nanofibrous GLAD film (red lines) and the traditional, open GLAD film (blue lines), with a maximum applied force of 1000  $\mu\text{N}$ . The nanofibrous film is clearly more resistant to the indentation tip. In fact, the

areal stiffness of the traditional square spiral film was found to be:

$$S_A(\text{traditional}) = 9 \text{ N/m}/\mu\text{m}^2,$$

which is much lower than the stiffness of the nanofibrous film.

Nanoindentation was also carried out on a PhiSweep GLAD film with a sweep pitch  $q$  of 15 nm, i.e., with a structure quite similar to traditional GLAD films. The inset in figure 10.12 shows that the mechanical response of the traditional GLAD film (blue lines) and the low sweep pitch PhiSweep film (red lines) are nearly identical, as would be expected given the structural similarities of these two film types. Indeed, the areal stiffness of the open PhiSweep film was:

$$S_A(\text{open PhiSweep}) = 13 \text{ N/m}/\mu\text{m}^2,$$

which is not too different from the  $9 \text{ N/m}/\mu\text{m}^2$  for the traditional GLAD film.

The nanoindentation data show that the areal stiffness of nanofibrous GLAD films is one order of magnitude higher than that of traditional GLAD films with an open structure. Moreover, this is true not just when comparing the nanofibrous films to other silicon square spiral GLAD films, but regardless of the material and helical shape of the traditional films. The increased stiffness of the nanofibrous GLAD films has yet to be explained, but the compact structure of tightly interwoven fibres or columns may result in significant interaction between the columns when the top surface of the film is depressed. If the columns thus grind against each other, the added friction could increase the combined resistance of the film to deformation. In open, traditional GLAD films, on the other hand, the columns are much farther apart and operate as separate entities, with little or no interaction to affect the mechanical stiffness.

With respect to mechanical properties, nanofibrous PhiSweep films provide a stiffness intermediate to those of traditional GLAD films and those of dense films deposited at normal incidence (whose stiffness for the case of silicon oxide is on the order of  $18500 \text{ N/m}/\mu\text{m}^2$  [154]). It is worth noting that all non-nanofibrous, open structured GLAD films analyzed so far have about the same areal stiffness, namely  $10 - 20 \text{ N/m}/\mu\text{m}^2$ , irrespective of material composition, thickness and helical shape. The fact that the stiffness of nanofibrous PhiSweep films deviate substantially from this range confirms that they represent a truly new class of GLAD films.

## Chapter 11

# Microfluidics in GLAD Films

The new GLAD capabilities developed as part of the thesis research on square spiral PBC engineering have numerous uses in both existing and potential GLAD thin film applications, well beyond the realm of PBCs. One of the new spin off GLAD applications is the fabrication of microfluidic networks with potential embedded size exclusion chromatography functionality, established by the author in collaboration with Dr. G. Kiema. By relying on the seed layer fabrication of chapter 5, the analysis of periodic GLAD growth of chapter 6, the new seed layer induced defect engineering technique of chapter 9, and the nanofibrous PhiSweep films of chapter 10, this new application integrates many of the thesis results.

The thesis research on GLAD microfluidics is under preparation for publication.

### 11.1 The Principles of GLAD Microfluidics

Microfluidics encompasses the downscaling of fluid handling systems to devices with sub millimetre features fabricated using the processing tools developed for the microelectronics industry. Applications are found in fluid dispensing and flow rate systems, and – increasingly – in analytical chemistry and biochemistry, where reagents are manipulated in minute channels lithographically defined on a chip [248]. Ink jet printing nozzles [249] and miniature gas chromatographs [250] were the first microfluidic devices, but the research area formed in earnest in the mid 1990s in parallel with micro electro mechanical systems (MEMS). Today, advanced microfluidic networks include channels, filters, mixers, pumps, valves, and many kinds of sensors and detectors (often optical) [251]. In addition to immediate benefits such as

drastic reductions in sample size, reagent consumption, reaction times, and device volume and power demands, microfluidics represents a novel platform for biochemistry capable of interaction with *individual* blood cells, proteins, etc. [248, 252, 253] However, due to the reliance on semiconductor processing technology, an outstanding limitation of microfluidics is the availability of materials. Many of the materials suitable for traditional microfabrication are incompatible with the intended (bio)chemical reactions, and some devices simply get eaten up by the reagents over time.

An application actively being pursued for microfluidics is chromatography, in which the constituents of a fluid mixture – be they chemical species, macromolecules, or cells – are separated for quantitative or qualitative analysis [254]. One of the many types of chromatography is size exclusion chromatography (SEC), where particles in a solution are separated due to size dependent migration paths arising as they flow through a conduit with a uniform array of physical obstacles. Depending on the geometry of the obstacles, particles of different sizes take different times to travel the same distance, or alternatively migrate in different directions. A traditional approach has been to employ capillary tubes packed with beads or microspheres and capped with frits, but the beads tend to clog and settle non-uniformly, which reduces accuracy and lifetime [254, 255]. Recently, efforts have turned toward microfabricated flow channels with the obstacles being two dimensional arrays of micrometre sized pillars, and with potentially more precise and much faster sorting of sub micrometre entities. Key examples include the work by Baba *et al.*, who used SEC in reactive ion etched arrays of silicon posts to separate DNA strands of various lengths [256], and the work by Huang *et al.*, who employed staggered silicon pillar arrays to obtain spatial sorting of polystyrene microspheres with resolutions on the order of 10 nm [257].

GLAD can be applied to microfluidic networks and SEC through defect engineered PhiSweep thin films. The principles are as follows:

First, a *seed layer* is fabricated with uniform arrays of seeds covering the substrate where flow channels are desired, and the substrate remaining bare elsewhere. This seed layer design approach is the ‘inverted’ method previously discussed in section 9.5, and LDWL should be employed to obtain sufficiently large patterns (microfluidic circuits typically extend over several centimetres).

Next, a *nanofibrous PhiSweep GLAD film* is deposited on the seed layer. From earlier chapters it is known that this will create a nanofibrous film structure with extremely small pores on the bare substrate, whereas on the seeded areas of the substrate a regular, periodic GLAD film will be gener-

ated. In other words, the GLAD film extruded from the 'inverse' seed layer now consists of a compact nanofibrous background with a defined embedded pattern of more openly spaced periodic GLAD columns.

Third, a *cover* is applied to seal the flow channels defined by the patterned, periodic regions of the GLAD film. Since the GLAD film thickness is identical over seeded and non-seeded areas, with the flow channels being filled with periodic columns rather than being empty grooves, a soft polymer cover should seal tightly.

Finally, a liquid/particle mixture injected at one end of the flow channel system can be forced through the network by applying a *pressure differential*, i.e., either positive pressure at the inlet or negative pressure at the outlet. (Electro-osmotic or electrophoretic flow systems could also be used.) The flow of different constituents in the liquid/particle mixture now selectively depends on their dimensions relative to the pore size in the nanofibrous GLAD film, and the column-to-column separation in the periodic GLAD film making up the flow channels:

- Particles larger than the periodic column-to-column separation will go nowhere, but just clog the inlet port.
- Particles smaller than the periodic column-to-column separation, but larger than the nanofibrous pores, will exclusively proceed down the flow channels defined by the seed arrays. Furthermore, these particles will experience SEC separation in accordance with their dimensions relative to the geometry of the periodic GLAD columns.
- The carrier liquid and any particles smaller than the nanofibrous pore size will proceed down the flow channels, as well as penetrate into the aperiodic nanofibrous background.

The extent to which the carrier liquid penetrates into the nanofibrous background film depends on the pore distribution of the film, which in turn depends on the film material. The flow will always be greater in a channel than in the nanofibrous background, and, as will be demonstrated below, the leakage can be kept so small that for practical purposes the nanofibrous film constitutes a flow barrier bounding the channels. The engineered GLAD film defects then represent true microfluidic circuits useful even for analytical chemical applications on particle-free reagents (which are oblivious to the periodic columns inside the channels).

However, even if the carrier liquid or small particles leak significantly into the nanofibrous film background, the GLAD flow channels remain a potential

SEC medium. Suspended particles with dimensions intermediate to the nanofibrous pores and the periodic column separation are fully confined to the channels, and as long as the pressure differential of the carrier liquid – infiltrating both the channels and the background – is in the general direction of the patterned channels, the particles will continue to experience an SEC effect due to the columnar array.

In comparison with other techniques for the fabrication of microfluidic circuits and SEC media, the defect engineered PhiSweep GLAD approach has several advantages. Once a seed layer has been prepared, fabrication of both channels and SEC obstacles consists of a single, bottom-up deposition step with no need for post deposition film processing other than application of a polymer cover. More importantly, unlike traditional microfluidic circuits etched in glass and select semiconductors (limited by standard microfabrication technology), the GLAD approach is potentially amenable to all PVD compatible materials, which includes a large number of metals, semiconductors, oxides, and fluorides. This allows for compatibility with many different chemical reagents and biological organisms, and for selection of a material which appropriately interacts with the particles to be sorted (since surface chemistry plays an important role in SEC). The only requirement is that the PVD material must be able to produce the nanofibrous PhiSweep GLAD film structure, which has so far been the case for all three materials attempted, namely silicon, titanium, and titanium oxide. Titanium is indeed a notable biocompatible material. Furthermore, independently of the film material itself, any transparent or opaque substrate is applicable as long as it can be coated with an LDWL compatible resist.

With respect to the columnar SEC array, seed layer induced periodic GLAD films offer great design flexibility. Any seed lattice geometry can be used, including regular or skewed tetragonal or hexagonal lattices, and as long as the seed layer planar fill factor and the film volume fill factor match, any seed lattice period and column width can be attained. In typical silicon PhiSweep nanofibrous films the pore size in the nanofibrous background is sub 30 nm, whereas the column-to-column separation can be 300 nm or higher. This size range is indeed relevant for SEC of many biochemical entities, such as DNA, viruses, and proteins.

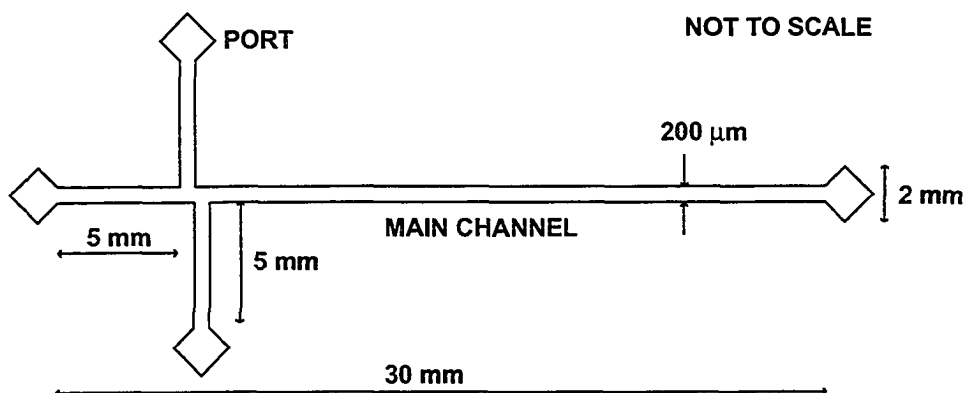


Figure 11.1: Schematic of a four port double-T microfluidic network design for a defect engineered PhiSweep GLAD thin film. The main channel is 30 mm by 200  $\mu\text{m}$ .

## 11.2 Design and Implementation of GLAD Microfluidic Networks

The key initial experiment for GLAD based microfluidics is the demonstration of liquid flow within a defect engineered PhiSweep defect. To achieve this, various potential microfluidic network components were first designed in dummy prototypes to confirm the viability of the PhiSweep algorithm to produce periodic GLAD films in a nanofibrous background. Next, a real microfluidic flow channel was designed, consisting of a 30 mm long and 200  $\mu\text{m}$  wide main conduit (for an aspect ratio of 150:1), with 2.2 mm large, diamond shaped inlet and outlet ports at either end. Finally, a four port double-T microfluidic injector network was designed, constructed from the same 30 mm main channel as before, but with two additional 5 mm long side arms attached perpendicularly to the main channel. This design is illustrated in figure 11.1, and is intended to allow a small (400  $\mu\text{m}$  long) sample plug to be injected sideways into a background buffer flow for analysis in the main channel.

The microfluidic GLAD film fabrication process is shown schematically in figure 11.2. Substrate seed layers were fabricated using EBL on SU-8 covered silicon wafers for the initial dummy prototypes, and using LDWL on AZ-1518 covered soda-lime glass substrates for the larger patterns. In both cases the seed lattices defining the flow channels had a tetragonal geometry with a lattice period  $\Delta$  of 1.0  $\mu\text{m}$ .

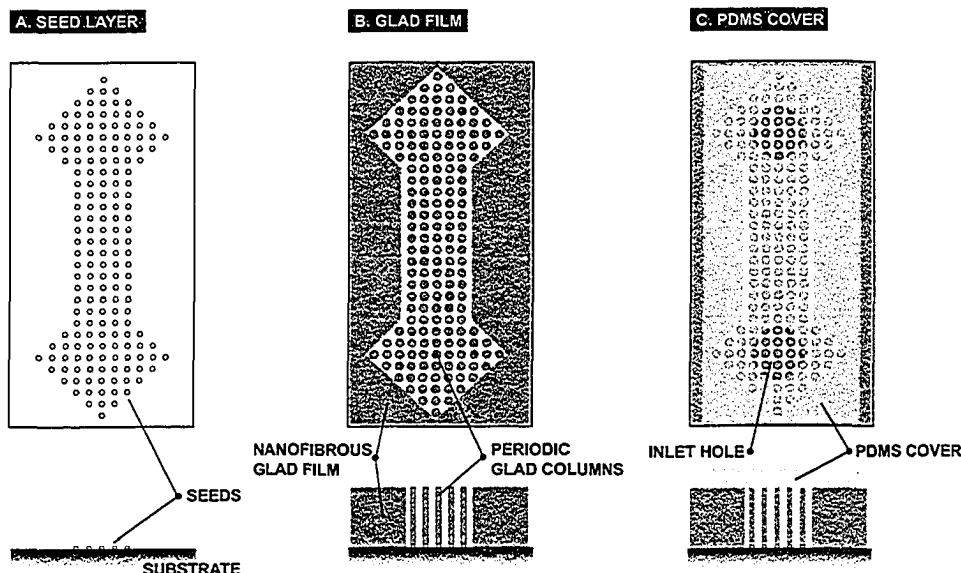


Figure 11.2: Planar (top row) and cross-sectional (bottom row) schematics of the three steps in fabrication of a GLAD microfluidic thin film. a) A substrate seed layer is prepared with periodic seeds defining the flow channels. b) A PhiSweep GLAD film leaves a nanofibrous film on the bare substrate and a periodic GLAD film on the seeded areas. c) A PDMS cover with inlet and outlet holes seals the flow channels.

GLAD films were deposited using the PhiSweep algorithm with a sweep angle  $\gamma$  of  $30^\circ$  and a sweep pitch  $q$  of 45 nm, i.e., the sweep settings discovered in chapters 9 and 10 to produce an aperiodic nanofibrous film structure on bare substrate regions, and to be suitable for defect engineering by evolution of a periodic GLAD structure on patterned substrate regions (see figure 11.2b). The deposited material was silicon, and the chiral column structure was square spirals with a pitch  $q$  of 1300 nm. The vapour incidence angle  $\alpha$  was  $84^\circ$ . A minimum film thickness of 10  $\mu\text{m}$  was found necessary to obtain sufficient flow rates through the films.

Sheets of the transparent elastomer polydimethylsiloxane (PDMS) – supplied by Dow Corning under the trade name Sylgard 184 – were used as covers to seal the GLAD flow channels (see figure 11.2c). The sheets were prepared by mixing two base and curing agent components, and pouring the high viscosity mixture into petri dishes. The polymer then cured for two days at room temperature to create a highly flexible but shape retaining material, with the sheet thickness depending on the amount of polymer poured

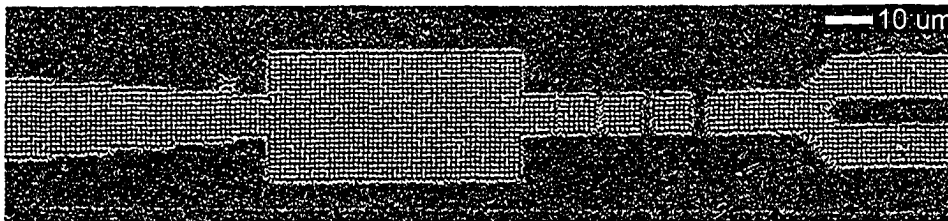


Figure 11.3: Top view of a prototype microfluidic network in a silicon PhiSweep GLAD film. The flow circuit is defined by the patterned, periodic regions of the film, bounded by an aperiodic, nanofibrous film structure.

into the dishes. After curing, an appropriate slab of PDMS was cut out of the petri dish, and a hypodermic was used to punch holes for the inlet and outlet ports. The PDMS sheets are slightly sticky, and adhere well to GLAD films to form a self-sealing cover. Some experimentation with different sheet thicknesses established 3 mm thick sheets as providing the best cover.

Flow experiments in the GLAD films were performed using a solution of the inorganic dye ruthenium 535 bis-TBA (supplied by Solaronix SA) in a 1:1 mixture of water and methanol, yielding a dark red colour distinguishable from the light brown tint of the GLAD films. Water and methanol are often used as solvents in chemical separation applications. To prevent detachment of the self-sealing PDMS cover, negative rather than positive pressure was used to drive flow through the microfluidic channels, implemented with a regulated laboratory vacuum line terminated in a pipette tip.

### 11.3 Demonstration of Flow in a GLAD Microfluidic Network

Figure 11.3 shows a dummy microfluidic network fabricated in a defect engineered PhiSweep GLAD film as described above, but with the pattern dimensions and film thickness being too small for actual flow experiments. The simple prototype components are a channel width reducer, a rectangular reaction chamber, a linear flow channel, and a Y splitter. The microfluidic circuit is defined by the patterned areas of periodic GLAD columns, characterized by having large gaps between the columns (given by the lattice period and the column width). Meanwhile, the background aperiodic GLAD film on the unpatterned areas of the substrate has a nanofibrous structure with no pores or gaps discernible at this image magnification. The linear channel segment in figure 11.3 contains perpendicular walls of aperiodic nanofibrous

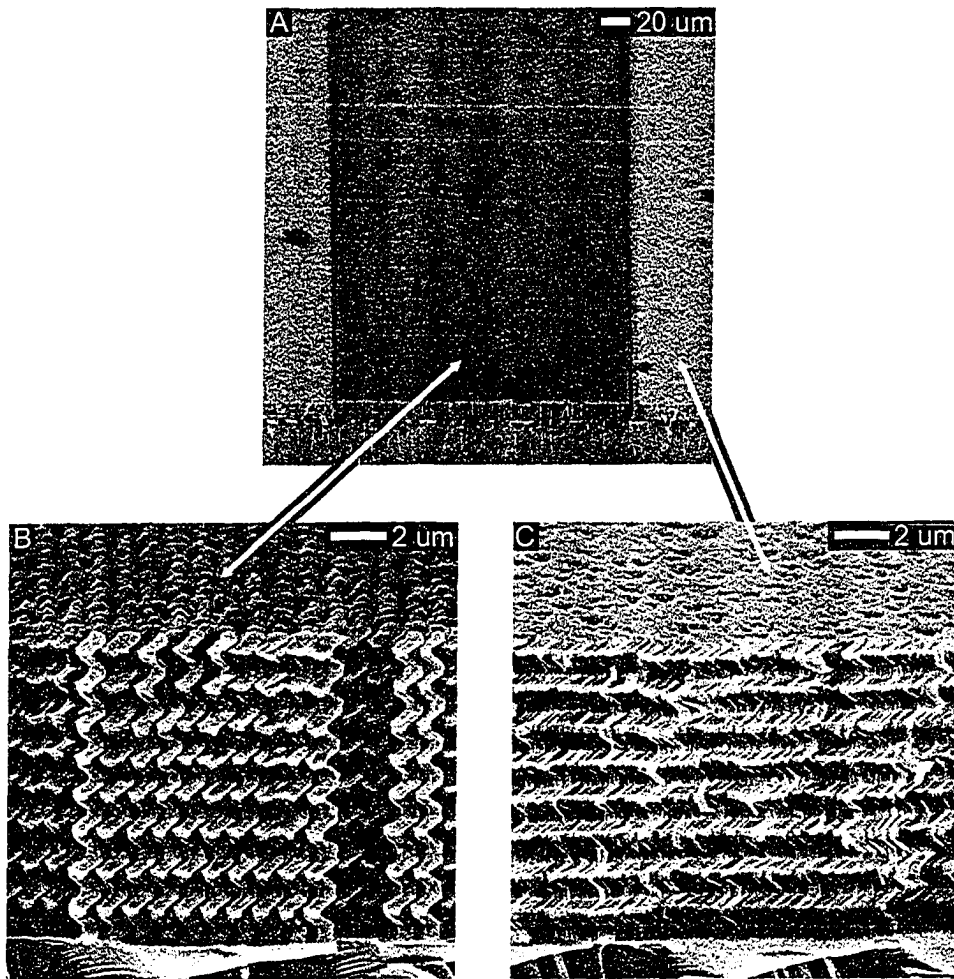


Figure 11.4: Oblique views of a GLAD microfluidic channel. a) Low magnification image of the full  $200\ \mu\text{m}$  wide channel, defined by seed layer induced defect patterning and using PhiSweep GLAD. b) Inside the channel is a periodic square spiral GLAD film structure with large gaps between the columns. c) In the background film outside the channel is an aperiodic, nanofibrous film with small pores prohibiting the leakage of large, fluid borne particles.

film – created by one to four row wide seed lattice defects – which could potentially be used as semi permeable filters for particles with dimensions similar to the nanometre sized pores in nanofibrous GLAD films.

A full size GLAD flow channel is illustrated in cross-section in figure 11.4a, prior to attachment of the PDMS cover. The channel is 200  $\mu\text{m}$  wide and 10.6  $\mu\text{m}$  thick. Figures 11.4b and c show detailed views of the film inside and outside the channel, respectively, and reveal the distinct morphological contrast between the periodic, open structure inside the channel, and the compact, nanofibrous morphology bounding the channel. In this film structure a pressurized liquid will tend to flow predominantly through the patterned, periodic channel, and particles with dimensions intermediate to the nanofibrous and periodic GLAD pore sizes will be exclusively confined to the channel.

Demonstration of liquid flow through a four port double-T GLAD microfluidic circuit is illustrated in figure 11.5. The flow channels in the GLAD film were identical to the one shown in figure 11.4, with a thickness of 10.5  $\mu\text{m}$ . Since the full circuit was too large to image in a microscope, a digital video camera with a suitably short focal distance was used to record the experiment, and the images in figure 11.5 are chronologically arranged frames from the resulting movie.

Figure 11.5a shows the device setup prior to the flow experiment, with a 3 mm thick PDMS cover attached on top of the GLAD film. The flow channels appear as grey lines in the brown GLAD film, since the periodic film structure inside the channels reflect light differently than the nanofibrous, aperiodic film structure outside the channels. Holes in the cover match the inlet and outlet ports of the microfluidic circuit, and a vacuum line (at this time turned off) has been inserted into the outlet port. Rather than attempting injection of a sample plug via the side arms perpendicular to the main channel – which would required differentiated pressure lines on three ports – this experiment simply lets liquid flow from the three inlet ports to the vacuum enabled outlet port.

Loading of an inlet port is shown in figure 11.5b, while figure 11.5c shows the device fully loaded with red dye on all three inlet ports. The vacuum on the outlet port was turned on just prior to figure 11.5d. Immediately, liquid dye from the three droplets fills the vertical holes in the PDMS cover, streams into the diamond shaped inlet ports underneath, and flows into the channels (giving the periodic GLAD film a darker tint as it gets wet). No leakage into the aperiodic GLAD background is observed. In figure 11.5e, the streams from the three inlet ports have converged at the hub of the double-T, and have progressed to just beyond this intersection. Figure 11.5f

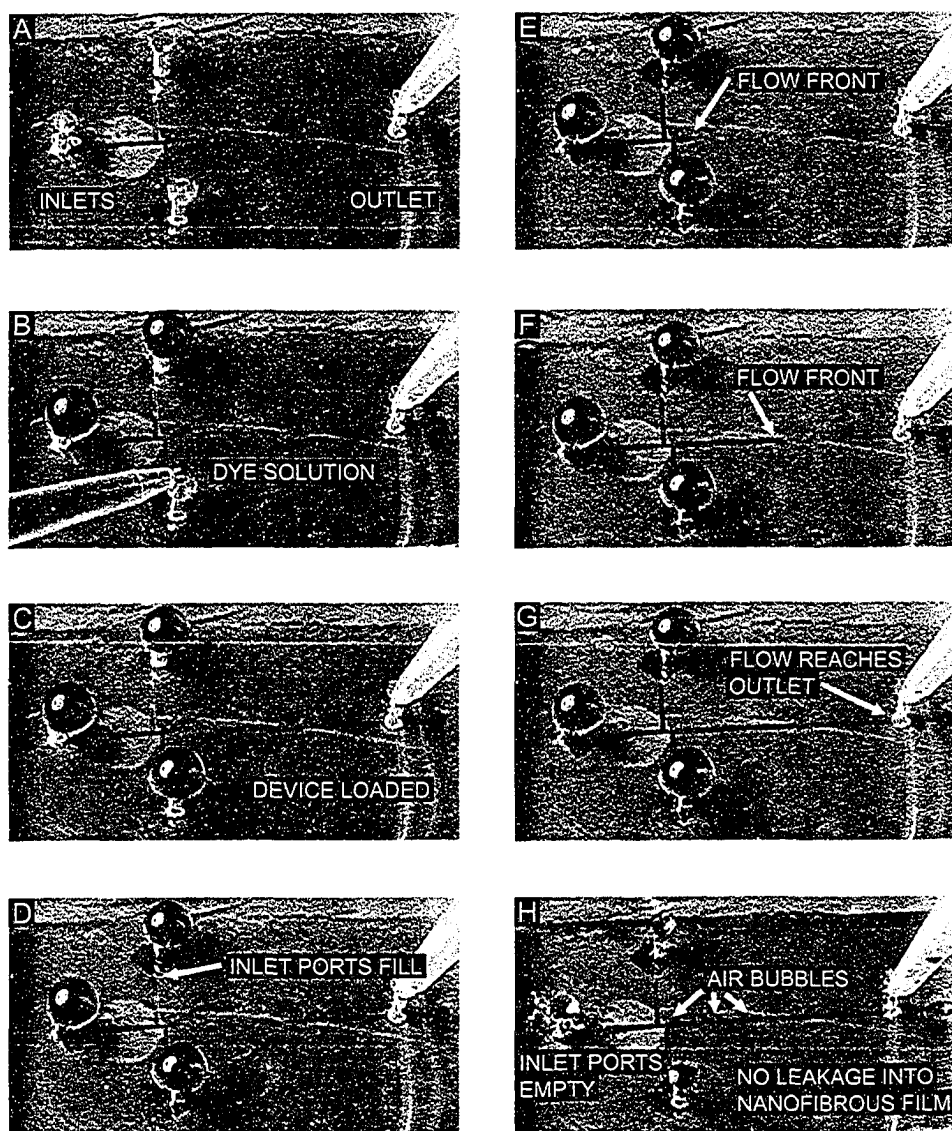


Figure 11.5: Chronological array of frames illustrating the flow of liquid through a defect engineered GLAD PhiSweep microfluidic circuit. The main channel nominal length is 30 mm. a) Empty device. bc) Loading of dye solution. d) Outlet vacuum turned on, flow proceeding through the inlet ports and into the initial part of the channels. efg) Liquid flow continues through the main channel and into the outlet. h) At the end of the experiment the inlet ports are empty, liquid has accumulated in the outlet pipette, and no leakage into the nanofibrous background film is observable.

shows the front of the liquid midway down the central main channel, and in figure 11.5g the liquid flow has reached all the way to the outlet port. Note that no air bubbles are observed in the microfluidic network, even as liquid continues to flow from the inlet ports to the outlet.

Finally, figure 11.5h shows the device at the end of the experiment after 8 minutes of pumping. The three inlet ports are now all but empty, whereas a few beads have accumulated inside the pipette tip of the outlet. On closer inspection, air bubbles caused by the emptying inlet ports are discernible as light grey areas inside the flow channels. Most critical of all, though, is that even after having run the GLAD microfluidic circuit until the inlet ports emptied, no leakage of liquid into the nanofibrous film bounding the channels is observable.

The next future step is to demonstrate selective flow of particles of different sizes by way of SEC in the periodic, columnar GLAD flow channels. This could initially be attempted by using a carrier liquid mixed with fluorescent beads (e.g., commercially available functionalized polystyrene microspheres), with beads of different sizes emitting light at different wavelengths, allowing the size dependent particle migration paths to be optically recorded. Subsequently, more advanced microfluidic circuit layouts could be designed, and if there is no need for optical access to the channels, covers might be fabricated using a dense GLAD capping layer (by reducing the vapour incidence angle to zero at the end of the deposition). In the longer term, it might even be feasible to integrate GLAD square spiral PBCs and GLAD microfluidics in one device, in order to exploit the PBCs for optical chemical detection [63, 258].

With the above experiment it has been demonstrated that defect engineered PhiSweep GLAD films can be used for microfluidic applications, enabling liquids to flow through a substrate seed layer induced periodic film pattern embedded in a nanofibrous, aperiodic film background. This not only proves the versatility and usefulness of the new GLAD growth algorithms and defect engineered periodic film structures developed in the preceding chapters, but also extends GLAD to biochemical applications for the first time.

No Text

## Chapter 12

# Conclusions and Perspectives

### 12.1 Summary of Results

The objective of this thesis has been to enable the engineering of three-dimensional photonic bandgap crystals (PBCs) using glancing angle deposition (GLAD) thin films. PBCs are optical materials which rely on coherent Bragg scattering within a periodic dielectric structure to prohibit the propagation of light in bandgaps of defined frequencies. This permits light localization and manipulation of radiative emission, and PBCs constitute a potentially superior medium for applications such as integrated optical circuits, small cavity lasers, and high efficiency LEDs. GLAD is a thin film deposition technique based on vapour impingement at highly oblique angles onto substrates rotating about two axes. In the absence of significant bulk or surface diffusion, geometrical shadowing yields columnar and highly porous films, with complex chiral microstructures achievable through dynamic substrate motion.

GLAD is a viable fabrication method for a PBC architecture consisting of tetragonally arranged square spirals, which approximately connect lattice points in the photonically desirable diamond lattice to generate large and robust bandgaps. Inspired by the structural similarity between square spiral GLAD films and the PBC architecture, and exploiting both the flexibility of practical GLAD fabrication and the theoretical advantages of the square spiral architecture, GLAD based PBCs hold a promise to address many of the shortcomings of existing, experimentally investigated 3D PBC structures. These challenges include fabrication of large area crystals, control over the crystal fine structure and lattice uniformity, the ability to engi-

near the position of the photonic bandgap, and the capacity to introduce intentional lattice defects. The thesis has endeavoured to develop GLAD solutions to each of them.

As a means to enforce a periodic structure in GLAD thin films, a complete set of design rules for substrate seed layers has been derived. These rules describe the geometrical relations between the seed layer dimensions and the GLAD deposition parameters, and emphasize the importance of matching the seed layer planar fill factor with the volume fill factor of the GLAD film. For prototype seed layer fabrication, electron beam and laser direct write lithography were identified as the most suitable technologies. SU-8 was developed to yield the highest resolution yet attained for a negative EBL resist, and through write field expansion and single pixel writing, high density EBL seed layers with 30 nm resolution over areas as large as 1 mm<sup>2</sup> were achieved. Much larger seed layer areas were obtained with LDWL, where careful optimization of the laser energy, beam focus, and AOM frequency ramp allowed an unprecedented sub 250 nm LDWL resolution to be maintained over areas as large as 40 mm<sup>2</sup>. In addition to providing a platform for large area GLAD PBC fabrication, the advances in seed layer fabrication may serve other GLAD applications, and indeed any lithographic job where high resolution prototype patterns with complete design freedom are required over large areas.

The ability of GLAD thin films to conform to periodic seed layers has been analyzed by studying the initial nucleation and subsequent evolution of periodic film structures. It was found that when the seed layer design rules are adhered to, and film growth on the bare substrate between seeds is suppressed, a periodic film structure can be maintained throughout the film, with significant morphological advantages over aperiodic GLAD films. The overall film structure is uniform, the columns are congruent, and column competition and extinction are eliminated. GLAD thus constitutes a unique approach to the fabrication of highly symmetric arrays of freestanding, sub micrometre columnar structures, with the substrate seed layers providing much greater control over the film uniformity and morphology than in aperiodic columnar thin films.

In research on bandgap engineering of GLAD PBCs, silicon square spiral GLAD films were scaled down to effect an increase in the frequency of the anticipated photonic bandgap. It was discussed how the photonic properties depend not only on the tetragonal lattice dimensions (driven by the seed layer and the spiral pitch), but even more so on the film volume fill factor and fine structural details, driven by the vapour incidence angle and

growth algorithm. By reducing the seed lattice period to as low as 600 nm, increasing the pitch to higher than theoretically prescribed values, and raising the vapour incidence angle to  $85^\circ$  or  $86^\circ$ , it was shown that square spiral GLAD films can be successfully scaled to dimensions that approach the ideal for a range of PBCs with higher bandgap frequencies than previously attained. However, it was also discovered that intrinsic growth problems in traditional square spiral GLAD films – notably spiral arm broadening and fanning, evolution of a crescent shaped arm cross-section, and column bifurcation at spiral corners – introduce a significant amount of disorder in the fine structure of the square spirals. These problems would detract from the optical quality of GLAD PBCs at any frequency, but are further exacerbated by efforts to shrink the GLAD film microstructure, and therefore prevent reliable bandgap engineering.

Closer examination of the detrimental growth effects revealed that their primary causes are alignment of the vapour arrival direction with the tetragonal seed layer, and unidirectionality in the geometrical shadowing among the growing columns. Two new advanced GLAD growth algorithms were developed to remove the fine structural problems. In PhiSweep GLAD, the vapour arrival direction is swept from side to side about a central axis defining the direction of column growth. The associated dispersion of the vapour stream and decoupling of the vapour arrival direction from the seed lattice unit vectors eliminate arm segment broadening and inter-seed film growth, improve the arm cross-section, and enhance the film uniformity. In the Off-Axis GLAD algorithm, the vapour arrival direction is shifted slightly away from the seed layer lattice to make the growing square spirals mutually cover each other as seen along the vapour trajectories. This algorithm generates a superior square spiral thin film morphology, which closely resembles the ideal architecture except for the lattice distortion caused by the off-axis spiral alignment.

The new GLAD algorithms yield highly uniform square spiral PBC structures with a minimum of roughness and lattice disorder. In conjunction with alteration of the direct write seed lattice designs and the GLAD deposition parameters, direct control over the crystal dimensions and even the fine structure has been achieved. This gives bandgap engineering in GLAD PBCs notable advantages over rival 3D PBC architectures at the same length scale, which rely on substantially more complex fabrication schemes.

Verification of the PBC bandgap engineering capabilities was provided by optical characterization using FTIR spectrometry and spectrophotometry. Initially, the periodic structure of the square spiral GLAD films was found

to be the exclusive source of spectral bands of simultaneous low transmittance and high reflectance, demonstrating the presence of a genuine photonic bandgap. Further characterization of the dependence of the bandgap on crystal direction and light polarization provided the most conclusive experimental evidence yet of a complete and three dimensional photonic bandgap in square spiral PBCs. The new GLAD growth algorithms were confirmed to improve the optical quality of the square spiral PBC structures, yielding a relative bandgap size as large as 10.9%, and through GLAD enabled bandgap engineering the wavelength location of the square spiral PBC bandgap was driven down as far as  $1.65 \mu\text{m}$ . To a large extent the achieved optical properties agreed with theoretical predictions, but further improvements in the depth and contrast of the bandgaps are desirable.

In an effort to address one of the most prominent experimental challenges of 3D PBCs, seed layer induced defect engineering was developed as a new method for patterning GLAD square spiral thin films. Exploiting the freedom of direct write seed layer fabrication, seed lattice defects can be transferred to the full thickness of periodic GLAD films with only limited broadening of film columns adjacent to the defects, and with no impact on the overall film morphology and periodicity. Through the use of PhiSweep GLAD, the film defects can selectively be kept free of film growth (up to a maximum width) or be filled with evaporant (in unlimited defect widths). The merits of the PhiSweep growth algorithm thus converge to simultaneously deliver both bandgap engineerable PBC structures with excellent fine structures, and defect engineering of air and dielectric defects. Seed layer induced defects are not ideal for making PBC waveguides, but do offer a more direct defect engineering approach than available in other PBC architectures, and has additional potential applications in other GLAD devices. For square spiral PBC waveguides, proof of principle of planar, multilayer defects was also provided.

As a spin-off of the PhiSweep growth algorithm, a new ability to alter the distribution and size of pores in GLAD thin films – without affecting the chiral microstructure or the overall film density – has been established. In particular, this porosity engineering capability has led to the discovery of a new type of nanofibrous aperiodic GLAD film in which the adverse effects of competition are postponed indefinitely, leading to slender fibres growing all the way from the substrate to the top of the film. The nanofibrous films are estimated to provide very high surface areas.

A new GLAD application enabled by the thesis research on advanced growth algorithms and defect engineering is microfluidic networks. By rely-

ing on the resistance to liquid flow of film structures with varying porosity, seed layer induced defects of periodic GLAD columns in a nanofibrous film background were demonstrated to function as flow channels. The GLAD fabrication approach is distinct from other microfluidic assembly techniques in simply extruding the flow circuit from a pre-designed seed layer, with no need for extensive planar processing. Furthermore, the columnar channel structure has a potential to facilitate integrated size exclusion chromatography.

## 12.2 Thesis Perspectives

With the results obtained, the thesis has achieved the stated research objectives of enabling bandgap and defect engineering in GLAD square spiral PBCs. Furthermore, the fine structure and optical quality of square spiral PBCs have been improved, the bandgap frequency has been increased, and a number of new GLAD capabilities relevant for diverse thin film applications have been established. In assessing the impact of the thesis and the future of the research area, it is worthwhile considering which remaining problems must be addressed, and which opportunities for new GLAD and PBC development the thesis research may have provided.

The most immediate task for continued GLAD PBC research is to improve the optical quality of the crystals, i.e., enhance the contrast of the bandgap edges and increase the attenuation inside the bandgaps. Currently the GLAD PBCs exhibit mediocre bandgap depths and tapered edges, presumably as a result of scattering caused by remaining disorder in the square spiral thin films. Sample wide uniformity could be enhanced by upgrading the existing GLAD substrate motion systems to provide greater accuracy – both with respect to substrate tilt and rotation – and improve the stability of the substrate position over the multiple deposition runs required to obtain reasonable crystal thicknesses. Efforts to implement these upgrades are currently underway. New electron beam evaporation systems affording greater source melt stability and higher chamber vacuum would also help reduce evaporant cluster ejection from the melt and oxygen contamination of the silicon films, respectively.

Although defect engineering in GLAD square spiral PBCs has now been demonstrated, actual waveguiding within such defects has not. A second task for future GLAD PBC research is therefore to experimentally evaluate the feasibility of capping seed layer induced defects in a square spiral PBC

thin film, and perform optical characterization of the potential waveguides. The use of multilayer defects should also be investigated further. In the long term, micromachined embedded defects will likely be the best way – although not the easiest – to obtain waveguides in GLAD PBCs. Significant research in post deposition processing of GLAD thin films must be performed to achieve this, but modelling of such advanced types of waveguides indicates that the rewards would be considerable. Colleague J. Sorge is continuing this work.

Some incremental and less critical advances can also be suggested for future GLAD PBC research. In seed layer fabrication by LDWL, software issues currently limit the pattern size of dense arrays of sub micrometre features to  $40 \text{ mm}^2$ . However, software optimization should allow for uniform substrate seed layers in excess of  $10000 \text{ mm}^2$ , while still maintaining acceptable write times. Since the GLAD process itself is readily applicable to wafer size samples, this would enable huge PBCs to be produced. Once seed layer fabrication reaches beyond the prototype stage, more efficient fabrication techniques should be considered, such as hot embossing or nanoimprinting.

At its current status, GLAD square spiral PBCs have reached a bandgap centre wavelength of  $1.65 \mu\text{m}$ . This has paved the way for reaching bandgaps at  $1.3 \mu\text{m}$  and  $1.55 \mu\text{m}$ , which are central in optical telecommunications. GLAD PBCs should be demonstrated at these wavelengths by shrinking the tetragonal seed lattice period and the square spiral dimensions still further.

Further down the road, when defect engineering in GLAD square spiral films has been further developed to achieve PBC waveguiding, actual PBC based devices may be contemplated. As part of advanced devices, active materials might be included for light emission or modulation. With the flexibility of the GLAD process, such materials could either be deposited as a thin film layer for subsequent patterning, or else be embedded through post deposition processing. Given the challenges of optical characterization of GLAD films discussed in this thesis, it would also be beneficial to implement coupling of light into and out of GLAD PBCs with optical fibres. Other GLAD PBC topics include inverse square spiral PBCs – where the improved film structures developed here could help produce high quality templates – and the use of materials other than silicon for direct or template square spiral PBC fabrication. Both of these topics are presently being pursued by colleague M. Summers.

Beyond PBC applications, the new GLAD capabilities presented in the thesis offer several ideas for future research. The analysis of the structural benefits provided by periodic GLAD film growth suggests that many GLAD

applications traditionally based on aperiodic films should migrate to periodic films. First of all, the uniformity in film and column morphology will make any film response depending on properties such as optical scattering, surface area or column spacing more distinctive. Secondly, the direct film structure control afforded by the substrate seed layer allows more reliable characterization and better device design. Among the GLAD applications that might benefit from a periodic film structure are optical filters, GLAD/liquid crystal hybrids, humidity sensors, and supercapacitors.

The evolution of advanced new GLAD growth algorithms is likely to continue as the limitations of traditional growth modes become increasingly apparent. As demonstrated by the PhiSweep method, such new growth algorithms may be as relevant to aperiodic GLAD films as periodic ones. Another future approach is to combine several different growth algorithms in composite programs that exploit the best of each algorithm at different stages in the deposition of a film.

In addition to its potential for PBC waveguiding and use in microfluidic networks, the flexibility of seed layer induced defect engineering warrants its exploration for other GLAD applications, such as field emitter arrays, magnetic storage, and GLAD/liquid crystal cells. Integration with more complex types of post deposition processing could also lead to the development of three dimensional functional defects.

Some of the most promising and immediate non-PBC research opportunities provided by the thesis are in the new area of PhiSweep GLAD thin films. Beyond the ability of the PhiSweep growth algorithm to function uniquely different on seeded, non-seeded, and patterned substrates – with tight control afforded by the sweep pitch and sweep angle – the properties of the new nanofibrous GLAD films are of particular interest. Colleague D. Gish is currently expanding nanofibrous PhiSweep GLAD to include titanium and titanium oxide films, and together with Dr. G. Kiema investigating the extreme surface area of such films in high efficiency dye sensitized photovoltaic cells. Another colleague, P. Hrudey, is evaluating nanofibrous GLAD for photoluminescent thin films, where the tightly packed, fibrous microstructure could be beneficial. Further exploitation of the capacity to engineer the porosity of GLAD films could see PhiSweep being used for catalysts, supercapacitors, thermal barriers, and biosensors.

Continuing development of defect engineered nanofibrous GLAD films for microfluidic applications is being undertaken by Dr. G. Kiema, with the hope of soon demonstrating size exclusion chromatography on fluorescent polystyrene microspheres inside the column filled flow channels. Experi-

ments on analytical chemistry and separation of biochemical bodies may then proceed in more advanced microfluidic network designs.

---

By developing critical new capabilities for bandgap and defect engineering of GLAD square spiral PBC thin films, this thesis has striven to enable GLAD as a viable technology for 3D PBCs, and contribute to realizing the promise of photonic crystals. The prospects for pioneering photonic crystal achievements, with GLAD PBCs among them, are bright but also long term. As with Herbert Kroemer's heterostructures, it takes time to develop a 'sufficiently new and innovative technology'. Certainly its very exploration is rewarding and throws off new knowledge and far flung uses, as this thesis has empowered many GLAD applications. But only later will we learn whether we succeeded answering questions not yet imagined.

# Bibliography

- [1] Gósta Ekspong. *Nobel Lectures, Physics 1996-2000*. World Scientific Publishing, Singapore, 2002.
- [2] James C. Maxwell. *A Treatise on Electricity and Magnetism*. Clarendon Press, Oxford, 1873.
- [3] Bent Elbek. *Elektromagnetisme*. Niels Bohr Institute for Astronomy, Physics and Geophysics, Copenhagen, 1997.
- [4] H. A. Macleod. *Thin Film Optical Filters*. Elsevier, New York, 1969.
- [5] Pochi Yeh. *Optical Waves in Layered Media*. Wiley, New York, 1988.
- [6] Kerry J. Vahala. Optical microcavities. *Nature*, 424:839–846, 2003.
- [7] Eli Yablonovitch. Inhibited spontaneous emission in solid-state physics and electronics. *Physical Review Letters*, 58(20):2059–2062, 1987.
- [8] Sajeev John. Strong localization of photons in certain disordered dielectric superlattices. *Physical Review Letters*, 58(23):2486–2489, 1987.
- [9] Bent Elbek. *Bølger*. Niels Bohr Institute for Astronomy, Physics and Geophysics, Copenhagen, 1997.
- [10] Joseph W. Goodman. *Introduction to Fourier Optics*. McGraw-Hill, New York, second edition, 1996.
- [11] S. R. Elliott. *The Physics and Chemistry of Solids*. John Wiley & Sons, Chicester, 1998.
- [12] O. Toader, M. Berciu, and S. John. Photonic band gaps based on tetragonal lattices of slanted pores. *Physical Review Letters*, 90(23):233901, 2003.

- [13] M. Woldeyohannes and S. John. Coherent control of spontaneous emission near a photonic band edge. *Journal of Optics B*, 5:R43–R82, 2003.
- [14] Sajeev John and Jian Wang. Quantum electrodynamics near a photonic band gap: Photon bound states and dressed atoms. *Physical Review Letters*, 64(20):2418–2421, 1990.
- [15] John D. Joannopoulos, Robert D. Meade, and Joshua N. Winn. *Photonic Crystals*. Princeton University Press, Princeton, 1995.
- [16] Kazuaki Sakoda. *Optical Properties of Photonic Crystals*. Springer, Berlin, 2001.
- [17] J. P. Dowling and C. M. Bowden. Anomalous index of refraction in photonic bandgap materials. *Journal of Modern Optics*, 41(2):345–351, 1994.
- [18] J. P. Dowling, M. Scalora, M. J. Bloemer, and C. M. Bowden. The photonic band edge laser: A new approach to gain enhancement. *Journal of Applied Physics*, 75(4):1896–1899, 1994.
- [19] Albert Birner, Ralf B. Wehrspohn, Ulrich M. Gösele, and Kurt Busch. Silicon-based photonic crystals. *Advanced Materials*, 13(6):377–388, 2001.
- [20] Jasprit Singh. *Semiconductor Optoelectronics*. McGraw-Hill, New York, 1995.
- [21] Eli Yablonovitch. Photonic band-gap crystals. *Journal of Physics: Condensed Matter*, 5:2443–2460, 1993.
- [22] P. W. Anderson. Absence of diffusion in certain random lattices. *Physical Review*, 109(5):1492–1505, 1958.
- [23] Attila Mekis, Shanhui Fan, and J. D. Joannopoulos. Bound states in photonic crystal waveguide and waveguide bends. *Physical Review B*, 58(8):4809–4817, 1998.
- [24] R. D. Meade, K. D. Brommer, A. M. Rappe, and J. D. Joannopoulos. Photonic bound states in periodic dielectric materials. *Physical Review B*, 44(24):13772–13774, 1991.

- [25] E. Yablonovitch, T. J. Gmitter, R. D. Meade, A. M. Rappe, K. D. Brommer, and J. D. Joannopoulos. Donor and acceptor modes in photonic band structures. *Physical Review Letters*, 67(24):3380–3383, 1991.
- [26] John D. Joannopoulos, P. R. Villeneuve, and S. Fan. Photonic crystals: Putting a new twist on light. *Nature*, 386:143–149, 1997.
- [27] J. S. Foresi, P. R. Villeneuve, J. Ferrera, E. R. Thoen, G. Steinmeyer, S. Fan, J. D. Joannopoulos, L. C. Kimerling, H. I. Smith, and E. P. Ippen. Photonic-bandgap microcavities in optical waveguides. *Nature*, 390:143–145, 1997.
- [28] I. Alvarado-Rodriguez and E. Yablonovitch. Separation of radiation and absorption losses in two-dimensional photonic crystal single defect cavities. *Journal of Applied Physics*, 92(11):6399–6402, 2002.
- [29] King-Ning Tu, James W. Mayer, and Leonard C. Feldman. *Electronic Thin Film Science*. Macmillan, New York, 1992.
- [30] K. M. Ho, C. T. Chan, and C. M. Soukoulis. Existence of a photonic gap in periodic dielectric structures. *Physical Review Letters*, 65(25):3152–3155, 1990.
- [31] C. T. Chan, K. M. Ho, and C. M. Soukoulis. Photonic band gaps in experimentally realizable periodic dielectric structures. *Europhysics Letters*, 16(6):563, 1991.
- [32] C. T. Chan, S. Datta, K. M. Ho, and C. M. Soukoulis. A7 structure: A family of photonic crystals. *Physical Review B*, 50(3):1988–1991, 1994.
- [33] D. Cassagne, C. Jouanin, and D. Bertho. Hexagonal photonic-band-gap structures. *Physical Review B*, 53(11):7134–7142, 1996.
- [34] K. M. Leung and Y. F. Liu. Full vector wave calculation of photonic band structures in face-centered-cubic dielectric media. *Physical Review Letters*, 65(21):2646–2649, 1990.
- [35] Z. Zhang and S. Satpathy. Electromagnetic wave propagation in periodic structures: Bloch wave solution of Maxwell’s equations. *Physical Review Letters*, 64(21):2650–2653, 1990.

- [36] H. S. Sözüer, J. W. Haus, and R. Inguva. Photonic bands: Convergence problems with the plane-wave method. *Physical Review B*, 45(24):13962–13972, 1992.
- [37] R. D. Meade, A. M. Rappe, K. D. Brommer, and J. D. Joannopoulos. Accurate theoretical analysis of photonic band-gap materials. *Physical Review B*, 48(11):8434–8437, 1993.
- [38] E. K. Miller. Time-domain modeling in electromagnetics. *Journal of Electromagnetic Waves and Applications*, 8(9–10):1125–1172, 1994.
- [39] S. Fan, P. R. Villeneuve, and J. D. Joannopoulos. Large omnidirectional band gaps in metallodielectric photonic crystals. *Physical Review B*, 54(16):11245–11251, 1996.
- [40] E. Yablonovitch, T. J. Gmitter, and K. M. Leung. Photonic band structure: The face-centered-cubic case employing nonspherical atoms. *Physical Review Letters*, 67(17):2295–2298, 1991.
- [41] C. C. Cheng, V. Arbet-Engels, A. Scherer, and E. Yablonovitch. Nanofabricated three dimensional photonic crystal operating at optical wavelengths. *Physica Scripta*, T68:17–20, 1996.
- [42] C. C. Cheng, A. Scherer, V. Arbet-Engels, and E. Yablonovitch. Lithographic band gap tuning in photonic band gap crystals. *Journal of Vacuum Science and Technology B*, 14(6):4110–4114, 1996.
- [43] C. C. Cheng, A. Scherer, R. C. Tyan, Y. Fainman, G. Witzgall, and E. Yablonovitch. New fabrication techniques for high quality photonic crystals. *Journal of Vacuum Science and Technology B*, 15(6):2764–2767, 1997.
- [44] K. M. Ho, C. T. Chan, C. M Soukoulis, R. Biswas, and M. Sigalas. Photonic band gaps in three dimensions: New layer-by-layer periodic structures. *Solid State Communications*, 89(5):413–416, 1994.
- [45] S. Y. Lin, J. G. Fleming, D. L. Hetherington, B. K. Smith, R. Biswas, K. M. Ho, M. M. Sigalas, W. Zubrzycki, S. R. Kurtz, and J. Bur. A three-dimensional photonic crystal operating at infrared wavelengths. *Nature*, 394:251–253, 1998.
- [46] Shawn-Yu Lin and J. G. Fleming. A three-dimensional optical photonic crystal. *Journal of Lightwave Technology*, 17(11):1944–1947, 1999.

- [47] E. Özbay, E. Michel, G. Tuttle, R. Biswas, M. Sigalas, and K.-M. Ho. Micromachined millimeter-wave photonic band-gap crystals. *Applied Physics Letters*, 64(16):2059–2061, 1994.
- [48] A. Blanco, E. Chomski, S. Grabtchak, M. Ibisate, S. John, S. E. Leonard, C. Lopez, F. Meseguer, H. Miguez, J. P. Mondia, G. A. Ozin, O. Toader, and H. M. van Driel. Large-scale synthesis of a silicon photonic crystal with a complete three-dimensional bandgap near 1.5 micrometres. *Nature*, 405:437–440, 2000.
- [49] Y. A. Vlasov, X. Z. Bo, J. C. Sturm, and D. J. Norris. On-chip natural assembly of silicon photonic bandgap crystals. *Nature*, 414:289–293, 2001.
- [50] Ovidiu Toader, Sajeev John, and Kurt Busch. Optical trapping, field enhancement and laser cooling in photonic crystals. *Optics Express*, 8(3):217–222, 2001.
- [51] J. Martorell and N. M. Lawandy. Observation of inhibited spontaneous emission in a periodic dielectric structure. *Physical Review Letters*, 65(15):1877–1880, 1990.
- [52] K. Busch and S. John. Photonic band gap formation in certain self-organizing systems. *Physical Review E*, 58(3):3896–3908, 1998.
- [53] H. Miguez, E. Chomski, F. Garcia-Santamaria, M. Ibisate, S. John, C. Lopez, F. Meseguer, J. P. Mondia, G. A. Ozin, O. Toader, and H. M. van Driel. Photonic bandgap engineering in germanium inverse opals by chemical vapor deposition. *Advanced Materials*, 13(21):1634–1637, 2001.
- [54] T. Y. M. Chan and S. John. Blueprint for wafer-scale three-dimensional photonic band-gap synthesis by photochemical etching. *Physical Review E*, 68:046607, 2003.
- [55] M. Plihal, A. Shambrook, and A. A. Maradudin. Two-dimensional photonic band structures. *Optics Communications*, 80(3–4):199–204, 1991.
- [56] R. D. Meade, K. D. Brommer, A. M. Rappe, and J. D. Joannopoulos. Existence of a photonic band gap in two dimensions. *Applied Physics Letters*, 61(4):495–498, 1992.

- [57] P. R. Villeneuve and Michel Piché. Photonic band gap in two-dimensional square and hexagonal lattices. *Physical Review B*, 46(8):4969–4972, 1992.
- [58] Thomas F. Krauss, Richard M. de la Rue, and Stuart Brand. Two-dimensional photonic-bandgap structures operating at near-infrared wavelengths. *Nature*, 383:699–702, 1996.
- [59] S. G. Johnson, S. Fan, P. R. Villeneuve, and J. D. Joannopoulos. Guided modes in photonic crystals slabs. *Physical Review B*, 60(8):5751–5758, 1999.
- [60] D. Labilloy, H. Benisty, C. Weisbuch, T. F. Krauss, R. M. de la Rue, V. Bardinal, R. Houdré, U. Oesterle, D. Cassagne, and C. Jouanin. Quantitative measurement of transmission, reflection, and diffraction of two-dimensional photonic band gap structures at near-infrared wavelengths. *Physical Review Letters*, 79(21):4147–4150, 1997.
- [61] Alongkarn Chutinan and Susumu Noda. Waveguides and waveguide bends in two-dimensional photonic crystal slabs. *Physical Review B*, 62(7):4488–4492, 2000.
- [62] S. Olivier, H. Benisty, C. Weisbuch, C. J. M. Smith, T. F. Krauss, R. Houdré, and U. Oesterle. Improved 60° bend transmission of submicron-width waveguides defined in two-dimensional photonic crystals. *Journal of Lightwave Technology*, 20(7):1198–1203, 2002.
- [63] J. Topolančik, P. Bhattacharya, J. Sabarinathan, and P. C. Yu. Fluid detection with photonic crystal-based multichannel waveguides. *Applied Physics Letters*, 82(8):1143–1145, 2003.
- [64] S. Y. Lin, J. G. Fleming, and I. El-Kady. Highly efficient light emission at  $\lambda = 1.5 \mu\text{m}$  by a three-dimensional tungsten photonic crystal. *Optics Letters*, 28(18):1683–1685, 2003.
- [65] Alongkarn Chutinan and Susumu Noda. Highly confined waveguides and waveguide bends in three-dimensional photonic crystal. *Applied Physics Letters*, 75(24):3739–3741, 1999.
- [66] S. Noda, K. Tomoda, N. Yamamoto, and A. Chutinan. Full three-dimensional photonic bandgap crystal at near-infrared wavelengths. *Science*, 289:604–606, 2000.

- [67] M. Bayindir, E. Ozbay, E. Temelkuran, M. M. Sigalas, C. M. Soukoulis, R. Biswas, and K. M. Ho. Guiding, bending, and splitting of electromagnetic waves in highly confined photonic crystal waveguides. *Physical Review B*, 63:081107, 2001.
- [68] Richard Syms and John Cozens. *Optical Guided Waves and Devices*. McGraw-Hill, London, 1992.
- [69] R. D. Meade, A. Devenyi, J. D. Joannopoulos, O. L. Alerhand, D. A. Smith, and K. Kash. Novel applications of photonic band gap materials: Low-loss bends and high Q cavities. *Journal of Applied Physics*, 75(9):4753–4755, 1995.
- [70] Gerd Keiser. *Optical Fibre Communications*. McGraw-Hill, Boston, third edition, 2000.
- [71] H. Benisty, S. Olivier, C. Weisbuch, M. Agio, M. Kafesaki, C. M. Soukoulis, M. Qiu, M. Swillo, A. Karlsson, B. Joskorzynska, A. Talneau, J. Mossburger, M. Kamp, A. Forchel, R. Ferrini, R. Houdré, and U. Oesterle. Models and measurements for the transmission of submicron-width waveguide bends defined in two-dimensional photonic crystals. *IEEE Journal of Quantum Electronics*, 38(7):770–785, 2002.
- [72] A. Mekis, J. C. Chen, I. Kurland, S. Fan, P. Villeneuve, and J. D. Joannopoulos. High transmission through sharp bends in photonic crystal waveguides. *Physical Review Letters*, 77(18):3787–3790, 1996.
- [73] E. Cassan, L. Vivian, and S. Laval. Polarization-independent 90°-turns in single-mode micro-waveguides on silicon-on-insulator wafers for telecommunication wavelengths. *Optics Communications*, 235(1–3):83–88, 2004.
- [74] S. Y. Lin, E. Chow, V. Hietala, P. R. Villeneuve, and J. D. Joannopoulos. Experimental demonstration of guiding and bending of electromagnetic waves in a photonic crystal. *Science*, 282:274–276, 1998.
- [75] Edmond Chow, S. Y. Lin, J. R. Wendt, S. G. Johnson, and J. D. Joannopoulos. Quantitative analysis of bending efficiency in photonic-crystal waveguide bends at  $\lambda = 1.55 \mu\text{m}$  wavelengths. *Optics Letters*, 26(5):286–288, 2001.

- [76] B. Temelkuran and E. Ozbay. Experimental demonstration of photonic crystal based waveguides. *Applied Physics Letters*, 74(4):486–488, 1999.
- [77] R. F. Cregan, B. J. Mangan, J. C. Knight, T. A. Birks, P. St. J. Russell, P. J. Roberts, , and D. C. Allan. Single-mode photonic band gap guidance of light in air. *Science*, pages 1537–1539, 1999.
- [78] S. Noda, A. Chutinan, and M. Imada. Trapping and emission of photons by a single defect in a photonic bandgap structure. *Nature*, 407:608–610, 2000.
- [79] M. Raburn, B. Liu, K. Rauscher, Y. Okuno, N. Dagli, and J. E. Bowers. 3-D photonic circuit technology. *IEEE Journal of Selected Topics in Quantum Electronics*, 8(4):935–942, 2002.
- [80] K. Busch and S. John. Liquid-crystal photonic-band-gap materials: The tunable electromagnetic vacuum. *Physical Review Letters*, 83(5):967–970, 1999.
- [81] Y. Shimoda, M. Ozaki, and K. Yoshino. Electric field tuning of a stop band in a reflection spectrum of synthetic opal infiltrated with nematic liquid crystal. *Applied Physics Letters*, 79(22):3627–3629, 2001.
- [82] Sajeev John and Marian Florescu. Photonic bandgap materials: Towards an all-optical micro-transistor. *Journal of Optics A*, 3:S103–S120, 2001.
- [83] O. Painter, R. K. Lee, A. Scherer, A. Yariv, J. D. O’Brien, P. D. Dapkus, and I. Kim. Two-dimensional photonic band-gap defect mode laser. *Science*, 284:1819–1821, 1999.
- [84] S. Y. Lin, J. G. Fleming, M. M. Sigalas, R. Biswas, and K. M. Ho. Photonic band-gap microcavities in three dimensions. *Physical Review B*, 59(24):15579–15582, 1999.
- [85] M. Qi, E. Lidorikis, P. T. Rakich, S. G. Johnson, J. D. Joannopoulos, E. P. Ippen, and H. I. Smith. A three-dimensional optical photonic crystal with designed point defects. *Nature*, 429:538–542, 2004.
- [86] S. Ogawa, M. Imada, S. Yoshimoto, M. Okano, and S. Noda. Control of light emission by 3d photonic crystals. *Science*, pages 227–229, 2004.

- [87] M. Boroditsky, T. F. Krauss, R. Coccioli, R. Vrijen, R. Bhat, and E. Yablonovitch. Light extraction from optically pumped light-emitting diode by thin-slab photonic crystals. *Applied Physics Letters*, 75(8):1036–1038, 1999.
- [88] A. Scherer, O. Painter, J. Vuckovic, M. Loncar, and T. Yoshie. Photonic crystals for confining, guiding, and emitting light. *IEEE Transactions on Nanotechnology*, 1:4–11, 2002.
- [89] M. Okano, S. Kako, and S. Noda. Coupling between a point-defect and a line-defect waveguide in three-dimensional photonic crystal. *Physical Review B*, 68:235110, 2003.
- [90] E. Rutner, P. Goldfinger, and J. P. Hirth, editors. *Condensation and Evaporation of Solids*, New York, 1964. Gordon and Breach.
- [91] A. C. Zettlemoyer. *Nucleation*. Marcel Dekker, New York, 1969.
- [92] Leon I. Maissel and Reinhard Glang. *Handbook of Thin Film Technology*. McGraw-Hill, New York, 1983.
- [93] Milton Ohring. *Materials Science of Thin Films*. Academic Press, San Diego, second edition, 2002.
- [94] B. A. Movchan and A. V. Demchishin. Study of the structure and properties of thick vacuum condensates of nickel, titanium, tungsten, aluminium oxide and zirconium dioxide. *Fiz. Metal. Metalloved.*, 28(4):83–90, 1969.
- [95] J. V. Sanders. In J. R. Anderson, editor, *Chemisorption and Reactions on Metal Films*. Academic Press, New York, 1971.
- [96] J. A. Thornton. High rate thick film growth. *Annual Review of Materials Science*, 7:239–260, 1977.
- [97] H. T. G. Hentzell, C. R. M. Grovenor, and D. A. Smith. Grain structure variation with temperature for evaporated metal films. *Journal of Vacuum Science and Technology A*, 2(2):218–219, 1984.
- [98] Rointan F. Bunshah. *Deposition Technologies for Films and Coatings*. Noyes, Park Ridge, 1982.
- [99] S. M. Rosnagel. Thin film deposition with physical vapor deposition and related technologies. *Journal of Vacuum Science and Technology A*, 21(5):S74–S87, 2003.

- [100] S. M. Sze. *Semiconductor Devices, Physics and Technology*. John Wiley & Sons, New York, 1985.
- [101] D. Vick, Y. Y. Tsui, M. J. Brett, and R. Fedosejevs. Production of porous carbon thin films by pulsed laser deposition. *Thin Solid Films*, 350(1-2):49-52, 1999.
- [102] L. Holland. The effect of vapor incidence on the structure of evaporated aluminum films. *Journal of the Optical Society of America*, 43(5):376-380, 1953.
- [103] D. O. Smith. Anisotropy in permalloy films. *Journal of Applied Physics*, 30(4):264S-265S, 1959.
- [104] T. G. Knorr and R. W. Hoffmann. Dependence of geometric magnetic anisotropy in thin iron films. *Physical Review*, 113:1039-1046, 1959.
- [105] M. S. Cohen. Anisotropy in permalloy films evaporated at grazing incidence. *Journal of Applied Physics*, 32(3):87S-88S, 1961.
- [106] Leon Abelmann and Cock Lodder. Oblique evaporation and surface diffusion. *Thin Solid Films*, 305:1-21, 1997.
- [107] A. G. Dirks and H. J. Leamy. Columnar microstructure in vapour-deposited thin films. *Thin Solid Films*, 47:219-233, 1977.
- [108] P. Meakin and J. Krug. Columnar microstructure in three-dimensional ballistic deposition. *Europhysics Letters*, 11(1):7-12, 1990.
- [109] P. Meakin and J. Krug. Three-dimensional ballistic deposition at oblique incidence. *Physical Review A*, 46(6):3390-3399, 1992.
- [110] M. J. Bloemer, T. L. Ferrell, M. C. Buncick, and R. J. Warmack. Optical properties of submicrometer-size silver needles. *Physical Review B*, 37(14):8015-8021, 1988.
- [111] D. Le Bellac, G. A. Niklasson, and G. C. Granqvist. Scaling of surface roughness in obliquely sputtered chromium films. *Europhysics Letters*, 32(2):155-159, 1995.
- [112] Y. Taga and T. Motohiro. Growth of birefringent films by oblique deposition. *Journal of Crystal Growth*, 99:638-642, 1990.
- [113] Q. Wu and I. Hodgkinson. Materials for birefringent coatings. *Applied Optics*, 33(34):8109-8110, 1994.

- [114] I. Hodgkinson, P. I. Bowmar, and Q. H. Wu. Scatter from tilted-columnar birefringent thin films: Observation and measurement of anisotropic scatter distributions. *Applied Optics*, 34(1):163–168, 1995.
- [115] Z. Dohnálek, Greg A. Kimmel, David E. McCready, James S. Young, Alice Dohnáková, R. Scott Smith, and Bruce D. Kay. Structural and chemical characterization of aligned crystalline nanoporous MgO films grown by reactive ballistic deposition. *Journal of Physical Chemistry B*, 106:3526–3529, 2002.
- [116] N. O. Young and J. Kowal. Optically active fluorite films. *Nature*, 183:104–105, 1959.
- [117] T. Motohiro and Y. Taga. Thin film retardation plate by oblique deposition. *Applied Optics*, 28(13):2466–2482, 1989.
- [118] A. J. McPhun, I. J. Hodgkinson, and Q. H. Wu. Birefringent rugate filters. *Electronics Letters*, 34(4):360–361, 1998.
- [119] I. Hodgkinson and Q. H. Wu. Serial bideposition of anisotropic thin films with enhanced linear birefringence. *Applied Optics*, 38(16):3621–3625, 1999.
- [120] K. Robbie, L. J. Friedrich, S. K. Dew, T. Smy, and M. J. Brett. Fabrication of thin films with highly porous microstructures. *Journal of Vacuum Science and Technology A*, 13(3):1032–1035, 1995.
- [121] K. Robbie, M. J. Brett, and A. Lakhtakia. First thin film realization of a helicoidal bianisotropic medium. *Journal of Vacuum Science and Technology A*, 13(6):2991–2993, 1995.
- [122] K. Robbie, M. J. Brett, and A. Lakhtakia. Chiral sculptured thin films. *Nature*, 384:616, 1996.
- [123] K. Robbie and M. J. Brett. Sculptured thin films and glancing angle deposition: Growth mechanics and applications. *Journal of Vacuum Science and Technology A*, 15(3):1460–1465, 1997.
- [124] K. Robbie, J. C. Sit, and M. J. Brett. Advanced techniques for glancing angle deposition. *Journal of Vacuum Science and Technology B*, 16(3):1115–1122, 1998.
- [125] Kevin J. Robbie and Michael J. Brett. Method of depositing shadow sculpted thin films. United States Patent, 2 February 1999. 5,866,204.

- [126] Kevin J. Robbie and Michael J. Brett. Shadow sculpted thin films. United States Patent, 19 June 2001. 6,248,422.
- [127] Kevin J. Robbie and Michael J. Brett. Glancing angle deposition of thin films. United States Patent, 27 March 2001. 6,206,065.
- [128] P. C. P. Hrudey, M. Taschuk, Y. Y. Tsui, R. Fedosejevs, J. C. Sit, and M. J. Brett. Luminescence of nanostructured  $Y_2O_3:Eu$  thin films fabricated using glancing angle deposition techniques. In *Proceedings of SPIE Volume: 5224 - Nanomaterials and Their Optical Applications*, pages 62–69, 2003.
- [129] M. Malac and R. F. Egerton. Observations of the microscopic growth mechanism of pillars and helices formed by glancing-angle thin-film deposition. *Journal of Vacuum Science and Technology A*, 19(1):158–166, 2001.
- [130] D. Vick, L. J. Friedrich, S. K. Dew, M. J. Brett, K. Robbie, M. Seto, and T. Smy. Self-shadowing and surface diffusion effects in obliquely deposited thin films. *Thin Solid Films*, 339:88–94, 1999.
- [131] D. Vick, T. Smy, and M. J. Brett. Growth behaviour of evaporated porous thin films. *Journal of Materials Research*, 17:2904–2911, 2002.
- [132] B. Dick, M. J. Brett, T. J. Smy, M. R. Freeman, M. Malac, and R. F. Egerton. Periodic magnetic microstructures by glancing angle deposition. *Journal of Vacuum Science and Technology A*, 18(4):1838–1844, 2000.
- [133] M. Malac and R. F. Egerton. Thin-film regular-array structures with 10-100 nm repeat distance. *Nanotechnology*, 12:11–13, 2001.
- [134] R. Messier, A. P. Giri, and R. Roy. Revised structure zone model for thin film physical structure. *Journal of Vacuum Science and Technology A*, 2(2):500–503, 1984.
- [135] R. Messier. Toward quantification of thin film morphology. *Journal of Vacuum Science and Technology A*, 4(3):490–495, 1985.
- [136] J. M. Nieuwenhuizen and H. B. Haanstra. Microfractography of thin films. *Philips Technical Review*, 27:87–91, 1966.

- [137] K. Hara, M. Kamiya, T. Hashimoto, K. Okamoto, and H. Fujiwara. Oblique-incidence anisotropy of iron films evaporated at low substrate temperatures. *Journal of Magnetism and Magnetic Materials*, 173(2):161–166, 1988.
- [138] R. N. Tait, T. Smy, and M. J. Brett. Modelling and characterization of columnar growth in evaporated films. *Thin Solid Films*, 226:196–201, 1993.
- [139] I. Hodgkinson, Q. H. Wu, and A. McPhun. Incremental-growth model for the deposition of spatially modulated thin film nanostructures. *Journal of Vacuum Science and Technology B*, 16(5):2811–2816, 1998.
- [140] G. S. Bales, R. Bruinsma, E. A. Eklund, R. P. U. Karunasiri, J. Rudnick, and A. Zangwill. Growth and erosion of thin solid films. *Science*, 249:264–268, 1990.
- [141] T. Smy, D. Vick, M. J. Brett, S. K. Dew, A. T. Wu, J. C. Sit, and K. D. Harris. Three-dimensional simulation of film microstructure produced by glancing angle deposition. *Journal of Vacuum Science and Technology A*, 18(5):2507–2512, 2000.
- [142] Motofumi Suzuki and Yasunori Taga. Numerical study of the effective surface area of obliquely deposited thin films. *Journal of Applied Physics*, 90(11):5599–5605, 2001.
- [143] J. C. Sit, D. Vick, K. Robbie, and M. J. Brett. Thin film microstructure control using glancing angle deposition by sputtering. *Journal of Materials Research*, 14(4):1197–1199, 1999.
- [144] B. Dick, M. J. Brett, T. Smy, M. Belov, and M. R. Freeman. Periodic submicrometer structures by sputtering. *Journal of Vacuum Science and Technology B*, 19(5):1813–1819, 2001.
- [145] K. D. Harris, K. L. Westra, and M. J. Brett. Fabrication of perforated thin films with helical and chevron pore shapes. *Electrochemical and Solid-State Letters*, 4(6):C39–C42, 2001.
- [146] A. C. van Popta, J. C. Sit, and M. J. Brett. Optical properties of porous helical thin films and the effects of post-deposition annealing. In *Proceedings of SPIE Volume: 5464 - Organic Optoelectronics and Photonics*, pages 198–208, 2004.

- [147] B. Dick, M. J. Brett, and T. Smy. Investigation of substrate rotation at glancing incidence on thin-film morphology. *Journal of Vacuum Science and Technology B*, 21(6):2569–2575, 2003.
- [148] K. Robbie, C. Shafai, and M. J. Brett. Thin films with nanometer-scale pillar microstructure. *Journal of Materials Research*, 14(7):3158–3163, 1999.
- [149] J. J. Steele, K. D. Harris, and M. J. Brett. Nanostructured oxide films for high-speed humidity sensors. In *Continuous Nanophase and Nanostructured Materials Symposium (Mater. Res. Soc. Symposium Proceedings Vol. 788)*, pages 473–478, 2004.
- [150] B. Dick, M. J. Brett, and T. Smy. Controlled growth of periodic pillars by glancing angle deposition. *Journal of Vacuum Science and Technology B*, 21(5):23–28, 2003.
- [151] K. Robbie, A. J. P. Hnatiw, M. J. Brett, R. I. MacDonald, and J. N. McMullin. Inhomogeneous thin film optical filters fabricated using glancing angle deposition. *Electronics Letters*, 33(14):1213–1214, 1997.
- [152] Jeremy C. Sit. *Thin film / liquid crystal composite optical materials and devices*. PhD thesis, University of Alberta, 2001.
- [153] M. W. Seto, K. Robbie, D. Vick, M. J. Brett, and L. Kuhn. Mechanical response of thin films with helical microstructure. *Journal of Vacuum Science and Technology B*, 17:2172–2177, 1999.
- [154] M. W. Seto, B. Dick, and M. J. Brett. Microsprings and microcantilevers: Studies of mechanical response. *Journal of Micromechanics and Microengineering*, 11(5):582–588, 2001.
- [155] S. R. Kennedy and M. J. Brett. Porous broadband antireflection coating by glancing angle deposition. *Applied Optics*, 42(22):4573–4579, 2003.
- [156] I. J. Hodgkinson and Q. H. Wu. Inorganic chiral optical materials. *Advanced Materials*, 13(12–13):889–897, 2001.
- [157] S. R. Kennedy, J. C. Sit, D. J. Broer, and Michael J. Brett. Optical activity of chiral thin film and liquid crystal hybrids. *Liquid Crystals*, 28(12):1799–1803, 2001.

- [158] A. C. van Popta, S. R. Kennedy, D. J. Broer, J. C. Sit, and M. J. Brett. Optical performance of porous TiO<sub>2</sub> chiral thin films. In *Proceedings of SPIE Volume: 5213 - Liquid Crystals VII*, pages 232–241, 2003.
- [159] J. C. Sit, D. J. Broer, and M. J. Brett. Alignment and switching of nematic liquid crystals embedded in porous chiral thin films. *Liquid Crystals*, 27(3):387–391, 2000.
- [160] K. Robbie, D. J. Broer, and M. J. Brett. Chiral nematic order in liquid crystals imposed by an engineered inorganic nanostructure. *Nature*, 399:764–766, 1999.
- [161] K. D. Harris, J. R. McBride, K. E. Nietering, and M. J. Brett. Fabrication of porous platinum thin films for hydrocarbon sensor applications. *Sensors and Materials*, 13(4):225–234, 2001.
- [162] M. Suzuki, T. Ito, and Y. Taga. Photocatalysis of sculptured thin films of TiO<sub>2</sub>. *Applied Physics Letters*, 78(25):3968–3970, 2001.
- [163] M. M. Gomez, J. Lu, E. Olsson, A. Hagfeldt, and C. G. Granqvist. High efficiency dye-sensitized nanocrystalline solar cells based on sputter deposited Ti oxide films. *Solar Energy Materials and Solar Cells*, 64(4):385–392, 2000.
- [164] G. K. Kiema, M. J. Colgan, and M. J. Brett. Dye sensitized solar cells incorporating obliquely deposited titanium oxide layers. In press.
- [165] J. N. Broughton and M. J. Brett. Electrochemical capacitance in manganese thin films with chevron microstructure. *Electrochemical Solid-State Letters*, 5:A279–A282, 2002.
- [166] K. D. Harris, D. Vick, E. J. Gonzalez, T. Smy, K. Robbie, and M. J. Brett. Porous thin films for thermal barrier coatings. *Surface & Coatings Technology*, 138(2–3):185–191, 2001.
- [167] T. Smy, D. Walkey, K. D. Harris, and M. J. Brett. Thin film microstructure and thermal transport simulation using 3D-Films. *Thin Solid Films*, 391(1):88–100, 2001.
- [168] Kenneth D. Harris, Michael J. Brett, Tom J. Smy, and Christopher Backhouse. Microchannel surface area enhancement using porous thin films. *Journal of the Electrochemical Society*, 147(5):2002–2006, 2000.

- [169] E. E. Steltz and A. Lakhtakia. Theory of second-harmonic-generated radiation from chiral sculptured thin films for bio-sensing. *Optical Communications*, 216(1–3):139–150, 2003.
- [170] A. T. Wu, M. Seto, and M. J. Brett. Capacitive SiO humidity sensors with novel microstructures. *Sensors and Materials*, 11(8):493–505, 1999.
- [171] K. D. Harris, A. Huizinga, and M. J. Brett. High-speed porous thin film humidity sensors. *Electrochemical and Solid-State Letters*, 5(11):H27–H29, 2002.
- [172] G. K. Kiema M. J. Brett. Electrochemical characterization of carbon films with porous microstructures. *Journal of The Electrochemical Society*, 150(7):E342–E347, 2003.
- [173] G. K. Kiema and M. J. Brett. Effect of thermal annealing on structural properties and electrochemical performance of carbon films with porous microstructure. *Journal of The Electrochemical Society*, 151(5):E194–E198, 2004.
- [174] F. Liu, M. T. Umlor, L. Shen, J. Weston, W. Eads, J. A. Barnard, and G. J. Mankey. The growth of nanoscale structured iron films by glancing angle deposition. *Journal of Applied Physics*, 85(8):5486–5488, 1999.
- [175] F. Liu, C. Yu, L. Shen, J. Barnard, and G. J. Mankey. The magnetic properties of cobalt films produced by glancing angle deposition. *IEEE Transactions on Magnetics*, 36(5):2939–2941, 2000.
- [176] M. Malac, R. F. Egerton, M. J. Brett, and B. Dick. Fabrication of submicrometer regular arrays of pillars and helices. *Journal of Vacuum Science and Technology B*, 17(6):2671–2674, 1999.
- [177] M. J. Colgan and M. J. Brett. Field emission from carbon and silicon films with pillar microstructure. *Thin Solid Films*, 389(1–2):1–4, 2001.
- [178] K. D. Harris, J. C. Sit, and M. J. Brett. Fabrication and optical characterization of template-constructed thin films with chiral nanostructure. *IEEE Transactions on Nanotechnology*, 1(3):122–128, 2002.
- [179] Alongkarn Chutinan and Susumu Noda. Spiral three-dimensional photonic band gap structure. *Physical Review B*, 57(4):2006–2008, 1998.

- [180] Ovidiu Toader and Sajeew John. Proposed square spiral microfabrication architecture for large three-dimensional photonic band gap crystals. *Science*, 292:1133–1135, 2001.
- [181] O. Toader and S. John. Square spiral photonic crystals: Robust architecture for microfabrication of materials with large three-dimensional photonic band gaps. *Physical Review E*, 66:016610, 2002.
- [182] Scott R. Kennedy, Michael J. Brett, Ovidiu Toader, and Sajeew John. Fabrication of tetragonal square spiral photonic crystals. *Nano Letters*, 2:59–62, 2002.
- [183] Private communication with Dr. Sajeew John, Department of Physics, University of Toronto.
- [184] Mark A. Summers, Scott Kennedy, Anastasia Elias, Martin Jensen, Ken Harris, Brian Szeto, and Michael J. Brett. Microfabrication of chiral optic materials and devices. In *Proceedings of SPIE Volume: 5347 - Micromachining Technology for Micro-Optics and Nano-Optics II*, pages 170–180, 2004.
- [185] R. W. Sprague, C. F. Hickey, and I. J. Hodgkinson. The influence of argon ion bombardment on form birefringence in thin films of titania. *Journal of Applied Physics*, 71(7):3201–3203, 1992.
- [186] Y. P. Zhao, D. X. Ye, P. I. Wang, G. C. Wang, and T. M. Lu. Fabrication of Si nanocolumns and Si square spirals on self-assembled monolayer colloid substrates. *International Journal of Nanoscience*, 1(1):87–97, 2002.
- [187] S. R. Kennedy and M. J. Brett. Advanced techniques for the fabrication of square spiral photonic crystals by glancing angle deposition. *Journal of Vacuum Science and Technology B*, 22(3):1184–1190, 2004.
- [188] S. Kennedy, M. J. Brett, H. Miguez, O. Toader, and S. John. Optical properties of a three-dimensional silicon square spiral photonic crystal. *Photonics and Nanostructures*, 1:37–42, 2003.
- [189] Mirwais Aktary, Martin O. Jensen, Kenneth L. Westra, Michael J. Brett, and Mark R. Freeman. High-resolution pattern generation using the epoxy novolak SU-8 2000 resist by electron beam lithography. *Journal of Vacuum Science and Technology B*, 21(4):L5–L7, 2003.

- [190] Martin O. Jensen and Michael J. Brett. Periodically structured glancing angle deposition thin films. In press.
- [191] K. D. Harris, K. L. Westra, and M. J. Brett. Fabrication of helically perforated thin films. In *Nonlithographic and Lithographic Methods of Nanofabrication - From Ultralarge-Scale Integration to Photonics to Molecular Electronics (Materials Research Society Symposium Proceedings Vol.636)*, pages D9.37.1–D9.37.6, 2001.
- [192] A. L. Elias, K. D. Harris, and M. J. Brett. Fabrication of perforated film nanostructures. In *Three-Dimensional Nanoengineered Assemblies. Symposium (Mater. Res. Soc. Symposium Proceedings Vol.739)*, pages 243–247, 2003.
- [193] B. He, N. Tait, and F. Regnier. Fabrication of nanocolumns for liquid chromatography. *Analytical Chemistry*, 70(18):3790–3797, 1998.
- [194] W. W. Ng, Chi-Shain Hong, and A. Yariv. Holographic interference lithography for integrated optics. *IEEE Transactions on Electron Devices*, ED-25:1193–1200, 1978.
- [195] Irmantas Mikulskas, Saulius Juodkazis, Rolandas Tomašiūnas, and Jean G. Dumas. Aluminum oxide photonic crystals grown by a new hybrid method. *Advanced Materials*, 13(20):1574–1577, 2001.
- [196] Jianyu Liang, Hope Chik, Aijun Yin, and Jimmy Xu. Two-dimensional lateral superlattices of nanostructures: Nonlithographic formation by anodic membrane template. *Journal of Applied Physics*, 91(4):2544–2546, 2002.
- [197] B. Dick, J. C. Sit, M. J. Brett, I. M. N. Votte, and C. W. M. Bastiaansen. Embossed polymeric relief structures as a template for the growth of periodic inorganic microstructures. *Nano Letters*, 1:71–73, 2000.
- [198] V. Grigaliunas, V. Kopustinskas, S. Meskinis, M. Margelevicius, I. Mikulskas, and R. Tomasiunas. Replication technology for photonic band gap applications. *Optical Materials*, 17:15–18, 2001.
- [199] S. W. Pang, T. Tamamura, and M. Nakao. Direct nano-printing on Al substrate using a SiC mold. *Journal of Vacuum Science and Technology B*, 16(3):1145–1149, 1998.

- [200] Christie R. K. Marrian and Donald M. Tennant. Nanofabrication. *Journal of Vacuum Science and Technology A*, 21(5):S207–S215, 2003.
- [201] J. A. Reynolds. An overview of e-beam mask-making. *Solid State Technology*, 22:87–94, 1979.
- [202] T. H. P. Chang, D. P. Kern, E. Kratschmer, K. Y. Lee, H. E. Luhn, M. A. McCord, S. A. Rishton, and Y. Vladimirovsky. Nanostructure technology. *IBM Journal of Research Development*, 32(4):462–492, 1988.
- [203] S. Thoms, S. P. Beaumont, and C. D. W. Wilkinson. A JEOL 100CXII converted for use as an electron-beam lithography system. *Journal of Vacuum Science and Technology B*, 7(6):1823–1836, 1989.
- [204] Greg Bázan and Gary H. Bernstein. Electron beam lithography over large scan fields. *Journal of Vacuum Science and Technology A*, 11(4):1745–1752, 1993.
- [205] Joseph I. Goldstein, Dale E. Newbury, Patrick Echlin, David C. Joy, A. D. Romig, Charles E. Lyman, Charles Fiori, and Eric Lifshin. *Scanning Electron Microscopy and X-Ray Microanalysis*. Plenum Press, New York, second edition, 1992.
- [206] A. N. Broers. Resolution limits for electron-beam lithography. *IBM Journal of Research Development*, 32(4):502–513, 1988.
- [207] W. Chen and H. Ahmed. Fabrication of 5-7 nm wide etched lines in silicon using 100 keV electron-beam lithography and polymethylmethacrylate resist. *Applied Physics Letters*, 62:1499–1501, 1993.
- [208] Xiaokang Huang, Gary H. Bernstein, Greg Bázan, and Davide A. Hill. Spatial density of lines exposed in poly(methylmethacrylate) by electron beam lithography. *Journal of Vacuum Science and Technology A*, 11(4):1739–1744, 1993.
- [209] R. R. Kunz, M. W. Horn, T. M. Bloomstein, and D. J. Ehrlich. Applications of lasers in microelectronics and micromechanics. *Applied Surface Science*, 79–80:12–24, 1994.
- [210] Kyung Hyun Park, Myong Wook Kim, Young Tae Byun, Sun Ho Kim, Wook Rae Cho, Sung Han Park, Ung Kim, and Sang Sam Choi. Negative pattern generation technique by laser beam writing for integrated optics. *Japanese Journal of Applied Physics*, 37:4844–4845, 1998.

- [211] M. T. Gale, M. Rossi, J. Pedersen, and H. Schütz. Fabrication of continuous-relief micro-optical elements by direct laser writing in photoresist. *Optical Engineering*, 33(11):3556–3566, 1994.
- [212] Y. Cheng, T. Huang, and C. C. Chieng. Thick-film lithography using laser write. *Microsystem Technologies*, 9:17–22, 2002.
- [213] Frank L. Pedrotti and Leno S. Pedrotti. *Introduction to Optics*. Prentice Hall, Upper Saddle River, second edition, 1993.
- [214] Leonidas E. Ocola. Resist requirements for electron projection and direct write nanolithography. In *Mater. Res. Soc. Symposium Proceedings Vol. 705*, pages Y1.1.1–Y1.1.12, 2002.
- [215] Private communication with Dr. Miro Belov, formerly with the Department of Physics, University of Alberta.
- [216] K. Y. Lee, N. LaBianca, S. A. Rishton, S. Zoghamain, J. D. Gelorme, J. Shaw, and T. H. P. Chang. Micromachining applications of a high resolution ultrathick photoresist. *Journal of Vacuum Science and Technology B*, 13(6):3012–3016, 1995.
- [217] H. Lorenz, M. Despont, N. Fahrni, N. Labianca, P. Renaud, and P. Vettiger. SU-8: A low-cost negative resist for MEMS. *Journal of Micromechanics and Microengineering*, 7:121–124, 1997.
- [218] W. H. Wong and E. Y. B. Pun. Exposure characteristics and three-dimensional profiling of SU8C resist using electron beam lithography. *Journal of Vacuum Science and Technology B*, 19(3):732–735, 2001.
- [219] C. Cremers, F. Bouamrane, L. Singleton, and R. Schenk. SU-8 as resist material for deep x-ray lithography. *Microsystem Technologies*, 7:11–16, 2001.
- [220] Private communication with Dr. Niels Wijnaendts van Resandt, President of Heidelberg Instruments Inc., USA.
- [221] Lotien Richard Huang, Edward C. Cox, Robert H. Austin, and James C. Sturm. Continuous particle separation through deterministic lateral displacement. *Science*, 304:987–990, 2004.
- [222] K. Starbova, V. Mankov, J. Dikova, and N. Starbov. The effects of vapour incidence on the microstructure and related properties of condensed GeS<sub>2</sub> thin films. *Vacuum*, 53(3–4):441–445, 1999.

- [223] Martin O. Jensen and Michael J. Brett. Porosity engineering in glancing angle deposition thin films. In press.
- [224] Edward D. Palik. *Handbook of Optical Constants of Solids*. Academic Press, Orlando, 1985.
- [225] R. Jacobsson. Inhomogeneous and coevaporated homogeneous films for optical applications. In G. Hass, M. Francombe, and R. Hoffman, editors, *Physics of Thin Films*, volume 8, pages 51–98. Academic Press, 1975.
- [226] M. J. Colgan, B. Djurfors, D. G. Ivey, and M. J. Brett. Effects of annealing on titanium dioxide structured films. *Thin Solid Films*, 466(1–2):92–96, 2004.
- [227] T. K. Gaylord and G. R. Kilby. Optical single-angle plane-wave transmittances/reflectances from Schwarzschild objective variable-angle measurements. *Review of Scientific Instruments*, 75(2):317–323, 2004.
- [228] S. G. Kaplan and L. M. Hanssen. Silicon as a standard material for infrared reflectance and transmittance from 2  $\mu\text{m}$  to 5  $\mu\text{m}$ . *Infrared Physics and Technology*, 43:389–396, 2002.
- [229] W. M. Robertson, G. Arjavalingam, R. D. Meade, K. D. Brommer, A. M. Rappe, and J. D. Joannopoulos. Measurement of photonic band structure in a two-dimensional periodic dielectric array. *Physical Review Letters*, 68(13):2023–2026, 1992.
- [230] S. Rowson, A. Chelnokov, and J. M. Lourtioz. Two-dimensional photonic crystals in macroporous silicon: From mid-infrared (10  $\mu\text{m}$ ) to telecommunications wavelengths (1.3–1.5  $\mu\text{m}$ ). *Journal of Lightwave Technology*, 17(11):1989–1995, 1999.
- [231] Martin O. Jensen and Michael J. Brett. Functional pattern engineering in glancing angle deposition thin films. In press.
- [232] Alongkarn Chutinan and Sajeew John. Diffractionless flow of light in 2D-3D photonic band gap heterostructures: Theory, design rules, and simulations. In press.
- [233] Alongkarn Chutinan, Sajeew John, and Ovidiu. Diffractionless flow of light in all-optical microchips. *Physical Review Letters*, 90(12):123901, 2004.

- [234] M. W. Horn, M. D. Pickett, R. Messier, and A. Lakhtakia. Blending of nanoscale and microscale in uniform large-area sculptured thin-film architectures. *Journal of Nanotechnology*, 15(3):303–310, 2004.
- [235] F. E. Vermeulen, C. R. James, and A. M. Robinson. Hollow microstructural waveguides for propagation of infrared radiation. *Journal of Lightwave Technology*, 9(9):1053–1060, 1991.
- [236] W. E. A. Van Petegem, C. R. James, F. E. Vermeulen, and A. M. Robinson. Numerical analysis of near-infrared wave propagation characteristics in dielectric-coated parallel plate microstructural waveguides. *IEEE Transactions on Microwave Theory and Techniques*, 45(3):367–375, 1997.
- [237] J. A. Harrington. A review of IR transmitting hollow waveguides. *Fibre and Integrated Optics*, 19:211–227, 2000.
- [238] K. Takatani, Y. Matsuura, and M. Miyagi. Theoretical and experimental investigations of loss behaviour in the infrared in quartz hollow waveguides with rough inner surfaces. *Applied Optics*, 34(21):4352–4357, 1995.
- [239] T. B. Massalski. *Binary Alloy Phase Diagrams*. American Society for Metals, Metals Park, 1986.
- [240] S. E. Shoaf and A. D. Feinerman. Aligned Au-Si eutectic bonding of silicon structures. *Journal of Vacuum Science and Technology A*, 12(1):19–22, 1994.
- [241] A. L. Tiensuu, M. Bexell, J. Å. Schweitz, L. Smith, and S. Johansson. Assembling three-dimensional microstructures using gold-silicon eutectic bonding. *Sensors and Actuators A*, 45:227–236, 1994.
- [242] G. T. A. Kovacs. *Micromachined Transducers Sourcebook*. McGraw-Hill, Boston, 1998.
- [243] D. Maas, B. Bustgens, J. Fahrenberg, W. Keller, P. Rutner, W. K. Schomburg, and D. Seidel. Fabrication of microcomponents using adhesive bonding techniques. In *IEEE Proceedings of the Ninth International Workshop on Micro Electromechanical Systems*, pages 331–336, 1995.

- [244] R. P. U. Karunasiri, R. Bruinsma, and J. Rudnick. Thin-film growth and the shadow instability. *Physical Review Letters*, 62(7):788–791, 1989.
- [245] Private communication with Peter Hruday, Department of Electrical and Computer Engineering, University of Alberta.
- [246] D. Gish, G. K. Kiema, M. O. Jensen, and M. J. Brett. Dye sensitized solar cells using nanostructured thin films of titanium dioxide. In *Materials Research Society Symposium Proceedings Vol. 636*, page L5.13, 2004.
- [247] M. W. Seto, B. Dick, and M. J. Brett. Nanoindentation of microspring thin films. In *MEMS Devices III Symposium (Mater. Res. Soc. Symposium Proceedings Vol. 657)*, pages EE5.15.1–EE5.15.6, 2001.
- [248] P. Gravesen, J. Branebjerg, and O. S. Jensen. Microfluidics – a review. *Journal of Micromechanics and Microengineering*, 3:168–182, 1993.
- [249] E. Bassous, H. H. Taub, and L. Kuhn. Ink jet printing nozzle arrays etched in silicon. *Applied Physics Letters*, 31:135–137, 1977.
- [250] S. C. Terry, J. H. Jerman, and J. B. Angell. A gas chromatographic air analyzer fabricated on a silicon wafer. *IEEE Transactions on Electron Devices*, ED-26:1880–1886, 1979.
- [251] E. Verpoorte and N. D. De Rooij. Microfluidics meets MEMS. *Proceedings of the IEEE*, 91(6):930–953, 2003.
- [252] H. Andersson and A. van den Berg. Microfluidic devices for cellomics: A review. *Sensors and Actuators B*, B92(3):315–325, 2003.
- [253] N. Lion, T. C. Rohner, L. Dayon, I. L. Arnaud, E. Damoc, N. Youhnovski, Z. Y. Wu, C. Roussel, J. Josserand, H. Jensen, J. S. Rossier, M. Przybylski, and H. H. Girault. Microfluidic systems in proteomics. *Electrophoresis*, 24(21):3533–3562, 2003.
- [254] E. Heftmann. *Chromatography: Fundamentals and Applications of Chromatography and Related Differential Migration Methods*. Elsevier, Amsterdam, fifth edition, 1992.
- [255] A. L. Dupont and G. Mortha. Comparative evaluation of size-exclusion chromatography and viscometry for the characteristics of cellulose. *Journal of Chromatography A*, 1026:129–141, 2004.

- [256] M. Baba, T. Sano, N. Iguchi, , K. Iida, T. Sakamoto, and H. Kawaura. DNA size separation using artificially nanostructured matrix. *Applied Physics Letters*, 83:1468–1470, 2003.
- [257] L. R. Huang, E. C. Cox, R. H. Austin, and J. C. Sturm. Continuous particle separation through deterministic lateral displacement. *Science*, 304:987–990, 2004.
- [258] M. Loncar, A. Scherer, and Y. Qiu. Photonic crystal laser sources for chemical detection. *Applied Physics Letters*, 82(26):4648–4650, 2003.